Simulatie van vloeistof-structuurinteractie bij (herstelde) aorta-coarctatie

Fluid-Structure Interaction Simulation of (Repaired) Aortic Coarctation

Liesbeth Taelman

Promotoren: prof. dr. ir. P. Segers, prof. dr. ir. J. Vierendeels
Proefschrift ingediend tot het behalen van de graad van
Doctor in de Ingenieurswetenschappen: Biomedische Ingenieurstechnieken

Vakgroep Elektronica en Informatiesystemen
Voorzitter: prof. dr. ir. J. Van Campenhout
Faculteit Ingenieurswetenschappen en Architectuur
Academiejaar 2014 - 2015

ISBN 978-90-8578-727-3
NUR 954
Wettelijk depot: D/2014/10.500/73

Supervisors:

Prof. dr. ir. Patrick Segers
Prof. dr. ir. Jan Vierendeels

Research lab:

Institute Biomedical Technology
Biofluid, Tissue and Solid Mechanics for Medical Applications (bioMMeda)
iMinds Medical IT
Ghent University
De Pintelaan 185 - Blok B
B–9000 Gent
BELGIUM

Members of the exam committee:

Chairman:	
Prof. dr. ir. Patrick De Baets	Faculty of Engineering and Architecture, UGent
Secretary:	
Prof. dr. ir. Abigail Swillens	Faculty of Engineering and Architecture, UGent
Reading committee:	
Prof. dr. ir. Jean-Frédéric Gerbeau	INRIA Paris-Rocquencourt, France
Prof. dr. ir. Patrick Segers	Faculty of Engineering and Architecture, UGent
Dr. ir. Pieter Rauwoens	Faculty of Engineering and Architecture, UGent
Other members:	
Dr. Katrien François	Faculty of Medicine and Health Sciences, UGent
Dr. Vivek Muthurangu	UCL, London, United Kingdom
Prof. dr. ir. Jan Vierendeels	Faculty of Engineering and Architecture, UGent
Prof. dr. ir. Joris Degroote	Faculty of Engineering and Architecture, UGent

This research was funded by a research grant of FWO-Vlaanderen (project nr. G.0085.09).

Preface

When I started my engineering studies at the university of Ghent in 2005, I always pictured myself working for an industrial company afterwards. Accordingly, I never would have guessed that in 2010, when I graduated as an electromechanical engineer, I would have started my career as a PhD student.

However, during my master thesis at the Department of Flow, Heat and Combustion Mechanics my fascination for research and numerical simulations in particular grew stronger. One of the main motivations for my increasing interest was the excellent support of our (Joris Bols and me) thesis supervisor prof. dr. ir. Joris Degroote. Patiently, he learned us to use numerical software packages and explore their many possibilities or circumvent their restrictions. But most of all he learned us to work independently and handle problems in a proper way; an unmistakable quality of a good researcher. Without this crucial training and this first experience with fluid-structure interaction simulations, the realization of this dissertation would not have been possible.

When after four months of research prof. dr. ir. Jan Vierendeels and prof. dr. ir. Patrick Segers offered me the opportunity to extend my knowledge in the area of fluid-structure interaction in a socially relevant, clinical context I decided to take the leap, tempted by the prospects to work in an excellent lab and having the opportunity to discover a part of the world.

Along these four years as a PhD student I gained a lot of technical knowledge about fluid and structural mechanics but also other skills (such as presentation and writing skills, the ability to handle complex problems systematically and independently, ...) that will be very useful later in life. Additionally, I learned a lot about myself, my strengths and weaknesses and it gave me a better idea of the qualities I was looking for in my new job. Nevertheless, the road to this final result was complicated and not without its up and downs. The many technical challenges and difficult reviews have repeatedly caused stress and frustrations, but fortunately I was well supported by my promoters, colleagues, family and friends who provided me with the necessary advice and pep talk. Herewith I would like to express my gratitude for their help and encouragement.

First of all I would like to thank my promoter Patrick Segers who always believed in my work and my abilities even when I was doubting myself after an unexpected critical review. He always made time to listen to my problems and provided me with new inspiration, positivism and confidence. I would also like to thank him for the many conference proceedings and papers that he revised and always returned in an improved format. I am grateful he gave me the opportunity to do this PhD at bioMMeda and that he brought me into contact with other people who helped me with my research.

Next, I would like to thank my co-promoter Jan Vierendeels. His exceptional technical knowledge, critical mind and perseverance were indispensible for the achievements obtained in this dissertation. I hope the collaboration between bioMMeda and the Department of Flow, Heat and Combustion Mechanics will continue to exist, as the combination of the knowledge and experience of both labs is the key feature to adequate research.

Undoubtedly, the work and help of Joris Degroote were essential for the realization of the fluid-structure interaction simulations in this dissertation. Not only did he create the coupling code Tango and learned me to work with it, he also provided an exceptional support (nearly 24/7!), updated and extended the coupling code and inspired me with new ideas and suggestions when my research was stuck. Additionally, I would like to thank him for his listening ear and advice and for the many abstracts and papers he carefully corrected.

I would like to dedicate a special thank you to prof. dr. ir. Vivek Muthurangu and Joseph Panzer for providing the clinical data. Furthermore, I would like to thank all my colleagues at bioMMeda and FloHeaCom and in particular my previous and current office mates (Alessandra, Danilo, Darya, David, Dieter, Gianluca, Koen, Luis, Margo and Wouter) for the pleasant coffee brakes, the many birthday parties and for supplying me with chocolate when I was a bit down (or felt like eating chocolate). Additionally I would like to thank Jurgen and Yves for their technical support and Saskia for her administrative support and all the practical arrangements she made. I Thank the members of my jury for their interest in my work and their comments and suggestions.

Finally, I want to express my gratitude to my family and friends for their encouragement. I especially thank my parents for giving me the opportunity to study at university and introducing me into the clinical field. I believe my interest in engineering combined with the clinical background of my parents were my motivation to choose for a research topic in biomedical engineering.
Last but not least, I would like to thank my partner in life Joris Bols. I had the incredible opportunity to experience this research adventure with him. Sharing and discussing my research with him, encouraged me to persist in my efforts as he was truly interested in and proud of my work. Not only he was there to help me with writing scripts and giving IT support, he also was the perfect companion to relax between or after working hours. I am

grateful we spend this journey together and, going to the same conferences, were able to discover part of the world together.

Liesbeth Taelman
Gent, September 2013

SAMENVATTING
SUMMARY

Samenvatting

INLEIDING

Aorta-coarctatie (CoA) is een congenitale aandoening, gekenmerkt door een vernauwing van de aorta descendens, die de bloedstroming van het hart naar het lagere lichaamsgedeelte verstoort. De vernauwing kan niet-invasief behandeld worden door middel van een stent en/of ballon katheter of wordt chirurgisch verwijderd. Ondanks een succesvolle behandeling blijft het risico op cardiovasculaire morbiditeit (zoals hypertensie en hypertrofie van het hart) en mortaliteit groot. Dit suggereert dat chirurgische of transkatheter behandelingen de complexe pathologie van aorta-coarctatie weliswaar wijzigen maar niet helemaal corrigeren. Aorta-coarctatie kan dan ook niet als een eenvoudige ziekte beschouwd worden. Om de langetermijn uitkomst van de behandeling voor individuele patiënten beter te begrijpen en te kunnen voorspellen zijn klinische en biomedische studies noodzakelijk.

De verhoogde morbiditeit na de behandeling van CoA werd in 1971 voor het eerst door O'Rourke gelinkt aan een nefaste hemodynamische en biomechanische belasting van de thoracale aorta en de vertakkingen als gevolg van de vernauwing. Gezien de bloedstroming in sterke mate de pathogenesis beïnvloedt en vice versa, is gedetailleerde hemodynamische informatie mogelijks van bijzonder klinisch belang. Zo kan de studie van de hemodynamica onder meer waardevolle informatie verschaffen bij het stellen van de diagnose van cardiovasculaire aandoeningen (zoals CoA) en bij de evaluatie van de behandeling. Ondanks het feit dat voorgaande hypothese al enige tijd bestaat, focust het merendeel van de klinische studies rond aorta-coarctatie zich in hoofdzaak op de ontwikkeling van cardiovasculaire complicaties, het sterftecijfer en het reduceren van de drukval over de coarctatie. De correlatie van meer gedetailleerde hemodynamische indices met de manifestatie van laattijdige morbiditeit wordt echter zelden bestudeerd. De onderliggende rol van de hemodynamica in de ontwikkeling van de ziekte is bijgevolg onvoldoende begrepen.

Numerieke simulaties vormen steeds meer een optimaal hulpmiddel in de studie van de patiëntspecifieke hemodynamica, dankzij de vorderingen in rekenkracht, klinische beeldvorming en segmentatie software. Zo verschaffen zij onder meer gegevens die moeilijk in vivo op te meten zijn, zoals het drukveld doorheen de aorta en details van de bloed-

stroming. De ontwikkeling van beeldvormende modaliteiten zoals MRI en CT laten toe een patiëntspecifieke geometrie te extraheren. Deze geometrische informatie gecombineerd met fase-contrast MRI, hartkatheterisatie of ultrageluid metingen laten toe om een 3D patiëntspecifiek model met aangepaste randvoorwaarden te creëren dat eveneens de biomechanische arteriële eigenschappen in rekening brengt. Toepassing van computationele patiëntspecifieke modellen in de studie van aorta-coarctatie kan bijdragen tot een beter inzicht in de oorzaak van de langetermijn morbiditeit, huidige behandelingsstrategieën verbeteren en de evaluatie van aorta-coarctatie vergemakkelijken door hemodynamische parameters te kwantificeren in de gehele aorta.

Dit proefschrift focust zich op de numerieke modellering van de hemodynamica in behandelde CoA. Vermits starre wand simulaties niet in staat zijn belangrijke fysiologische patronen zoals golfpropagatie en -reflectie te modelleren, wordt hierbij de fluïdum-structuurinteractie (FSI) tussen de bloedstroming en de vervormbare arteriële wand in rekening gebracht.

Deze dissertatie is opgedeeld in twee delen. Het eerste is een meer technisch deel waarin bepaalde numerieke aspecten gerelateerd aan cardiovasculaire simulaties en in het bijzonder aan de fluïdum-structuurinteractie aanpak worden toegelicht. Het tweede deel focust op de (klinische) applicatie van de computationele modellen van aorta-coarctatie.

DEEL I. NUMERIEKE ASPECTEN BETREFFENDE (CARDIOVASCULAIRE) FLUÏDUM-STRUCTUURINTERACTIE SIMULATIES

Hoofdstuk 1. Modellering van de hemodynamica in vasculaire netwerken gebruik makende van een geometrische multischaal aanpak: numerieke aspecten

Enerzijds vereist de zeer sterke heterogeniteit van de bloedsomloop het gebruik van verschillende modellen in zijn afzonderlijke compartimenten (de aorta, grote slagaders, microcirculatie, orgaansystemen), die gekenmerkt worden door verschillende aannames met betrekking tot de ruimtelijke vrijheidsgraden (0D, 1D of 3D). Anderzijds impliceert de interactie tussen deze compartimenten het gecombineerd gebruik van deze modellen, i.e. geometrische multischaal modellen, waarbij de hoofdgedachte bestaat uit het koppelen van 3D modellen met vereenvoudigde 1D en/of 0D modellen. Aldus kan gedetailleerde informatie omtrent de bloedstroming in een specifieke regio verkregen worden, rekening houdend met de globale circulatie en de connectiviteit tussen de verschillende compartimenten. De combinatie van verschillende modellen (gekarakteriseerd door verschillende mathematische beschrijvingen) geeft niettemin aanleiding tot vele moeilijkheden zoals de toewijzing van randvoorwaarden aan het raakvlak tussen twee modellen en de ontwikkeling van robuuste koppelingsalgoritmes. Deze laatste uitdaging heeft enkel betrekking op gepartitioneerde

oplossingsmethodes waarbij de deelproblemen afzonderlijk aangepakt worden. Deze literatuurstudie geeft een overzicht van de belangrijkste aspecten betreffende 3D-1D-0D gekoppelde modellen. Aanvullend worden enkele applicaties voorgesteld ter illustratie van de mogelijkheden van deze gekoppelde modellen.

In dit proefschrift wordt verder de nadruk gelegd op de studie van de lokale bloedstroming in behandelde aorta-coarctatie, omdat bestaande CoA modellen belangrijke limitaties kennen, en dit zowel vanuit een numeriek als een klinisch standpunt. De belangrijkste doelstellingen van dit onderzoek omvatten dan ook de ontwikkeling van een 3D computationeel model, de verbetering van de huidige oplossingsstrategieën en de toepassing ervan voor het verwerven van inzicht in relevante klinische toepassingen. De koppeling van de 3D modellen ontwikkeld in deze thesis met bestaande 1D-0D modellen is een toekomstperspectief voor onze onderzoeksgroep.

Hoofdstuk 2. Fluïdum-structuurinteractie simulatie van de pulspropagatie in arteriën: numerieke valkuilen

Bij de numerieke simulatie van de voortplanting van een drukpuls in de arteriën moeten de discretisatie parameters (met name de tijdstapgrootte Δt en de grootte van het rekenrooster Δx) zorgvuldig gekozen worden. Dit vermijdt een afname in amplitude van de lopende golf ten gevolge van numerieke dissipatie. Numerieke dissipatie en de invloed hiervan op de oplossing worden soms over het hoofd gezien bij fluïdum-structuurinteractie simulaties, waar de numerieke parameters vaak geoptimaliseerd zijn met betrekking tot tijdsefficiëntie en stabiliteit eerder dan nauwkeurigheid. Gebruik makende van een numeriek FSI model van de pulspropagatie in een arterie wordt in dit hoofdstuk het effect van de numerieke dissipatie bestudeerd. Aan de hand van een analytische studie waarin de scalaire, lineaire één-dimensionale transportvergelijking beschouwd wordt, krijgen we meer inzicht in de invloed van de temporele en spatiale resolutie van de golf op de resultaten. Hoewel dit model niet de volledige complexiteit van het coarctatie probleem in rekening brengt, kunnen deze resultaten toch gebruikt worden als een richtlijn bij de selectie van de numerieke parameters.

Er wordt aangetoond dat de numerieke dissipatie van drie parameters afhangt: $\Delta t/T$ en $\Delta x/\lambda$, die de temporele en spatiale resolutie van de golfharmonischen bepalen en $t/\Delta t$, die het aantal opeenvolgende tijdstappen waarbinnen de dissipatie zich voordoet definieert. Het is bewezen dat voor een tweede-orde upwind discretisatie schema in combinatie met een tweede-orde impliciet tijdsintegratie schema, de numerieke dissipatie na een propagatietijd t meer dan lineair toeneemt met toenemende $\Delta t/T$ en met toenemende $\Delta x/\lambda$. Bovendien is de vergelijking gemaakt met een simulatie waarvoor een eerste-orde impliciet tijdsintegratie schema gebruikt is. Uit deze vergelijking volgt dat een sterk verhoogde temporele resolutie nodig is bij het gebruik van een eerste orde schema. Gezien in cardio-

vasculaire simulaties de roostergrootte typisch een paar ordes kleiner is dan de golflengte van de aanwezige golfharmonischen, heeft de spatiale resolutie weinig impact op de numerieke dissipatie.

De resultaten van de analytische en numerieke studies zijn vervolgens gebruikt om de numerieke parameters te bepalen noodzakelijk voor een rooster en tijdstap geconvergeerde simulatie van de golfpropagatie en -reflectie in een vereenvoudigd model van een aorta met herstelde aorta-coarctatie.

Hoofdstuk 3. Stabiliteitsanalyse van een fluïdum-structuurinteractie simulatie met toepassing van verschillende tijdsintegratie schema's en tijdstapgroottes voor het stromings- en structuurprobleem

Gekoppelde numerieke problemen, zoals fluïdum-structuurinteractie simulaties, gebruiken dikwijls verschillende tijdsintegratie schema's om de verscheidene deelproblemen te discretiseren en in sommige gevallen zijn verschillende tijdstapgroottes aangewezen. Aangezien deze aanpak stabiliteitsproblemen kan induceren, werd een stabiliteitsanalyse uitgevoerd van het FSI probleem waarin de stroming in een arterie berekend werd gebruik makende van verschillende tijdsintegratie schema's en zogenaamde 'sub-cyles' in de individuele deelproblemen. Het backward Euler schema en het backward Euler/Hilber-Hughes-Taylor schema werden hierbij gebruikt voor de temporele discretisatie van, respectievelijk, het stromings- en structuurprobleem. Ondanks het gebruik van deze specifieke schema's, blijft de analyse algemeen toepasbaar voor iedere combinatie van tijdsintegratie schema's. Naast de geselecteerde tijdsintegratie schema's beïnvloedt ook de interpolatie methode, gebruikt in de sub-cycles, de stabiliteit en de nauwkeurigheid van de oplossing. Voor sub-cycling in het stromingsprobleem werd een procedure ontwikkeld waarvan de stabiliteit tevens aangetoond is. In vergelijking met een FSI simulatie waarin de tijdstap aangepast is aan de kleinste vereiste tijdschaal, verlaagt deze procedure de rekentijd aanzienlijk zonder verlies in nauwkeurigheid. Sub-cycling in het structuurdomein daarentegen resulteerde in een onstabiel gedrag. Om deze analytische resultaten na te gaan werd een numerieke studie uitgevoerd waarin twee-dimensionale axisymmetrische FSI simulaties gebruikt werden.

Hoofdstuk 4. Ontwikkeling en validatie van een patiëntspecifiek FSI model van de aortaboog

Het fluïdum-structuurinteractie probleem wordt op een gepartitioneerde manier opgelost. Dit betekent dat de stromings- en structuurvergelijkingen berekend worden door aparte solvers. Deze aanpak behoudt software modulariteit en laat toe de stromings- en structuurvergelijkingen op te lossen met technieken die bijzonder geschikt zijn om de respectievelijke vergelijkingen op te lossen. Behalve een stromings- en een structuurpakket is ook een koppelingsalgoritme nodig om de interactie tussen de stroming en de beweging van de structuur in rekening te brengen. In dit onderzoek werd de IQN-ILS (interface quasi-Newton

algoritme met een benadering voor de inverse van de Jacobiaan) techniek gebruikt, een algoritme dat minder koppelingsiteraties nodig heeft in vergelijking met andere gepartitioneerde procedures.

Het stromings- en structuurmodel werden ontwikkeld met bijzondere aandacht voor de randvoorwaarden en de materiaaleigenschappen. De stromingsvergelijkingen werden opgelost in een Arbitraire Lagrange-Euler formulering op een vervormend rooster om een accurate berekening van de spanning op de fluïdum-structuurinterface te bekomen. Gezien het aantal rooster cellen gerelateerd is met de simulatietijd, is het gebruik van een efficiënt rooster belangrijk om de rekentijd te beperken. De complexiteit van de stroming distaal van de stenosis vereist het gebruik van een fijn rekenrooster in deze regio teneinde het stromingsveld voldoende nauwkeurig op te lossen in de ruimte. Dit werd gerealiseerd door het rooster van het stromingsdomein lokaal te verfijnen. In dit proefschrift werd een tijdstapgrootte van 2 ms gebruikt voor de FSI simulaties. Deze waarde vormt een compromis tussen nauwkeurigheid en rekentijd. De fout bekomen met deze tijdstapgrootte is voldoende lager dan het verschil in de resultaten, bekomen met de parameter modellen van herstelde CoA (zie hoofdstuk 7).

We maakten ook de vergelijking tussen de stroming aan de aorta descendens bekomen met een vaste wand en een flexibele wand simulatie. Het model met een vaste wand laat niet toe propagatie van de golf te modelleren, en geeft ook aanleiding tot een significante overschatting van de drukpuls.

DEEL II. KLINISCHE APPLICATIE: SIMULATIE VAN AORTA-COARCTATIE

Hoofdstuk 5. Een introductie tot aorta-coarctatie en zijn computationele modellering

Dit hoofdstuk omvat een literatuurstudie rond de computationele modellering van aorta-coarctatie. De belangrijkste motivatie voor de hemodynamische studie van (herstelde) aorta-coarctatie is de wederzijdse beïnvloeding van de bloedstroming en het vasculaire ziekteproces. Studie van de hemodynamica is dusdanig van klinisch belang, onder meer om cardiovasculaire aandoeningen te detecteren en de behandeling ervan te evalueren. Computationele modellen kunnen bijdragen tot een beter begrip van de langetermijn prognose van herstelde CoA en bieden de mogelijkheid om processen geassocieerd met de langetermijn morbiditeit te detecteren alvorens ze klinisch relevant worden.

De literatuur rond computationele modellering van (behandelde) coarctatie is niettemin vrij beperkt. In dit hoofdstuk wordt een overzicht gegeven van de meest recente numerieke analyses rond CoA met een bespreking van de tekortkomingen in deze studies. In vergelijking met de numerieke studies die dateren van een decennium terug, werden significante

vorderingen gemaakt met betrekking tot een meer fysiologische modellering. Deze omvatten onder meer de extractie van een patiëntspecifieke anatomie uit medische beeldvorming, het gebruik van gepaste randvoorwaarden (die de stroomafwaartse vasculaire weerstand en compliantie vertegenwoordigen) en de modellering van arteriële compliantie. Andere aspecten zoals de incorporatie van de vasculaire hermodellering en de inclusie van de collaterale bloedstroming bevinden zich nog in een beginnend stadium van ontwikkeling en vereisen experimentele of in vivo validatie. Naast de vereenvoudigingen gemaakt in de huidige modellen, moet men ook rekening houden met het feit dat klinische applicaties op grote schaal ontbreken. Al de geciteerde numerieke studies rapporteren resultaten van een beperkt aantal gevallen die bevestigd moeten worden in uitgebreidere studies.

Niettegenstaande hun beperkte applicatie, ondersteunen deze preliminaire studies de hypothese vooropgesteld door O'Rourke dat de hemodynamica en biomechanica een cruciale rol spelen in de prognose van behandelde coarctatie. Met de recente vooruitgang in computationele modellering in het achterhoofd, geloven wij dat deze simulaties het potentieel hebben de overige klinische vragen, met in het bijzonder de rol van golfreflecties, te beantwoorden.

Hoofdstuk 6. Analyse van de hemodynamische impact van een lokale verstijving

De specifieke factoren die bijdragen tot de verhoogde langetermijn morbiditeit na de behandeling van coarctatie zijn tot op heden onvoldoende gekend. Twee factoren die mogelijks een rol spelen in de prognose van behandelde CoA zijn de aanwezigheid van een residuele vernauwing (recoarctatie) en een stijvere zone, veroorzaakt door de aanwezigheid van een stent of littekenweefsel. Aangezien bij benadering 60% van de buffercapaciteit van de aorta gelokaliseerd is in de proximale aorta, beïnvloedt deze verstijving de dempingsfunctie van de aorta aanzienlijk. De lokale vernauwing anderzijds, leidt tot een additionele weerstand in het arterieel systeem. Daarnaast genereren de lokale verstijving en vernauwing golfreflecties die het hart vroegtijdig bereiken, gezien de beperkte afstand tot het hart. De vele interfererende factoren en adaptieve fysiologische mechanismen die in vivo simultaan aanwezig zijn verhinderen de studie van de geïsoleerde impact van de individuele factoren. Omdat experimentele of computationele studies gemakkelijker toelaten de impact van een enkele parameter te repliceren, zijn deze benaderingen cruciaal in het begrip van de centrale hemodynamica na de behandeling van CoA.

Gezien de complexiteit, inherent aan patiëntspecifieke aorta modellen, de inzichten verschaft door deze modellen beperkt, werd in eerste plaats een vereenvoudigd model toegepast. Het doel van deze studie is de simulatie van de golfpropagatie in een lokaal verstijfde buis en de analyse van de hemodynamische impact van een stijf segment. Het voordeel van

dit model is dat alle aanwezige reflecties gegenereerd zijn door de lokale verstijving en dus gemakkelijk geïnterpreteerd kunnen worden.

De simulatieresultaten tonen aan dat de aanwezigheid van een stijf segment een belangrijke impact heeft op een korte drukpuls, maar nauwelijks effect heeft op een fysiologische drukpuls. Dit fenomeen werd verklaard aan de hand van een analyse van de reflecties geïnduceerd door de verstijving. Bij de overgang van een drukpuls van de flexibele aorta naar de verstijving wordt een achterwaartse compressiegolf gegenereerd, gevolgd door een sequentie van achterwaartse expansiegolven, die gecreëerd worden aan het distaal einde van de verstijving. Proximaal overlappen deze golven en heffen ze elkaar op zodat de hemodynamica bijna ongewijzigd blijft.

Hoofdstuk 7. Impact van een lokale verstijving en residuele vernauwing op de centrale hemodynamica gezien in herstelde aorta-coarctatie: een computationele studie

De basis voor deze numerieke studie is de creatie van een patiëntspecifieke geometrie, inclusief de residuele vernauwing die vaak optreedt na de behandeling van CoA. Gezien de huidige modellen een al te sterke vereenvoudiging inhouden van de fysiologische systemen of een uitgebreide toepassing en/of parameterstudie missen, heeft dit onderzoek tot doelstelling een patiëntspecifiek parametrisch model te ontwikkelen dat toelaat de impact van een (gecombineerde) vernauwing en verstijving in herstelde CoA te voorspellen. Verschillende lengtes, stijfheden en diameter reducties van de coarctatie zone werden bestudeerd en hun resultaten vergeleken met de hemodynamische toestand in een gezonde aorta.

Er werd aangetoond dat de FSI modellering een belangrijke rol speelt in de correcte evaluatie van CoA. De buffering van de bloedstroming in de proximale aorta dempt de drukpuls uit en reduceert de bloedsnelheid in de coarctatie en de geassocieerde drukval. In het distaal gedeelte van de aorta resulteert de vernauwing in een sterke niet-uniforme stroming en de ontwikkeling van vortices. Deze observaties tonen aan dat het gebruik van 1D modellen in de voorspelling van de stenose-geïnduceerde drukval en golfreflecties incorrecte resultaten oplevert.

In overeenkomst met de resultaten gerapporteerd in hoofdstuk 6, blijft de globale impact van een lokale verstijving op de hemodynamica vrij beperkt. Lokaal neemt de piek systolische druk toe met een maximum van 8 mmHg. De stroming in de aorta en de gemiddelde drukval langsheen de aorta blijven hierbij min of meer constant (0.8 mmHg). In het geval van een residuele vernauwing zijn de veranderingen van de bloeddruk in de proximale aorta meer uitgesproken en zijn ze gedurende de volledige systolische fase aanwezig. De drukval over de CoA wordt gevolgd door een drukherstel dat plaats vindt in een groot gedeelte van de aorta descendens. Een ernstige vernauwing wordt gekarakteriseerd door een beperkt drukherstel (i. e. een grotere energie dissipatie ten gevolge van de ontwikkeling van turbu-

lentie). Voor een korte stenose heeft een additionele verstijving een belangrijk effect op de evolutie van de druk opwaarts van de vernauwing (toename tot 27 mmHg). De impact van een langere verstijving is relatief beperkt (tot 9 mmHg).

Een evaluatie van CoA gebaseerd op de netto golfintensiteit alleen resulteert in een aanzienlijke onderschatting van de compressiegolf gegenereerd door de aanwezigheid van een vernauwing en bevat misleidende informatie betreffende de afstand tot de reflectiebron.

Hoofdstuk 8. De aorta reservoir-golf als een paradigma voor arteriële hemodynamica: inzichten van 3D fluïdum-structuurinteractie simulaties in een model van aorta-coarctatie

Het reservoir-golf paradigma beschouwt de druk in de aorta als de superpositie van een 'reservoir druk', gerelateerd aan de veranderingen in reservoir volume en een 'overdruk' gelinkt met de golfdynamica. De verandering in de reservoir druk wordt verondersteld proportioneel te zijn met het verschil tussen in- en uitstroming. Deze aanname is echter onmogelijk in vivo te valideren. Het doel van deze studie is het reservoir-golf paradigma te toetsen aan en toe te passen op de aortadruk en de stromingsgolf bekomen met 3D FSI simulaties in een model van (a) een normale aorta, (b) aorta-coarctatie (vernauwde aorta descendens) en (c) gestente coarctatie (stijf segment in de aorta descendens). In geen van deze simulaties werd een lineaire relatie tussen het volume van de aorta en de reservoir druk gevonden. In een druk-volume diagram werden hysteresislussen bekomen die doorlopen worden in tegenwijzerzin. Dit wijst er op dat de reservoir druk lager is dan de druk geassocieerd met de verandering van het volume. De reservoir-golf analyse leidt tot zeer hoge overdrukken, in het bijzonder bij de coarctatie modellen. Ondanks de verminderde buffer capaciteit van de aorta werd slechts een kleine verandering van de reservoir component gevonden. Samenvattend kan worden gesteld dat, met de observatie dat de reservoir druk niet gerelateerd is met het volume van het aorta reservoir in systole, een intrinsieke aanname van het golf-reservoir concept ontkracht wordt en bijgevolg ook de aanname dat de overdruk de component is van de druk die bijdraagt tot golfpropagatie en -reflectie.

CONCLUSIES

Met dit onderzoek zijn we er in geslaagd belangrijke hemodynamische veranderingen te wijten aan de aanwezigheid van een lokale verstijving en vernauwing na de behandeling van coarctatie, toe te lichten. De correlatie van deze nefaste hemodynamische indices met de langetermijn morbiditeit blijft voer voor toekomstig onderzoek en meer grootschalige numerieke studies. Deze zouden de rol van de verstoorde bloedstroming in de progressie van de ziekte verder moeten kunnen verklaren. Dit onderzoek is dus zeker geen eindpunt. Suggesties voor toekomstig onderzoek zijn opgenomen op het einde van deze thesis. We zijn ervan overtuigd dat in de nabije toekomst, numerieke simulaties zullen leiden tot een

beter begrip van de hemodynamische en biomechanische veranderingen als gevolg van cardiovasculaire aandoeningen en/of de behandeling ervan.

Summary

INTRODUCTION

Aortic coarctation (CoA) is a congenital disease, characterized by a narrowing of the upper descending aorta, obstructing the blood flow from the heart towards the lower part of the body. The treatment can be minimally invasive using a stent and/or a balloon catheter to dilate the coarctation zone, or the narrow section can be removed surgically. Even after a successful treatment, a high risk of cardiovascular morbidity and mortality remains. This suggests that surgical or transcatheter treatments modify rather than correct the complex pathology of aortic coarctation and that coarctation cannot be considered as an uncomplicated disease. Clinical and biomechanical studies are needed to better understand and predict the long-term outcome of the treatment of individual patients.

In 1971 O'Rourke first related morbidity in CoA (repair) to adverse hemodynamics and biomechanics in the thoracic aorta and the side branches. Considering disturbed blood flow strongly affects vascular pathogenesis, and vice versa, hemodynamic information is of high clinical importance, amongst others to diagnose cardiovascular malfunctioning and evaluate treatment outcomes. However, the majority of the clinical CoA studies focuses on the prevalence of cardiovascular complications, the rates of mortality and the post-interventional relief of the pressure drop across the coarctation zone rather than the correlation of hemodynamic indices with manifestation of late morbidity. As such, the underlying role of hemodynamics in the progression of the disease is currently not well understood.

With advances in computing power, clinical imaging and segmentation software, computational simulations are nowadays an optimal tool to study the patient specific hemodynamics and/or the biomechanics, as they can retrieve data that are difficult to obtain in vivo. The development of imaging techniques such as magnetic resonance imaging and computed tomography, allows to extract the patient specific anatomy. This geometrical data together with phase-contrast MRI, cardiac catheterization data or ultrasound measurements can be used to create a 3D patient specific model with properly assigned boundary conditions that, moreover, considers biomechanical arterial properties. Application of computational patient specific models in the context of aortic coarctation can enhance understanding of long-term

morbidity, improve current treatment strategies and facilitate the assessment of coarctation severity by providing a quantification of hemodynamic parameters throughout the entire aorta.

This dissertation focuses on the computational modeling of hemodynamics after coarctation treatment, since hemodynamics are assumed to play an important role in the long-term outcome. As simulations with rigid walls fail to capture some physiological patterns (such as wave propagation and reflection), the fluid-structure interaction (FSI) between the blood flow and the deformation of the arterial wall is taken into account.

This dissertation is divided into two distinct parts. The first one is a more technical part and aims to highlight some issues with respect to cardiovascular simulations and in particular the fluid-structure interaction approach. The second part focuses on the clinical application of a computational model of repaired aortic coarctation.

PART I. NUMERICAL ISSUES CONCERNING (CARDIOVASCULAR) FSI SIMULATIONS

Chapter 1. Modeling hemodynamics in vascular networks using a geometrical multiscale approach: numerical aspects

On the one hand the heterogeneity of the circulatory system requires the use of different models in its different compartments, featuring different assumptions on the spatial degrees of freedom (0D, 1D and 3D). On the other hand, the mutual interactions between its compartments imply that these models should preferably not be considered separately. These requirements have led to the concept of *geometrical multiscale modeling*, where the main idea is to couple 3D models with reduced 1D and/or 0D models. As such detailed information on the pressure and flow field in a specific region of interest can be obtained while accounting for the global circulation. However, the combination of models with different mathematical features gives rise to many difficulties such as the assignment of boundary conditions at the interface between two models and the development of robust coupling algorithms, as the sub-problems are usually solved in a partitioned way. This review aims to give an overview of the most important aspects concerning 3D-1D-0D coupled models. In addition, some applications are presented in order to illustrate the potential of these coupled models.

Nevertheless, in this dissertation, we focus on the study of the local blood flow patterns in (repaired) aortic coarctation. As current CoA models are associated with some important limitations from a computational and a clinical point of view, this research involves the development of a 3D computational model, the improvement of current solution strategies and the clinical application of the model. The coupling of the 3D models, developed in this

research, and the currently existing 1D-0D models is a future perspective for our research group.

Chapter 2. Fluid-structure interaction simulation of pulse propagation in arteries: numerical pitfalls

When simulating the propagation of a pressure pulse in arteries, the discretization parameters (i.e. the time step size Δt and the grid size Δx) need to be chosen carefully in order to avoid a decrease in amplitude of the traveling wave due to numerical dissipation. This feature and its effect on the solution is sometimes overlooked in FSI simulations, where the numerical parameters are often optimized with respect to time efficiency and stability rather than accuracy. In this paper the effect of numerical dissipation is examined using a numerical FSI model of the pulse propagation in an artery. More insight in the influence of the temporal and spatial resolution of the wave on the results of these simulations is gained using an analytical study in which the scalar linear one-dimensional transport equation is considered. Although this model does not take into account the full complexity of the problem under consideration, the results can be used as a guidance for the selection of the numerical parameters.

It is shown that the numerical dissipation depends on three parameters: $\Delta t/T$ and $\Delta x/\lambda$, determining the temporal and spatial resolution of the wave harmonics and $t/\Delta t$, defining the number of consecutive time steps during which the dissipation occurs. It is shown that for a second-order upwind discretization scheme in combination with a second-order implicit time integration scheme, the numerical dissipation *after a propagation time* t increases more than linearly with increasing $\Delta t/T$ and with increasing $\Delta x/\lambda$. Furthermore, the comparison is made with a simulation for which a first-order implicit time integration scheme is used, demonstrating the need for a much higher temporal resolution in the latter case. Since in cardiovascular simulations, the grid size is typically a few orders of magnitude smaller than the wavelength of the present wave harmonics, the spatial resolution will have no significant effect on the numerical dissipation.

The results from the analytical and numerical studies are subsequently used to determine the settings necessary to obtain a grid and time step converged simulation of the wave propagation and reflection in a simplified model of an aorta with repaired aortic coarctation.

Chapter 3. Stability analysis of a fluid-structure interaction simulation using different time integration schemes and time step sizes for the fluid and the structure

Coupled problems, such as fluid-structure interaction simulations, often use different time integration schemes to discretize the different sub-problems and in some cases different time step sizes are required. This approach can, however, induce stability problems. In this chapter, a stability analysis is performed of the FSI problem in which the flow in an artery

is computed using different time integration schemes and sub-cycling within the individual sub-problems. The backward Euler scheme and the backward Euler/Hilber-Hughes-Taylor scheme are used for the temporal discretization of the fluid and the structural problem respectively. Nevertheless, the analysis is generally applicable for any other combination of time integration schemes. Apart from the selected time integration schemes, the interpolation method applied during the sub-cycles strongly affects the stability and the accuracy of the solution. For sub-cycling in the fluid problem, a procedure is devised for which stability is demonstrated. Compared to an FSI simulation for which the time step is adapted to the smallest required time scale, this procedure significantly speeds up the calculation without loss in accuracy. Sub-cycling in the structural domain, however, results in an unstable behavior. To verify the analytical results, a numerical study is performed using two-dimensional axisymmetric FSI simulations.

Chapter 4. Development and validation of a patient specific FSI model of the aortic arch

The fluid-structure interaction problem is solved in a partitioned way, which means the flow and the structural equations are solved separately. This approach preserves software modularity and allows the flow equations and the structural equations to be solved with different techniques that are particularly suited to solve the respective equations. Besides a flow solver and a structural solver, also a coupling algorithm is required to take into account the interaction between flow and motion of the structure. In this research the IQN-ILS technique (quasi-Newton algorithm with an approximation for the inverse of the Jacobian) is used, requiring fewer coupling iterations per time step compared with other partitioned schemes.

A flow and structural model are developed with particular attention for the boundary conditions and the material properties. To obtain an accurate calculation of the stress on the fluid-structure interface, the flow equations are solved in the Arbitrary Lagrangian-Eulerian formulation on a deforming mesh. Since the number of grid cells is related to the simulation time, the use of an efficient computational grid is important to limit the calculation time. As the flow distal to a stenosis is complex and highly disturbed, a high mesh density is required in this region to resolve the flow field in space. This is realized by locally adapting the fluid mesh. In this dissertation a time step size of 2 ms is used for the FSI simulations, as a compromise between accuracy and computation time. The error obtained with this time step size is sufficiently smaller than the mutual differences in results, retrieved with the parameter models of CoA (chapter 7).

The comparison is made between the flows obtained at the descending aorta for a rigid wall and a flexible wall model. No propagation of the pressure wave is modeled and an overestimation of the pressure at the descending aorta is found in the rigid wall simulation.

PART II. CLINICAL APPLICATION: SIMULATION OF AORTIC COARCTATION

Chapter 5. An introduction to aortic coarctation and its computational modeling

In this chapter a literature review on the computational modeling of aortic coarctation is given together with a motivation for this approach and the need to continue research on this topic. The main motivation for the hemodynamic study of (repaired) aortic coarctation is that disturbed blood flow strongly affects vascular pathogenesis, and vice versa. As such, hemodynamic information is of high clinical importance, amongst others to diagnose cardiovascular malfunctioning and evaluate treatment outcomes. Provided the model parameters faithfully represent the physical quantities of the arterial system, computational models can contribute to a better understanding of the long-term prognosis of CoA repair and have the potential to detect associated processes before they become clinically relevant.

Literature on computational modeling of (treated) coarctation is, however, still sparse. An overview of the state of the art in numerical analysis of CoA is given, together with some shortcomings. Compared to numerical studies performed a decade ago, huge improvements towards more realistic, physiological modeling have been made. These include the extraction of a patient specific anatomy, the application of appropriate boundary conditions (replicating downstream vascular resistance and compliance) and the modeling of arterial compliance. Other aspects, such as, the incorporation of vascular remodeling and the inclusion of collateral blood flow are still in their early stage of development and require experimental or in vivo validation. Apart from the modeling constraints, one should keep in mind that large scale clinical applications are lacking. All of the cited numerical studies report results from a very limited number of cases and should be confirmed in a more extensive study.

In spite of their restricted application, these preliminary studies support the hypothesis proposed by O'Rourke that hemodynamics and biomechanics play a crucial role in the prognosis of repaired coarctation. With recent advancements in computational modeling in mind, we believe that these simulations have the potential to address open clinical questions related to the long-term outcome of treated CoA.

Chapter 6. Analysis of the hemodynamic impact of a local stiffening

Uncertainty exists on the factors contributing to the increased long-term morbidity after coarctation treatment among others the presence of a residual narrowing (recurrent coarctation) and a less distensible zone, caused by the presence of a stent or scar tissue. As approximately 60% of the buffer capacity of the aorta is located in the proximal aorta, this local stiffening affects the cushioning function of the aorta. The local narrowing, on the

other hand, leads to an additional resistance in the arterial system. In addition, a local narrowing and stiffening generate wave reflections that reach the heart fast, given the short distance to the heart. The many interfering factors and adaptive physiologic mechanisms present in vivo prohibit the study of the isolated impact of these individual factors. As experimental or computational studies more easily allow to mimic the alterations caused by a single parameter, these approaches are crucial in the understanding of central aortic hemodynamics following coarctation treatment.

As the high level of complexity, inherent to patient specific aortic models, may hamper the insights provided by these models, a simplified model of repaired aortic coarctation is first used. The aim of this study is to simulate the pulse propagation in a locally stiffened tube and to analyze the hemodynamic impact of this stiff segment. The advantage of this model is that the only reflections present in the model originate from the local stiffening and can thus easily be interpreted.

The simulation results demonstrate that the presence of a stiff segment has an important impact on a short pressure pulse, but has almost no influence on a physiological pressure pulse. This phenomenon is explained by analyzing the reflections induced by the stiff segment. At the transition from the flexible artery to the stiffening, a backward compression wave is generated, immediately followed by a sequence of backward expansion waves, created at the outlet of the stiffening. Proximal to the stiff segment, these waves overlap and cancel each other out, as such leaving the hemodynamic quantities almost undisturbed.

Chapter 7. Insights into the effect of local stiffness and residual narrowing on central hemodynamics seen in repaired aortic coarctation: a computational study

To obtain a complete analysis, a patient specific geometry is applied, including the residual narrowing, which often remains after the treatment of aortic coarctation. Since current models (including the one analyzed in chapter 6) are an oversimplification of the physiological system or miss an extensive application and/or parameter study, the aim of this chapter is to develop a relevant patient specific parameter model to predict the impact of (coexisting) stiffening and narrowing in CoA repair. Varying lengths, stiffnesses and diameter reductions of the coarctation zone are studied and their results compared against the hemodynamic response in a healthy subject.

It is demonstrated that fluid-structure interaction modeling plays a significant role in the correct assessment of CoA severity. Buffering of the blood flow in the proximal aorta dampens out the pressure pulse and reduces the velocity in the constriction and the correlated pressure difference. In the distal part of the aorta, the presence of a narrowing results in a highly nonuniform flow and the development of vortices. These observations question the use of 1D models in the prediction of stenosis-induced pressure drops and wave reflections.

In agreement with the results reported in chapter 6, the overall impact of a local stiffening on the hemodynamics is fairly limited. Local changes in peak systolic pressure up to 8 mmHg are retrieved, whereas the flow distribution in the aorta and the mean pressure drop along the aorta remain more or less constant (0.8 mmHg). With respect to the presence of a residual narrowing, blood pressure alterations in the proximal aorta are much more pronounced, covering the whole systolic phase and are dominated by the convective acceleration across the CoA. This pressure drop is followed by pressure recovery persisting in a larger part of the descending aorta. Severe coarctation is characterized by a smaller pressure recovery (i.e. a larger energy dissipation due to the development of turbulence). For a short constriction an additional stiffening will have a significant impact on the pressure evolution (up to 27 mmHg) whereas the impact for a longer stiffening is relatively limited (up to 9 mmHg).

An evaluation of CoA severity based on the net wave intensity alone, results in a considerable underestimation of the backward compression wave generated by the presence of a narrowing and provides misleading information regarding the distance to the reflection site.

Chapter 8. The aortic reservoir-wave as a paradigm for arterial hemodynamics: insights from 3D fluid-structure interaction simulations in a model of aortic coarctation

The reservoir-wave paradigm considers aortic pressure as the superposition of a 'reservoir pressure', directly related to changes in reservoir volume, and an 'excess pressure' ascribed to wave dynamics. The change in reservoir pressure is assumed to be proportional to the difference between aortic inflow and outflow, an assumption that is virtually impossible to validate in vivo. The aim of this study is therefore to apply the reservoir-wave paradigm to aortic pressure and flow waves obtained from 3D fluid-structure interaction simulations in a model of (a) a normal aorta, (b) aortic coarctation (narrowed descending aorta) and (c) stented coarctation (stiff segment in descending aorta). We found no unequivocal relation between the intra-aortic volume and the reservoir pressure for any of the simulated cases. When plotted in a pressure-volume diagram, hysteresis loops are found that are looped in a clockwise way indicating that the reservoir pressure is lower than the pressure associated with the change in volume. The reservoir-wave analysis leads to very high excess pressures, especially for the coarctation models, but to surprisingly little changes of the reservoir component despite the impediment of the buffer capacity of the aorta. With the observation that reservoir pressure is not related to the volume in the aortic reservoir in systole, an intrinsic assumption in the wave-reservoir concept is invalidated and, consequently, also the assumption that the excess pressure is the component of pressure that can be attributed to wave travel and reflection.

CONCLUSIONS

So did this research manage to explain the long-term morbidity observed after coarctation treatment? No, but we were able to highlight some important hemodynamic alterations due to the presence of a local stiffening and a residual narrowing in the post-interventional case. The correlation of these adverse hemodynamic consequences with the long-term morbidity remains, however, a topic of future research. This should further elucidate the role of disturbed flow patterns in the progression of the disease. As such, this research is certainly not an endpoint. Suggestions for future work are included at the end of this dissertation. We believe that in the near future, computational simulations will further improve understandings of the severity of hemodynamic and biomechanic alterations. Through the mutual interaction between engineers and clinicians, the regions of increased susceptibility can be identified and mitigated, consequently alleviating the potential genesis of long-term morbidity.

Contents

Abbreviations and Symbols

Abbreviations

1D	One-dimensional
2D	Two-dimensional
3D	Three-dimensional
ALE	Arbitrary Lagrangian-Eulerian
Ao	Aorta
AsAo	Ascending aorta
BA	Balloon angioplasty
BAV	Bicuspid aortic valve
BC	Boundary condition
BCA	Brachiocephalic artery
BCW	Backward compression wave
BE	Backward Euler scheme
BEW	Backward expansion wave
BP	Blood pressure
CFD	Computational fluid dynamics
CO	Cardiac output
CoA	Aortic coarctation
CT	Computer tomography
CVD	Cardiovascular disease
DAo	Descending aorta
ECG	Electrocardiogram
EOA	Effective orifice area
FCW	Forward compression wave
FEW	Forward expansion wave
FFT	Fast Fourier transform
FSG	Fluid-solid growth
FSI	Fluid-structure interaction
GMRES	Generalized minimal residual
HHT	Hilber-Hughes-Taylor operator
HR	Heart rate
ILS	Approximation for the inverse of the Jacobian from a least squares model
IQN	Interface quasi-Newton algorithm

LCCA	Left common carotid artery
LES	Large eddy simulations
LSA	Left subclavian artery
MP	Mean pressure
MR(I)	Magnetic resonance (imaging)
OSI	Oscillatory shear index
R	Refinement
RM	Reflection magnitude
RMS	Root mean square
S/D	Systole diastole ratio
SEM	Standard error of the mean
SIMPLE	Semi-implicit method for pressure-linked equations
TAWSS	Time-average wall shear stress
TKE	Turbulent kinetic energy
TRI	Tricuspid valve
WSS	Wall shear stress

Subscripts

$+$	Forward wave
$-$	Backward wave
0	Reference value (Ch. 3)
0	Upstream value (App. A)
1	Downstream value (App. A)
Ao	Aorta
CoA	Halfway the coarctation zone
exc	Excess pressure
f	Fluid
$i \pm 1/2$	Value at cell faces (Ch. 3)
i	Value at cell center (Ch. 3)
max	Maximal value
min	Minimal value
ptp	Peak-to-peak value
P	Proximal to the coarctation zone
res	Reservoir pressure
s	Structure
vol	Volume
w	Wall
l	Fourier mode

Superscripts

$'$	Perturbation term
$^-$	Average
^{n}	Time step

Operators

Δ	Difference
$\int$	Integral
∂	Partial derivative
$\sum$	Sum
$\boldsymbol{\nabla\cdot}$	Divergence
$\boldsymbol{\nabla}$	Gradient
$\ddot{}$	Second time derivative
$\dot{}$	Time derivative
d	Derivative

Symbols

α	HHT time integrator parameter	(Ch. 3)	
α	Momentum-flux correction coefficient	(Ch. 1)	
α	Rayleigh damping coefficient	(Ch. 4)	
β	HHT time integrator parameter	(Ch. 3)	
β	Rayleigh damping coefficient	(Ch. 4)	
β	Stiffness index	(Ch. 7)	
χ	Constant depending on wall properties	(Ch. 3)	[kg/s^2]
ϵ	Convergence tolerance		[Pa]
Γ	Boundary		
γ	HHT time integrator parameter		
κ	Dimensionless stiffness	(Ch. 4)	
κ	Timoshenko shear correction factor	(Ch. 3)	
λ	Eigenvalue	(Ch. 3)	
λ	Lagrange multiplier	(Ch. 1)	[Pa]
λ	Wavelength	(Ch. 2)	[m]
ν	Kinematic viscosity	(Ch. 1)	[m^2/s]
ν	Poisson coefficient	(Ch. 3)	
Ω	Domain		
ω	Angular wave number		[rad/m]
ω	Relaxation parameter	(Ch. 1)	
ϕ	Shape function	(Ch. 1)	
ϕ	Time dependent part of the wave	(Ch. 2)	
ψ	Constant depending on wall properties	(Ch. 3)	[kg m^2/s^2]
ψ	Space dependent part of the wave	(Ch. 1)	

ρ	Density	[kg/m^3]
τ	Dimensionless time step (Ch. 4)	[s]
τ	Time delay (Ch. 6)	[s]
$\boldsymbol{\eta}$	Wall displacement (Ch. 2)	[m]
$\boldsymbol{\sigma}$	Cauchy stress tensor	[Pa]
$\boldsymbol{\tau}$	Viscous stress tensor (Ch. 1 and 2)	[Pa]
$\boldsymbol{f}$	Body forces	[N/m^3]
$\boldsymbol{I}$	Unit tensor	
$\boldsymbol{n}$	Normal vector	[m]
$\boldsymbol{u}$	Velocity vector (Ch. 1)	[m/s]
$\boldsymbol{v}$	Velocity vector (Ch. 2)	[m/s]
A	Cross sectional area (Ch.1, 2, 4 and App. A)	[m^2]
A	Matrix (Ch.3)	
a	Rate constant	[1/s]
B	Matrix (Ch.3)	
b	Rate constant	[1/s]
C	Compliance	[kg/Pa]
C	Courant number (Ch.2)	
c	Wave speed	[m/s]
C_{01}	Hyperelastic constant	[Pa]
C_{10}	Hyperelastic constant	[Pa]
C_{11}	Hyperelastic constant	[Pa]
C_{20}	Hyperelastic constant	[Pa]
CI	Coarctation index	
D	Diameter	[m]
dI	Wave intensity	[W/m^2]
E	Young's elasticity modulus	[Pa]
G	Amplification factor (Ch.2)	
G	Shear modulus (Ch.3)	[Pa]
h	Wall thickness	[m]
j	Imaginary unit	
k	Wavenumber	[rad/m]
K_r	Friction parameter	[m^2/s]
L	Length	[m]
m	Mach number	
N	Spatial intervals	
P	Spatially averaged pressure (Ch.1 and 8)	[Pa]
p	Pressure	[Pa]
Q	Flow rate	[m^3/s]
R	Reflection coefficient (App. A)	
R	Resistance	[Pa/(kg/s)]
r	Correlation coefficient (Ch. 8)	
r	Radius	[m]
s	Cross sectional area (Ch. 3)	[m^2]
T	Period	[s]
T	Transmission coefficient (App. A)	

t	Time	[s]
T_N	End of systole	[s]
u	Axial velocity (Ch. 1, 3)	[m/s]
u	Scalar (Ch. 2)	
V	Volume	[m^3]
v	Axial velocity (Ch. 2, 5, 6, 7 and App. A)	[m/s]
x	Axial coordinate (Ch. 2 and 3)	[m]
z	Axial coordinate (Ch. 1)	[m]
Z_0	Characteristic impedance (Ch. 1)	[Pa/(kg/s)]
Z_c	Characteristic impedance	[Pa/(kg/s)]
Z_{in}	Input impedance	[Pa/(kg/s)]
η	Constant depending on wall properties (Ch. 3)	[kg/(m^2s^2]
θ	Dimensionless wavenumber	

INTRODUCTION

Introduction

CLINICAL RATIONALE

Aortic coarctation is a congenital disease, characterized by a narrowing of the upper descending aorta, obstructing the blood flow from the heart towards the lower part of the body. Even after successful treatment, a high risk of cardiovascular morbidity and mortality exists [1–3]. Uncertainty remains among the factors contributing to this increased risk. Clinical and biomechanical studies are needed to better understand and predict the long-term outcome of the treatment of individual patients.
The role of hemodynamics in the development of cardiovascular diseases is nowadays widely accepted, mainly because of the correlation between experimental hemodynamic measurements and observed disease progression [4–10]. With respect to aortic coarctation, this interdependency was first suggested by O'Rourke in 1971 [11].

With advances in medical imaging, computing power and numerical algorithms, the computational study of the link between hemodynamics, biomechanics and the increased morbidity following coarctation treatment is becoming particularly interesting [12–14]. The development of imaging techniques such as magnetic resonance imaging (MRI) and computed tomography (CT), allows to extract the patient specific anatomy [15, 16]. This geometrical data together with phase-contrast MRI, cardiac catheterization data or ultrasound measurements can be used to create a 3D patient specific model with properly assigned boundary conditions that, moreover, considers biomechanical arterial properties. Solving the equations governing blood flow and wall dynamics in the discretized geometric models using a computational mesh, this strategy results in a visualization and quantification of physiological information that is difficult to obtain in vivo [12].

This image-based approach has successfully been applied to the assessment of surgical procedures of other congenital heart diseases such as single ventricle malformations. In this setting, the most studied procedure is most likely the Fontan surgery [17–19]. Enhancing the flow conditions after treatment, computational models of the Fontan technique have led to the improvement of previous surgical intervention strategies [20, 21]. In a similar way, application of computational patient specific models in the context of aortic coarctation can

enhance perception of long-term morbidity, improve current treatment strategies and facilitate the assessment of coarctation severity by providing a quantification of hemodynamic parameters throughout the entire aorta. Furthermore, image-based models can provide data on the impact of devices (such as stents) on physiological functioning. Another application involves the outcome prediction of a given therapeutic intervention for an individual patient.

RESEARCH GOALS

Since hemodynamics are assumed to play an important role in the long-term outcome after coarctation repair, this dissertation focused on the computational modeling of hemodynamics after coarctation treatment. Uncertainty exists on the factors contributing to the increased risk of long-term cardiovascular morbidity among others the presence of a residual narrowing, leading to an additional resistance in the arterial system and a less distensible zone disturbing the buffer function of the aorta. As the many interfering factors and adaptive physiologic mechanisms present in vivo prohibit the study of the isolated impact of these individual factors, a numerical fluid-structure interaction model is developed, to predict the central aortic hemodynamics in coarctation treatment. For this purose, three major research goals are specified:

Goal 1 *The development of a simplified fluid-structure interaction model of repaired aortic coarctation as a first step towards a more complex physiological representation, providing deeper understanding with respect to wave propagation and reflection.* (See chapters 2 and 3 for some technical issues related to this model and chapter 6 for an application of the model.)

Goal 2 *The development and validation of a patient specific fluid-structure interaction model of the aortic arch including (repaired) aortic coarctation.* (See chapter 4)

Goal 3 *The application of this model to gain insights into the effect of local stiffening and residual narrowing on central hemodynamics seen in repaired aortic coarctation.* (See chapter 7)

OUTLINE

This dissertation is divided into two distinct parts that can be read separately. The first one is a more technical part and aims to highlight some issues with respect to the fluid-structure interaction (FSI) modeling of repaired aortic coarctation. A first issue that is discussed concerns the application of a geometrical multiscale representation of the systemic circulation and the technical challenges inherent to this approach. Therefore, chapter (1) provides a literature review on the current state of the art of geometrical multiscale modeling. Secondly, the numerical dissipation inevitably related to the numerical solution strategy of an FSI problem is examined using both a numerical and analytical study (chapter 2). A third

concern that is analyzed involves the stability of FSI simulations using different time integration schemes and time step sizes to discretize the fluid and solid problem (chapter 3). The final chapter (4) of the first part discusses the construction and validation of the patient specific FSI model further used in the second part of this research.

Whereas the first part attempts to answer some technical questions associated with FSI modeling, the second part provides clinical insights related to repaired aortic coarctation. In a first chapter (5) a literature review on the computational modeling of aortic coarctation is given together with a motivation for this approach and for the need for continued research on this topic. This is followed by an analysis of the hemodynamic impact of a local stiffening using a simplified FSI model (chapter 6). The 3D patient specific model is finally used in chapters 7 and 8 to analyze the hemodynamic impact of repaired aortic coarctation and to study the aortic reservoir-wave as a paradigm for arterial hemodynamics. Although the studies performed in the first part were essential with respect to the development of the models applied in the second part, the later one is the most important part as it provides unique insights. The developed model thus allows to quantify the altered hemodynamic response due to the presence of (repaired) CoA. The correlation of these indices with the long-term morbidity remains a topic for future research.

Each chapter can be considered as an individual part of the global story, but can be read and understood independently. The symbols used in this research are introduced in each chapter separately and can differ from one chapter to another. The most important conclusions of this dissertation and some future perspectives are dealt with at the end of this work.

LIST OF PUBLICATIONS

First author peer-reviewed papers

- Taelman L., Degroote J., Verdonck P., Vierendeels J. and Segers P. *"Modeling hemodynamics in vascular networks using a geometrical multiscale approach: numerical aspects."* Annals of Biomedical Engineering, 41(7):1445-1458, 2013.
- Taelman L., Degroote J., Swillens A., Vierendeels J. and Segers P. *"Fluid-structure interaction simulation of pulse propagation in arteries: numerical pitfalls and hemodynamic impact of local stiffening."* International Journal of Engineering Science, 77:1-13, 2014.
- Segers P.*, Taelman L.*, Degroote J., Bols J. and Vierendeels J. *"The aortic reservoir-wave as a paradigm for arterial hemodynamics: insights from 3D fluid-structure interaction simulations in a model of aortic coarctation."* submitted for publication.
  *Both authors contributed equally to the study

- Taelman L., Bols J., Degroote J., Muthurangu V., Panzer J., Vierendeels J. and Segers P. *"Insights into the effect of local stiffness and residual narrowing on central hemodynamics seen in repaired aortic coarctation: a computational study."* submitted for publication.

Coauthor peer-reviewed papers

- Segers P., Mynard J., Taelman L., Vermeersch S. and Swillens A. *"Wave reflection: Myth or reality?"* Artery Research, 6(1):7-11, 2012.
- Swillens A., Taelman L., Degroote J., Vierendeels J. and Segers P. *"Comparison of noninvasive methods for measurement of local pulse wave velocity using FSI-simulations and in vivo data."* Annals of Biomedical Engineering, 41(7):1567-1578, 2013.
- Segers P., Swillens A., Taelman L. and Vierendeels J. *"Wave reflection leads to over- and underestimation of local wave speed by the PU- and QA-loop methods: theoretical basis and solution to the problem."* Physiological measurement, 35:847-861, 2014.
- Bols J., Taelman L., De Santis G., Degroote J., Verhegghe B., Segers P. and Vierendeels J. *"Unstructured hexahedral mesh generation in complex vascular structures using a grid-based approach."* Computer Methods in Biomechanics and Biomedical Engineering, submitted for publication.

One

NUMERICAL ISSUES CONCERNING (CARDIOVASCULAR) FSI SIMULATIONS

CHAPTER 1

Modeling hemodynamics in vascular networks using a geometrical multiscale approach: numerical aspects[1]

In this work, we focus on the study of the local blood flow patterns in (repaired) aortic coarctation. This is motivated by the hypothesis that adverse hemodynamics and biomechanics are related to the increased morbidity in aortic coarctation (CoA) repair, proposed by O'Rourke in 1971 [11]. As current CoA models are associated with some important limitations from a computational and a clinical point of view (see section 5.6), this research involves the development of a 3D computational model, the improvement of current solution strategies and the clinical application of the model.
Within our research group, several efforts towards the 1D-0D modeling of the arterial tree have been made, see for example [22]. The coupling of the 3D models, developed in this research, and the currently existing 1D-0D models is a future perspective for our research group. As demonstrated by the next literature review, such models will enhance the understanding of the mutual interaction between local (i.e. the presence of treated CoA) and global phenomena.

1.1 INTRODUCTION

Cardiovascular disease (CVD) is the leading cause of death worldwide, accounting for one-third of all global deaths [23], and has a significant economic impact on the health care

[1]This chapter is based on the work *"Modeling hemodynamics in vascular networks using a geometrical multiscale approach: numerical aspects."*, as published in *Annals of Biomedical Engineering* 41(7):1445-1458, 2013.

system, predominantly because of the escalating costs of advanced disease treatment. In 2010 CVD was responsible for 17% of national health expenditures in the United States [24]. Early detection and intervention of CVD can delay or prevent the symptoms from developing. It is therefore essential to have a profound understanding of cardiovascular (patho-) physiology to further improve diagnostic and therapeutic strategies and to tailor them to the individual patient rather than making clinical decisions based on population means. A powerful tool to gain insight into the hemodynamics and their relationship to vascular (dys)function is the numerical simulation of the blood circulation.

Modeling the fluid mechanics of the cardiovascular system is, however, a challenging task due to heterogeneity of the vascular tree in terms of geometrical and mechanical properties. Particularly, the diameters of the large arteries (> 10 mm), which carry the blood away from the heart, are considerably different from those of the capillaries (5-10 μm), where the smaller diameters and dense networks improve the actual exchange of water and chemicals between the blood and the tissues. Because of a decrease in characteristic length and velocity moving more distally in the arterial tree, viscous forces gain importance with respect to inertia forces. As a result, in the microcirculation, the viscous forces predominate the inertial forces and, in its most elementary form, a linear relation can be assumed between pressure and flow. Generally the blood flow is laminar. However, under conditions of high flow rate, particularly in the large arteries, laminar flow can be disrupted and become turbulent [25]. Another consequence of the decrease in characteristic length is the change in rheological behavior of the blood. In medium to large vessels, blood can be modeled as a continuum, obeying a Newtonian behavior [26] or, alternatively, incorporating the shear-thinning rheology [27, 28]. In the microcirculation, where the diameter of the blood vessels is comparable to the size of the red blood cells (8 μm), the blood cells are forced to migrate towards the center and move in single file, hereby strongly deforming (Fahraeus-Lindqvist effect). Consequently, the assumption that blood behaves as a fluid with uniform properties does no longer apply in smaller blood vessels and capillaries. Apart from the difference in geometrical properties, a significant diversity in mechanical properties of the vessel wall exists. The larger arteries are generally more elastic than the smaller ones. Deformations up to 10% of the vessel radius are common in large arteries. This elasticity gives rise to the windkessel effect (i.e. the distension of the large arteries during systole, functioning as a buffering reservoir for blood) [29, 30] and provides a passive mechanism for smoothing the pulsatile blood flow from the heart to the periphery. Although in most CFD simulations the wall is treated as rigid, it is important to consider the arterial wall behavior when one wants to simulate wave propagation in the arterial tree.

This heterogeneous composition of the cardiovascular system triggered the development of three classes of models (3D, 1D and 0D ones), featuring different assumptions on the

spatial degrees of freedom. Three-dimensional (3D) models are usually applied when detailed information on the flow field (e.g. the wall shear stress distribution) is needed in a specific region. As the local blood flow is associated with the initiation and progression of certain cardiovascular diseases, such as atherosclerosis [5, 6], these 3D models provide a great contribution to the understanding of these diseases. Mathematically, the blood dynamics are described by the Navier-Stokes equations for incompressible fluids. These equations can be coupled to the equations of motion of the vessel wall to include the fluid-structure interaction (FSI). In [31–33] FSI simulations of the blood flow in cerebral aneurysms, a healthy aorta and Fontan patients are compared to rigid wall simulations, demonstrating the importance of including the flexible wall modeling, in particular with respect to the simulation of wall shear stress (which is overestimated in the rigid wall case of all three studies). Despite the advances made in computing power and numerical algorithms, the high computational cost and the intrinsic challenge of the FSI problem still restricts their use to a limited region, such as a bifurcation, the aortic arch or the examples listed above.
This limitation motivates the adoption of one-dimensional (1D) models, as they allow to compute the fluid dynamics in a large part of the arterial tree at a reasonable computational cost [34, 35]. The reduced model is obtained by assuming axial symmetry and by restricting the spatial variation of the degrees of freedom to the axial direction. This restriction is justified, since the spectrum of wavelengths of the pressure waves generated by the heart is much longer than the diameter of the blood vessel [30]. Despite their lower level of accuracy, 1D models are an optimal tool to analyze arterial wave propagation. The spatial degrees of freedom of these models makes it, however, still unfeasible to model the whole capillary network with them.
A further simplification in the mathematical modeling is obtained by eliminating the variation in space. Zero-dimensional (0D) models, also called lumped parameter models, allow to describe the time evolution of the pressure and flow in a specific compartment of the circulatory system, like the heart or the capillary bed, although these models may also be used to describe the systemic or pulmonary circulation, or large parts of it.

Yet, the cardiovascular system is a closed system with a high level of interdependence. A global redistribution of the blood flow, which is a systemic feature, influences the hemodynamics in each vascular district, being a local feature (see for instance [36]). On the other hand, a local alteration, such as a vascular occlusion [37] or the presence of an aneurysm [38], can modify the systemic dynamics and give rise to compensatory mechanisms. For example in [39], it is shown that the presence of a stenosis in the carotid bifurcation does not imply a relevant reduction of the blood supply to the brain. Neglecting these interactions between local and global scales would therefore result in an inaccurate prediction of the fluid dynamics.
Thus, on the one hand the heterogeneity and extent of the circulatory system requires the

use of different models in its different compartments. On the other hand, the mutual interactions between its compartments imply that these models should preferably not be considered separately. These requirements have led to the concept of geometrical multiscale modeling [36, 40–44], where the main idea is to couple dimensionally heterogeneous models, representing different physical compartments, to study the interaction between different geometrical scales. This approach applies 3D models only in those regions where a detailed knowledge of the flow field is needed, whereas 1D and 0D models are applied to represent the remaining part of the vascular tree. As such detailed information on the flow field in a specific region of interest can be obtained while at the same time accounting for the global circulation. Figure 1.1 conceptually illustrates a geometrical multiscale representation of the systemic circulation, where a 3D model of the left carotid bifurcation is included in a 1D model of the arterial tree and the microcirculation is described by three-element windkessel models.

Several groups [45–49] have successfully coupled 3D models with 0D models, few of which take into account the fluid-structure interaction. As proposed by [13, 50], the prescription of a downstream vascular impedance at the boundaries of the 3D model, results in a more realistic incorporation of the wave reflections generated by the downstream vascular beds. However, the use of Womersley's linear wave theory to calculate the impedance restricts their application to time-periodic conditions. To extent their use to non-periodic conditions, an approach for prescribing lumped parameter outflow boundary conditions that accommodate transient phenomena has been presented in [51]. Few groups have studied the coupling of 3D-1D-0D models to consider the interactions between the local and systemic circulation [40, 42, 52, 53].
The choice between a 3D-1D-0D model or a 3D-0D model mainly depends on the objective of the application. Providing the reduced models are included to obtain proper boundary conditions at the artificial boundaries of a 3D model, both models can be used. However, often a 3D-0D model is preferred as it requires fewer parameters to determine and the ordinary differential equations describing the 0D models are easier to solve than the partial differential equations describing the 1D models. If, on the other hand, one wants to embed the 3D model into the (complete) circulatory system and study the interaction between global and local hemodynamics, a 3D-1D-0D coupled model should be used.

Despite the intuitiveness of multiscale modeling, the combination of models with different mathematical features, gives rise to many difficulties. The Navier-Stokes equations are nonlinear partial differential equations which can be parabolic, hyperbolic or elliptic (depending on the nature of the studied problem), while 1D models are described by hyperbolic partial differential equations, and 0D models are expressed in terms of a system of ordinary differential equations. This review aims to give an overview of the most important aspects concerning the geometrical multiscale approach and, in particular, the coupling between 3D

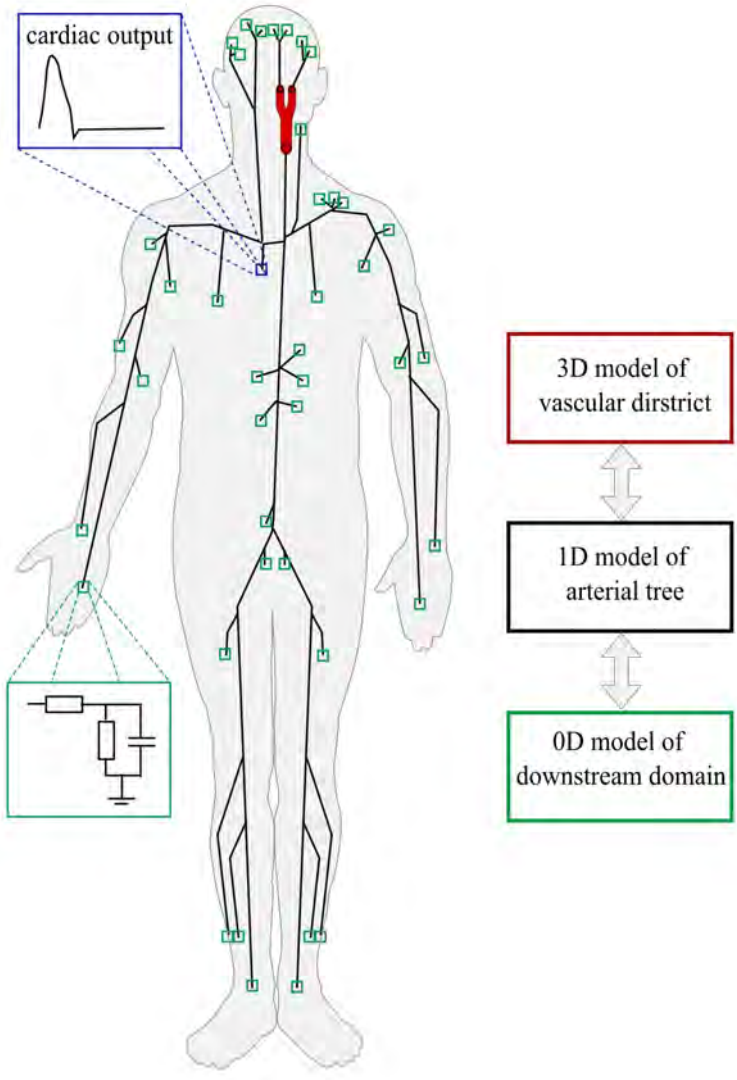

Figure 1.1: Geometrical multiscale model of the circulatory system, including a detailed model of the carotid bifurcation and windkessel models to represent the downstream circulation.

and 1D models. In a first section, a description of the different models is given, followed by the mathematical and numerical issues related to their coupling. The next section is dedicated to the applicability of the geometrical multiscale approach to clinically relevant cases. Finally, some remarks are made on patient specific modeling and the assessment of the quality of 3D-1D-0D coupled models representing the cardiovascular system.

1.2 Numerical Methods to Model the Fluid Dynamics at Different Scales

1.2.1 The zero-dimensional model

The main assumption in the modeling of the cardiovascular system as a windkessel, is the hypothesis that the systemic pressure is homogeneous in space (Ω_{0D}). This assumption is justified if the wavelength of the pressure waves is sufficiently large compared to the dimensions of the system in which they propagate. As aging and high blood pressure lead to stiffer arteries with an associated increase in wavelength, the arterial system - somewhat paradoxically - better resembles a windkessel in these conditions [54]. Based on the analogy between hydraulic networks and electrical circuits, the two-element windkessel model, introduced by Frank [29], consists of a parallel combination of a resistance R (representing the total peripheral resistance) and a compliance C (modeling the total arterial compliance). In the frequency domain, the input impedance of this model decreases from a value R at 0 Hz to a value close to zero at higher frequencies. This in contrast to the in vivo input impedance, which at higher frequencies corresponds to the characteristic impedance Z_0 of the system. To address this shortcoming, Westerhof [55] expanded the RC model to a three-element windkessel model by placing the characteristic impedance in series with the RC model (see Figure 1.2). The differential equation describing the three-element windkessel model is given by

$$(1 + \frac{Z_0}{R})Q + CZ_0\frac{dQ}{dt} = \frac{P}{R} + C\frac{dP}{dt} \qquad \text{in } \Omega_{0D} \tag{1.1}$$

in which d/dt denotes the time derivative, Q the flow rate and P the spatially averaged pressure. In an attempt to further improve the accuracy of the input impedance, other more complex models have been developed, all of which can be expressed in terms of systems of ordinary differential equations [56].

Lumped parameter models can be used as well to model the functioning of the heart (i.e. the ventricular contraction). In [57], Suga et al. proposed a time-varying elastance model of the left ventricle. This model describes the ventricular pressure as a function of the change in ventricular volume and the ventricular elastance, which in turn is determined by three cardiac parameters: the maximal and minimal elastance and the time to maximum

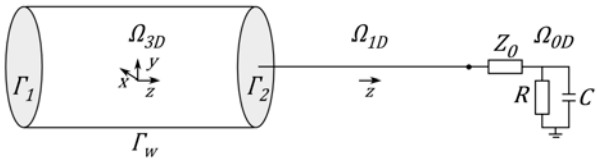

Figure 1.2: A simple 3D-1D-0D model, consisting of a cylindrical artery coupled to a 1D domain and a three-element windkessel model.

elastance. Many alternatives to this model are proposed such as the single-fiber model [58]. In this model the ventricular volume is determined by the change in fiber length and the ventricular pressure is related to the fiber stress. We refer to [56] for further details on lumped parameter models of the heart.

1.2.2 The one-dimensional model and 0D distributed model

In 1D models the arterial circulation is considered as a network of compliant vessels (Ω_{1D}) in which the flow is described by the one-dimensional equations for the conservation of mass and momentum. Several approaches have been developed to deduce and solve these 1D flow equations [56, 59]. Following the approach in [43], the blood vessels are assumed to be axisymmetric, having a fixed axis of symmetry. Furthermore, only radial displacements are taken into account and the pressure profile on each axial section is presumed constant. Finally, a particular velocity profile u_z is considered for which the axial components are assumed dominant. Under these assumptions, the flow equations are given by

$$\begin{aligned} \frac{\partial A}{\partial t} + \frac{\partial Q}{\partial z} &= 0 \\ \frac{\partial Q}{\partial t} + \frac{\partial}{\partial z}\left(\frac{\alpha Q^2}{A}\right) + \frac{A}{\rho_f}\frac{\partial P}{\partial z} &= -K_r \frac{Q}{A} \end{aligned} \qquad \text{in } \Omega_{1D} \tag{1.2}$$

in which z denotes the axial coordinate and ρ_f the fluid density. The cross sectional area A, the flow rate Q and the pressure P are the unknowns in Eq 1.2. The friction parameter K_r and the momentum-flux correction coefficient α depend on the assumptions made regarding the shape of the velocity profile u_z. In general these coefficients are a function of the axial coordinate and time. However, most studies use a rather simplified velocity profile that can be written as

$$u_z(r, z, t) = \varphi(r)\bar{u}_z(z, t) \tag{1.3}$$

where the shape function φ is radius dependent and the mean velocity $\bar{u}_z$ depends on the axial coordinate and the time. For these velocity profiles, the value of K_r and α reduces to a constant (e.g. $K_r = 8\pi\nu$ (ν denotes the kinematic viscosity) and $\alpha = 4/3$ correspond to a Poiseuille profile).

In order to close system 1.2 a constitutive law is needed, relating the vessel section A to the pressure P. Generally, circumferential stresses dominate radial and axial stresses and the inertia of the wall motion is neglected. With these restrictions, the wall mechanics reduce to an algebraic relation linking the pressure to the wall distension and consequently to the cross sectional area. This structural model corresponds to the so-called *independent rings* model [60]. More sophisticated models can be introduced by applying a differential law for the mechanics of the vessel wall. Using an appropriate numerical technique (such as finite differences or the method of characteristics) and imposing continuity of (total) pressure and flow at the bifurcations, it is possible to compute the hemodynamics in the entire arterial tree.

Alternatively, the arterial tree can be treated as a transmission line [22, 61], based on the analogy between hydraulic networks and electrical circuits. In that case, the distributed model consists of a network of 0D models of which the parameters are defined using the Womersley theory. Constructing a transfer function between the pressures and flows at the inlet and the outlet of each segment, it is possible to compute the pressure and flow harmonics throughout the arterial tree in the frequency domain. Under the assumption of linearity, superposition of the different harmonics yields the final pressure and flow waves. More details on the modeling of arterial wave propagation using 1D and 0D distributed models and the validation of the models against in vitro measurements can be found in [56, 59] and [62, 63] respectively.

1.2.3 The three-dimensional model

Consider the bounded domain Ω_{3D} representing a truncated artery (see for example Figure 1.2). The equations describing the unsteady Newtonian blood flow are given by the Navier-Stokes equations

$$\begin{aligned} \rho_f \frac{\partial \boldsymbol{u}}{\partial t} + \rho_f \boldsymbol{u}.\boldsymbol{\nabla}\boldsymbol{u} - \boldsymbol{\nabla}.\boldsymbol{\sigma}_f &= \rho_f \boldsymbol{f} \\ \boldsymbol{\nabla}.\boldsymbol{u} &= 0 \end{aligned} \qquad \text{in } \Omega_{3D} \tag{1.4}$$

with $\boldsymbol{u}$ the flow velocity and $\boldsymbol{f}$ the body forces acting on the blood per unit of mass. The Cauchy stress tensor $\boldsymbol{\sigma}_f$ is defined as

$$\boldsymbol{\sigma}_f = -p\boldsymbol{I} + \boldsymbol{\tau} \tag{1.5}$$

with p the pressure, $\boldsymbol{I}$ the unit tensor and $\boldsymbol{\tau}$ the viscous stress tensor. The prescription of boundary conditions is required to obtain a mathematically well posed problem. Typically, the velocity components (Dirichlet condition), the projection of the Cauchy stress tensor on the surface normal (Neumann condition) or a combination of both (Robin condition) are prescribed at the artificial boundaries Γ_i $(i = 1, \ldots, n)$ and a no-slip condition is assumed

at the physical arterial wall, denoted by Γ_w. The set of equations is discretized in space and time and solved iteratively.

The compliance of the model can be accounted for in fluid-structure interaction simulations, solving the flow and structural problem in a (strongly) coupled way. Several constitutive models have been devised to describe the mechanical dynamics of the arterial wall for 3D models, ranging from linear elastic and hyperelastic models to complex anisotropic models capturing the orientation of the collagen fibers, the dispersion in orientation and the mechanical behavior associated with the activation of smooth muscle cells. Reference [64] provides an overview of the current state of the art in constitutive modeling of the arterial wall behavior.
The interaction between the blood flow and the structure is enforced by imposing kinematic and dynamic equilibrium at the fluid-structure interface.

$$\begin{aligned} \boldsymbol{u} &= \frac{\partial \boldsymbol{\eta}}{\partial t} \\ \boldsymbol{\sigma}_f.\boldsymbol{n}_f &= -\boldsymbol{\sigma}_s.\boldsymbol{n}_s \end{aligned} \qquad \text{on } \Gamma_w \tag{1.6}$$

In these equations $\boldsymbol{\eta}$ represents the wall displacement with respect to a reference position and $\boldsymbol{\sigma}_s$ the stress exerted by the structure on the fluid. $\boldsymbol{n}_f$ and $\boldsymbol{n}_s$ denote the unit normal vector pointing outwards from the fluid respectively the structural domain. A review on the numerical approaches used to solve the FSI problem and a discussion of the most important challenges can be found in [65, 66].

1.3 THE GEOMETRICAL MULTISCALE APPROACH COUPLING ISSUES

A common approach to handle dimensionally heterogeneous problems is to decompose the global domain into subdomains where the partitioning takes place at the interfaces between the models. Prescribing the continuity of some of the involved quantities at the coupling interfaces, the interaction between the subdomains is induced through the transfer of boundary data only. This way, a sequential solution of the 3D, 1D and/or 0D models can be used to obtain the global solution at each time step.

In case the 3D model is a rigid wall model, problems will occur when coupling the 3D model to a 1D model. As the compliance of the blood vessels is the driving mechanism of wave propagation in the 1D model, the coupling to a rigid 3D model will therefore, result in a discontinuous wall behavior at the interface, which in turn generates wave reflections and affects the numerical solution [67]. Compliance mismatch between 3D and 1D models can be prevented using fluid-structure interaction. FSI simulation is, however, not always relevant (providing the arterial wall deformation is limited and one is not interested in the

stress distribution throughout the wall) and increases the computational cost significantly (as both the equations governing the flow and the arterial deformation need to be solved). To still allow coupling a 3D CFD simulation to a 1D model, one might introduce a simplified representation of the compliance of the 3D vessel at the interface with the 1D model [67]. The quantification of the parameters in these models is, however, a cumbersome task and unreliable results can be obtained if the quantification is incomplete [67].

1.3.1 Coupling 3D to 0D/1D models: options for boundary treatment

The numerical simulation of dimensionally heterogeneous problems implies the assignment of proper boundary conditions at the interface between two models. The choice of the transferred boundary data depends upon the underlying models and, in particular, upon the physical quantities for which some sense of conservation or continuity exists. The prescription of the continuity of mass flow rate at the coupling interface guarantees the conservation of mass. This boundary condition addresses the so-called *flow rate problem*, assigning a flow rate Q_i through each of the boundaries Γ_i $(i = 1, \ldots, n)$ of the 3D domain.

$$\int_{\Gamma_i} \boldsymbol{u}.\boldsymbol{n} d\gamma = Q_i \qquad \text{on } \Gamma_i \tag{1.7}$$

Due to the incompressibility of the fluid, the compatibility condition $\sum_{i=1}^{n} Q_i = 0$ must be fulfilled at each instant of time for the rigid CFD case. For FSI simulations, incorporating the compliance of the arteries, the difference between in- and outflow is buffered in the deforming fluid domain. The second quantity for which continuity is enforced at the interface, is the spatially averaged pressure P_i.

$$\frac{1}{|\Gamma_i|} \int_{\Gamma_i} p d\gamma = P_i \qquad \text{on } \Gamma_i \tag{1.8}$$

This condition in combination with the Navier-Stokes equations 1.4, is often referred to as the *mean pressure problem*. In [41] continuity of the spatially averaged total (static + dynamic) pressure is preferred above continuity of the spatially averaged static pressure, as for this case conditional stability of the iterations between the 3D and 1D FSI models is proved analytically [42]. Nevertheless, whenever the dynamic pressure is small compared to the static pressure, both the continuity of pressure and total pressure work equally well in terms of number of iterations between the 3D and 1D model and spurious wave reflections generated at the interface [41].

Still, the continuity of the flux and spatially averaged (total) pressure does not guarantee the continuity of cross sectional area at the interface. One can impose a zero stress boundary condition on the structure interface. However, in curved geometries, this might result in undesired wall deformations. On the other hand, clamping the vessel wall at the interface is unphysiological, since it generates spurious wave reflections at the interface. Alternatively, the continuity of the cross sectional area can be imposed as an additional coupling condition

between two models [41, 68]. Yet, the prescription of the continuity of area combined with the continuity of mass flow rate and pressure, can provoke numerical instability due to a discrepancy in the structural models at the interface [68, 69]. Therefore, this condition is usually omitted [37, 68, 69].

From a mathematical point of view, the 3D Navier-Stokes problem requires the prescription of three scalars (such as the velocity components or the projection of the Cauchy stress tensor on the surface normal) at each point of the discretized boundaries. However, reduced 1D or 0D models provide only spatially averaged quantities. These conditions (referred to as *defective boundary conditions*) are insufficient to generate a well posed 3D problem, since its solution is not unique. Different techniques have been devised to translate these defective boundary sets into mathematically sound boundary conditions for the Navier-Stokes problem, where we address 5 methods: (i) the prescription of an a priori selected flow profile, (ii) the do-nothing approach, (iii) a Lagrange multiplier approach, (iv) a minimization approach and (v) an extended variational approach.

(i) A common approach consists of prescribing an a priori selected velocity profile (flat, parabolic, Womersley) fitting the given flow rate, which has the drawback that the chosen velocity profile strongly affects the numerical solution in the 3D domain [70]. In order to reduce the sensitivity of the numerical solution in the zone of interest to the selected velocity profile, the computational domain is often extended (see for example [70, 71]).

(ii) In [72] a less perturbative strategy, the so-called *do-nothing approach*, was devised to address the mean pressure and flow rate problem using variational formulations. These formulations implicitly complete the defective data-set with homogeneous Neumann conditions. Among all the possible physical solutions these formulations select the one that satisfies

$$(p - \nu \frac{\partial u_n}{\partial n}) = P_i, \qquad \frac{\partial \boldsymbol{u}_\tau}{\partial \boldsymbol{n}} = 0 \qquad \text{on } \Gamma_i \tag{1.9}$$

with $u_n = \boldsymbol{u}.\boldsymbol{n}$ and $\boldsymbol{u}_\tau = \boldsymbol{u} - u_n \boldsymbol{n}$. In case the flow rates are prescribed at the boundaries, the pressures P_i present in these equations are unknown constants (in space). Consequently, the variational formulation devised to solve the flow rate problem, cannot be transformed into a fully equivalent formulation in terms of classical boundary conditions. Moreover, a non-standard functional space is used to handle the flow rate problem, which complicates the numerical implementation.

(iii) A different approach to solve the flow rate problem has therefore been proposed in [73, 74]. The basic idea is to consider Eq 1.7 as a set of constraints for the solution of the Navier-Stokes problem, rather than defective boundary conditions. Imposing of these constraints is achieved through the use of Lagrange multipliers λ_i $(i = 1, \ldots, n)$. In terms of defective boundary data, the *Lagrange multiplier approach* is very similar to the do-nothing approach. The corresponding solution satisfies the additional boundary conditions

$$(p - \nu \frac{\partial u_n}{\partial n}) = \lambda_i, \qquad \frac{\partial \boldsymbol{u}_\tau}{\partial \boldsymbol{n}} = 0 \qquad \text{on } \Gamma_i \tag{1.10}$$

in which the Lagrange multipliers λ_i replace the role of the unknown constants P_i of the do-nothing approach. The effectiveness of the proposed Lagrange multiplier methodology is illustrated in Figure 1.3, comparing the numerical solution of the flow in a rigid axisymmetric cylindrical pipe with the analytical one [75]. In case a steady flow rate is prescribed ($Q = 10^{-6}\text{m}^3/\text{s}$ the well-known Hagen-Poiseuille profile is recovered (see Figure 1.3, A). For a transient flow rate ($Q = cos(2\pi t)10^{-6}\text{m}^3/\text{s}$) an excellent agreement with the analytical Womersley solution is found (see Figure 1.3, B and C). Using a standard functional

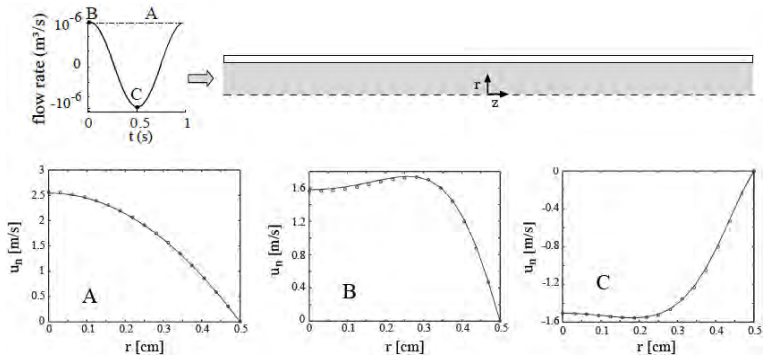

Figure 1.3: Comparison of the axial velocity profile (u_n) in a rigid axisymmetric cylindrical pipe, obtained analytically and using the Lagrange multiplier approach. The results are shown for both, a steady inflow condition (A) and a periodic flow condition, (B) at the beginning of the period and (C) halfway the period. The markers refer to the numerical solution, the line to the analytical one. Figure reproduced with the permission from Veneziani (2007) [75].

space, the Lagrange multiplier formulation allows for a more straightforward numerical implementation. In [74] some numerical solution methods are proposed, based on the splitting of the computation of velocity and pressure and the computation of the Lagrange multipliers. This allows to perform the Navier-Stokes simulations with a standard solver, however, the iterative approach increases the computational cost significantly. Using an approximate reformulation of the problem (proposed in [75]), the computation becomes less expensive. On the other hand, a small error is introduced in the vicinity of the artificial boundaries.

(iv) While the do-nothing approach is not well-suited to solve the flow rate problem, the Lagrange multiplier approach cannot be applied to the mean pressure problem, since it provides unfeasible boundary conditions. In [76] a *minimization approach* is proposed, which allows to treat both problems efficiently and can therefore be used to solve problems where the two conditions are prescribed simultaneously. The approach is based on the minimization of a functional, quantified by the difference between the solution at the boundaries

and the prescribed data. Despite the fact that the previously mentioned methods (ii, iii and iv) were devised for rigid wall models, they can easily be extended to compliant models. Providing the flow and structural problem are solved separately, a rigid fluid problem in a frozen domain is addressed at each FSI iteration. Consequently, the approaches described above can easily be applied. Solution strategies for the flow rate problem that allow for both a monolithic and partitioned FSI approach are developed in [77].

(v) A final method discussed here is based on an extended variational formulation for problems where fields can become discontinuous at some artificial internal boundary (regarded as the coupling interface) [37]. This approach is motivated by the discontinuities that arise in the velocity profiles at the interfaces due to the differences in underlying kinematics of the 3D and reduced models. The extended variational formulation allows for both a monolithic and partitioned solution of the 3D-1D coupled problem.

It is clear that all of the above described approaches provide relatively poor information at the coupling interfaces of the 3D-1D or 3D-0D models. As such, no reliable solutions must be expected in these regions.

1.3.2 Techniques to couple 3D and 1D models

In the following, some numerical techniques devised to solve 3D-1D coupled models are discussed. Remark that these techniques can also be used to couple 3D models with lumped parameter models, however, more efficient approaches (such as the coupled multidomain method [13]) can be applied there. The first strategy to handle geometrical multiscale models in an iterative way is based on an explicit approach [42]. In an explicit coupling, the flow rates Q_i $(i = 1, \ldots, n)$ computed by the 3D solver are imposed as boundary conditions to the 1D models, which in turn compute the mean (total) pressures P_i $(i = 1, \ldots, n)$ to be fed into the 3D model during the next time step. The 3D problem with imposed mean (total) pressures can be solved following the do-nothing approach or the minimization approach. Alternatively, the coupling conditions can be reversed, solving the 3D model with imposed flow rate resorting to the Lagrange multiplier approach or the minimization approach. Since only one iteration per time step is performed, the continuity of normal (total) stress and mass flow rate is not strictly preserved.

A straightforward approach to overcome this issue resorts to Dirichlet-to-Neumann (Gauss-Seidel) iterations with a relaxation procedure [37, 68]. A flow chart illustrating this approach is given in Figure 1.4. Each time step, coupling iterations between the 3D and 1D solver are performed until the pressure residuals fall below a prescribed tolerance ϵ. Fine-tuning of the relaxation parameter ω is, however, a time-consuming task and convergence of the algorithm is not guaranteed, especially when an elevated number of coupling interfaces are involved.
This concern led to the development of more robust iterative strong coupling techniques

[53, 78]. The idea behind these techniques is to reinterpret the original coupled problem as an interface problem in terms of interface variables. This reformulation of the Dirichlet-to-Neumann problem allows to apply more sophisticated algorithms such as the Broyden-type methods or the Newton generalized minimal residual (GMRES) method. Another advantage of this approach is the flexibility concerning the type of boundary conditions imposed at the coupling interface. The chosen type of boundary condition on one side of the interface does not depend on the choice made on the other side of the interface.

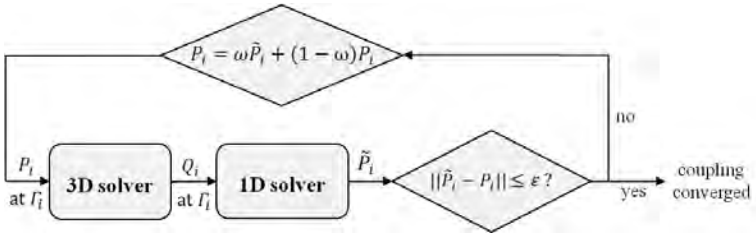

Figure 1.4: Flow chart illustrating Gauss-Seidel iterations with a relaxation procedure between a 3D and 1D flow solver.

1.4 NUMERICAL EXAMPLES AND (CLINICAL) APPLICATIONS

In this section, we present some applications of 3D-0D and 3D-1D-0D coupled models in hemodynamic simulations, in order to illustrate the potentialities of geometrical multiscale modeling.

A simple yet numerically most interesting case is the study of the propagation of a pressure pulse in a cylindrical blood vessel, see Figure 1.5 (left), where the propagation of a pressure pulse (10 mmHg, imposed during 3 ms) simulated with a full 3D FSI model is compared to the propagation obtained using a 3D-1D coupled model (interface at 5 cm). This clearly illustrates the potential of the 1D model as an absorbing boundary condition, eliminating spurious wave reflections at the outlets of the 3D model [42, 44]. Although this case is unphysiological in terms of geometry and boundary conditions, it is extremely useful for validation and to assess the characteristics of the coupling and, in particular, the reflections generated at the interface. A more quantitative comparison on the same case is given in Figure 1.5 (right), depicting the temporal evolution of the averaged pressure of the reference and the coupled solution at two different cross sections. The first section is located at 2.5 cm from the inlet and the second one at the 3D-1D interface. Apart from some small spurious reflections, a good agreement between both solutions is found.

The application of 3D-1D-0D models to clinically relevant cases, is mainly devoted to simulations in which the interactions between the global (arterial tree) and the local scales

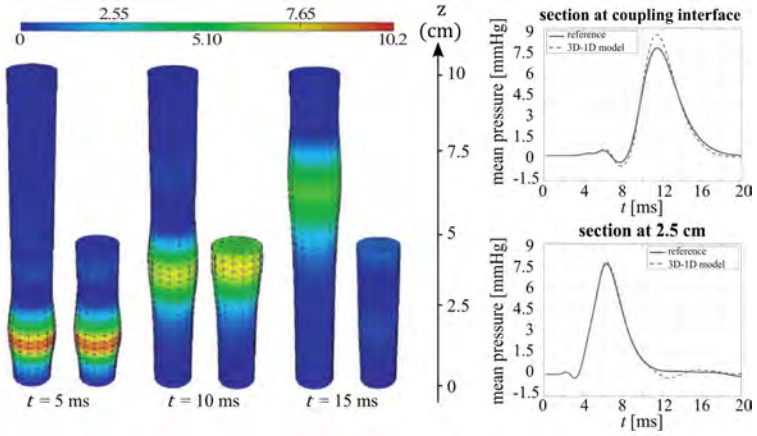

Figure 1.5: (left) Comparison between the pressure contours (mmHg) at three different times, obtained using a fully 3D model and a 3D-1D coupled model of which the interface is located halfway the flexible tube. (right) Comparison between the averaged pressure evolution at two different sections (top) 2.5 cm from the inlet and (bottom) at the coupling interface. Figure reproduced with the permission from Nobile (2009) [44].

(specific arterial district) are of particular interest. In [36] the sensitivity of local hemodynamics to modifications in the heart inflow boundary condition is studied using a 3D-1D-0D coupled FSI model. Here, the functioning of the heart is represented by a prescribed flow rate (which in itself is a quite hard inlet boundary condition; coupling with a lumped parameter model of the heart might be the more flexible and physiologically correct option). In this study the heart rate (HR) is increased from 50 to 150 bpm to predict the effect of exercise on the local blood flow behavior in the carotid bifurcation using the model shown in Figure 1.1. In order to compare resting and exercise conditions, the inflow profile at the aortic root (taken from [79]) was scaled in time and flow rate such that the cardiovascular parameters depicted in Table 1.1 were retrieved. To obtain a total systemic resistance consistent with the prescribed cardiac output (CO) and mean pressure (MP), all terminal resistances were multiplied by the same scaling factor.

Quantitative results are given in Figure 1.6, comparing the calculated flow at the inlet of the bifurcation and the oscillatory shear index (OSI) for the different heart rates considered. Although the shape of the imposed inlet profile was the same in all cases, the flow rate at the bifurcation is significantly affected by the HR, a non-trivial finding illustrating the relevance of multiscale modeling. For a low HR (50bpm) a small recirculation region is present at the carotid sinus with OSI values up to 0.4. This region enlarges for a HR of 70 bpm, whereas for higher HRs a ring pattern is formed containing higher OSI values close to 0.5. Regarding the mean wall shear stress (i.e. the WSS index integrated over the whole arterial wall) two observations can be made: (1) the mean WSS increases linearly with increasing

HR (bpm)	CO (l/min)	S/D	MP (mmHg)
50	5	0.5	100
70	10	0.65	108
90	15	0.8	115
120	20	0.9	122
150	25	1.05	130

Table 1.1: Cardiovascular parameters (heart rate HR, cardiac output CO, systole diastole ratio S/D and mean pressure MP) for the comparison of hemodynamic response at rest and during exercise. These data have been taken from [60].

CO and (2) the mean WSS is piecewise linear for HRs from 50 to 90 bpm and 90 to 150 bpm.

Another relevant application is the study of the influence of a pathological condition on the local and global hemodynamics. In [80], for instance, the effect of a stenosed coronary artery on the coronary flow and pressure is studied using a model that accounts for the interactions between the heart and the arterial system, rather than imposing hard boundary conditions (such as flows or predetermined flow distribution). It is demonstrated that the coronary flow remains unchanged up to 75% diameter reduction, which is a result matching clinical observations.
Apart from the analysis of alterations in the hemodynamic response, these studies also allow to evaluate whether the boundary conditions taken in a healthy case are still valid when simulating the pathological one. An example here is [38], where the sensitivity of the arterial pulse to the presence of an aneurysm in the internal carotid artery is studied by coupling a 3D FSI model of the carotid artery to a 1D model of the arterial tree. The hemodynamic quantities proximal to the aneurysm are the most perturbed and show larger fluctuations compared to the healthy case, indicating that boundary conditions applying to the healthy case cannot simply be transferred to the pathological case.

Other applications involve the simulation of cardiovascular interventions. In [45] for example, the reduction of the cardiac load is studied when comparing the pre-intervention and post-intervention hemodynamic conditions in an aorta with an aortic coarctation. In this quite advanced yet elegant study, a lumped parameter model of the heart is coupled to a 3D patient specific model of an aorta with an aortic coarctation. The downstream circulation is modeled using three-element windkessel models and the surgical procedure is simulated by applying surgical guidelines to connect the aorta proximal and distal to the coarctation. As the surgical resection entails a decrease of the arterial resistance, a reduced afterload and contractility of the left ventricle were obtained. The reduced pressure loss in the post-intervention case is clearly visible in Figure 1.7.

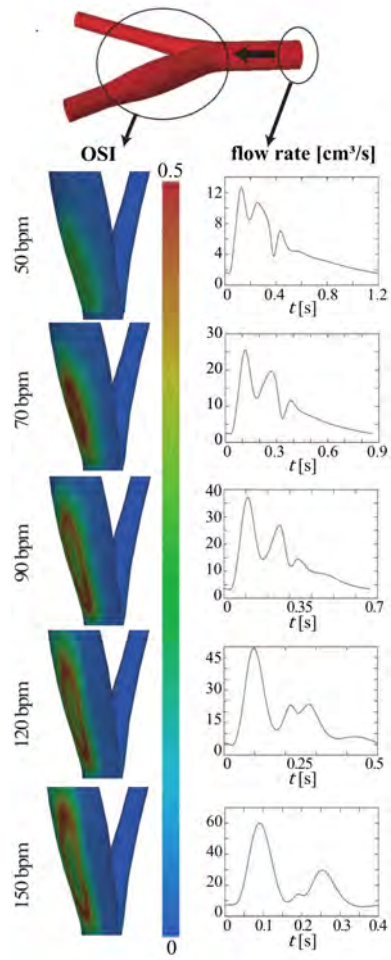

Figure 1.6: Flow rate at the inlet of the common carotid and OSI index as a function of heart rate. These results were obtained using the model depicted in Figure 1.1. Figure taken with the permission from Blanco (2010) [36].

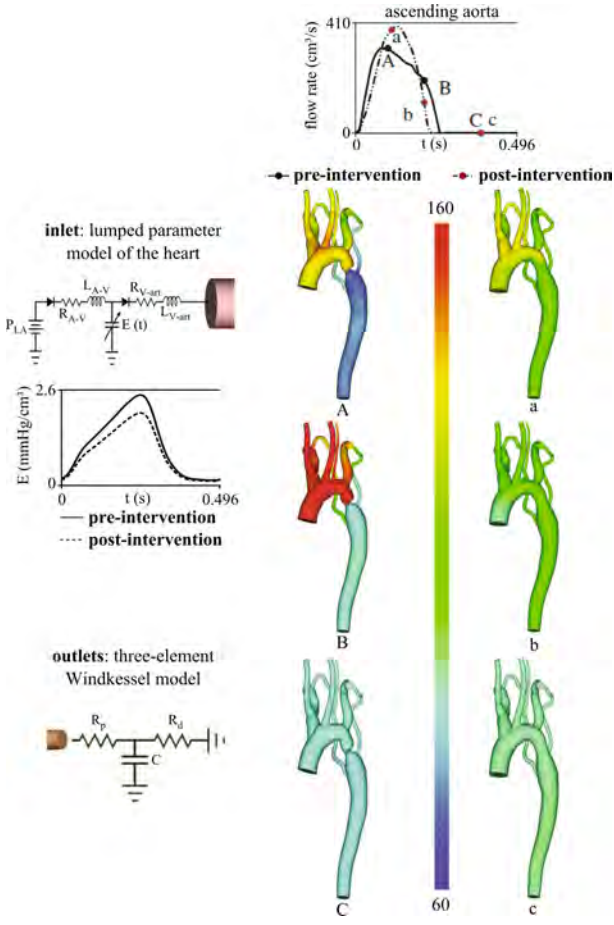

Figure 1.7: (left) Lumped parameter models coupled to the 3D model of the aorta with an aortic coarctation. (right) Pressure contours (mmHg) in the aorta at three different times for the case of pre-intervention and post-intervention. Figure taken with the permission from Taylor (2009) [45].

Other examples can be found in [47, 81], in which a multiscale model is applied to quantitatively compare hemodynamics after the treatment of single ventricle malformations.

From the previous examples it should be clear that a local alteration in a vascular district (such as a stenosis or an aneurysm) induces a redistribution of the global blood flow. This redistribution may, however, give rise to compensatory mechanisms to maintain arterial blood pressure and overall cardiovascular functioning within a narrow range of variation. Consequently, when simulating a medical intervention or pathological condition, some geometrical, mechanical and/or parameters of the coupled 0D models might require adjustment. With respect to this issue, a 3D-1D-0D model for the entire cardiovascular system has been extended with a 0D model of the homeostatic mechanisms corresponding to baroreflex actions in [82]. This self-regulating model allows to study the impact of baroreflex (dys)function on the local and global hemodynamics.

1.5 FINAL CONSIDERATIONS

An issue that arises when applying the geometrical multiscale approach involves the correctness of the partitioning that divides the global domain into subdomains for which different kinematics are assumed. For instance, the length of the 3D model of the carotid artery in Figure 1 might affect the local and global flows predicted by the multiscale model. To avoid that a change in interface position significantly affects the solution of the coupled problem, a location needs to be determined for which the assumptions made on the spatial degrees of freedom are valid. This location depends on the solution of the problem and can thus not a priori be defined [83].
To assess the validity of the partitioning of a domain, a sensitivity analysis can be used [84] to determine the sensitivity of a given cost functional when the configuration of the coupled model is altered. Providing the sensitivity of the solution is small, reliable results are obtained. The main advantage of this approach is that the analysis can be performed without changing the actual interface position [83].

When applying 3D-1D-0D coupled models for patient specific modeling approaches, it is important to use a patient specific geometry of the arterial tree (extracted from medical images) and to properly fit the mechanical and lumped parameters of the models to noninvasive measurements (e.g. MRI, Doppler, ...). This is, however, a difficult and time-consuming task and is probably the biggest limitation to the use of dimensionally heterogeneous models in large-scale clinical studies [59].

In order to describe the entire systemic circulation, a model of the venous system and the heart should be included. Due to the presence of the valves, the noncircular cross sections and the highly nonlinear pressure-diameter relation in the venous system, this is a rather

challenging task. Obviously, this also applies to closed loop models of the complete cardiovascular system, accounting for both the pulmonary and systemic circulation. Contributions in this direction are provided by [47, 81, 82, 85, 86].

In general, it can be stated that geometrical multiscale models allow to perform quantitative and qualitative studies on the interaction between local and global quantities in the cardiovascular system. These are indeed applications that are beyond the capabilities of stand-alone 3D, 1D and 0D models. Despite the number of applications of 3D-1D coupled models is still fairly limited, the strength of these models suggests they will provide an important contribution in the next step towards more realistic hemodynamic simulations. Some foreseen applications include the simulation of (surgical) treatments to study the alterations in local and global hemodynamics and the shape sensitivity analysis of a 3D geometry to optimize anastomosis procedures with respect to some hemodynamic quantities involving both scales.

This review is limited to geometrical multiscale models for cardiovascular hemodynamic research, and does not consider coupling with, for instance, cellular or subcellular models describing biological functions which might interplay and interfere with the parameters of the 3D, 1D or 0D models described here. In addition to different geometrical scales, also different time scales need to be crossed and linked.

CHAPTER 2

Fluid-structure interaction simulation of pulse propagation in arteries: numerical pitfalls[1]

This chapter presents some considerations about numerical dissipation. Although the methods presented in this chapter are well-known in literature, it is important to understand the possible limitations of the numerical methods used in this and other research.

2.1 INTRODUCTION

With advances in computing power and numerical algorithms, computational simulations are extensively used for applications where experimental data are limited or unavailable. Provided that the model parameters faithfully represent the physical quantities of the arterial system and the numerical parameters are chosen carefully, these computational models can accurately predict the pressure and flow fields.

However, in many simulations, too little attention is paid to the proper selection of the numerical parameters. In that case considerable numerical dissipation and dispersion may influence the results and have a significant impact on the calculated waveforms and subsequent data interpretation. When simulating the propagation of a short pulse in an artery, for instance, the time step size needs to be carefully chosen in order to avoid a decrease in pulse amplitude that is not only caused by viscous dissipation [87, 88]. Parameters that

[1]This chapter is based on the work *"Fluid-structure interaction simulation of pulse propagation in arteries: numerical pitfalls and hemodynamic impact of local stiffening."*, as published in *International Journal of Engineering Science* 77:1-13, 2014.

affect the numerical dissipation are the time step size Δt and the grid size Δx, which are mostly chosen sufficiently large to reduce the calculation time, but should be adapted to the period of the present wave harmonics and their wavelength.

The aim of this study is threefold. First, a numerical study is performed to illustrate the effect of the previously mentioned parameters on the simulation of the pulse propagation in a flexible artery. Second, the FSI problem under consideration is simplified to the 1D blood flow in a flexible tube and a von Neumann analysis [89, 90] is presented in which the relation between the numerical dissipation and the discretization parameters is derived for a certain combination of discretization in space and time. The methodology followed in this study can, however, be used in a straightforward way to study other discretization schemes. Third, the numerical parameters necessary for the simulation of the pulse propagation in a locally stiffened tube (i.e. a simple model representative for an aorta with repaired aortic coarctation) are determined. These results will be further applied in chapter 6, where the hemodynamic impact of the stiff segment is studied.

2.2 MATERIALS AND METHODS

2.2.1 Numerical study

To illustrate the effect of the discretization parameters, a numerical study is performed in which the propagation of a sinusoidal pressure pulse in a straight tube is simulated using a two-dimensional axisymmetric FSI model. Different time step sizes and grid sizes are used to analyze their influence on the numerical dissipation.

2.2.1.1 FSI model

The geometrical model consists of a two-dimensional axisymmetric tube with a length of 60 cm, an inner diameter of 1.5 cm and a wall thickness of 0.15 cm (see Figure 2.1). At the inlet of the fluid domain a sinusoidal pressure pulse (period of 15 ms, amplitude of 250 Pa) is applied. At the outlet a reflection free boundary is implemented. This is done by imposing the following relation between the change in outlet pressure, $\Delta p(t) = p(t) - p(t - \Delta t)$, and outlet velocity (averaged over the cross section) $\Delta v(t) = v(t) - v(t - \Delta t)$ at two consecutive time steps.

$$\Delta p = \rho_f c \Delta v \tag{2.1}$$

In this equation ρ_f represents the blood density and c the wave speed. Remark that a different symbol is applied to represent the velocity compared to the one used in chapter 1. The wave speed is adapted according to the pressure level by means of the Bramwell-Hill equation.

$$c = \sqrt{\frac{dp}{\rho_f \frac{dA}{A}}} \tag{2.2}$$

In this equation A represents the cross section of the tube. c is calculated in a separate structural analysis (SIMULIA Abaqus/Standard) for different values of p in a range from 500 to 1500 Pa and linear interpolation between these data points is performed.

Both ends of the tube wall are fixed in longitudinal direction. Blood is modeled as an incompressible and Newtonian fluid (density 1050 kg/m^3, viscosity 3 mPas) and the flow is assumed to be laminar. A linear elastic material model is used to describe the wall behavior (Young's modulus 250 kPa, Poisson's ratio 0.49, density 1200 kg/m^3). These parameters yield a pulse wave velocity of 4.86 m/s and thus a wavelength of 0.073 m in unloaded state. All simulations are performed until time-periodic solutions are obtained (i.e. until the change in amplitude of the pressure wave at the end of the tube at two consecutive periods becomes less than 0.2%).

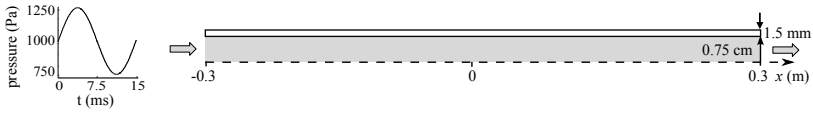

Figure 2.1: Two-dimensional axisymmetric FSI model.

The FSI problem is solved in a partitioned way, as such the equations for the blood flow and the deformation of the structure are solved separately. The flow equations are solved using a pressure-based solver (ANSYS Fluent), which computes the flow in a segregated manner using the SIMPLE algorithm [91, 92]. A second-order upwind discretization scheme is used for the convective term in the momentum equation. The diffusion terms are central differenced and are second-order accurate. For the temporal discretization of the flow equations a second-order implicit scheme is applied. A finite element package (SIMULIA Abaqus/Standard) is applied to calculate the wall deformations. The nonlinear equilibrium equations are solved using the Newton method with a fixed time increment. For the temporal discretization of the structure the operator defined by Hilber, Hughes and Taylor [93] is applied, which is an unconditionally stable scheme and possesses controllable algorithmic damping properties.

To obtain an accurate calculation of the stress on the fluid-structure interface, the flow equations are solved in an Arbitrary Lagrangian-Eulerian (ALE) formulation on a deforming mesh. The structural equations are solved in a Lagrangian frame.

Besides a flow solver (ANSYS Fluent) and a structural solver (SIMULIA Abaqus Standard), a coupling algorithm is required to take into account the interaction between the flow and the motion of the structure. Due to the flexibility of the arterial wall and the compara-

ble density of the blood and the structure, this interaction is strong. A stable and efficient algorithm is therefore needed to solve the coupled problem within an acceptable time. In this work a quasi-Newton algorithm with an approximation for the inverse of the Jacobian (IQN-ILS) is used [94].

2.2.1.2 Governing equations

The equations that describe the unsteady flow of the Newtonian, incompressible, viscous fluid are the conservation of mass and the Navier-Stokes equations, given by

$$\nabla.\boldsymbol{v}_f = 0 \tag{2.3}$$

$$\rho_f \frac{\partial \boldsymbol{v}_f}{\partial t} + \rho_f \nabla.(\boldsymbol{v}_f \boldsymbol{v}_f) = \rho_f \boldsymbol{f}_f + \nabla.\boldsymbol{\sigma_f} \tag{2.4}$$

with $\boldsymbol{v}_f$ the flow velocity, t the time and $\boldsymbol{f}_f$ the body forces per unit of mass on the fluid. The stress tensor $\boldsymbol{\sigma}_f$ is defined as

$$\boldsymbol{\sigma}_f = -p\boldsymbol{I} + \boldsymbol{\tau} \tag{2.5}$$

with $\boldsymbol{I}$ the unit tensor and $\boldsymbol{\tau}$ the viscous stress tensor.

The velocity of the structure $\boldsymbol{v}_s$ is determined by the Cauchy momentum equation that describes the non-relativistic momentum transport in any continuum.

$$\rho_s \frac{D\boldsymbol{v}_s}{Dt} = \rho_s \boldsymbol{f}_s + \nabla.\boldsymbol{\sigma}_s \tag{2.6}$$

In this equation ρ_s represents the structural density, $\boldsymbol{\sigma}_s$ the Cauchy stress tensor and $\boldsymbol{f}_s$ the body forces per unit of mass on the structure. The notation *D/Dt* refers to the material derivative.

The equilibrium conditions on the fluid-structure interface are the kinematic condition

$$\boldsymbol{v}_f = \boldsymbol{v}_s \tag{2.7}$$

and the dynamic condition

$$\boldsymbol{\sigma}_f.\boldsymbol{n}_f = -\boldsymbol{\sigma}_s.\boldsymbol{n}_s. \tag{2.8}$$

$\boldsymbol{n}_f$ and $\boldsymbol{n}_s$ represent the unit normal vector that points outwards from the fluid respectively the structural domain.

2.2.2 Analytical study

One possibility to examine the effect of the discretization parameters at the start of a simulation, is to perform a numerical study as described in section 2.2.1. However, this can be very time consuming as FSI simulations are characterized by a high computational cost.

Another possibility to gain insight in the influence of the temporal and spatial discretization on the numerical dissipation is to perform an analytical study in which the 2D or 3D FSI problem is simplified to the one-dimensional one and the scalar linear transport equation is

considered. Even though the von Neumann analysis is a well documented topic, this option is often overlooked or unknown to researchers performing numerical FSI simulations. A brief description of the analysis is given in the next section. A more distinguished analysis can be found in [89, 90]. Although the model does not take into account the full complexity of the problem under consideration, the results can be used as a guidance for the selection of the numerical parameters.

2.2.2.1 Transport equation

The scalar linear one-dimensional transport equation is given by

$$\frac{\partial u}{\partial t} = -c\frac{\partial u}{\partial x} \tag{2.9}$$

where c is the speed of propagation of the scalar u, which is a function of time (t) and space (x). Assuming that c is constant, the wave component of the solution with wavenumber k can be written as

$$u(x,t) = Be^{jk(x-ct)} \tag{2.10}$$

with B a constant and j the imaginary unit. The wavenumber k is inversely proportional to the wavelength λ, given by the product of the speed of propagation c and the period of the wave T.

$$k = \frac{2\pi}{\lambda} = \frac{2\pi}{cT} \tag{2.11}$$

Eq. (2.10) can be split into a time dependent $\phi(t)$ and a space dependent part $\psi(x)$.

$$u(x,t) \quad = \quad \phi(t)\psi(x) = \phi(t)e^{jkx} \tag{2.12}$$

with

$$\begin{cases} \phi(t) & = Be^{-jkct} \\ \psi(x) & = e^{jkx} \end{cases} \tag{2.13}$$

2.2.2.2 Spatial discretization

The artery through which the pressure pulse propagates is discretized in spatial intervals of equal length Δx. For the analysis, a second-order upwind discretization scheme [91] is used for the convective term in the transport equation, as this scheme will be used in the numerical simulations afterwards. Nevertheless, this analysis can be repeated for other schemes in a straightforward way. The spatial discretization of Eq. (2.9) is thus given by

$$\frac{\partial u}{\partial t} = c\left[-\frac{3}{2}\frac{u(x)-u(x-\Delta x)}{\Delta x} + \frac{1}{2}\frac{u(x-\Delta x)-u(x-2\Delta x)}{\Delta x}\right]. \tag{2.14}$$

After substitution of Eq. (2.12), the spatially discretized transport equation becomes

$$\begin{aligned} \frac{\partial u}{\partial t} &= \frac{c}{\Delta x}\left[-\frac{3}{2}(e^{jkx} - e^{jk(x-\Delta x)}) + \frac{1}{2}(e^{jk(x-\Delta x)} - e^{jk(x-2\Delta x)})\right]\phi(t) \\ &= \frac{c}{\Delta x}\left[-\frac{3}{2}(1 - e^{-jk\Delta x}) + \frac{1}{2}(e^{-jk\Delta x} - e^{-jk2\Delta x})\right]\phi(t)e^{jkx} \\ &= \frac{c}{\Delta x}F\phi(t)e^{jkx} \end{aligned} \tag{2.15}$$

with

$$F = -\frac{3}{2}(1 - e^{-j\theta}) + \frac{1}{2}(e^{-j\theta} - e^{-2j\theta}) \tag{2.16}$$

and

$$\theta = k\Delta x. \tag{2.17}$$

2.2.2.3 Temporal discretization

Eq. (2.15) is subsequently discretized in time. Two schemes were applied, however, the analysis can easily be repeated for other discretization schemes. Using a second-order implicit scheme, the temporal discretization of Eq. (2.15) is given by

$$\frac{\frac{3}{2}u(t+\Delta t) - 2u(t) + \frac{1}{2}u(t-\Delta t)}{\Delta t} = \frac{c}{\Delta x}F\phi(t+\Delta t)e^{jkx}. \tag{2.18}$$

This scheme is unconditionally stable and is well suited for the simulation of wave propagation.

To examine the effect of the accuracy of the time integration scheme, the numerical dissipation obtained with the second-order scheme is compared to the one obtained with a first-order scheme. Using the backward Euler scheme, the temporal discretization of Eq. (2.15) is given by

$$\frac{u(t+\Delta t) - u(t)}{\Delta t} = \frac{c}{\Delta x}F\phi(t+\Delta t)e^{jkx}. \tag{2.19}$$

Although this scheme is not very accurate, it is unconditionally stable and is implemented in most numerical solvers and is therefore used in many applications [87].

Substituting Eq. (2.12) and the Courant number, given by

$$C = \frac{c\Delta t}{\Delta x} \tag{2.20}$$

in the previous equations, Eqs. (2.18) and (2.19) respectively become

$$\frac{3}{2}\phi(t+\Delta t) - 2\phi(t) + \frac{1}{2}\phi(t-\Delta t) = CF\phi(t+\Delta t) \tag{2.21}$$

$$\phi(t+\Delta t)[1 - CF] \quad = \quad \phi(t). \tag{2.22}$$

2.2.2.4 Numerical dissipation

Defining the amplification factor G as

$$G = \frac{\phi(t+\Delta t)}{\phi(t)} = \frac{\phi(t)}{\phi(t-\Delta t)} \tag{2.23}$$

the numerical dissipation *after one time step* of a sine wave traveling with a constant speed can be calculated by

$$1 - |G| = 1 - \left|\frac{1}{2 - \sqrt{1 + 2CF}}\right| \tag{2.24}$$

for the second-order scheme and by

$$1 - |G| = 1 - \left| \frac{1}{1 - CF} \right| \tag{2.25}$$

for the first-order scheme. The numerical dissipation *after one time step* is thus a function of two dimensionless parameters: $\Delta x/\lambda$, being a measure of the spatial resolution of the wave and $\Delta t/T$, which is a measure of the temporal resolution of the wave. Remark that, in some methods, due to restrictions in the Courant number, Δx and Δt cannot be chosen independently [95]. This is, however, not the case for the implicit method used in this analysis.

Usually, the simulation of wave travel does not consist of one time step, but a certain time t is needed for the pressure pulse to propagate through the computational domain, given by the ratio of the length of the domain to the speed of the wave. As $t/\Delta t$ consecutive time steps are needed for the simulation of this propagation, only a factor $|G|^{t/\Delta t}$ of the original pulse will remain after the last time step. The numerical dissipation *after a propagation time* t is thus given by

$$1 - |G|^{t/\Delta t}. \tag{2.26}$$

Note that if one is interested in capturing the reflections at the boundaries of the computational domain, also their propagation time should be considered in the calculation of the total numerical dissipation.

2.2.3 Numerical study on the hemodynamic impact of a local stiffening

The results from the previous studies are finally used to determine the settings necessary to obtain a grid and time step converged simulation of the wave propagation and reflection in a simplified model of an aorta with repaired aortic coarctation. A description of this model can be found in section 6.2.1 of chapter 6.

2.3 RESULTS

2.3.1 Numerical study

The importance of a proper time step size is illustrated in Figure 2.2. This figure shows the pressure contours along the tube obtained for a simulation with a low (top) and a high temporal resolution (bottom). A strong decrease in amplitude during wave propagation can be observed for the simulation with the lowest temporal resolution and inaccurate results are obtained due to numerical dissipation.

The simulation of the wave propagation is performed for different values of $\Delta t/T$, ranging from 0.0667 to 0.0042. Besides numerical dissipation of the pressure pulse, also viscous dissipation occurs during propagation. The numerical dissipation can thus not simply be determined by considering the reduction in amplitude of the pressure wave. As the amplitudes of the propagating waves, simulated with $\Delta t/T$ equal to 0.0083 and 0.0042 are

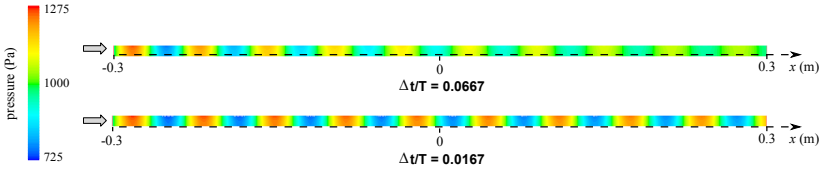

Figure 2.2: Simulation of the wave propagation in a two-dimensional axisymmetric tube obtained with (top) a low and (bottom) a high temporal resolution. Pressure contours (Pa) in the fluid interior obtained using a second-order implicit time integration scheme.

almost equal, it can be concluded that the numerical dissipation becomes negligible using a value of 0.0042 for $\Delta t/T$. In that case the amplitude reduction is considered to be only due to viscous dissipation. As the viscous dissipation after a time t is independent of the time step size, additional amplitude reductions in the simulations with a larger time step size are caused by numerical dissipation.

To calculate the numerical dissipation *after a propagation time* t, the relative reduction in amplitude ϕ of the time-periodic wave at two positions (x_1 and x_2) along the tube is considered. These positions are chosen such that the time for the wave to propagate with a speed c from point x_1 to x_2 is equal to t. To clear out the effect of viscous dissipation, the relative amplitude reduction obtained for the time step size independent simulation is subtracted from this relative amplitude reduction. Using a value for $\Delta t/T$ equal to δ, the numerical dissipation *after a propagation time* t, is thus calculated by

$$\frac{[\phi(x_2)/\phi(x_1)]_{\Delta t/T=0.0042} - [\phi(x_2)/\phi(x_1)]_{\Delta t/T=\delta}}{[\phi(x_2)/\phi(x_1)]_{\Delta t/T=0.0042}}. \tag{2.27}$$

Figure 2.3 shows the thus obtained numerical dissipation as a function of the temporal resolution of the wave. The numerical dissipation increases more than linearly with increasing $\Delta t/T$.

Similar, simulations with different values of $\Delta x/\lambda$ ranging from 0.0027 to 0.044 are performed. Grid independent results are obtained for a value of $\Delta x/\lambda$ equal to 0.0027 and this simulation is thus used as a reference for the other simulations. Using a value of $\Delta x/\lambda$ equal to δ, the numerical dissipation *after a propagation time* t, is thus calculated by

$$\frac{[\phi(x_2)/\phi(x_1)]_{\Delta x/\lambda=0.0027} - [\phi(x_2)/\phi(x_1)]_{\Delta x/\lambda=\delta}}{[\phi(x_2)/\phi(x_1)]_{\Delta x/\lambda=0.0027}}. \tag{2.28}$$

In Figure 2.4 the effect of $\Delta x/\lambda$ on the numerical dissipation *after a propagation time* t is shown for different values of t/T. It can be seen that the numerical dissipation increases more than linearly with increasing $\Delta x/\lambda$. For the configuration studied here (second-order

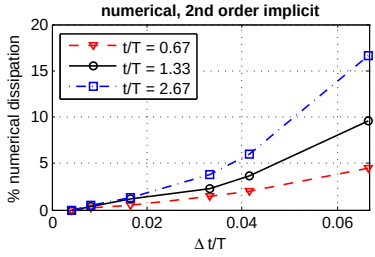

Figure 2.3: The numerical dissipation *after a propagation time* t as a function of $\Delta t/T$ for different values of t/T ($\Delta x/\lambda = 0.0067$).

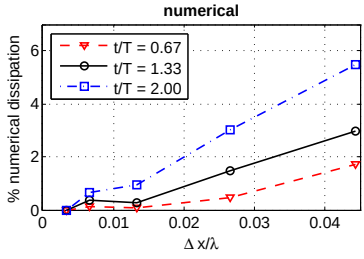

Figure 2.4: The numerical dissipation *after a propagation time* t as a function of $\Delta x/\lambda$ for different values of t/T ($\Delta t/T = 0.0167$).

accurate in space and time), a relatively low temporal and spatial resolution can be sufficient to restrict the numerical dissipation. Since in cardiovascular simulations the grid size is typically a few orders smaller than the wavelength of the present wave harmonics (approximately ranging from 5 to 0.25 m), the spatial resolution will have no significant effect on the numerical dissipation. Only for very short pulses, the grid size may become influential.

Figures 2.3 and 2.4 demonstrate that the propagation time t has a large impact on the total numerical dissipation.

2.3.2 Analytical study

Fig 2.5 depicts the relation between the temporal resolution of a wave and the numerical dissipation *after a propagation time* t as derived in the analytical study and compares the results obtained with a first-order scheme (left) to the ones obtained with a second-order scheme (right). According to this figure the numerical dissipation increases less than linearly with decreasing temporal resolution for the first-order scheme whereas for the second-order scheme, a more than linear increase can be observed. On the other hand, a much higher temporal resolution is required to obtain the same degree of numerical dissipation. For example, to limit the numerical dissipation after a time t/T = 2.67 to 5%, a temporal resolution of 1000 time steps per period is needed for the simulation using the first-order scheme while only 27 time steps per period are required for the simulation using the second-order scheme. Compared to the results derived in the numerical study (Figure 2.3), the same nonlinear relationship between the numerical dissipation and $\Delta t/T$ can be observed and a qualitative and quantitative agreement is found.

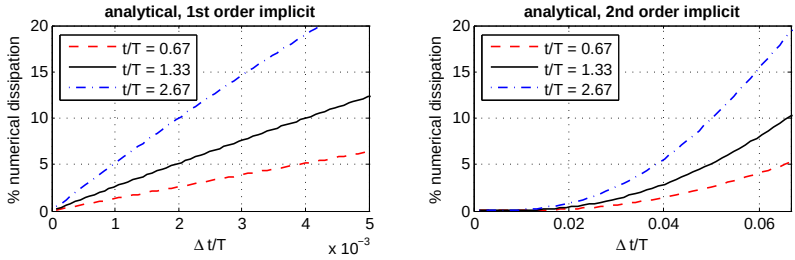

Figure 2.5: The grid independent numerical dissipation *after a propagation time* t as a function of $\Delta t/T$ for different values of t/T obtained using (left) a first-order and (right) a second-order implicit scheme.

Figure 2.6 depicts the effect of the spatial resolution on the numerical dissipation *after a propagation time* t for different values of t/T. Compared to the numerical results (Figure 2.4), the analytical results slightly overestimate the numerical dissipation. The analytical

study, however, considers the damping in time of a wave that remains periodic in space, whereas in the numerical study, the dissipation is analyzed by studying the reduction in amplitude of a wave while it propagates along the tube and is thus not periodic in space. One should keep in mind, however, that the analytical study is only a guidance for the selection of the numerical parameters as is considers a very simplified model of the blood flow in an artery.

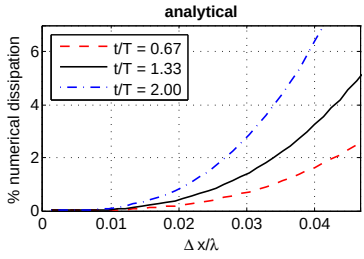

Figure 2.6: The time step size independent numerical dissipation *after a propagation time* t as a function of $\Delta x/\lambda$ for different values of t/T.

Although the period T and the speed of propagation c of the wave harmonics present in the system can mostly not be chosen arbitrarily, attention should be paid if their values are altered (which is for example the case during exercise or when the stiffening of the arterial wall is modeled). Figure 2.7 (right) shows the numerical dissipation *after one time step* as a function of the period of the wave and the wave speed for a fixed Δx and Δt. Since both $\Delta t/T$ and $\Delta x/\lambda$ decrease with increasing wave period, the numerical dissipation will decrease exponentially with increasing period. A decrease of the wave speed leads to a reduced spatial resolution of the pressure wave (for a particular T and Δx). This reduced spatial resolution results in a slightly increased numerical dissipation.

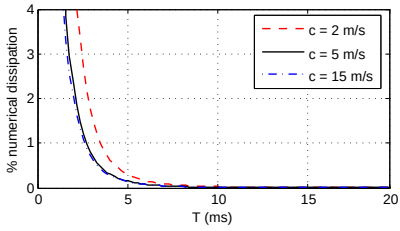

Figure 2.7: The numerical dissipation *after one time step* as a function of the period T of a sinusoidal wave for different wave speeds c ($\Delta t = 0.25$ ms, $\Delta x = 0.5$ mm).

2.3.3 Numerical study on the hemodynamic impact of a local stiffening

Figure 2.8 depicts the effect of the accuracy of the time integration scheme and illustrates the importance of a proper time step size selection when simulating the propagation of a short pulse in a locally stiffened artery (using the model from Figure 6.1). As these simulations involve the propagation of a pressure pulse, different wave harmonics will be present in the system. The lower the frequency of the wave component, the better this wave is resolved in space and time and the more accurate it is simulated. Figure 2.8 shows the pressure evolution along the artery at different times t during the propagation. A coarse time step size of 4 ms is used to simulate the results on the left, whereas the results on the middle and the right are generated with a small time step size of 1 and 0.25 ms respectively. As demonstrated in the analytical study, the simulation using the first-order scheme requires a much higher temporal resolution to obtain the same degree of numerical dissipation. As such, smaller time steps (2, 0.25 and 0.1 ms) are applied for this simulation. A strong decrease in amplitude during wave propagation can be observed for the simulations with the lowest temporal resolution. Another effect of the use of a coarse time step size is the damping of the wave reflections proximal to the stiff segment (indicated with an arrow in the figure on the right).

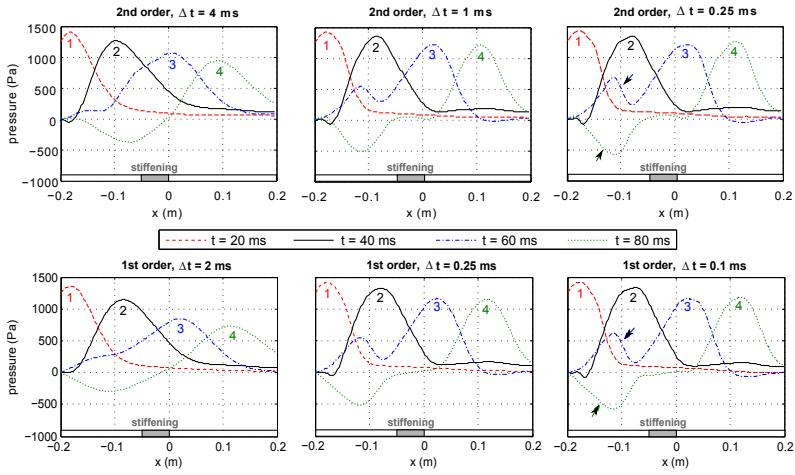

Figure 2.8: Simulation of the propagation of a short pressure pulse in a locally stiffened tube using different time integration schemes (second-order, top, versus first-order implicit, bottom) and different time step sizes.

2.4 Discussion and conclusion

When solving a differential equation by a numerical approximation method, numerical dissipation and dispersion may occur. The study of these errors and their effect on the solution

is a well-documented topic, but is sometimes overlooked in FSI simulations, where the numerical parameters are often optimized with respect to time efficiency and stability rather than accuracy [87, 88]. Numerical dissipation is a general problem, occurring both in monolithic and partitioned FSI simulations. This papers aims to elucidate the effect of numerical dissipation on the solution of cardiovascular FSI simulations using both numerical simulations of the blood flow in an artery and an analytical study in which the scalar linear one-dimensional transport equation is considered.

The numerical dissipation depends on three parameters: $\Delta t/T$ and $\Delta x/\lambda$, determining the temporal and spatial resolution of the wave harmonics and $t/\Delta t$, defining the number of consecutive time steps during which the dissipation occurs. It is shown that for a second-order upwind discretization scheme in combination with a second-order implicit time integration scheme, the numerical dissipation *after a propagation time* t increases more than linearly with increasing $\Delta t/T$ (Figure 2.3 and Figure 2.5 right) and with increasing $\Delta x/\lambda$ (Figure 2.4 and Figure 2.6). Furthermore, the comparison is made with a simulation for which a first-order implicit time integration scheme is used, demonstrating the need for a much higher temporal resolution in the latter case (Figure 2.5 and Figure 2.8). Since in cardiovascular simulations, the grid size is typically a few orders smaller than the wavelength of the present wave harmonics, the spatial resolution will have no significant effect on the numerical dissipation.

As both the time step size and the grid size can affect the numerical results considerably, their influence should be examined at the start of the simulation. This can be done analytically and/or numerically. The analytical study in which a simplified model of the problem is applied can be used as a guidance for the selection of the discretization parameters. The final choice of these parameters should preferable be made by studying the accuracy of the numerical simulations in which the full complexity of the problem is considered. When the pulse period and/or the wavelength change (which is the case during exercise) or the propagation time increases the grid size and/or the time step size need to be adapted in order to obtain the same degree of numerical dissipation.

CHAPTER 3

Stability analysis of a fluid-structure interaction simulation using different time integration schemes and time step sizes for the fluid and the structure

In this research, a partitioned approach is used to solve the FSI problem. As such, two different solvers, using different time integration schemes, are applied. During the performance of cardiovascular FSI simulations (both in a simplified and patient specific model), we experienced some stability problems. These were the motivation to perform a numerical and analytical study of the stability issues related to the coupling of solvers using different time integration schemes and time step sizes.

3.1 INTRODUCTION

Coupled problems often use different time integration schemes to discretize the different sub-problems. As each time integration method is characterized by its accuracy, stability and numerical dissipation, this approach allows the different equations to be solved with schemes that are particularly suited to solve each individual sub-problem.

Furthermore, coupled problems sometimes require different time step sizes in the different sub-problems. For example, in fluid-structure interaction (FSI) problems where the flow requires large eddy simulation (LES), small time step sizes are needed to resolve the flow field in time [96]. Another example involves the simulation of thermo mechanics [97, 98].

Likewise, the global domain in structural or fluid dynamics can be considered as an assembly of sub-domains with their own time integration scheme and time step size. This is done in [99] to couple surface routing and subsurface flow processes and in [100] to model the atmosphere-ocean interaction. Also for transient structural dynamics (such as impact simulations) this approach can be of great interest [101].

However, according to our experience with cardiovascular FSI simulations, coupling different time integration schemes and time step sizes can induce stability problems. The stability issues that emerged from these simulations were the motivation to perform an analytical study of the temporal stability of the flow in an artery. The stability of a coupled problem with one degree of freedom, using different time integration schemes, has been studied before for a one-dimensional damped spring-mass system [102] and the motion of a rigid body in a moving fluid, representative for the motion of a rigid heart valve [103]. Here, a problem with more than one degree of freedom is investigated and, in addition, the influence of different time step sizes for the fluid and the structure (so-called 'sub-cycling') on the temporal stability is studied. In [104] the effect of sub-cycling in the fluid problem on the stability of a staggered FSI algorithm is discussed. To the best of our knowledge, the effect of sub-cycling on the stability of a strongly coupled FSI simulation, has not been studied before.

An analytical study is presented in which two particular combinations of time integration schemes are applied. The methodology followed in this study can, however, be used in a straightforward way to study other combinations of time integration schemes. The influence of some numerical and physiological parameters on the stability and the damping of the spurious modes is studied. Particular attention is paid to the effect of the fluid to solid time step size ratio and the selection of an appropriate interpolation scheme during the sub-cycles.

To illustrate the usefulness of the methodology, the analytical results are verified by a numerical study in which the propagation of a sinusoidal flow wave in a straight tube is simulated using nonlinear two-dimensional axisymmetric FSI simulations.

3.2 Analytical study

3.2.1 Governing equations

As a simplified model for the blood flow in an artery, the one-dimensional flow in a straight, flexible tube is considered. Gravity and viscosity are not taken into account. The equations that describe the unsteady flow of the incompressible fluid are the continuity and the momentum equation, given by

$$\frac{\partial s}{\partial t} + \frac{\partial su}{\partial x} = 0 \tag{3.1a}$$

$$\frac{\partial su}{\partial t} + \frac{\partial su^2}{\partial x} + \frac{1}{\rho_f}(\frac{\partial s\hat{p}}{\partial x} - \hat{p}\frac{\partial s}{\partial x}) = 0 \tag{3.1b}$$

in which s represents the cross sectional area of the tube, u the axial velocity, x the axial coordinate, t the time, ρ_f the fluid density and $\hat{p}$ the pressure. Remark that a different symbol is applied compared to the one used in the previous chapter to indicate the velocity. In the remainder of this paper the kinematic pressure $p = \hat{p}/\rho_f$ will be used.

Neglecting the anisotropic, viscoelastic behavior of the vascular wall and the circumferential and longitudinal deformation, the deformation in radial direction is determined by

$$\rho_s h\frac{\partial^2 r}{\partial t^2} + \chi\frac{\partial^4 r}{\partial x^4} - \psi\frac{\partial^2 r}{\partial x^2} + \eta(r - r_0) = \rho_f(p - p_0) \tag{3.1c}$$

with r describing the inner radius, ρ_s the arterial wall density, h the wall thickness and p_0 the pressure corresponding to the reference radius at rest r_0 [105]. This structural model is an extension to the so-called independent-rings model [106], as the terms $\chi\frac{\partial^4 r}{\partial x^4}$ and $\psi\frac{\partial^2 r}{\partial x^2}$ take into account the longitudinal interaction between the tube segments. χ, ψ and η are positive constants depending on the wall properties, where χ accounts for the inner action of the bending in the tissue and ψ for the shear deformation. ψ is calculated as $\kappa G h$ with κ the Timoshenko shear correction factor and G the shear modulus. η is given by $\frac{Eh}{(1-\nu^2)r_0^2}$ with E the young modulus and ν the Poisson coefficient.

3.2.2 Spatial discretization

The tube with length L is discretized in N spatial intervals of equal length Δx. For the analysis, a first-order upwind scheme is used for the convective term in the momentum equation, while central discretization is used for the other terms in the flow equations. Nevertheless, the analysis can easily be repeated for other discretization schemes. With the subscripts i and $i \pm 1/2$ indicating the value at the cell centers and cell faces respectively (with $i = 1, ..., N$), the spatial discretization of the continuity and momentum equation is given by

$$\Delta x\frac{\partial s_i}{\partial t} + s_{i+1/2}u_{i+1/2} - s_{i-1/2}u_{i-1/2} - \hat{\delta}(p_{i+1} - 2p_i + p_{i-1}) = 0 \tag{3.2a}$$

$$\begin{aligned}\Delta x\frac{\partial s_i u_i}{\partial t} &+ u_i s_{i+1/2}u_{i+1/2} - u_{i-1}s_{i-1/2}u_{i-1/2} + \frac{1}{2}(s_{i+1/2}(p_{i+1} - p_i) \\ &+ s_{i-1/2}(p_i - p_{i-1})) = 0\end{aligned} \tag{3.2b}$$

for $u_i \geq 0$. As the pressure term is discretized with a central scheme, pressure stabilization is needed. Therefore artificial diffusion is added in the continuity equation with coefficient $\hat{\delta} = s_0/(u_0 + \Delta x/\Delta t)$ [107].

For the spatial discretization of the structural equation the central difference scheme is used, resulting in

$$\begin{aligned}\rho_s h\frac{\partial^2 r_i}{\partial t^2} \quad &+ \quad \frac{\chi}{\Delta x^4}(r_{i+2} - 4r_{i+1} + 6r_i - 4r_{i-1} + r_{i-2}) \\ &- \quad \frac{\psi}{\Delta x^2}(r_{i+1} - 2r_i + r_{i-1}) + \eta(r_i - r_0) = \rho_f(p_i - p_0) \end{aligned} \tag{3.2c}$$

3.2.3 Linearization

The cross sectional area s in Eq. (3.2) is substituted by πr^2 and the velocity, radius and pressure are linearized as the sum of a reference value (indicated with a subscript 0) and a perturbation term (indicated with a prime).

$$p_i = p_0 + p_i^{'} \tag{3.3a}$$

$$s_i = \pi(r_0 + r_i^{'})^2 \tag{3.3b}$$

$$u_i = u_0 + u_i^{'} \tag{3.3c}$$

Neglecting the terms quadratic in the perturbed quantities, this gives

$$\begin{aligned}\Delta x\frac{\partial 2r_0 r_i^{'}}{\partial t} &+ {r_0}^2(u_{i+1/2}^{'} - u_{i-1/2}^{'}) + 2r_0u_0(r_{i+1/2}^{'} - r_{i-1/2}^{'}) \\ &- \delta(p_{i+1}^{'} - 2p_i^{'} + p_{i-1}^{'}) = 0\end{aligned} \tag{3.4a}$$

$$\begin{aligned}\Delta x\frac{\partial(r_0^2 u_i^{'} + 2r_0u_0r_i^{'})}{\partial t} &+ {r_0}^2u_0(u_i^{'} - u_{i-1}^{'} + u_{i+1/2}^{'} - u_{i-1/2}^{'}) \\ &+ 2r_0u_0^2(r_{i+1/2}^{'} - r_{i-1/2}^{'}) + \frac{1}{2}r_0^2(p_{i+1}^{'} - p_{i-1}^{'}) = 0\end{aligned} \tag{3.4b}$$

$$\begin{aligned}\rho_s h\frac{\partial^2 r_i^{'}}{\partial t^2} \quad &+ \quad \frac{\chi}{\Delta x^4}(r_{i+2}^{'} - 4r_{i+1}^{'} + 6r_i^{'} - 4r_{i-1}^{'} + r_{i-2}^{'}) \\ &- \quad \frac{\psi}{\Delta x^2}(r_{i+1}^{'} - 2r_i^{'} + r_{i-1}^{'}) + \eta(r_i^{'}) = \rho_f(p_i^{'}) \end{aligned} \tag{3.4c}$$

with $\delta = \hat{\delta}/\pi$.

3.2.4 Fourier equations

The pressure, radius and velocity perturbation are then decomposed as the sum of N Fourier modes. For the radius perturbation this results in

$$r_i^{'} = \frac{1}{N}\sum_{l=0}^{N-1}\tilde{r}_l \exp(\jmath\omega_l i\Delta x) \tag{3.5}$$

with $\omega_l = 2\pi l/L$ the angular wave number. As Eq. (3.4) is linear in velocity, pressure and radius perturbation, the temporal stability of the flow in the flexible tube is determined by the temporal stability of each individual wave component. In order to study the different wave components separately, $r_i^{'}$, $u_i^{'}$ and $p_i^{'}$ are substituted by $\tilde{r}_l \exp(\jmath\omega_l i\Delta x)$, $\tilde{u}_l \exp(\jmath\omega_l i\Delta x)$ and $\tilde{p}_l \exp(\jmath\omega_l i\Delta x)$ respectively. To keep the equations readable the product $\omega_l\Delta x$ is substituted by θ_l and the tilde and subscript l are omitted.

$$\Delta x\frac{\partial 2r_0 r}{\partial t} + \jmath r_0^2\sin(\theta)u + 2\jmath r_0 u_0\sin(\theta)r + 2\delta(1-\cos(\theta))p = 0 \tag{3.6a}$$

$$\begin{aligned}\Delta x\frac{\partial(r_0^2 u + 2r_0u_0 r)}{\partial t} + (1-\exp(-\jmath\theta)+\jmath\sin(\theta))r_0^2u_0u + 2\jmath u_0^2 r_0\sin(\theta)r \\ + \jmath r_0^2\sin(\theta)p = 0\end{aligned} \tag{3.6b}$$

$$\rho_s h\frac{\partial^2 r}{\partial t^2} + \left(\frac{4\chi}{\Delta x^4}(1-\cos(\theta))^2 + \frac{2\psi}{\Delta x^2}(1-\cos(\theta)) + \eta\right)r = \rho_f p \tag{3.6c}$$

3.2.5 Temporal discretization of the flow

Eq. (3.6) is subsequently discretized in time. First, the same time step size (Δt) is used for the discretization of the flow and the structural problem. The effect of sub-cycling is studied in 3.2.8. For the discretization of the flow equations the backward Euler scheme (BE) is used, as this scheme is unconditionally stable and is implemented in most numerical solvers (such as ANSYS Fluent which will be used in the numerical study afterwards). However, this analysis can be repeated for other schemes in a straightforward way. Using the BE scheme, this results in

$$\begin{aligned}\frac{2r_0\Delta x}{\Delta t}(r^{n+1}-r^n) + \jmath r_0^2\sin(\theta)u^{n+1} + 2\jmath r_0u_0\sin(\theta)r^{n+1} \\ + 2\delta(1-\cos(\theta))p^{n+1} = 0\end{aligned} \tag{3.7a}$$

$$\begin{aligned}\frac{r_0^2\Delta x}{\Delta t}(u^{n+1}-u^n) + \frac{2r_0u_0\Delta x}{\Delta t}(r^{n+1}-r^n) \\ + (1-\exp(-\jmath\theta)+\jmath\sin(\theta))r_0^2u_0u^{n+1} \\ + 2\jmath u_0^2 r_0\sin(\theta)r^{n+1} + \jmath r_0^2\sin(\theta)p^{n+1} = 0\end{aligned} \tag{3.7b}$$

3.2.6 Temporal discretization of the structure

For the temporal discretization of the structure two schemes are used.

a) The first one being the compatible backward Euler scheme,

$$\rho_s h\ddot{r}^{n+1} + \left(\frac{4\chi}{\Delta x^4}(1-\cos(\theta))^2 + \frac{2\psi}{\Delta x^2}(1-\cos(\theta)) + \eta\right)r^{n+1} = \rho_f p^{n+1} \tag{3.8a}$$

in which the acceleration and velocity are calculated as

$$\ddot{r}^{n+1} = \frac{1}{\Delta t}(\dot{r}^{n+1} - \dot{r}^n) \tag{3.8b}$$

$$\dot{r}^{n+1} = \frac{1}{\Delta t}(r^{n+1} - r^n) \tag{3.8c}$$

An overdot signifies a time derivative.

b) The second scheme used for the time integration of the dynamic problem is the operator defined by Hilber, Hughes and Taylor [93], which is an unconditionally stable scheme and possesses controllable algorithmic damping properties. The internal and external forces in Eq. (3.6c) are treated similarly and are replaced by a weighted average of the forces at the beginning and end of the time step, as opposed to a fully implicit treatment of the external forces in [93]. This approach corresponds to the approach imposed in the structural solver (Abaqus\Standard), used for the numerical validation afterwards.

$$\begin{aligned}&\rho_s h \ddot{r}^{n+1} \\ &+ (1+\alpha)\left[\left(\frac{4\chi}{\Delta x^4}(1-\cos(\theta))^2 + \frac{2\psi}{\Delta x^2}(1-\cos(\theta)) + \eta\right) r^{n+1} - \rho_f p^{n+1}\right] \\ &- \alpha\left[\left(\frac{4\chi}{\Delta x^4}(1-\cos(\theta))^2 + \frac{2\psi}{\Delta x^2}(1-\cos(\theta)) + \eta\right) r^{n} - \rho_f p^{n}\right] = 0\end{aligned} \tag{3.9a}$$

The operator definition is completed by the Newmark formula for acceleration and velocity integration

$$\ddot{r}^{n+1} = \frac{1}{\beta \Delta t^2}(r^{n+1} - r^n) - \frac{1}{\beta \Delta t}\dot{r}^n - (\frac{1}{2\beta} - 1)\ddot{r}^n \tag{3.9b}$$

$$\dot{r}^{n+1} = \dot{r}^n + \Delta t(1-\gamma)\ddot{r}^n + \Delta t \gamma \ddot{r}^{n+1} \tag{3.9c}$$

with α, β and γ parameters governing the stability and numerical dissipation of the algorithm. To preserve desirable characteristics of the integrator, β and γ are defined as

$$\gamma = \frac{1}{2} - \alpha \tag{3.10}$$

$$\beta = \frac{1}{4}(1-\alpha)^2 \tag{3.11}$$

The smaller the value of α ($\in [-1/3, 0]$), the more artificial damping is induced in the numerical solution. In the limit, the choice $\alpha = 0$ results in the trapezoidal method with no numerical damping.

3.2.7 Stability of the time integration scheme

Two combinations of time integration schemes are studied: in 3.2.7.1 the BE scheme is used for the time discretization of both the flow and structural equations, in 3.2.7.2 the combination BE-HHT is analyzed.

3.2.7.1 BE-BE combination

Eqs (3.7) and (3.8) are written in matrix form

$$Ax^{n+1} = Bx^n \tag{3.12}$$

with $x = [r\ \dot{r}\ \ddot{r}\ u\ p]^T$. Stability requires the absolute value of all eigenvalues λ_i (with $i = 1, ..., 5$) of the amplification matrix $A^{-1}B$ to be less than or equal to one. As the analytical expressions of the eigenvalues are too long and complex and provide therefore almost no insight in the influence of the numerical and physiological parameters on the stability, they are not included in this study. However, the effect of an individual parameter is studied by calculating the eigenvalues as a function of this parameter, whereas the other parameter values are chosen representative for the flow in an artery (see Table 3.1).

Parameter	**Value**	**Unit**
E	300,000	N/m^2
ν	0.49	
χ	0	kg m^2/s^2
ψ	55	kg/s^2
ρ_s	1200	kg/m^3
ρ_f	1000	kg/m^3
u_0	0.1	m/s
r_0	0.005	m
L	0.05	m
h	0.001	m

Table 3.1: Dimensions of the model and material properties.

Using the BE scheme for the discretization of both the flow and the structural equations, two eigenvalues $\lambda_{1,2}$ are found with an absolute value close to, but smaller than one. In the limit where Δx and Δt approach zero, $\lambda_{1,2}$ become equal to one, as the numerical dissipation is reduced to zero. The solution of the one-dimensional case is a linear combination of the corresponding eigenvectors. Modes that do not correspond to this solution are spurious and the absolute value of the corresponding eigenvalues should be close to zero for a good damping. For the BE scheme two of these eigenvalues $\lambda_{3,4}$ are zero, corresponding to the spurious mode where only the acceleration differs from zero ($[0\ 0\ 1\ 0\ 0]^T$) and the mode where only the pressure differs from zero ($[0\ 0\ 0\ 0\ 1]^T$). The fifth eigenvalue λ_5 is zero for $\omega = 0$, but increases with increasing angular wave number. For small ω the spurious modes are thus damped very well.

3.2.7.2 BE-HHT combination

A similar approach as in 3.2.7.1 is followed for Eqs (3.7) and (3.9). Again, two eigenvalues $\lambda_{1,2}$ with an absolute value close to but smaller than 1 are obtained, of which the eigenvectors are the same as those found using the BE scheme. Consequently, they correspond

to the solution of the one-dimensional case. To study the stability of the time integration scheme and the damping of the spurious modes, the absolute value of the three remaining eigenvalues $\lambda_{3,4,5}$ (which are determined by the value of the numerical and physiological parameters) need to be analyzed.

Figure 3.1 depicts the evolution of the maximal absolute value of these eigenvalues as a function of the numerical damping factor α and the angular wave number ω. The grid size and time step size are chosen sufficiently small ($\Delta x = 10^{-4}$ m, $\Delta t = 10^{-5}$ s) so that, even for the high wave numbers, the eigenvalues are not significantly influenced by numerical dissipation. According to this figure, the combination of the BE and HHT scheme is stable ($|\lambda| \leq 1$) if the geometrical and mechanical parameters are chosen physiologically relevant. As $|\lambda|$ is close to 1 for simulations with $\alpha = 0$ and low angular wave numbers, there will be almost no damping of the spurious modes in these cases. It can be seen that the simulation of a wave with a high wave number will experience a better damping of the spurious modes than the simulation of a wave with a small wave number. Only for small wave numbers, the damping of the spurious modes can be improved by increasing the numerical damping.

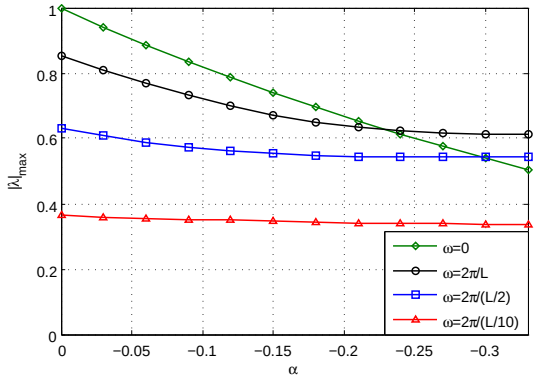

Figure 3.1: Maximal absolute value of the eigenvalues corresponding to the spurious modes as a function of the artificial damping factor α and the angular wave number ω.

Variations of the grid size Δx in the range $5\text{x}10^{-3}$ to $5\text{x}10^{-5}$m do not significantly influence the eigenvalues corresponding to the spurious modes. The grid size determines, however, the highest possible wave number that can be resolved ($\omega_{max} = \pi/\Delta x$ rad/m). Since the highest wave numbers are associated with the best damping, this will not result in a different stability behavior between coarse and fine grids.

The effect of the time step size Δt, depends on the angular wave number ω. For $\omega = 0$, Δt has no influence on the eigenvalues of the amplification matrix. However, for $\omega = 2\pi/L$ (or higher) an increase in Δt will decrease the absolute value of the eigenvalues corresponding to the solution of the one-dimensional case, as can be seen in Figure 3.2.

This can be explained by the increase in numerical dissipation with increasing Δt [108]. The absolute value of the eigenvalues corresponding to the spurious modes, on the other hand, will increase slightly with increasing Δt.

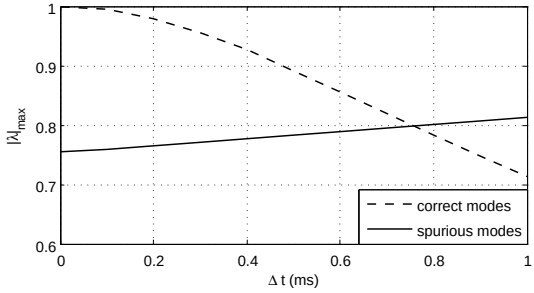

Figure 3.2: Maximal absolute value of the eigenvalues corresponding to the solution of the one-dimensional case (dashed line) and the spurious modes (solid line) for $\omega = 2\pi/L$ and $\alpha = -0.07$.

Although the physiological parameters can mostly not be chosen arbitrarily, also their impact on the temporal stability is discussed. The parameters E, ν, ψ and u_0 have no significant effect on the stability and the damping of the spurious modes. The influence of ρ_f, ρ_s, r_0 and h on the maximal absolute value of the eigenvalues corresponding to the spurious modes is shown in Figure 3.3 for the combination of the BE and the HHT scheme. The legend in this figure indicates the range wherein these parameters are varied along the horizontal axis. Increasing the density of the solid improves the damping of the spurious modes, whereas an increase in fluid density has the opposite effect. The higher the ratio of solid to fluid density, the better the spurious modes are damped. It can be observed that both an increase in reference radius and wall thickness have a positive effect on the damping of the spurious modes.

3.2.8 Effect of sub-cycling

In the previous section, a single time step was used for the time integration of the flow and the structural problem. However, in practice cardiovascular fluid-structure interaction problems sometimes display different time scales in the different sub-problems. For example, the simulation of turbulent blood flow in the vicinity of the aortic or pulmonary valves or in the region of a severely stenosed artery, requires the use of small time step sizes to resolve the flow field in time [109], whereas the time scale associated with the vibration of the structure generally will be much larger. To obtain an accurate simulation, the specified time step size must be of the same order of magnitude as the smallest characteristic time scale. On the one hand, adapting the global time step size to the smallest required time scale (as is done in [96]), would increase the computational time and, in case of a strongly coupled partitioned approach, the number of coupling iterations [107, 110]. On the other hand, a

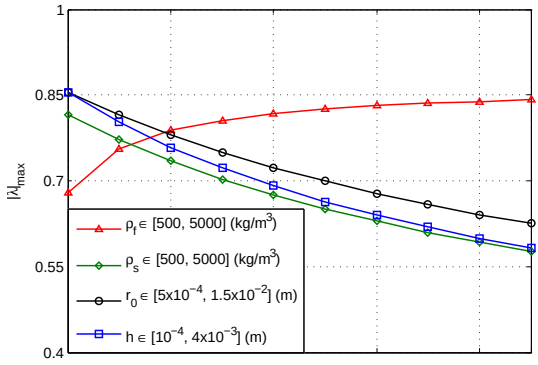

Figure 3.3: Maximal absolute value of the eigenvalues corresponding to the spurious modes as a function of the fluid density ρ_f, the structural density ρ_s, the reference radius r_0 and the wall thickness h ($\omega = 2\pi/L$ and $\alpha = -0.07$). The scale for the horizontal axis is shown in the legend and is different for each curve.

difference in time step size can affect the temporal stability. Therefore, the influence of different time step sizes for the fluid and structure on the temporal stability is analyzed. In this analysis the time step size of one sub-domain is considered to be k times the time step size of the other sub-domain with k a positive integer. For $k > 1$ 'sub-cycling' is applied, performing smaller time steps in one of the sub-domains.

3.2.8.1 Sub-cycling in the structural problem

First, an analytical study is performed for a case in which the time step size, Δt_s, used to discretize the structural equation is smaller than the time step size, Δt_f, used to discretize the flow equations. To restrict the number of equations, Δt_s is chosen equal to $\Delta t_f/2$. In that case, three additional variables should be introduced $r^{n+1/2}$, $\dot{r}^{n+1/2}$ and $\ddot{r}^{n+1/2}$, representing the inner radius, the wall velocity and the acceleration at a time intermediate between time step n and $n+1$. In the remaining, $\Delta t_f = \Delta t$ is called 'a time step'. The two structural sub-time steps $\Delta t_s = \Delta t/2$ will be referred to as 'sub-cycles'.

During each sub-cycle, the structural deformation is calculated for a given pressure on the fluid-structure interface. Different approaches are possible to vary the pressure exerted on the tube wall throughout a time step. For a linear approach, the pressure applied during the first sub-cycle of time step $n+1$ is given by $(p^{n+1} + p^n)/2$, and the pressure applied during the second sub-cycle is p^{n+1}.

a) In case the BE scheme is used for the temporal discretization of the structure, Eq. (3.8)

is transformed to

$$\rho_s h \ddot{r}^{n+1/2} + \left(\frac{4\chi}{\Delta x^4}(1-\cos(\theta))^2 + \frac{2\psi}{\Delta x^2}(1-\cos(\theta)) + \eta \right) r^{n+1/2} = \rho_f \frac{p^n + p^{n+1}}{2} \tag{3.13a}$$

$$\ddot{r}^{n+1/2} = \frac{1}{(\Delta t/2)}(\dot{r}^{n+1/2} - \dot{r}^n) \tag{3.13b}$$

$$\dot{r}^{n+1/2} = \frac{1}{(\Delta t/2)}(r^{n+1/2} - r^n) \tag{3.13c}$$

to describe the wall movement during the first sub-cycle and to

$$\rho_s h \ddot{r}^{n+1} + \left(\frac{4\chi}{\Delta x^4}(1-\cos(\theta))^2 + \frac{2\psi}{\Delta x^2}(1-\cos(\theta)) + \eta \right) r^{n+1} = \rho_f p^{n+1} \tag{3.13d}$$

$$\ddot{r}^{n+1} = \frac{1}{(\Delta t/2)}(\dot{r}^{n+1} - \dot{r}^{n+1/2}) \tag{3.13e}$$

$$\dot{r}^{n+1} = \frac{1}{(\Delta t/2)}(r^{n+1} - r^{n+1/2}) \tag{3.13f}$$

during the second sub-cycle.

b) In case the HHT operator is used, Eq. (3.9) is replaced by

$$\begin{aligned} &\rho_s h \ddot{r}^{n+1/2} \\ &+ (1+\alpha)\left[\left(\frac{4\chi}{\Delta x^4}(1-\cos(\theta))^2 + \frac{2\psi}{\Delta x^2}(1-\cos(\theta)) + \eta \right) r^{n+1/2} - \rho_f \frac{p^n + p^{n+1}}{2} \right] \\ &- \alpha \left[\left(\frac{4\chi}{\Delta x^4}(1-\cos(\theta))^2 + \frac{2\psi}{\Delta x^2}(1-\cos(\theta)) + \eta \right) r^n - \rho_f p^n \right] = 0 \end{aligned} \tag{3.14a}$$

$$\ddot{r}^{n+1/2} = \frac{1}{\beta(\Delta t^2/4)}(r^{n+1/2} - r^n) - \frac{1}{\beta(\Delta t/2)}\dot{r}^n - (\frac{1}{2\beta} - 1)\ddot{r}^n \tag{3.14b}$$

$$\dot{r}^{n+1/2} = \dot{r}^n + \frac{\Delta t}{2}(1-\gamma)\ddot{r}^n + \frac{\Delta t}{2}\gamma \ddot{r}^{n+1/2} \tag{3.14c}$$

during the first sub-cycle, and by

$$\begin{aligned} &\rho_s h \ddot{r}^{n+1} + (1+\alpha)\left[\left(\frac{4\chi}{\Delta x^4}(1-\cos(\theta))^2 + \frac{2\psi}{\Delta x^2}(1-\cos(\theta)) + \eta \right) r^{n+1} - \rho_f p^{n+1} \right] \\ &- \alpha \left[\left(\frac{4\chi}{\Delta x^4}(1-\cos(\theta))^2 + \frac{2\psi}{\Delta x^2}(1-\cos(\theta)) + \eta \right) r^{n+1/2} - \rho_f \frac{p^n + p^{n+1}}{2} \right] = 0 \end{aligned} \tag{3.14d}$$

$$\ddot{r}^{n+1} = \frac{1}{\beta(\Delta t^2/4)}(r^{n+1} - r^{n+1/2}) - \frac{1}{\beta(\Delta t/2)}\dot{r}^{n+1/2} - (\frac{1}{2\beta} - 1)\ddot{r}^{n+1/2} \tag{3.14e}$$

$$\dot{r}^{n+1} = \dot{r}^{n+1/2} + \frac{\Delta t}{2}(1-\gamma)\ddot{r}^{n+1/2} + \frac{\Delta t}{2}\gamma\ddot{r}^{n+1} \tag{3.14f}$$

during the second sub-cycle.

To study the temporal stability of the system, Eqs (3.7) and (3.13) are written in matrix form

$$Ax = By \tag{3.15}$$

with $x = [r^{n+1}\ \dot{r}^{n+1}\ \ddot{r}^{n+1}\ r^{n+1/2}\ \dot{r}^{n+1/2}\ \ddot{r}^{n+1/2}\ u^{n+1}\ p^{n+1}]^T$ and $y = [r^n\ \dot{r}^n\ \ddot{r}^n\ r^{n-1/2}\ \dot{r}^{n-1/2}\ \ddot{r}^{n-1/2}\ u^n\ p^n]^T$. The same is done for Eqs (3.7) and (3.14). The parameters shown in Table 3.1 are used to calculate the eigenvalues λ_i (with $i = 1, ..., 8$) of the amplification matrix $A^{-1}B$. For both combinations of time discretization schemes, two eigenvalues $\lambda_{1,2}$ with an absolute value close to but smaller than one are found. Their eigenvectors (which are the same for both schemes) correspond to the solution of the one-dimensional case. The stability of the FSI problem is thus determined by the absolute value of the other six eigenvalues.

BE-BE combination In case the BE scheme is used for both the flow and solid problem, four of them are equal to zero, corresponding to the eigenvectors $[0\ 0\ 1\ 0\ 0\ 0\ 0\ 0]^T$, $[0\ 0\ 0\ 1\ 0\ 0\ 0\ 0]^T$, $[0\ 0\ 0\ 0\ 1\ 0\ 0\ 0]^T$ and $[0\ 0\ 0\ 0\ 0\ 1\ 0\ 0]^T$. The largest absolute value of the two remaining eigenvalues $\lambda_{7,8}$ is shown in Figure 3.4 as a function of the wave number (red line). According to this figure the simulation remains stable. However, for ω close to zero, their will be almost no damping of the spurious modes.

BE-HHT combination Using the HHT operator to discretize the structural equation combined with the BE scheme for the flow equations, three eigenvalues $\lambda_{3,4,5}$ equal to zero are obtained, corresponding to the eigenvectors $[0\ 0\ 0\ 1\ 0\ 0\ 0\ 0]^T$, $[0\ 0\ 0\ 0\ 1\ 0\ 0\ 0]^T$ and $[0\ 0\ 0\ 0\ 0\ 1\ 0\ 0]^T$. The maximal absolute value of the three remaining eigenvalues $\lambda_{6,7,8}$ is shown in Figure 3.4 (black line). For small wave numbers, the HHT operator becomes unstable ($|\lambda| > 1$) and cannot be used. The depicted eigenvalues are calculated for $\alpha = -0.07$, but the same conclusion is found for any other value of α.

The same study is performed for $\Delta t_s = \Delta t_f/3$, where the pressure applied during the first, the second and the third sub-cycle is $\frac{2}{3}p^n + \frac{1}{3}p^{n+1}$, $\frac{1}{3}p^n + \frac{2}{3}p^{n+1}$ and p^{n+1} respectively. The corresponding equations are similar to those for $\Delta t_s = \Delta t_f/2$ and are thus not included in this study. The resulting eigenvalues are compared to the eigenvalues obtained for $\Delta t_s = \Delta t_f/2$ in Figure 3.4. According to this figure, an increase in the number of sub-cycles has a negative effect on the stability as it causes the simulations using the BE-BE

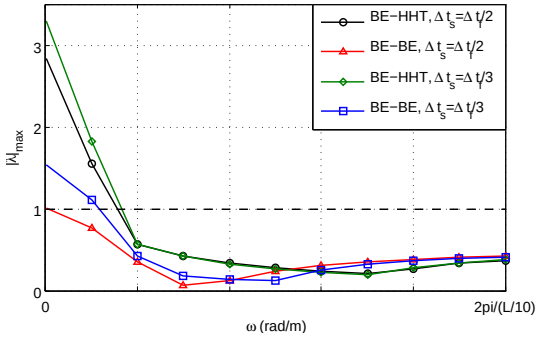

Figure 3.4: Effect of sub-cycling in the structural problem on the maximal absolute value of the eigenvalues corresponding to the spurious modes ($\alpha = -0.07$).

combination to become unstable for small ω and it causes the instability of the simulations using the BE-HHT combination to grow even faster.

To illustrate the effect of the interpolation scheme applied during the sub-cycles, the stability of a simulation with a linear pressure evolution during a time step is compared in Figure 3.5 to the stability of a simulation in which the entire pressure p^{n+1} is applied during the first sub-cycle of time step $n+1$ and is then kept constant during the rest of the time step. The computation using a linear pressure evolution is indicated as 'ramp'. The notation 'jump' refers to a simulation with a sudden pressure increase. Although this pressure jump will slow down the convergence of the structural problem, the entire system will be more stable. In case the BE-BE combination is used, the computation remains stable and the spurious modes are damped well. The simulation using the HHT operator for the structure is unstable and cannot be used.

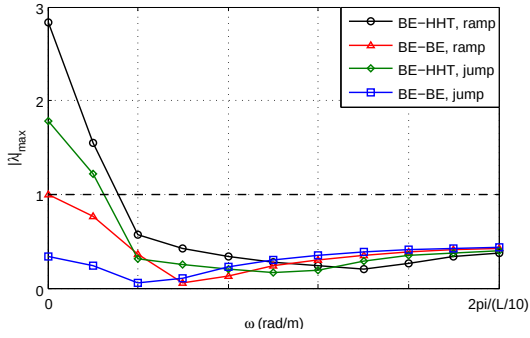

Figure 3.5: Influence of the pressure evolution (linear ramp vs. jump) during a time step on the maximal absolute value of the eigenvalues corresponding to the spurious modes ($\Delta t_s = \Delta t/2$, $\alpha = -0.07$).

3.2.8.2 Sub-cycling in the flow problem

The analysis is repeated for a case in which Δt_f is smaller than Δt_s. As opposed to the allocations used in 3.2.8.1, $\Delta t_s = \Delta t$ is now called 'a time step' and a flow sub-time step is referred to as 'a sub-cycle'. Attention should be paid to the selection of the interpolation method used to determine the wall displacement during the sub-cycles. A linear wall displacement or an adjustment of wall displacement during the first sub-cycle only would, for instance, result in zero wall acceleration during the sub-cycles and unphysiological results would be obtained. To obtain a linear wall acceleration throughout the sub-cycles, a third degree polynomial per point on the interface is used to prescribe the wall displacement during time step $n+1$. The 4 parameters in this polynomial are determined by the wall displacements r^n and r^{n+1} at the beginning and the end of the time step and by matching the discretized second derivative of the polynomial at the beginning and the end of the time step with the wall accelerations $\ddot{r}^n$ and $\ddot{r}^{n+1}$ as calculated by the structural solver.

To restrict the number of equations, Δt_f is chosen equal to $\Delta t_s/2$ (other ratios are analyzed in the numerical study). The wall displacement imposed during the first sub-cycle of time step $n+1$ is then given by $r^{n+1/2} = \frac{r^{n+1}}{2} + \frac{r^n}{2} - \frac{3\ddot{r}^{n+1}\Delta t^2}{16} + \frac{\ddot{r}^n \Delta t^2}{16}$ and r^{n+1} during the second sub-cycle. Two new variables are introduced $u^{n+1/2}$ and $p^{n+1/2}$, representing the fluid velocity and the pressure at a time intermediate between time step n and $n+1$. Eq. (3.7) is consequently replaced by

$$\begin{aligned}\frac{2r_0\Delta x}{(\Delta t/2)}(r^{n+1/2}-r^n) + \jmath r_0^2 \sin(\theta) u^{n+1/2} + 2\jmath r_0 u_0 \sin(\theta) r^{n+1/2} \\ + 2\delta(1-\cos(\theta))p^{n+1/2} = 0\end{aligned} \tag{3.16a}$$

$$\begin{aligned}\frac{r_0^2\Delta x}{(\Delta t/2)}(u^{n+1/2}-u^n) + \frac{2r_0u_0\Delta x}{(\Delta t/2)}(r^{n+1/2}-r^n) \\ + (1-\exp(-\jmath\theta)+\jmath\sin(\theta))r_0^2 u_0 u^{n+1/2} \\ + 2\jmath u_0^2 r_0 \sin(\theta) r^{n+1/2} + \jmath r_0^2 \sin(\theta) p^{n+1/2} = 0\end{aligned} \tag{3.16b}$$

during the first sub-cycle and by

$$\begin{aligned}\frac{2r_0\Delta x}{(\Delta t/2)}(r^{n+1}-r^{n+1/2}) + \jmath r_0^2 \sin(\theta) u^{n+1} + 2\jmath r_0 u_0 \sin(\theta) r^{n+1} \\ + 2\delta(1-\cos(\theta))p^{n+1} = 0\end{aligned} \tag{3.16c}$$

$$\begin{aligned}\frac{r_0^2\Delta x}{(\Delta t/2)}(u^{n+1}-u^{n+1/2}) + \frac{2r_0u_0\Delta x}{(\Delta t/2)}(r^{n+1}-r^{n+1/2}) \\ + (1-\exp(-\jmath\theta)+\jmath\sin(\theta))r_0^2 u_0 u^{n+1} \\ + 2\jmath u_0^2 r_0 \sin(\theta) r^{n+1} + \jmath r_0^2 \sin(\theta) p^{n+1} = 0\end{aligned} \tag{3.16d}$$

during the second sub-cycle.

Eqs (3.16) and (3.8) are written in matrix form

$$Ax = By \tag{3.17}$$

with $x = [r^{n+1}\ \dot{r}^{n+1}\ \ddot{r}^{n+1}\ r^{n+1/2}\ u^{n+1/2}\ u^{n+1}\ p^{n+1/2}\ p^{n+1}]^T$ and $y = [r^{n}\ \dot{r}^{n}\ \ddot{r}^{n}\ r^{n-1/2}\ u^{n-1/2}\ u^{n}\ p^{n-1/2}\ p^{n}]^T$. The same is done for Eqs (3.16) and (3.9). For both combinations of time integration schemes, two eigenvalues $\lambda_{1,2}$ of the amplification matrix $A^{-1}B$ are close to but smaller than one. Their eigenvectors correspond to the solution of the one-dimensional case.

BE-BE combination Using the BE scheme for the discretization of both the flow and the structural equations, four of the other eigenvalues are zero, corresponding to the spurious modes $[0\ 0\ 0\ 1\ 0\ 0\ 0\ 0]^T$, $[0\ 0\ 0\ 0\ 1\ 0\ 0\ 0]^T$, $[0\ 0\ 0\ 0\ 0\ 0\ 1\ 0]^T$ and $[0\ 0\ 0\ 0\ 0\ 0\ 0\ 1]^T$. The maximal absolute value of the other eigenvalues $\lambda_{7,8}$ is shown in Figure 3.6 as a function of the wave number ω. For small wave numbers, the use of sub-cycles has a negative effect on the damping behavior. The absolute value remains, however, smaller than one and thus a stable solution should be obtained.

BE-HHT combination In case the HHT operator is used for the structure combined with

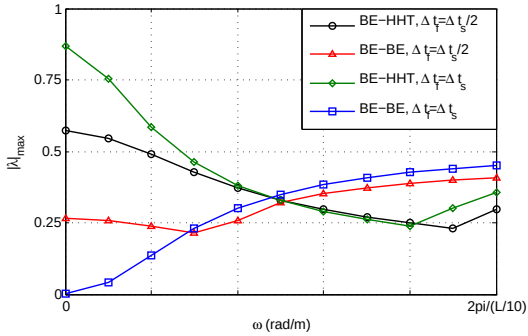

Figure 3.6: Effect of sub-cycling in the flow problem on the maximal absolute value of the eigenvalues corresponding to the spurious modes ($\alpha = -0.07$).

the BE scheme for the flow, three eigenvalues $\lambda_{3,4,5}$ equal to zero are found, corresponding to the eigenvectors $[0\ 0\ 0\ 1\ 0\ 0\ 0\ 0]^T$, $[0\ 0\ 0\ 0\ 1\ 0\ 0\ 0]^T$ and $[0\ 0\ 0\ 0\ 0\ 0\ 1\ 0]^T$. The largest absolute value of the three remaining eigenvalues $\lambda_{6,7,8}$ is shown in Figure 3.6. According to this figure the use of sub-cycling reduces the absolute value of the eigenvalues and the FSI problem remains stable for all wave numbers.

3.3 NUMERICAL STUDY

To verify the analytical results, a numerical study is performed in which the propagation of a sinusoidal flow wave in a straight tube is simulated using a nonlinear two-dimensional axisymmetric FSI model (see Figure 3.7).

3.3.1 Method

Figure 3.7: Two-dimensional axisymmetric FSI model.

The FSI problem is solved in a partitioned way and, consequently, separate solvers are used for the flow and structural computations. The equilibrium at the fluid-structure interface is established using a quasi-Newton algorithm with an approximation for the inverse of the Jacobian from a least-squares model (IQN-ILS) [94]. The convergence criterion in the Euclidean norm for the residual of the interface displacement is set to 10^{-8} m and for the residual of the interface load to 10^{-2} Pa. More severe convergence criteria have no significant impact on the results. The coupling iterations have thus converged sufficiently and the same solution is obtained as would have been found with a monolithic solver.

The flow equations are solved in an Arbitrary Lagrangian-Eulerian formulation on a deforming mesh. The structural equations are solved in a Lagrangian frame. The first-order upwind scheme is used to discretize the momentum equation. The BE scheme is used for the temporal discretization of the flow equations. For the time integration of the structural problem, the BE or HHT operator is used.

The parameters listed in Table 1 are used as approximate values for the flow in an artery. Blood is modeled as an incompressible, Newtonian fluid with a viscosity of 3 mPas. At the inlet, an axial fluid velocity of $u_0 + \frac{u_0}{2}\sin(2\pi t)H(t)$ is imposed, where H represents the Heaviside function. Given an initial velocity field of 0.1 m/s (u_0), the inlet velocity has a discontinuity in its derivative at $t = 0$ s. At this time, spurious modes can enter the solution and the stability and damping behavior can be evaluated. The pressure at the outlet of the tube is set to zero. Along the tube longitudinal and circumferential wall displacements are prevented. A structured grid of 10^4 cells and 2500 quadratic elements is constructed in the fluid and the structural domain respectively. This allows the high wave numbers to be sufficiently spatially resolved. A time step size Δt of 10^{-4} s is used. As we are interested in the numerical behavior of the FSI simulation rather than the propagation of the flow wave itself, only the first 100 time steps are simulated.

3.3.2 Stability of the time integration scheme

Figure 3.8 shows the evolution of the inlet pressure and the acceleration of the wall at the inlet during the first 25 time steps (as the damping behavior is most visible during the first time steps) as a function of the numerical damping factor α. In case the BE scheme is used for the solid problem, the spurious modes are damped immediately. This case can thus be treated as a reference for the other simulations using the HHT operator. As predicted by the stability analysis, all the simulations using the HHT operator remain stable. Large oscillations in the wall acceleration and small oscillations in the pressure are found if no artificial damping is used ($\alpha = 0$). In case of maximal artificial damping ($\alpha = -0.3$) both oscillations are damped well. However, from this figure, it cannot be derived which angular wave numbers are present and how the damping behavior of the individual wave components is influenced by α.

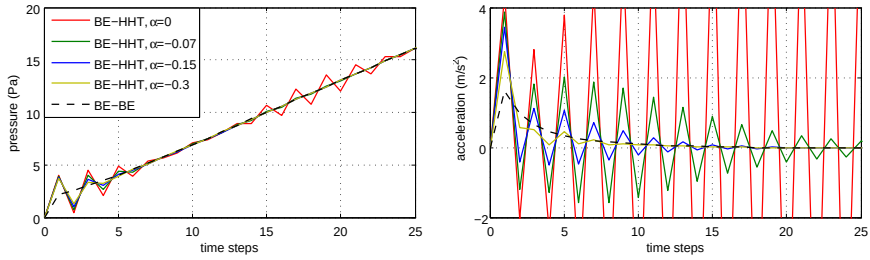

Figure 3.8: Evolution of the inlet pressure (left) and the acceleration of the wall (right), as a function of the artificial damping factor α.

To study the damping behavior of the individual wave components, a fast Fourier transform (FFT) on the spatial distribution of the pressure on the fluid-structure interface is performed. According to the FFT analysis, the wave numbers $\omega = 0$ and $\omega = 2\pi/L$ are the most dominant components and, consequently, their behavior mainly determines the damping behavior of the entire solution. The error determined by

$$\left| \frac{P_{BE}(\omega, t) - P_{HHT}(\omega, t)}{P_{BE}(\omega, t_1) - P_{HHT}(\omega, t_1)} \right| \tag{3.18}$$

is shown in Figure 3.9 as a function of time for three small wave numbers. In this equation $P(\omega, t)$ represents the FFT component of the pressure corresponding to an angular wave number ω at a time t. The FFT components $P_{BE}(\omega, t)$ obtained using the BE scheme for the structure are treated as reference values for the FFT components $P_{HHT}(\omega, t)$ obtained using the HHT operator for the structure. This is motivated by the results shown in Figure 3.6, where, for small ω, the eigenvalue obtained using the BE scheme for the structure is much smaller than the eigenvalue obtained using the HHT operator. For small ω, the error

made using the BE scheme for the structure will thus be negligible compared tot the error made using the HHT operator. The error between P_{BE} and P_{HHT} at a time t is compared with the initial error at a time t_1. The faster this initial error is reduced, the better the spurious modes are damped.

According to Figure 3.9, the damping of the spurious modes is significantly affected by the numerical damping factor for $\omega = 0$ and $\omega = 2\pi/L$. For these wave numbers, decreasing $|\alpha|$ has a negative effect on the damping of the spurious modes. For $\omega = 0$ and $\alpha = 0$ the spurious modes are hardly damped, which is in agreement with the results from Figure 3.1, where $|\lambda|$ equal to one was found. An improvement of the damping with increasing ω can be observed for $\alpha = 0$. For the other numerical damping factors the influence is less pronounced, but is still visible. This confirms the results shown in Figure 3.1.

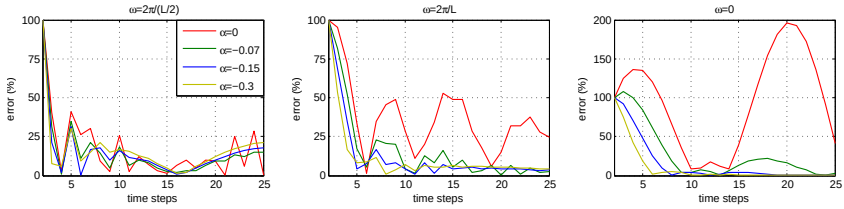

Figure 3.9: Evolution of the error as a function of the angular wave number ω and the numerical damping factor α.

As predicted by the analytical study, variations of the grid size do not significantly influence the damping behavior. The error defined by Eq. (3.18) is calculated for different time step sizes Δt and a wave number equal to $2\pi/L$. For the simulations using the HHT operator for the structural problem, a numerical damping factor of -0.07 is used. The effect of Δt on the damping is shown in Figure 3.10. Decreasing Δt will lead to a faster error reduction and thus a better damping of the spurious modes, which is in agreement with the results of the stability analysis (see Figure 3.2).

Finally, the influence of the physiological parameters on the damping behavior is checked. The same error definition as in Eq. (3.18) is used for $\omega = 2\pi/L$ and $\alpha = -0.07$. A good agreement with the analytical results from Figure 3.3 is obtained. An increase in wall thickness, reference radius and structural density improves the damping, whereas an increase in fluid density reduces the damping of the spurious modes (see Figure 3.11). The other physiological parameters do not significantly affect the numerical stability.

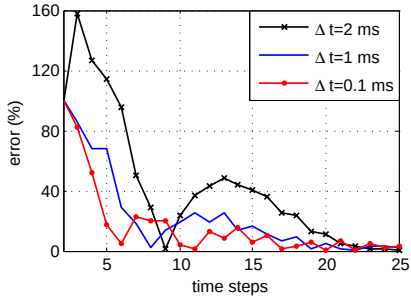

Figure 3.10: Influence of the time step size (Δt) on the damping of the spurious modes.

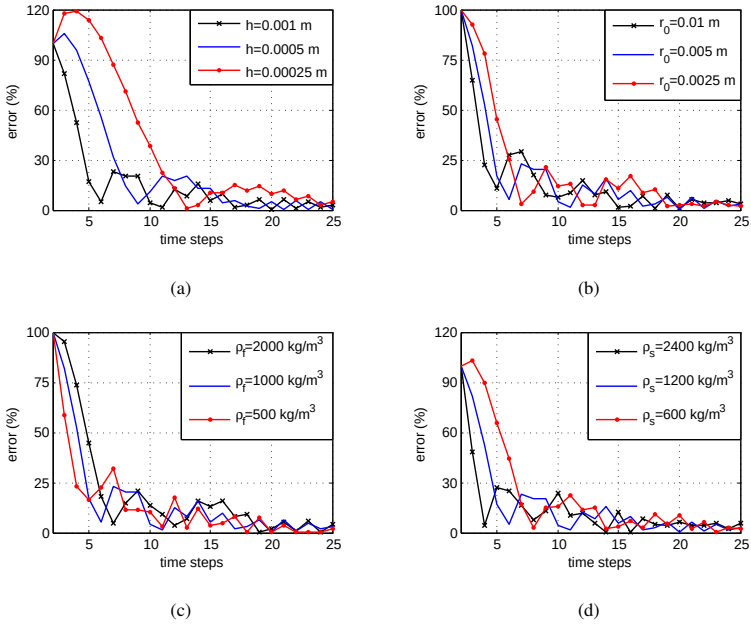

Figure 3.11: Influence of (a) the wall thickness h, (b) the reference radius r_0, (c) the fluid density ρ_f and (d) the structural density ρ_s on the damping of the spurious modes.

3.3.3 Effect of sub-cycling

3.3.3.1 Sub-cycling in the structural problem

In this section the effect of sub-cycling on the stability of the FSI simulation is evaluated for ratios of Δt_s to Δt_f smaller than one. In Figure 3.12 the inlet pressure evolution is shown for both combinations of time integration schemes and different values of $\Delta t_s / \Delta t_f$. The results are obtained for a linear pressure evolution throughout a time step. The results confirm the conclusions of the stability analysis. In case $\frac{\Delta t_s}{\Delta t_f} = \frac{1}{k}$, with k a natural number, the BE-HHT combination is unstable for $\frac{\Delta t_s}{\Delta t_f} \leq \frac{1}{2}$ and the BE-BE combination for $\frac{\Delta t_s}{\Delta t_f} \leq \frac{1}{3}$. Δt_s to Δt_f ratios down to 10^{-2} are simulated (not shown in Figure 3.12). The smaller this time step size ratio is chosen, the faster the instability grows.

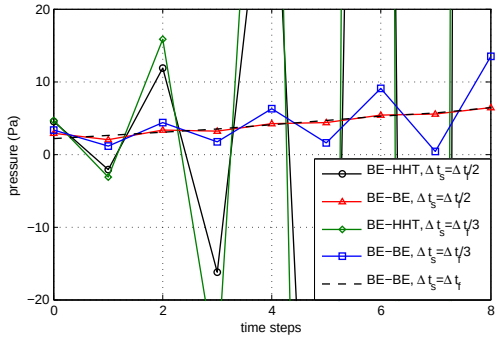

Figure 3.12: Effect of sub-cycling in the structural problem on the evolution of the inlet pressure ($\Delta t_f = 10^{-4}$ s).

Also the influence of the pressure variation throughout a time step is evaluated. In Figure 3.13 the inlet pressure, obtained using a simulation with a linear pressure variation throughout a time step ('ramp'), is compared to the inlet pressure of a simulation with a sudden pressure increase during the first sub-cycle ('jump'). The inlet pressure, obtained using the BE scheme for both the flow and the structure and a single time step, is shown as a reference. As predicted by the analytical study (see Figure 3.5), both BE-HHT simulations are unstable and the instability grows faster in case a linear pressure evolution is used. The BE-BE simulations are stable regardless of the pressure at the intermediate step.

3.3.3.2 Sub-cycling in the flow problem

Using a flow time step size $\Delta t_f = \Delta t_s / 2$ and a cubic wall displacement throughout the sub-cycles, a stable solution is obtained for both combinations of time integration schemes, which is in agreement with the results from the stability analysis (Figure 3.6). Figure 3.14 depicts the inlet pressure evolution throughout the sub-cycles during the first 15 time steps

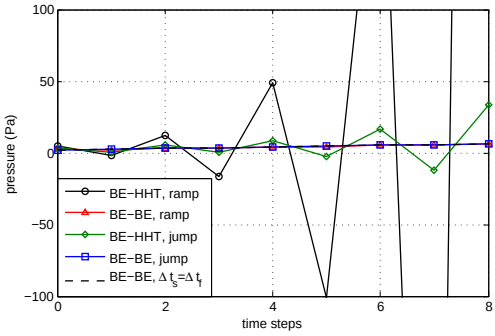

Figure 3.13: Influence of the pressure evolution (linear ramp vs. jump) during a time step on the inlet pressure evolution ($\Delta t_s = \Delta t_f/2$).

for a simulation using 2 (red curve) and 10 sub-cycles (blue curve). During the first sub-cycle of each time step a peak in inlet pressure can be observed. For the BE-BE combination this peak decreases each time step, resulting in a proper calculation of the inlet pressure after a few time steps, whereas for the BE-HHT combination, this peak continues to exist and the pressure calculated at the end of each time step slightly differs from the solution obtained with matching time steps.

To illustrate the potential of sub-cycling (using the BE-BE combination), the evolution of the inlet pressure and outlet flow (during 0.5 s) obtained using a simulation with sub-cycling in the flow problem ($\Delta t_f = \Delta t_s/10 = 10^{-4}$ s, red curve) is compared to the evolution of the inlet pressure and outlet flow of two simulations in which the time step size of the structural problem is adapted to the time step size of the flow problem ($\Delta t_f = \Delta t_s = 10^{-4}$ s for which time independent results are obtained, blue curve and $\Delta t_f = \Delta t_s = 10^{-3}$ s, black curve) in Figure 3.15. For this simulation a smooth inlet profile is used to avoid discontinuities in acceleration. As can be seen in the figure, the simulation with sub-cycling accurately resolves the high frequency components present at the start of the simulation, which are not captured for a simulation with $\Delta t_f = \Delta t_s = 10^{-3}$ s. Yet, the calculation time is decreased by a factor 5, compared to the simulation for which $\Delta t_f = \Delta t_s = 10^{-4}$ s. This is an important reduction as FSI simulations can be very time consuming.

3.3.4 Comparison of the different results

To further illustrate the effect of different combinations of time integration schemes and sub-cycling on the results of a simulation, the wave propagation simulated with different combinations of time integration schemes and $\Delta t_s/\Delta t_f$ values is compared in Figure 3.16 during the first 5 time steps. Using the BE scheme for both the flow and the structural problem and matching time step sizes (equal to 0.5 ms), the wave propagation in Figure 3.16 (a) is clearly visible. The results obtained with the BE-HHT combination are less

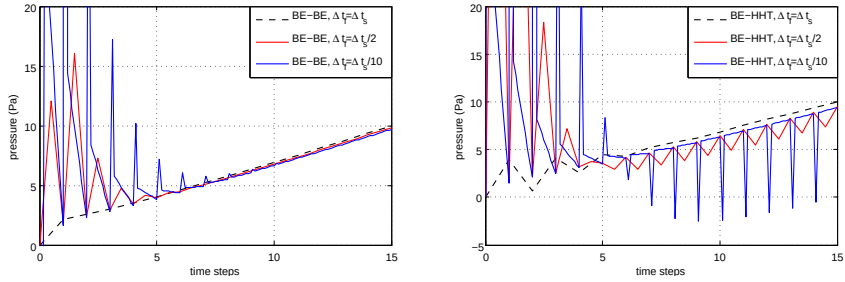

Figure 3.14: Effect of sub-cycling in the flow problem on the evolution of the inlet pressure using the BE-BE combination (left) and the BE-HHT combination (right) ($\Delta t_s = 10^{-4}$ s).

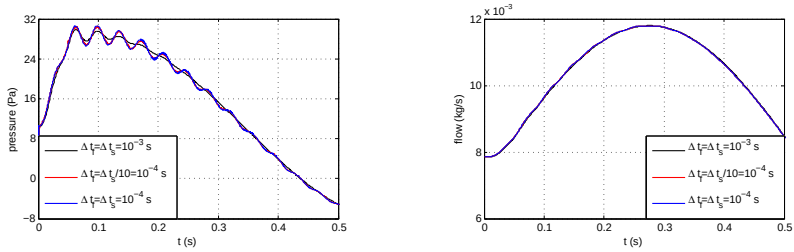

Figure 3.15: Effect of sub-cycling in the flow problem on the evolution of the inlet pressure (left) and the outlet flow (right).

accurate. Small pressure oscillations can be observed in Figure 3.16 (b) as the wave jumps back and forth. Using a time step size ratio ($\Delta t_s / \Delta t_f$) of 1/10, the wave propagation is no longer visible and the results are unusable (shown in Figure 3.16 (c)). Using a time step size ratio ($\Delta t_s / \Delta t_f$) of 10, the wave propagation in Figure 3.16 (d) is again visible.

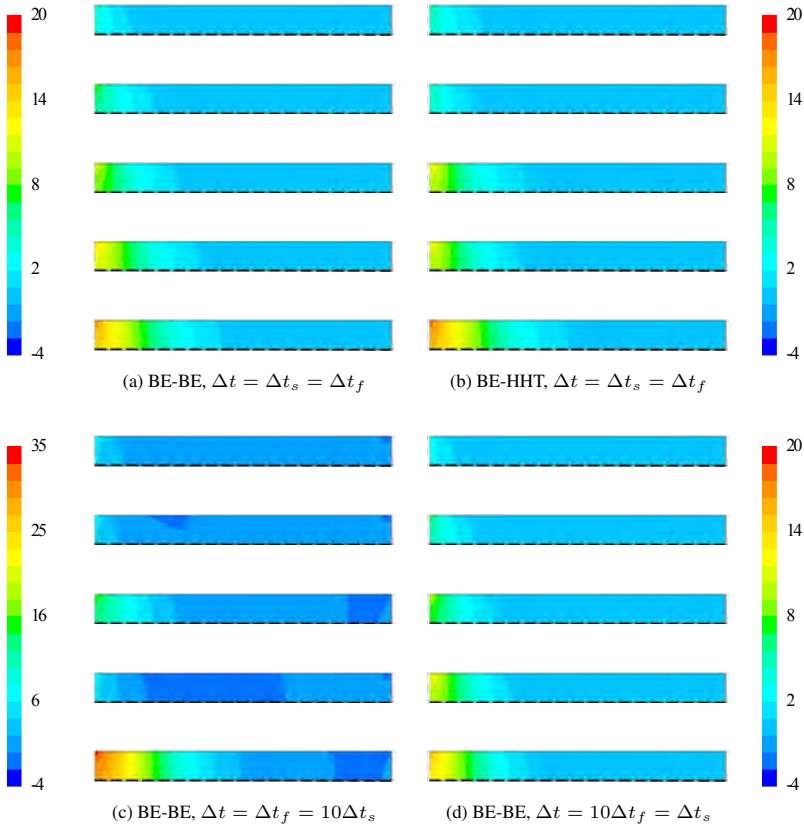

(a) BE-BE, $\Delta t = \Delta t_s = \Delta t_f$ (b) BE-HHT, $\Delta t = \Delta t_s = \Delta t_f$

(c) BE-BE, $\Delta t = \Delta t_f = 10\Delta t_s$ (d) BE-BE, $\Delta t = 10\Delta t_f = \Delta t_s$

Figure 3.16: Comparison of the wave propagation during the first 5 time steps obtained with different combinations of time integration schemes and different values of $\Delta t_s/\Delta t_f$ ($\Delta t = 0.5$ ms, $\alpha = -0.07$). Two-dimensional axisymmetric pressure contours (Pa) of the fluid interior are shown. The axis of symmetry is indicated with a dashed line.

3.4 CONCLUSIONS

A stability analysis has been performed of the FSI problem in which the flow in a flexible tube is computed using different time integration schemes and time step sizes for the fluid and the structure. In this work, the combinations BE-BE and BE-HHT have been studied. Similar analyses are possible for other (combinations of) discretization schemes, however, it is impossible to include them all in this work. Apart from the selected time integration schemes, the interpolation method applied during the sub-cycles strongly affects the stability and the accuracy of the solution.

For parameter values that approximate the flow in an artery and a ratio of the fluid to solid time step size smaller than or equal to one, both combinations of schemes are stable. Compared to an FSI simulation for which the specified time step is adapted to the smallest required time scale, sub-cycling in the fluid significantly speeds up the calculation without loss in accuracy (in case a third order interpolation scheme is used to determine the wall displacement during the sub-cycles). If, on the other hand, the smallest required time step size is determined by the solid problem, the matching of the time step sizes of the fluid and the solid problem is very important to obtain a stable solution.

In case the BE-HHT combination is used, spurious modes with a large wave number are damped more than those with a small wave number. Increasing the artificial damping improves the damping of the spurious modes with a small wave number. Using the BE scheme and the HHT operator for the flow and solid problem respectively, FSI problems with a high solid density to fluid density ratio will experience a better damping of the spurious modes. Likewise, a large radius and wall thickness have a positive effect on the damping of the spurious modes.

These conclusions are confirmed by the results of nonlinear, two-dimensional axisymmetric FSI simulations.

CHAPTER 4

Development and validation of a patient specific FSI model of the aortic arch

This chapter presents an introduction to fluid-structure interaction, which is a major phenomenon in the aorta. A patient specific model of the aortic arch is developed that will be applied in the studies presented in chapter 7 and 8.

4.1 Introduction on the fluid-structure interaction approach

Fluid-structure interaction (FSI) is the interaction between a deformable (and in some cases a moving) structure and the surrounding fluid. The numerical simulation of such a multi-physics problem is challenging, especially if the interaction between the fluid and the structure is strong due to the flexibility of the structure and the comparable density of the fluid and the structure. Considering the extensive development of numerical software packages to perform flow and structural calculations and the increasingly growing computing power, the numerical simulation of FSI problems is still arduous but possible nowadays. Particularly in the biomedical and aerospace sector, research on fluid-structure interaction has gained significant attention. The design of aircraft wings, on which FSI induces fatigue which can cause fracture on a long-term, is an example of an application. With respect to cardiovascular applications, FSI often refers to the interaction between the arterial wall and the blood flow or the interaction between (heart) valves and the blood flow. In this dissertation the fluid-structure interaction in a subject specific aortic arch is modeled to study central hemo-

dynamics in a normal aorta and several cases mimicking (repaired) aortic coarctation (see chapter 7 for an extensive discussion of the latter models).

The FSI problem is solved in a partitioned way, which means that the flow and the structural equations are solved separately. This approach preserves software modularity and allows the flow equations and the structural equations to be solved with different techniques that are particularly suited to solve the respective equations. However, solving the governing equations separately, no equilibrium of the stress on and the displacement of the fluid-structure interface is imposed. Besides a flow solver and a structural solver, also a coupling algorithm is required to take into account the interaction between flow and motion of the structure. If the interaction is strong, several coupling iterations may need to be performed in each time step. A stable and efficient algorithm is therefore needed to solve the coupled problem within an acceptable time. In this work a quasi-Newton algorithm with an approximation for the inverse of the Jacobian (IQN-ILS) is used [94] (which is implemented in the software Tango). This algorithm influences only the interface displacement, all remaining variables in the fluid and solid domain are considered as internal variables. It thereby treats both the flow and the structural solver as a black box which allows the use of commercial software packages.

In each coupling iteration, the flow solver receives the discretized interface displacement from the coupling code Tango and adapts the fluid grid accordingly. It then calculates the flow in the entire domain, including the stress distribution on the interface. Based on this stress distribution, the structural code will calculate the displacement of the structure including the displacement of the interface. In the next coupling iteration, a new interface displacement is calculated by the coupling code (based on the information from the previous iterations) which is again passed to the flow solver. This procedure is repeated until the residuals become sufficiently small.

The IQN-ILS technique creates an approximation for the inverse of the Jacobian in the quasi-Newton iterations. The use of an approximation is motivated by [94, 110], where it is shown that only an approximate Jacobian is needed, as long as it describes the reaction to the components of the error on the position of the interface that are unstable or disappear slowly in Gauss-Seidel iterations between the flow solver and the structural solver. The approximation of the *inverse* of this Jacobian avoids the need to solve a linear system with a dimension equal to the number of degrees of freedom on the fluid-structure interface in each coupling iteration.
In [94] the IQN-ILS technique is compared with other partitioned schemes, such as Aitken relaxation [111] and Interface-GMRES(R) [112]. This comparison indicates that fewer coupling iterations per time step are required if the IQN-ILS algorithm is used. The performance of this algorithm can further be improved (i.e. the convergence accelerated) by

reusing information from previous time steps in the calculation of the approximate Jacobian, if that information is relevant for the current time step. In systole, where the hemodynamic response alters notable each time step, the reusable information is limited to 4 in a normal aorta and to 2 time steps (for a time step size Δt of 2 ms) in the case of severe aortic coarctation. This number increases during diastole, where a reuse of information from the last 8 time steps still accelerates the convergence. The number of useful time steps was found using an iterative approach, in which the number of coupling iterations needed to obtain convergence was evaluated for calculations using information from a different number of time steps.

The equations describing the unsteady flow, the deformation of the structure and equilibrium on the fluid-structure interface are given in section 2.2.1.2.

4.2 THE FLOW MODEL

To obtain the geometric model of the aortic arch, MRI images of a healthy 39 years old male volunteer were taken (see Figure 4.1 in which the aorta and its side branches are indicated in blue). The pixel spacing of the images is 1.25 mm and a slice thickness 1.3 mm. mi-automatic segmentation (Mimics, Materialize, Leuven, Belgium) resulted in a 3D reconstruction of the aortic arch and thoracic aorta (shown in Figure 4.2) in which a hexahedral mesh was constructed using the software pyFormex [113].

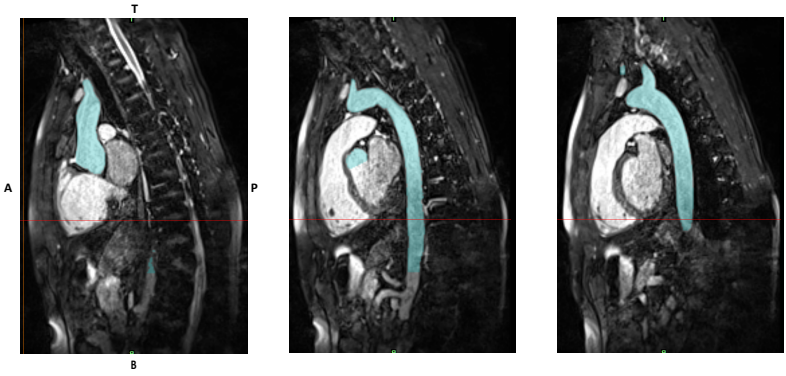

Figure 4.1: MRI images of a 39 years old male volunteer, applied to extract the geometry of the aortic arch (indicated in blue).

At the boundaries of the computational domain, the flow rates were measured with phase-contrast MRI with a temporal resolution of 23.4 ms and processed using Osirix (see Figure 4.3 for an example of the PC MR images taken at the descending aorta). These measured flows were imposed as a boundary condition at the ascending aorta and the three side branches (see Figure 4.4). At the descending aorta, a three element windkessel model

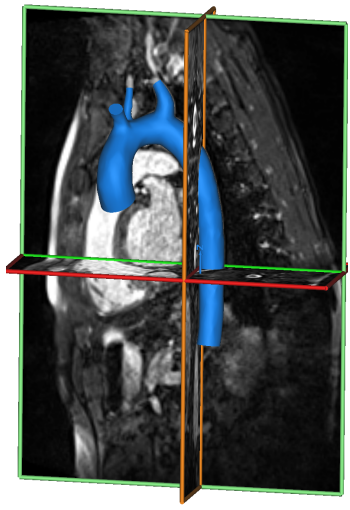

Figure 4.2: 3D model of the aortic arch extracted from MRI images.

was implemented of which the resistance (R) and the characteristic impedance (Z_c) were calculated using the equations below

$$Z_c + R = \frac{P_{mean}}{Q_{mean}} = \frac{94 \text{ mmHg}}{85.2 \text{ ml/s}} = 1.1035 \frac{\text{mmHg}}{\text{ml/s}} \tag{4.1a}$$

$$Z_c = \frac{\rho_f c}{A} = 0.08 \frac{\text{mmHg}}{\text{ml/s}} \tag{4.1b}$$

The second equation is only valid at the start of systole which is presumably reflection free. The mean pressure P_{mean} was measured at the brachial artery and is assumed to be comparable to the value existing at the descending aorta. Q_{mean} corresponds to the mean flow at the descending aorta obtained from the MRI data. The wave speed c (4.1 m/s) was estimated from the distance between the ascending and descending aorta (Δx) divided by the time (Δt) needed for the (foot of the) wave to travel that distance. A represents the cross sectional area of the descending aorta at the beginning of systole and ρ_f the density of the blood. The value of the distal compliance C (2.0 ml/mmHg) was defined such that physiological pressure variations were retrieved (a pulse pressure of approximately 35 mmHg, corresponding to the measured one). Blood was modeled as a Newtonian fluid (density 1050 kg/m^3; viscosity 3 mPa.s).

The flow equations are solved using a pressure-based solver (ANSYS Fluent), which computes the flow in a segregated manner using the SIMPLE algorithm [91, 92]. A second-order upwind discretization scheme is used for the convective term in the momentum equation. The diffusion terms are discretized with central differences and are second-order accurate. For the temporal discretization of the flow equations a second-order implicit scheme

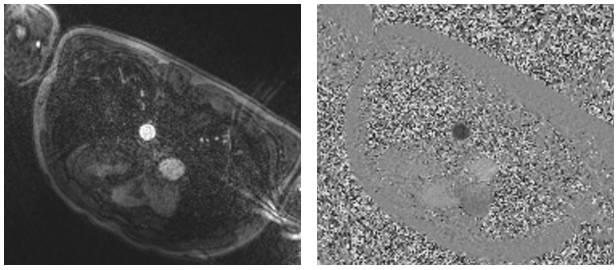

Figure 4.3: Phase contrast images used to visualize the fluid motion at the boundaries of the fluid domain (i.e. the descending aorta in the figure under consideration). (left) Magnitude image and (right) phase information.

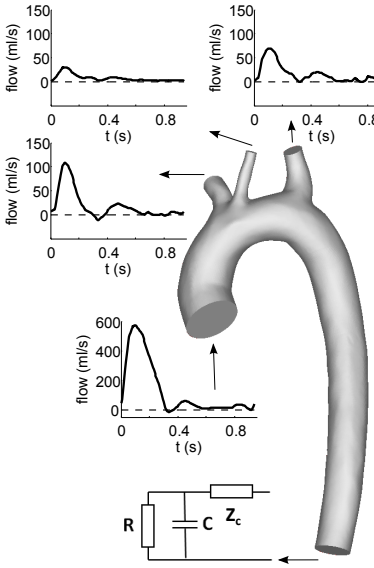

Figure 4.4: Methodological figure with setup and boundary conditions.

is applied. The convergence criteria for the scaled residuals of the momentum and continuity equation were set to 10^{-6}. These residuals are scaled relative to the largest absolute value of the residuals obtained in the first five iterations. To obtain an accurate calculation of the stress on the fluid-structure interface, the flow equations are solved in the Arbitrary Lagrangian-Eulerian formulation on a deforming mesh.

4.3 STRUCTURAL SOLVER

To create a geometric model of the aortic tissue, the aortic lumen was extended such that a diameter to thickness ratio of 10% was obtained and a hexahedral mesh was constructed. At the ends of the branches, only radial displacement was allowed. At the outer wall, the displacement is free.

A finite element package (SIMULIA Abaqus/Standard) is applied to calculate the wall deformations. The nonlinear equilibrium equations are solved using the Newton method with a fixed time increment. For the temporal discretization of the structure equations the operator defined by Hilber, Hughes and Taylor [93] is applied, which is an unconditionally stable scheme and possesses controllable algorithmic damping properties. The structural equations are solved in a Lagrangian frame.

As the stiffness of the aortic wall increases with increasing pressure, a hyperelastic model was used to mimic the wall behavior. Two types of material models were considered to represent the nonlinear stress-strain relation. The first one is a neo-Hookean material model for which only one material constant has to be defined (C_1 equal to the shear modulus divided by 2). The second one is a reduced form of the generalized Mooney-Rivlin model requiring four material constants. In [114], uniaxial and biaxial experiments on a human femoral artery were used to develop a hyperelastic constitutive model of the vascular tissue, resulting in the coefficients C_{10} = 18.9 kPa, C_{01} = 2.75 kPa, C_{20} = 590.4 kPa and C_{11} = 85.72 kPa.

The impact of the different material models on the stress-strain curve and the flow at the descending aorta (which is an output of our FSI model) is shown in Figure 4.5 and 4.6 respectively. Figure 4.6 also allows to make the comparison with the measured flow (dashed line) obtained from MRI data and thus provides a criterion to evaluate the performance of the different models.
As can be observed in Figure 4.5 a neo-Hookean model results in a nearly linear material behavior in the 0 to 10% strain range (corresponding to physiological deformations). Two neo-Hookean models with a different material parameter (C_1) were investigated. C_1 = 50 kPa (blue line) represents the most flexible material with a mean E modulus (= stress/strain) equal to 270 kPa in the 0 to 10% strain range. It can be observed that this model performs well with regard to the timing of the arrival of the flow pulse (shown in Figure 4.6). In other words, a good agreement at the beginning of the systolic phase is retrieved. However, the high compliance inherent to this model significantly dampens out the flow pulse, resulting in a low amplitude and a widening of the flow pulse at the descending aorta. Therefore, a stiffer material was applied (C_1 = 85 kPa and a mean E modulus of 470 kPa) (indicated by the black line). A better correlation between the flow predicted using this model and the

measured one is obtained, except for the timing of the wave arrival. This earlier increase in outflow is explained by the reduced compliance of this model.

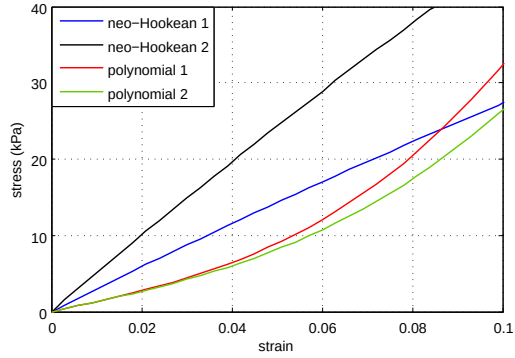

Figure 4.5: Influence of the hyperelastic material model on the stress-strain curve. Neo-Hookean 1 represents a neo-Hookean material model for which the material constant was chosen equal to 50 kPa. For neo-Hookean 2 this parameter is 85 kPa. The red line thereby shows the hyperelastic polynomial material model obtained from literature [114] (C_{10} = 18.9 kPa, C_{01} = 2.75 kPa, C_{20} = 590.4 kPa and C_{11} = 85.72 kPa). The hyperelastic material model used in this research, polynomial 2 (green line), is represented by the parameters C_{10} = 18.9 kPa, C_{01} = 2.75 kPa, C_{20} = 400 kPa and C_{11} = 85.72 kPa.

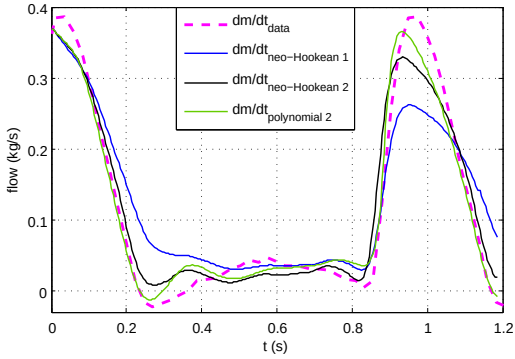

Figure 4.6: Influence of the material model on the flow at the descending aorta. dm/dt_{data} corresponds to the flow measured with MRI. Neo-Hookean 1 represents a neo-Hookean material model for which the material constant was chosen equal to 50 kPa. For neo-Hookean 2 this parameter is 85 kPa. The polynomial hyperelastic material model is represented by the parameters C_{10} = 18.9 kPa, C_{01} = 2.75 kPa, C_{20} = 400 kPa and C_{11} = 85.72 kPa.

The good performance of the flexible model with respect to the arrival of the foot of the wave combined with the better correlation during the systolic phase obtained with the stiffer model, calls for the use of another hyperelastic model that incorporates both features. It can be seen that the polynomial hyperelastic model presented in [114] (red line) mimics the desired behavior. Low stresses are characterized by a more elastic behavior, whereas stiffer

material properties are obtained under high stresses. This material model is, nevertheless, deduced from experiments on a human femoralis, which behaves stiffer than the aortic arch. To retrieve a material model with the same hyperelastic nature but a reduced stiffness in the 5 to 10% strain range, one of the material constants in the existing models was adapted. To identify the impact of the individual coefficients on the stress-strain curve, their values were reduced by 20% and the results from a uniaxial tension test are shown in Figure 4.7 and compared to the stress-strain relation obtained with the original coefficients. It can be observed that we can reduce the stiffness for strains in the 4 to 10% range by altering the value of C_{20}. Variations of the other coefficients affect the global evolution of the stress-strain curve.

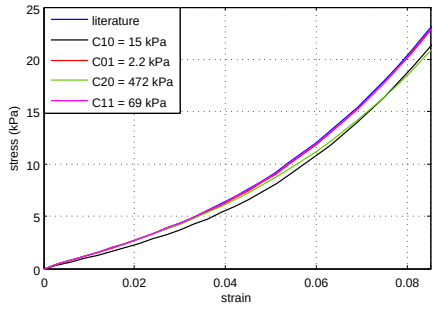

Figure 4.7: Influence of the hyperelastic material coefficients on the stress-strain curve. The blue line thereby shows the reference material obtained from literature [114] (C_{10} = 18.9 kPa, C_{01} = 2.75 kPa, C_{20} = 590.4 kPa and C_{11} = 85.72 kPa).

The desired value of C_{20} (400 kPa) was obtained in an iterative way, such that the deformations of the descending aorta in our FSI simulation corresponded to the deformations measured with MRI (9%). The resulting flow at the descending aorta is shown in Figure 4.6 (green line). An acceptable agreement with the measured flow is retrieved. Remark that the slope of the flow curve also depends on the windkessel parameters. As this model is a simplification of the downstream vascular behavior, a 100% agreement between the modeled flow and the measured one will never be possible. We feel confident that the error obtained with our model (4.4% regarding the amplitude of the flow wave) is small enough for the applications of the model used in this research. This work focuses specifically on the alterations caused by a single parameter of the model and the comparison between the corresponding model results, rather than focusing on the absolute values of the simulated hemodynamics.

4.4 SETTINGS

4.4.1 Grid convergence

As the number of grid cells is related to the simulation time, the use of an efficient computational grid is important to limit the calculation time. Especially in the case of a partitioned FSI approach, where both a fluid and a structural simulation have to be performed multiple times in each time step, this is a crucial aspect. This calls for an optimization of the mesh with respect to efficiency, i.e. the generation of an as coarse grid as possible at the same time minimizing the impact on the accuracy.
Computational grids comprising of hexahedral instead of tetrahedral volume elements have been reported to require less cells to obtain a mesh independent result, especially when simulating the flow in segments of the cardiovascular or the respiratory system using computational fluid dynamics (CFD) [115, 116]. This has been ascribed to the fact that adequate hexahedral grids consist of well organized cells along the predominant direction of the flow, aligning the cell face normals with the physical flux [117, 118] and allowing an efficient distribution of the cells as they can be stretched or subdivided anisotropically without deteriorating the cell quality [115, 119]. Using the extended Treemesh method [120] an automated high quality hexahedral mesh was generated. This method furthermore allowed to create an additional refinement in regions with highly disturbed flow, as such obtaining accurate results while limiting the number of cells in the rest of the computational domain.

In the following section, a mesh sensitivity analysis is performed for a case of severe coarctation. As turbulent zones will develop in this case, a denser mesh compared to a normal aorta will be required to resolve the flow field in space. The stenosis should thus be considered in the specification and generation of a proper computational mesh. The use of a similar mesh in a setting without obstruction (i.e. a healthy aorta) will automatically result in mesh independent results. Due to the complexity of the problem under consideration and the highly nonuniform flow observed in the model of aortic coarctation, the analytical study (based on the 1D flow) presented in chapter 2 is no longer applicable. This calls for the need of a (3D) numerical study to investigate the mesh sensitivity. All the simulations in the grid refinement study were performed with a time step size of 4 ms.

The functional impact of aortic coarctation was modeled by including a stenosed region with a length of 1 cm (L) and a coarctation index ($CI = D_{CoA}/D_{DAo}$) of 0.5 (see Figure 4.8). As the pressure difference between the ascending and descending aorta is the most important indication of aortic coarctation but is, however, difficult to assess in a noninvasive way, this output parameter is of high clinical relevance. The grid convergence study thus focused on the accuracy of the predicted pressures along the aortic arch.
Four different, uniform meshes (R1, R2, R3, R4) with an increasing number of elements in the boundary layer (ranging from 4 to 8 layers), the transversal and axial direction were

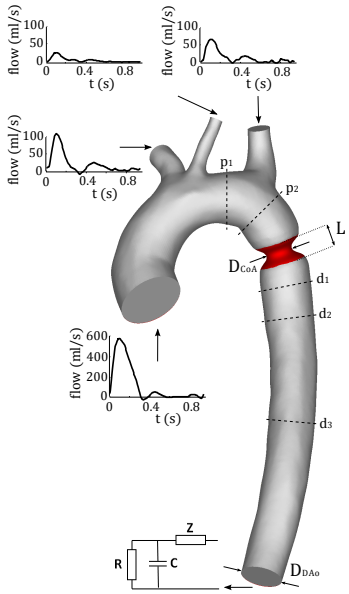

Figure 4.8: Geometrical model of the aortic arch with aortic coarctation (red), including the cross sectional regions (p1, p2, coa, d1, d2, d3, desc) in which the convergence was analyzed numerically (see Table 4.1).

constructed. A conform mesh is applied in the fluid and solid domain. The number of cells is depicted in Table 4.1, together with the calculation time required to compute one cardiac cycle (on two 10-core Intel Xeon E5-2680v2 processors). As the flow distal to the stenosis is complex and highly disturbed (Reynolds numbers up to 11 139), a high mesh density is required in this region to resolve the flow field in space. This is realized by locally adapting the fluid mesh. The resulting fluid mesh has, compared to the finest mesh (R4), a higher mesh density in the coarctation zone, but a coarser grid proximal to the stenosis and in the lower part of the descending aorta (see Figure 4.9). Figure 4.10 depicts the mesh of the arterial wall for the five different grid refinements, whereas Figure 4.11 shows the cross sectional grid of the fluid mesh at the ascending aorta.

The results of the grid refinement study are shown in Figure 4.12, depicting the pressure evolution along the centerline of the aorta at peak systole, and in Table 4.1, showing the mean error of the pressure evolution in different cross sections (indicated by the dashed lines in Figure 4.8). These errors are defined with respect to the reference grid R4 and relative to the pressure amplitude in the corresponding cross section. The *mean* error thereby denotes the error averaged over one cardiac cycle and over the respective cross section. From the results in Table 4.1, it can be seen that even for meshes with a low cell density, the mean errors proximal, halfway and distal to the coarctation zone remain low ($< 2\,\%$). When comparing the locally refined grid R5 with the uniformly refined grids R3 and R4, an important reduction in computation time is gained (23 h 38 min per cardiac cycle versus 30 h 33 min and 40 h 38 min) without a loss in accuracy. The mean error obtained with the mesh R5 stays below $1.15\,\%$ and comparable errors are found as for the mesh R3.

Grid	# Fluid cells	# Solid elem.	Calc. time per cycle	Mean error [%]							
				asc	p_1	p_2	coa	d_1	d_2	d_3	desc
R1	42k	21k	12 h 29 min	1.44	1.42	1.42	1.72	1.61	1.56	1.33	0.77
R2	105k	37k	17 h 29 min	1.01	0.98	0.98	1.26	1.54	1.88	1.26	0.71
R3	281k	74k	30 h 55 min	0.38	0.34	0.34	0.75	1.22	1.07	0.94	0.64
R4	408k	102k	40 h 38 min				Reference grid				
R5	216k	51k	23 h 38 min	0.5	0.47	0.47	0.86	1	1.15	0.98	0.6

Table 4.1: Grid refinement study of the pressure in an FSI model of aortic coarctation.

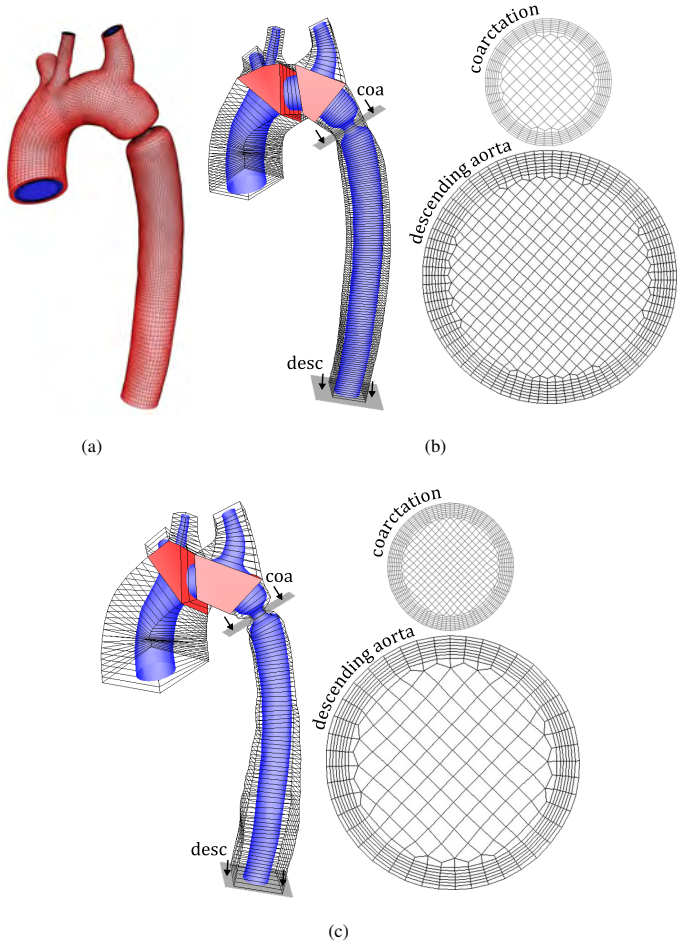

Figure 4.9: (a) Mesh for the fluid domain (blue) and the arterial wall (red) of an aortic arch with aortic coarctation. Note the axial coarsening towards the descending aorta (R5). (b) and (c) The cross sectional grids of the fluid mesh at the coarctation (coa) and the descending aorta (desc), which result from multi-block structures R4 (uniform grid refinement) and R5 (local grid refinement).

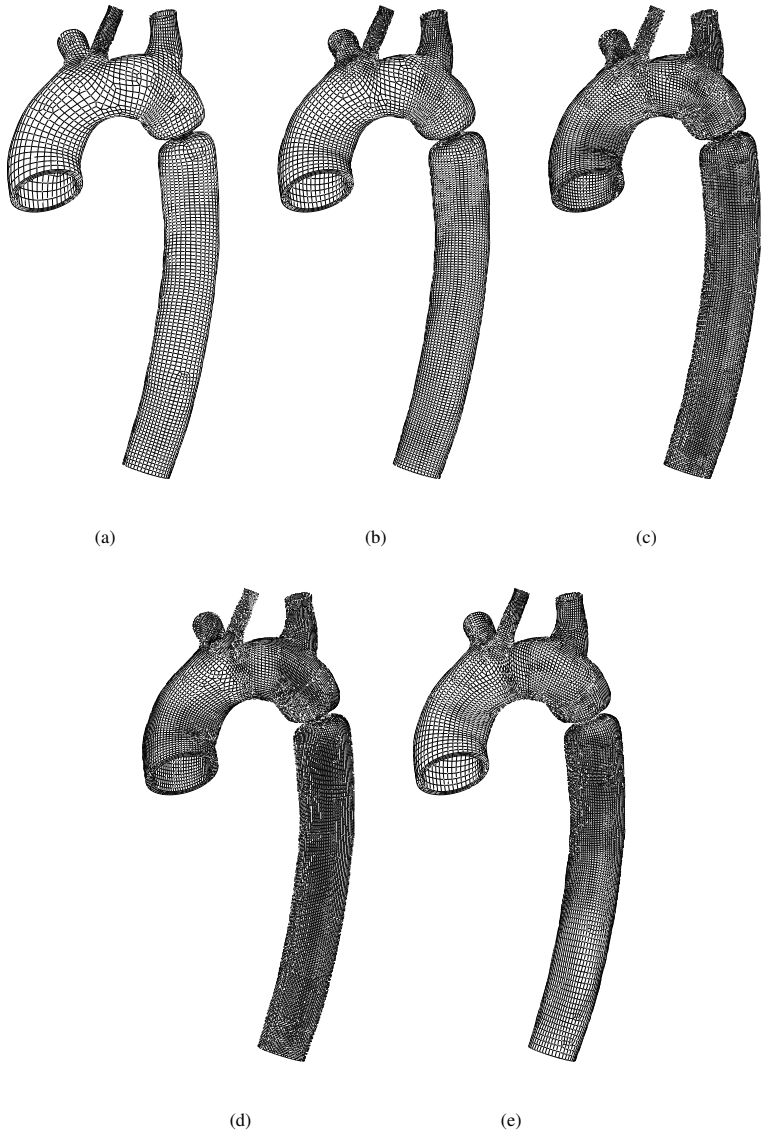

Figure 4.10: Mesh of the arterial wall of the four uniformly refined grids (a) R1, (b) R2, (c) R3, (d) R4 and (e) of the locally refined grid R5. Remark the local refinement at the coarctation region and the gradual coarsening towards the descending aorta.

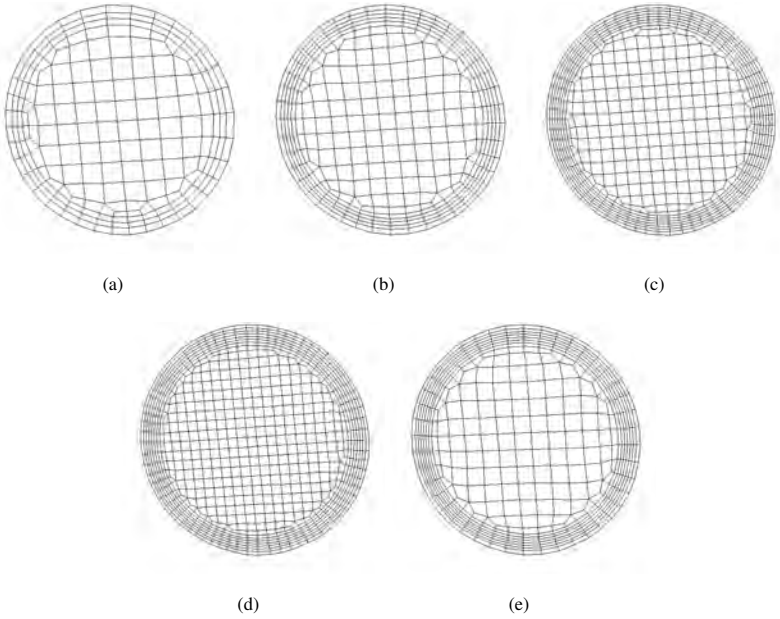

Figure 4.11: The cross sectional grid of the fluid mesh at the ascending aorta of the four uniformly refined grids (a) R1, (b) R2, (c) R3, (d) R4 and (e) of the locally refined grid R5. Remark that the grid size applied in the proximal aorta of R5 is rather coarse compared with the grid sizes used in R3 and R4.

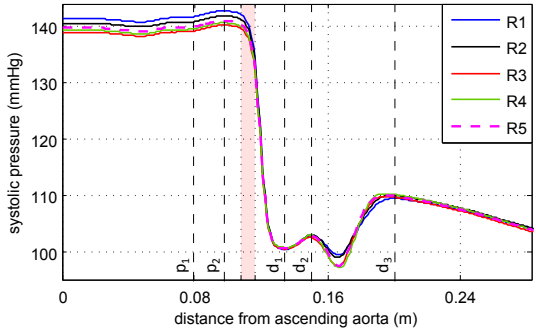

Figure 4.12: Pressure along the centerline at peak systole for increasing mesh densities (R1 to R4) and a grid with a local refinement at the coarctation region and a gradual coarsening towards the descending aorta (R5).

In the previous study a conform mesh was used for the fluid and solid domain (i.e. both meshes were the same at the fluid-structure interface). This restriction is, however, not required as an interpolation of the properties on the fluid-structure interface can be applied, allowing one of the meshes to be coarser than the other. Whether a reduced structural mesh

can be applied without affecting the accuracy and the calculation time that can be gained using this approach is discussed next.

To illustrate the influence of the structural mesh, a simulation using a coarse grid both in the fluid and solid domain (R2) is compared with a simulation applying a fine grid in both domains (R4) and a simulation in which the fine fluid mesh was combined with the coarse structural mesh ($R4_{w\,R2}$, in which the subscript w denotes the wall). The results are shown in Figure 4.13, depicting the pressure evolution along the centerline of the aorta at peak systole and in Table 4.2, showing the mean error of the pressure evolution in different cross sections. It can be observed that the density of the arterial wall mesh has almost no impact on the accuracy of the simulation results, but has a significant impact on the simulation time (25 h 59 min versus 40 h 38 min). Errors smaller than 0.24% are obtained for $R4_{w\,R2}$. The different results between the simulations R2 and R4 can thus be explained by the difference in fluid mesh refinement.

Even though the number of cells used in the structural domain is limited compared to the number of cells applied in the fluid domain, the simulation of the structural deformation takes approximately as much time as the flow simulations. This is partially explained by the notable restart time of the structural solver in each coupling iteration. As both this restart time and the calculation time itself are related to the grid size, a considerable reduction in simulation time is obtained with a coarser grid.

Grid	# Fluid cells	# Solid elem.	Calc. time per cycle	Mean error [%]							
				asc	p_1	p_2	coa	d_1	d_2	d_3	desc
R2	105k	37k	17 h 29 min	1.01	0.98	0.98	1.26	1.54	1.88	1.26	0.71
$R4_{w\,R2}$	408k	37k	25 h 59 min	0.07	0.08	0.08	0.19	0.15	0.14	0.24	0.15
R4	408k	102k	40 h 38 min	Reference grid							

Table 4.2: Influence of the grid refinement of the arterial wall on the pressure in an FSI model of aortic coarctation.

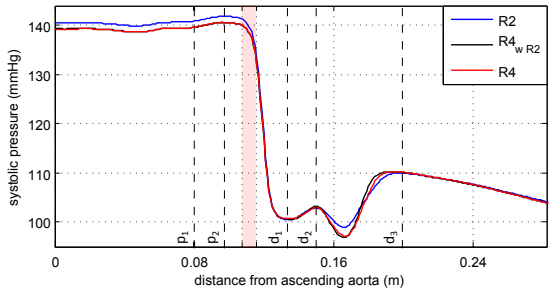

Figure 4.13: Pressure along the centerline at peak systole for a coarse mesh R2, a fine mesh R4 and a mesh combining the coarse grid of the arterial wall with the fine grid of the fluid domain $R4_{w\,R2}$. It can be observed that the density of the arterial wall mesh has almost no impact on the simulation results.

Finally, the numbers of wall layers present in the arterial wall mesh in radial direction is investigated. A simulation using a structural mesh consisting of 3 wall layers is compared to a simulation using a structural mesh with 4 wall layers. A small error limited to a mean value of 0.25% is obtained (see Table 4.3) and a similar pressure evolution along the centerline of the aorta at peak systole is found (shown in Figure 4.14)

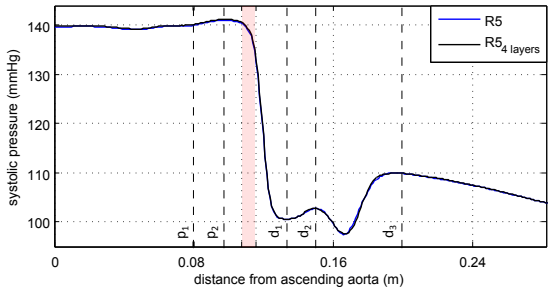

Figure 4.14: Pressure along the centerline at peak systole obtained with the mesh R5. The comparison is made between a structural mesh consisting of 3 and 4 layers respectively. A very good agreement between both is found, illustrating that the number of wall layers has almost no influence on the simulation results.

Grid	# Fluid cells	# Solid elem.	Mean error [%]							
			asc	p_1	p_2	coa	d_1	d_2	d_3	desc
R5	105k	37k	0.16	0.17	0.21	0.16	0.15	0.25	0.14	0.12
$R5_{4\ layers}$	105k	49k	Reference grid							

Table 4.3: Influence of the number of wall layers present in the arterial wall mesh on the pressure in an FSI model of aortic coarctation.

Considering the small errors and the reasonable computation time, the locally refined mesh R5 will further be applied in this research. The computational time could have been further reduced by coarsening the structural mesh as outlined above, but this has not been done.

4.4.2 Time step convergence

Similar as for the grid refinement study, the time step dependency is evaluated for an FSI model of aortic coarctation. The development of turbulence in the expansion zone will indeed require smaller time step sizes to resolve the flow field in time compared to the case of a normal aorta. The application of the analytical study presented in chapter 2 is thereby no longer valid. The highly disturbed flow field calls for a (3D) numerical study to evaluate the time step dependency and prohibits the use of a simplified 1D model. The same model of aortic coarctation was applied as the one used in the grid refinement study (see Figure 4.8).

The impact of the temporal discretization order on the pressure evolution in different cross sections along the aorta is depicted in Figure 4.15 for a first-order (blue line) and a second-order (black line) implicit time integration scheme. For both simulations a time step size of 4 ms was applied. Although the global evolution of the pressure is similar in both simulations, small local changes (oscillations) in the cross sections distal to the coarctation (d_1, d_2 and d_3) are not resolved by the simulation using the first-order scheme. This observation is in agreement with the findings from chapter 2 where it was demonstrated that a much higher temporal resolution is needed in the first-order case. To improve the temporal resolution of the flow field without decreasing the temporal resolution of the structural problem, sub-cycling was applied. The temporal resolution of the flow field was thereby improved by a factor 10, while limiting the additional computation time. Nevertheless, as is demonstrated in Figure 4.15 the accuracy improvement made is very limited and the second order scheme (for which a time step size of 4 ms was used in both the fluid and the solid problem) still performs better. The application of the developed sub-cycling procedure has thus no additional value in this case. Since a sub-cycling procedure for a simulation using a second-order implicit time integration scheme is missing, a second-order scheme with matching time step sizes in the fluid and solid problem is used in the rest of this dissertation.

Figure 4.16 illustrates the impact of the time step size on the pressure evolution at different cross sections along the aorta. p_1 and p_2 represent two planes in the part proximal to the coarctation whereas d_1, d_2 and d_3 are planes in the distal part (see Figure 4.8). It can be observed that the results in the proximal part and at the coarctation zone are more or less time step independent, whereas the small pressure oscillations in the distal part are not captured with a large time step size (of 4 or 5 ms). Moreover, the oscillations developing in d_3 are not even resolved properly with a time step size of 1 ms.

As such, the time step size was further decreased to 0.5 and 0.25 ms and the results are shown in Figure 4.17. An unstable behavior was found if a small time step size was applied. The observed oscillations responsible for this behavior were indeed not resolved for the simulations using larger time step sizes. Because the oscillations itself are resolved by multiple time steps and the frequency of the oscillations is more or less time step independent, it is presumed that these oscillations do not arise from a numerical instability but have a physical origin, triggered by the disturbed blood flow. In a physiological setting, this oscillation would however be cushioned by the damping nature of the surrounding tissue. We believe that the lack of physical damping in our model resulted in the observed oscillations that eventually got unstable when using a time step size smaller than 1 ms.

To test our hypothesis, Rayleigh damping was added to the structural model and the simulation using a time step size of 0.5 ms was repeated. The Rayleigh damping coefficients α and β were selected such that 1% damping of the waves with a 1 Hz frequency (close to

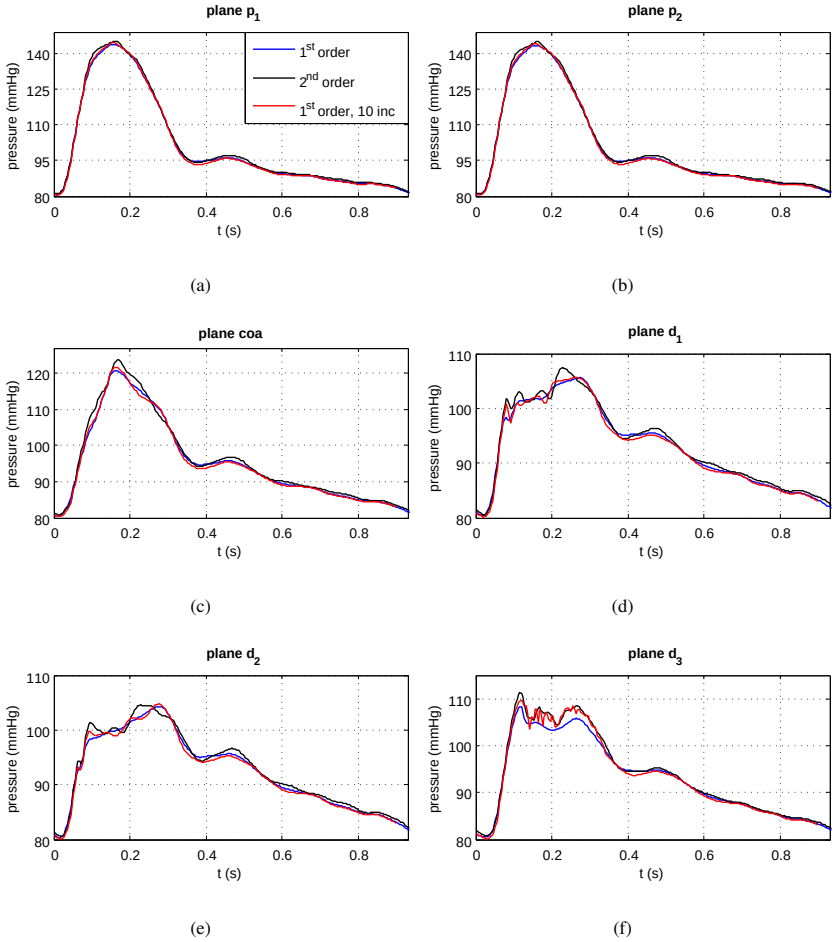

Figure 4.15: Influence of the temporal discretization order on the pressure evolution at two proximal cross sections (p_1 and p_2), halfway the coarctation zone (coa) and at three distal cross sections (d_1, d_2 and d_3). See Figure 4.8 for an indication of these plane locations. The red line indicates the results for which sub-cycling and a first-order scheme were used in the fluid simulations ($\Delta t_f = \Delta t_s/10$). It can be observed that regardless of the better temporal resolution of the wave in the case of sub-cycling, a better temporal resolution of the flow field is obtained for the second-order scheme ($\Delta t_f = \Delta t_s = 4$ ms).

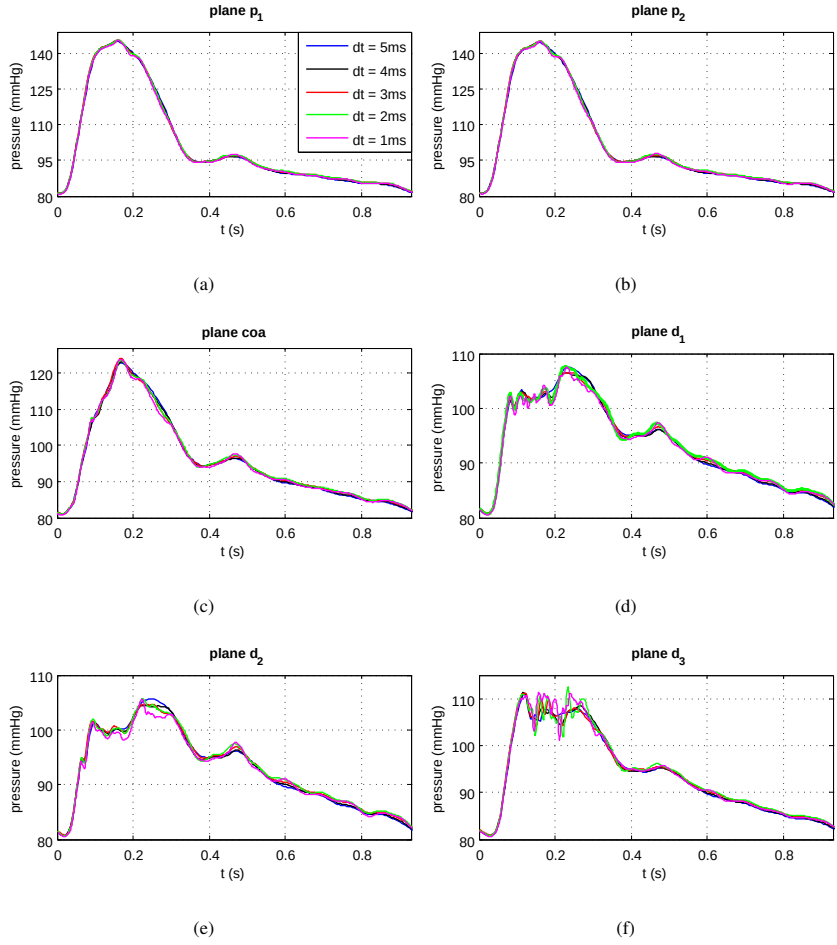

Figure 4.16: Influence of the time step size on the pressure evolution at two proximal cross sections (p_1 and p_2), halfway the coarctation zone (coa) and at three distal cross sections (d_1, d_2 and d_3). See Figure 4.8 for an indication of these plane locations.

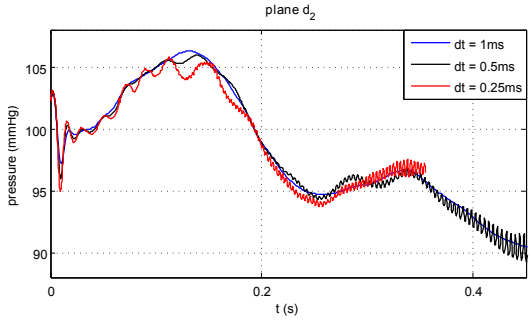

(a)

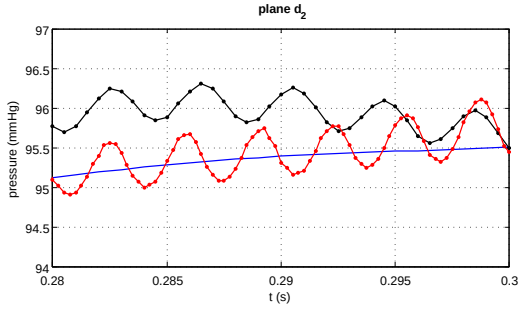

(b)

Figure 4.17: (a) Influence of the time step size on the pressure evolution at a cross section distal to the coarctation (d_2). See Figure 4.8 for an indication of this plane location. Remark that the simulation becomes unstable for small time step sizes (Δt = 0.5 and 0.25 ms). These pressure oscillations are not resolved with larger time step sizes. (b) Detail of the pressure evolution, illustrating the temporal resolution of the oscillations.

the frequency of the cardiac cycle) was obtained and 20% damping for the 250 Hz waves (i.e. the frequency of the observed oscillations). These constrictions resulted in a value of 0.116 for the mass proportional damping parameter α and 0.000255 for the stiffness proportional damping β. In Figure 4.18 it is demonstrated that the unstable behavior indeed disappears with the use of Rayleigh damping.

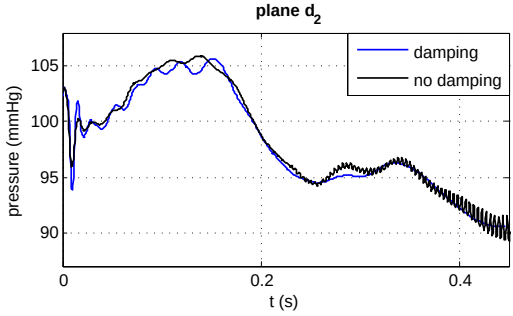

Figure 4.18: Influence of Rayleigh damping on the pressure evolution at a cross section distal to the coarctation (d_2). See Figure 4.8 for an indication of this plane location. Inclusion of Rayleigh damping prevents the simulation from unstable behavior.

The larger pressure oscillations at the start of the simulation (t < 0.2 s) for the case with Rayleigh damping is explained by the temporal discretization schemes used at the start. The simulation without damping is started with a first-order scheme, to facilitate the startup. After 0.2 s the accuracy is improved by switching to a second-order scheme. For the case with damping, a second-order scheme can be used from the start on.

In this dissertation a time step size of 2 ms will be used for the aortic arch simulations, as a compromise between accuracy and computation time. The error obtained with this time step size is sufficiently smaller than the mutual differences in results, retrieved with the parameter models of CoA (chapter 7).

4.4.3 Simulation startup

In this section the simulation startup is discussed. This part of the FSI simulation is very challenging as there is no equilibrium state to start from and the IQN-ILS technique is not applicable yet, as there is no information from previous coupling iterations or previous time steps available to define the approximation of the Jacobian. The methodology used in this dissertation is described and can be used as a guideline for the startup of similar (cardiovascular) simulations. However, this is not necessarily a guarantee to success, as every FSI simulation is characterized by its own challenges and difficulties.

Following aspects should be considered at the beginning of an FSI simulation:

- Starting from an initial state of rest (i.e. zero flow and pressure in the fluid domain) whereby the flows at the boundaries are progressively increased, would require a considerable number of cardiac cycles to obtain a periodic solution [121]. As FSI simulations are computationally expensive and time consuming, this approach is strongly discouraged.
- During the first coupling iterations of the first time step, the IQN-ILS technique is not applicable. The simulation starts with zero displacement of the fluid-structure interface in the first coupling iteration and a relaxation with a factor ω of the interface's displacement is performed in the second iteration of the first time step. The pressure field thus calculated, differs a lot from the one that would be obtained if the coupling iterations were converged. These unphysiological pressures are applied to the structural model and will result in strong deformations and possibly problems with the grid motion in the fluid domain if this strong deformation is applied at the interface.

To circumvent the first problem, a semi-static FSI simulation was performed, being an unsteady simulation with a time step size of 0.5 s (which is in the same order of magnitude as the period of the cardiac cycle). In this simulation, the aorta was inflated to a certain pressure level and the flows were linearly increased until the corresponding flows in the cardiac cycle were obtained (see Figure 4.19 (left)).This simulation was followed by another semi-static simulation, in which the flows and pressure were kept constant (shown in Figure 4.19 (left)). This resulted in an equilibrium state between the flow and the structural deformation. As the flows and pressure remained constant in this last simulation, no wall displacement and zero net flow were retrieved. The flow through the descending aorta thus corresponded to the flow at the ascending aorta minus the flows at the three side branches. In order to be physiological, a time point of zero imbalance (which is the inflow reduced by the outflow) should be selected as the starting point for our simulations. These time points are indicated with a red dot in Figure 4.20. This approach allows the actual FSI simulation to start from a physiological equilibrium state and will result in a nearly periodic simulation from the first cycle on.

Considering the second problem, we took advantage of the hyperelastic property of the material model. Remark that the aortic geometry was extracted under diastolic pressure. The interface pressure passed to the structural solver will therefore in converged conditions adopt a value between zero and the pulse pressure. Due to the hyperelastic nature, an overestimation of the pressure will not result in a large deformation as the wall will behave stiffer in that case. A negative pressure on the other hand, will result in a reduced aortic volume and possibly negative cell volumes. Therefore, simulation startup was chosen close to peak systole, where high pressures are retrieved. The high pressure imposed at the descending

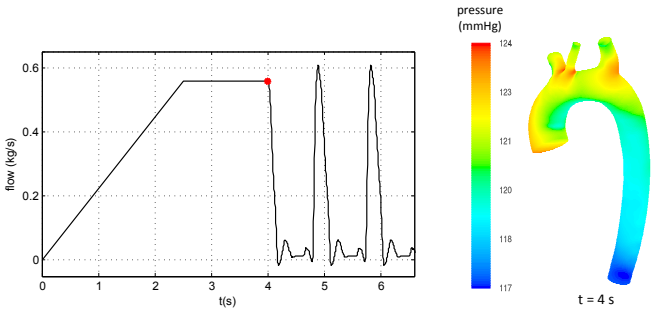

Figure 4.19: (left) Flow imposed at the ascending aorta during startup and the first two cardiac cycles. The corresponding contourplot of the pressure is shown on the right at a time point after semi-static inflation.

aorta will as such limit the risk for negative pressures in the rest of the fluid domain. The first point of mass imbalance equal to zero is thus chosen as a start point for our simulation (indicated by the first red dot in Figure 4.20) as it satisfies both criteria formulated above. Using the measured flow at the descending aorta and the windkessel parameters allowed us to predict the pressure evolution that will be obtained at the descending aorta and the pressure that needs to be imposed in the simulation startup. Figure 4.19 shows the contourplots of the pressure at a time point after semi-static inflation (right).

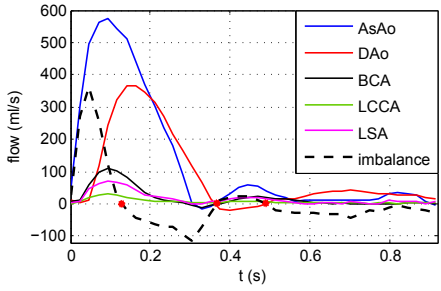

Figure 4.20: Flows measured at the ascending aorta (AsAo), the descending aorta (DAo), the three side branches (BCA, LCCA and LSA) and the corresponding mass imbalance (i.e. the inflow reduced by the outflow). The time points corresponding to a zero net flow are indicated by the red dots.

To illustrate that this startup approach indeed results in a nearly periodic simulation from the first cycle on, the pressure and the flow obtained at the descending aorta during the first 4 cardiac cycles is shown in Figure 4.21. The difference in amplitude of the flow pulse between the third and fourth cycle is 0.82%, whereas the difference in amplitude of the pressure pulse is 0.45%. In chapter 7 the results from the third cycle will be reported as a compromise between accuracy and computation time.

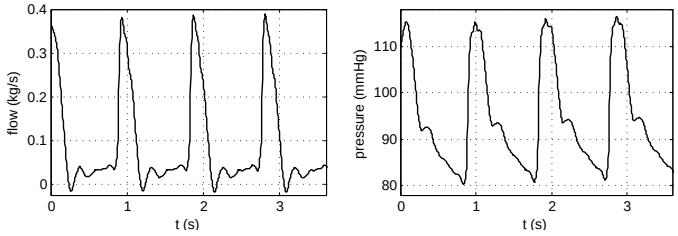

(a) (b)

Figure 4.21: (left) Flow and (right) pressure obtained at the descending aorta during the first 4 cardiac cycles. It can be seen that the hemodynamic response is nearly periodic from the first cycle on. The difference in amplitude of the flow pulse between the third and fourth cycle is 0.82%, whereas the difference in amplitude of the pressure pulse is 0.45%.

4.4.4 Convergence of the coupling iterations

The absolute convergence criterion in the Euclidean norm for the residual of the interface displacement is set to 10^{-5} m and for the residual of the interface load to 1 Pa. In [122] it was demonstrated that the number of unstable Fourier modes during Gauss-Seidel iterations increases with decreasing time step (see Figure 4.22). In other words, more coupling iterations are required if a small time step size is applied. This observation was derived using a simplified and linearized model of a straight tube with a constant cross section and indeed applied for the simulations of a normal aorta for which a time step size of 5 to 2 ms was used. However, for the case of aortic coarctation, a time step size of 4 ms significantly slows down the convergence compared with a time step size of 2 ms. For the case of severe narrowing, this resulted in a divergence of the coupling iterations in the systolic phase.

An average number of 6.6 coupling iterations was needed in the healthy aorta, with a maximum of 10 for a time step size of 2 ms. In the most severe case of aortic coarctation, this average number increased to 8.9 with a maximum of 19.

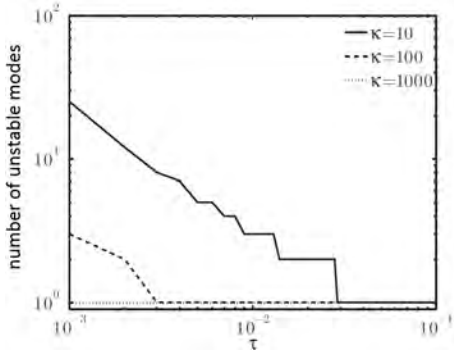

Figure 4.22: Number of unstable Fourier modes as a function of the dimensionless time step τ and the dimensionless stiffness κ for a simplified model of the blood flow in an artery. Taken from [122].

4.5 IMPACT OF FLEXIBLE WALL MODELING

Until quite recently, only simulations with rigid walls were performed, but they fail to capture some important phenomena, such as wave propagation and reflection. This can clearly be seen in Figure 4.23 where the comparison is made between the flows obtained at the descending aorta for a rigid wall (CFD) and a flexible wall (FSI) model. No wave propagation is found in the CFD simulation, the outlet flow (dm/dt_{DAo}) starts to increase the moment the inlet flow increases (dm/dt_{AsAo}). The same is true for the outlet pressure found with a rigid wall simulation. In this case an additional overestimation of the pressure amplitude is found.

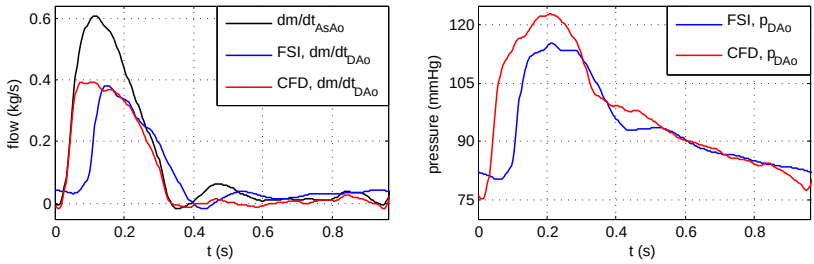

(a) (b)

Figure 4.23: Comparison of (a) the flow and (b) the pressure at the descending aorta obtained with a rigid (CFD) and a flexible wall model (FSI).

4.6 CONCLUSIONS

The fluid-structure interaction problem is solved in a partitioned way, which means the flow and the structural equations are solved separately. Besides a flow solver and a structural solver, also a coupling algorithm is required to take into account the interaction between flow and motion of the structure. In this research the IQN-ILS technique (quasi-Newton algorithm with an approximation for the inverse of the Jacobian) is used, requiring fewer coupling iterations per time step compared with other partitioned schemes.
A flow and structural model are developed with particular attention for the boundary conditions and the material properties. The need to include the hyperelastic nature of the arterial wall is demonstrated. To obtain an accurate calculation of the stress on the fluid-structure interface, the flow equations are solved in the Arbitrary Lagrangian-Eulerian formulation on a deforming mesh.
The comparison is made between the flows obtained at the descending aorta for a rigid wall and a flexible wall model. No propagation of the pressure wave is modeled and an overestimation of the pressure at the descending aorta is found in the rigid wall simulation.

Since the number of grid cells and the time step size are related to the simulation time, the use of an efficient computational grid and a proper time step size is important to limit the calculation time. As the flow distal to a stenosis is complex and highly disturbed, a high mesh density is required in this region to resolve the flow field in space. This is realized by locally adapting the fluid mesh. In this dissertation a time step size of 2 ms is used for the FSI simulations, as a compromise between accuracy and computation time. The error obtained with this time step size is sufficiently smaller than the mutual difference in results, retrieved with the parameter models of CoA (chapter 7).

These findings and the numerical model developed in this chapter were the basis for the simulations performed in chapter 7. In addition, the applied methodology and the insights provided by the simulations performed in this research can be relevant for a broader range of (biomedical) applications (in or outside the university of Ghent) in which fluid-structure interaction is involved.

Two

Clinical application: simulation of aortic coarctation

CHAPTER 5

An introduction to aortic coarctation and its computational modeling

5.1 PATHOLOGY OF AORTIC COARCTATION

Aortic coarctation (CoA) is a congenital heart disease encountered in approximately 0.1% of the newborns [123]. It thereby accounts for 5-8% of all congenital heart disorders [124, 125]. The condition has a male predominance [126] with a male to female ratio of approximately 2:1. As the word 'coarctation' signifies narrowing, this disease is (in 98% of all cases [127]) characterized by an isolated narrowing of the proximal descending aorta (Figure 5.1) at the level of the ligamentum arteriosum, the remains of the ductus arteriosus, originating from the fetal circulation (Figure 5.2). Hypotheses on the development of CoA include a reduced flow through the aorta in utero, resulting from intracardiac anomalies, or an extension of the ductal tissue into the aortic wall and its successive contraction, generating a posterior shelf in the lumen of the aorta.

The presence of the narrowing leads to an additional resistance in the arterial system. Consequently, the heart has to generate a higher blood pressure to provide a sufficient blood flow through the aorta. CoA often presents with hypertension in the vessels proximal to the coarctation, combined with a low blood pressure and weak pulses in the distal vasculature. Failure to thrive, seizures, irritability, lack of energy, and breathing difficulties can be associated with chronic hypertension in neonates and young infants [130]. In case of severe narrowing, the left ventricle might not be strong enough to overcome the pressure drop along the coarctation zone, impeding the supply of oxygen-rich blood to the lower part of

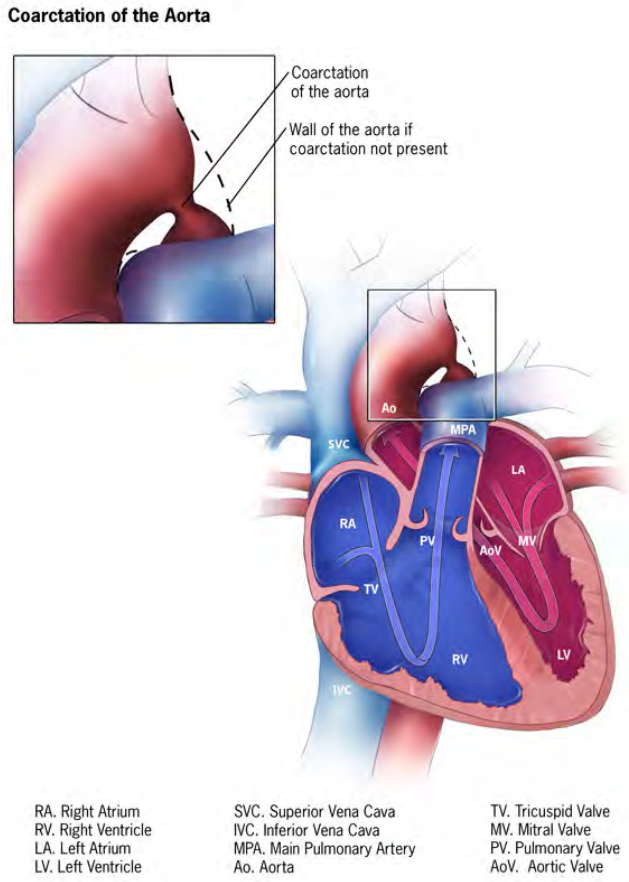

Figure 5.1: Illustration of an aortic coarctation [128].

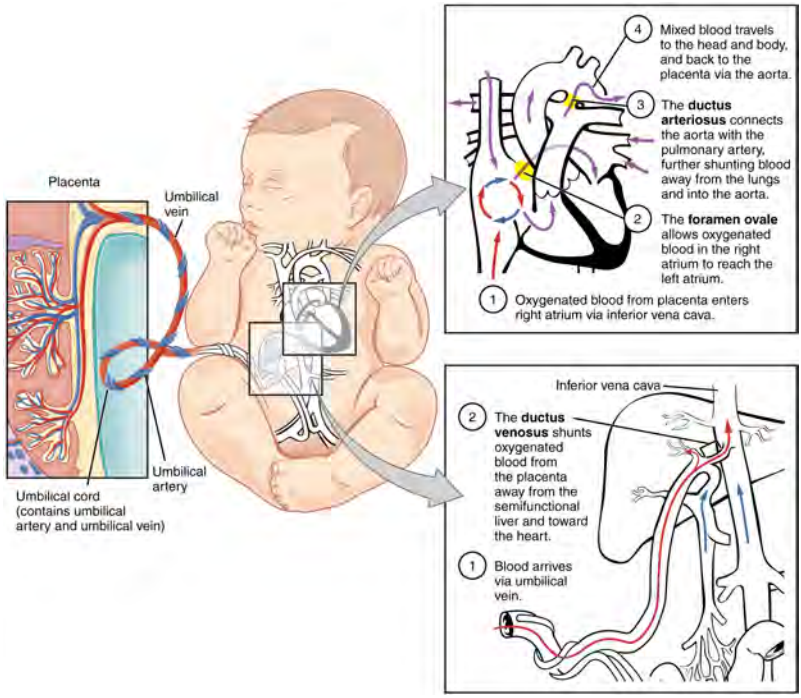

Figure 5.2: Illustration of the fetal circulatory system. OpenStax College. Anatomy & Physiology, Connexions Web site [129].

the body. This poor blood flow manifests in leg weakness, underdevelopment of the lower limbs and pain during exercise. These symptoms usually appear within the first few weeks of life. Symptomatic neonates and infants should undergo urgent intervention, as the age at CoA repair is an important predictor of long-term cardiovascular complications [131–136]. In mild narrowings, symptoms may be absent in the first years of life. In these cases coarctation is detected later on in childhood and occasionally during adulthood. Uncorrected CoA can result in serious complications: 60% of 40-plus adults with untreated coarctation show symptoms of heart failure, 75% of which die by the age of 50 and 90% by the age of 60 [137].

Coarctation is often associated with other congenital cardiovascular defects including ventricular septum anomalies, single ventricle lesions or a bicuspid aortic valve (BAV) (see Figure 5.3). BAV prevails in 50-80% of patients with aortic coarctation [138] (compared to 2% in a general population) and increases the risk of aortic dissection by a factor of 9 [139]. Additionally, CoA is often associated with certain genetic disorders, such as Turner syndrome [140].

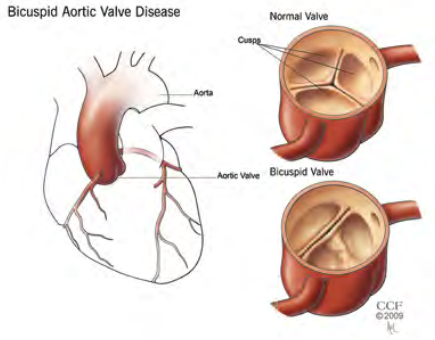

Figure 5.3: Illustration of a tricuspid and bicuspid aortic valve [141].

5.2 Diagnosis and imaging

5.2.1 Prenatal diagnosis

In the fetal circulation, the ductus arteriosus connects the pulmonary artery to the proximal descending aorta (see Figure 5.2). As such, the blood flow from the right ventricle bypasses the non-functioning lungs and only 10% of the fetal cardiac outflow passes through the coarctation region [142–144]. Since the pressure gradient at the coarctation site significantly decreases with decreasing flow rate, this limited flow impedes the estimation of the hemodynamic severity of the present coarctation by antenatal ultrasound. Additionally, the

presence of the ductus may result in a less severe anatomic narrowing, further disturbing detection modalities. The presence of other cardiac defects (e.g. undersized left ventricle and/or mitral annulus or dilated right ventricle), on the other hand, improves detection.

5.2.2 Postnatal diagnosis

The postnatal diagnosis of CoA is based upon the following indications:

- the presence of a narrowing, quantified by the coarctation index (CI). This parameter is defined as the ratio of the stenosis diameter to the diameter of the unaffected descending aorta. Severe narrowing, requiring intervention, is indicated by an index below 0.5 (area reduction of at least 75%), mild coarctation by an index between 0.65 and 0.5 (area reduction between 55% and 75%).
- a large difference in blood pressure between the upper and lower limbs ($>$ 20 mmHg [145]). This characteristic is the most distinguishing diagnostic factor to determine the functional severity of the coarctation. Remark that the term 'pressure gradient' used in biomedical literature often refers to this pressure drop across the coarctation zone rather than the change in pressure per unit of length.
- a diminished femoral pulse, which is delayed compared to the brachial pulse.
- a harsh-sounding heart murmur due to turbulent blood flow. This murmur can be observed with a stethoscope placed at the back of the patient.
- a persistent diastolic flow within the descending thoracic aorta (run-off).
- the presence of an important network of collateral blood vessels, transporting part of the proximal blood to the level of the diaphragm (e.g. internal thoracic arteries via the subclavian arteries).

The diagnosis can be confirmed using different types of techniques, particularly echocardiography, which is often used in the post-treatment follow-up [146, 147].

Sphygmomanometry A traditional method to estimate the pressure drop across the coarctation zone is the measurement of the arm-to-leg pressure difference by sphygmomanometry. This procedure quantifies the peak-to-peak pressure difference of the systolic pressures at the arm and leg. Although this is an easy and inexpensive examination, it lacks some accuracy. In [148–151] it is demonstrated that this pressure difference underestimates the instantaneous (actual) pressure drop and changes significantly with flow rate.

Chest X-ray By passing an X-ray beam through the chest, this technique may reveal an enlarged heart or a local narrowing of the descending aorta.

Electrocardiogram (ECG) Based on a recording of the electrical activity in the heart, an ECG can reveal ventricular hypertrophy, often associated with aortic coarctation.

Doppler echocardiography Using Doppler echocardiography, a local narrowing can be demonstrated by the measurement of elevated velocities, diastolic run-off or turbulence. As

a direct measurement of the pressure drop across the coarctation site requires invasive measurements, easily accessible velocity information from Doppler echocardiography is often used to quantify this parameter. With this imaging modality, the pressure drop (Δp) across the coarctation segment can be estimated based on the measured peak velocity through the narrowing (v_{CoA}) and proximal to the coarctation site (v_P) using following simplified energy equation:

$$\Delta p \approx 4(v_{CoA}^2 - v_P^2) \tag{5.1}$$

in which the pressure drop is expressed in mmHg and the velocities in m/s. This equation, however, neglects the unsteady flow component, the energy losses due to friction and turbulence and the pressure recovery distal to the coarctation. This last simplification in particular, leads to an overestimation of the actual pressure difference, especially in the post-operative case [146, 148, 152–157]. On the contrary, in adults with untreated coarctation, the presence of collateral blood flow will diminish the calculated pressure gradient, despite a severe degree of obstruction might exist [158]. Likewise, misalignment of the Doppler beam leads to an underestimation of the measured velocities and subsequent pressure gradient prediction. As the quantification of CoA severity can not be solely determined by this pressure drop, other diagnostic factors (see above) should be considered. Also the shape of the Doppler signal is used to assess coarctation severity. Severe coarctation is characterized by a diastolic antegrade flow in the descending aorta which manifests in a typical sawtooth pattern. Although echocardiography has some theoretical and technical limitations, it is considered the gold standard for the assessment of coarctation severity, owning to its noninvasive, low cost nature and the absence of radiation during examination.

Magnetic resonance imaging (MRI) Despite its higher costs, MRI is a more accurate, noninvasive evaluation method compared to Doppler echocardiography. Apart from an assessment of stenosis morphology (site and area reduction), it allows to visualize and quantify the collateral blood flow as the difference in flow rate in the proximal and distal descending aorta. In a similar manner as described above, velocity information can be used to identify patients with a significant pressure gradient across the coarctation [159, 160].

Computerized tomography (CT) angiogram Alternatively, CT angiography is applied to assess the location and severity of aortic coarctation together with the presence of collateral blood vessels. Because of the radiation associated with CT, MRI is generally preferred. Different imaging techniques of aortic coarctation are shown in Figure 5.4.

Image-based computational modeling In [152, 161] a computational fluid dynamics (CFD) based approach is proposed for the noninvasive hemodynamic evaluation of (repaired) CoA. Starting from medical imaging data and noninvasive clinical measurements, patient specific computational models are constructed which allow to predict the pressure drop across the coarctation site in a much more accurate way compared to Doppler derived pressure drops and cuff-pressure measurements in the lower and upper limbs [152]. More detail on these

studies can be found in section 5.6.

Cardiac catheterization Cardiac catheterization is used to study various functions of the heart in real time, amongst others to measure the blood pressure generated by the heart. It is considered the gold standard to assess pressure differences across the CoA in an invasive way and to evaluate the performance of the previously described methods. Cardiac catheterization is rarely associated with serious complications. If present they include: bleeding and infection at the catheter site, damage to blood vessels (by scraping and puncturing a hole in the vessel wall), arrhythmia, low blood pressure, stroke or heart attack (caused by blood coagulation). In adults and children, cardiac catheterization is commonly performed in combination with a therapeutic intervention (see section 5.3.2) [162], or if coarctation is associated with other cardiac disorders such as coronary artery disease.

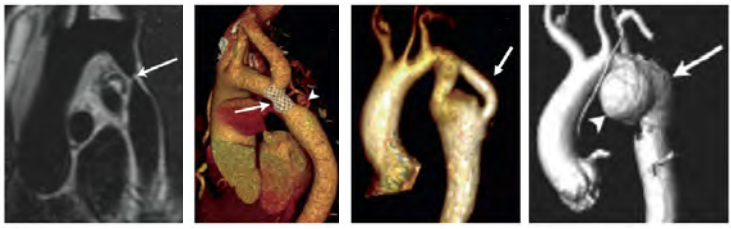

(a) (b) (c) (d)

Figure 5.4: (a) 'Black-blood' MRI oblique sagittal view showing discrete, tight coarctation at the aortic isthmus (arrow). (b) 3D, contrast-enhanced CT angiogram showing mildly narrowed bare metal stent (arrow) that partially overlies the left subclavian artery origin. The arrowhead shows a subtle pseudo-aneurysm at the distal end of the stent. (c) 3D, contrast-enhanced MR angiogram showing aortic arch hypoplasia and coarctation with a 'jump' by-pass graft posteriorly (arrow). (d) 3D, contrast-enhanced MR angiogram showing large pseudo-aneurysm (arrowhead) after previous patch angioplasty repair. The true lumen is shown posteriorly (arrow) [163].

5.3 CURRENT INTERVENTION TECHNIQUES FOR COARCTATION REPAIR

Significant hypertension and/or congestive heart failure are indications of intervention. Providing hypertension (rather than heart failure) is the clinical problem, it is advised to relieve the constriction promptly rather than treating hypertension with antihypertensive medications. Aortic coarctation is currently treated by surgical correction or in a minimal invasive way through balloon angioplasty or stent deployment.

5.3.1 Surgical repair

Three types of surgical intervention are commonly used: resection with reanastomosis (Figure 5.5), patch aortoplasty (Figure 5.6) and subclavian artery patch repair (Figure 5.7). The

repair strategy depends on the age of the patient, the individual anatomy, associated defects and the preference of the surgeon [164].

In a first type of surgical repair the constriction is excised and the two ends of the aorta are reconnected by direct end-to-end anastomosis, resulting in a small, circular segment of scar tissue (Figure 5.5). Successful surgical correction of CoA by end-to-end anastomosis was first reported by Crafoord and Nylin in 1945 [165]. This intervention is usually restricted to infants and small children because of the absence of enlarged collaterals and the short distance for reanastomosis.

Figure 5.5: Illustration showing end-to-end anastomosis for repair of aortic coarctation [166].

For a long stenosis the distance between the two ends of the unaffected aorta may become too large for reanastomosis. In 1957 an alternative method was proposed by Vosschulte in which an incision along the aorta is made and a patch of prosthetic material is sutured in place [167] (Figure 5.6). Because the use of a prosthetic patch material inhibits the growth potential and elevates the risk for aneurysm and pseudoaneurysm formation [168], this technique has lost interest.

A commonly employed alternative is the subclavian-flap aortoplasty introduced by Waldhausen in 1966 [169]. For this intervention the left subclavian artery is sacrificed to enlarge the aortic lumen at the site of the coarctation, as such, avoiding the use of prosthetic materials (Figure 5.6). Complications of this intervention include a decreased perfusion of the left arm, often combined with impaired growth. Other, less common surgical techniques include interposition graft, in which the narrowed segment is resected and replaced by a graft of synthetic material and ascending to descending aorta bypass, in which the obstruction is circumvented by a synthetic tube sewn into the aorta proximal and distal to the narrowing.

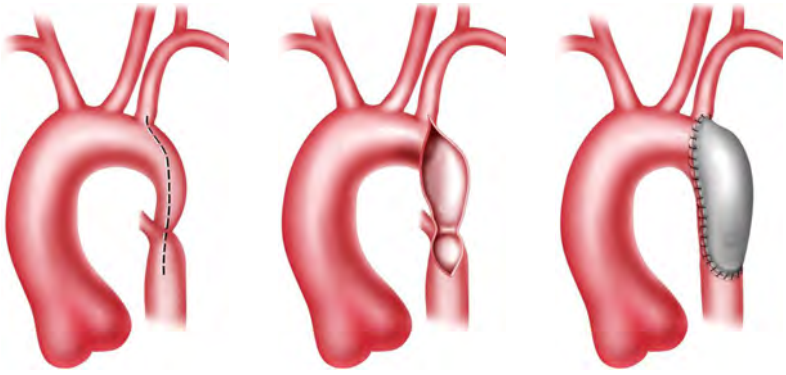

(a) (b) (c)

Figure 5.6: Illustrations showing patch aortoplasty for repair of aortic coarctation [166]. (a) Incision site for patch repair (dashed line). (b) Incision has been performed prior to patch placement. (c) Patch repair of coarctation.

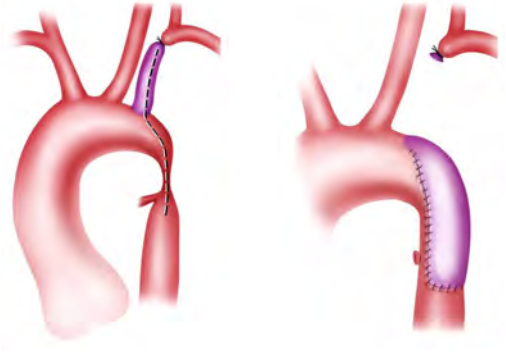

(a) (b)

Figure 5.7: Illustrations showing Waldhausen repair of aortic coarctation [166]. (a) Incision site (dashed line) before Waldhausen repair. (b) Coarctation has been repaired.

5.3.2 Minimally invasive procedures

Due to the invasive nature of surgery, compared to the decreased pain sensation, the reduced costs and the shorter recovery time associated with minimally invasive procedures, balloon angioplasty and, at a later stage, stent implantation have gained importance in the treatment of CoA. These techniques are often applied for the treatment of recoarctation (residual or recurrent stenosis), as repeated application of surgery complicates the intervention and is only partially successful [170].

Balloon angioplasty (BA) mechanically relieves the obstruction by the use of a guide wire (catheter) and a balloon which is inflated to a fixed size, forcing tearing and dilation of the arterial wall (Figure 5.8). The balloon is then deflated and both, the catheter and the balloon are withdrawn. This intervention is considered safe, based on the assumption that the post-surgical scar tissue at the CoA zone is resistant to rupture and aneurysm formation [164]. In 1982, this procedure was first applied for the treatment of native CoA. The application of BA in untreated CoA remains, nevertheless, a point of discussion [171].

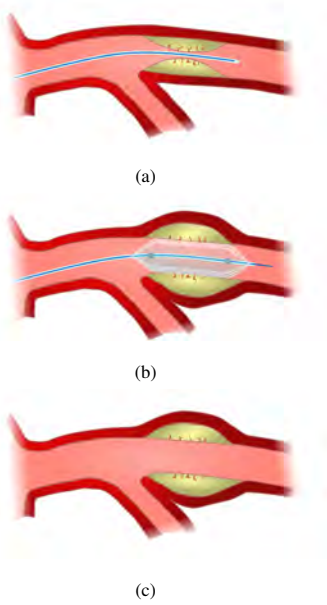

(a)

(b)

(c)

Figure 5.8: Illustration of balloon angioplasty for repair of a stenosed artery [172].

Alternatively, stent deployment can be used. A stent is a coiled wire-mesh tube which is inserted into the stenosed artery and expanded using balloon inflation. This device is left in place to prevent acute elastic recoil of the coarctation segment and ensures the passage of blood. As the principle of stenting is based on stretching and scaffolding rather than tearing

the aortic wall, it minimizes the risk for subsequent dissection and aneurysm formation possibly following treatment with BA alone [173–176]. In infants, their use is still limited due to the need for redilation associated with somatic growth and the dimensions of the current delivery systems.

5.4 LONG-TERM OUTCOME

Current treatment procedures are associated with low short-term mortality and morbidity [1–3] and alleviate the pressure drop across the coarctation segment and thus the workload on the heart. Despite successful anatomic correction, long-term prognoses in this population are not favorable: a substantial morbidity usually exists and life expectancies are decades less than in the general population [177, 178], with an average lifespan of 35-50 years [179]. Long-term morbidity following CoA treatment includes hypertension (11-75% [178, 180, 181]), early coronary artery disease (5-23% [181, 182]), stroke (3%), (growth-induced) recoarctation (3.1-60% [183–185]), aneurysm formation and aortic rupture (5.4-20% [186, 187]). Late post-operative mortality rate was first reported in 1973 by Maron et al. [188]. In this study a group of 194 patients was followed up after CoA repair, 12% of which died after a mean period of 8.8 years. Currently, an improvement of patient survival is recorded, due to improved diagnosis, treatment procedures and post-interventional care [189]. Although the age of CoA repair is an important risk factor for long-term cardiovascular complications [131–136], even early intervention cannot prevent progression of cardiovascular diseases and end-organ damage [190, 191]. This suggests that surgical or transcatheter treatments modify rather than correct the complex pathology of aortic coarctation [190, 192–194] and that coarctation cannot be considered as an uncomplicated disease.

5.5 MOTIVATION FOR COMPUTATIONAL MODELING OF (TREATED) COA

In 1971 O'Rourke [11] first related morbidity in CoA (repair) to adverse hemodynamics and biomechanics in the thoracic aorta and the side branches. Adverse hemodynamics include disturbed or turbulent flow, resulting in abnormal flow patterns and detrimental biomechanical forces, which can in turn, induce thrombosis, vessel wall degradation or ineffective systemic transport. Considering disturbed blood flow strongly affects vascular pathogenesis, and vice versa, hemodynamic information is of high clinical importance, amongst others to diagnose cardiovascular malfunctioning and evaluate treatment outcomes. However, the majority of the clinical CoA studies focuses on the prevalence of cardiovascular complications [177, 178, 181–184, 186, 187], the rates of mortality [177–179, 188] and the post-interventional relief of the pressure drop across the coarctation zone [195–197] rather than the correlation of hemodynamic indices with manifestation of late morbidity. As such,

the underlying role of hemodynamics in the progression of the disease is currently not well understood. Only a limited number of papers [198, 199] correlate biomechanical alterations to the substantial morbidity reported in literature.

With advances in computing power, numerical algorithms and clinical imaging, computational simulations are nowadays an optimal tool to study the patient specific hemodynamics and/or the biomechanics in (repaired) CoA, as they can retrieve data that are difficult to obtain in vivo. Provided the model parameters faithfully represent the physical quantities of the arterial system, these models can contribute to a better understanding of the long-term prognosis of CoA repair and have the potential to detect associated processes before they become clinically relevant. Literature on computational modeling of (treated) coarctation is still sparse. In the following section, an overview of the state of the art in numerical analysis of CoA is given, together with some shortcomings. In [200] important considerations on CoA modeling are listed and a few applications are reported.

5.6 Overview of recent computational studies

5.6.1 Reduced order models

In [152] a reduced order model (1D, coupled with terminal windkessel elements) is proposed to quantify the pre- and post-operative pressure drop across the coarctation region in a noninvasive way. To determine patient specific boundary conditions (BC), a fully automated parameter estimation technique has been developed, allowing this procedure to be applied in a clinical setting relatively easily. Validation of the simulations (4 cases) against cardiac catheterization measurements demonstrated excellent agreement (see Figure 5.9). Contrarily, a relatively bad correlation between pressure differences obtained using cardiac catheterization, Doppler echocardiography and cuff pressure measurements is retrieved. The advantage of this approach is the short computation time (6-8 min), which is at least two orders of magnitude smaller than the one needed to perform 3D flow simulations. On the other hand, detailed information on the local hemodynamics is not provided, prohibiting the correlation of flow indices with late morbidity.

5.6.2 3D CFD simulations

As CoA is often associated with bicuspid and tricuspid aortic stenosis, a numerical study was performed in [201] to assess detailed local flow patterns in a simplified model of the aorta (i.e. a curved tube) with coexisting coarctation of the aorta and aortic stenosis. These simulations demonstrated that the coexistence of both pathologies significantly alter the flow and wall shear stress distribution. A jet with a maximal velocity of 5 m/s thereby impacts on the outer aortic wall, just downstream of the coarctation (see Figure 5.10).

As an extension of the study above, a more physiological model (in terms of geometry and BC) was developed in [138] to include the impact of aortic valve morphology in CFD

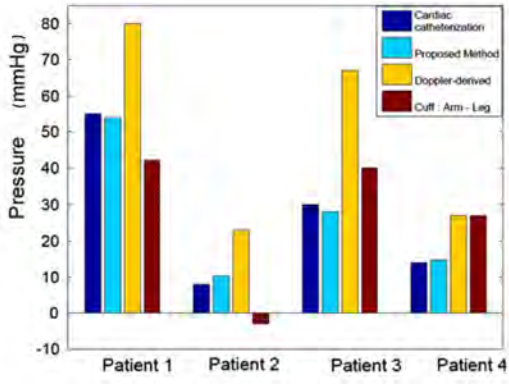

Figure 5.9: Comparison of pressure drops between ascending aorta and the descending aorta at peak systole obtained using four different methods: (i) invasive measurement from cardiac catheterization, (ii) results obtained with the reduced order model, (iii) Doppler echocardiography based measurement from modified Bernoulli's equation, and (iv) cuff pressure measurement in upper and lower body. For the proposed method, a mean absolute error of 1.45 mmHg was obtained, while the Doppler derived and the cuff pressure derived pressure drops have an absolute error of 23 mmHg, and of 11.75 mmHg, respectively [152].

simulations. A bicuspid valve was imposed as a BC in a model of a post-surgical CoA patient (BAV), whereas a tricuspid valve (TRI) was applied in the reference model of a normal patient (TRI). These simulations allow to identify the regions which are most affected by the inlet conditions. It was found that TRI and BAV will expose other portions of the ascending aorta to adverse wall shear stress (WSS) and oscillatory shear index (OSI). Compared to their corresponding plug inlet velocity profiles, differences in time-average wall shear stress (TAWSS) were present throughout the whole thoracic aorta for BAV, but were restricted to the ascending aorta for TRI (see Figure 5.11). With respect to OSI, alterations were reported in the ascending aorta only.

Another patient specific study of the hemodynamics was carried out in [161], where the main research goal was to predict the pressure drop across the coarctation segment at rest and during pharmacological stress. As a validation, the results of the CFD models were compared against catheterization measurements. An accurate prediction of the invasive pressure drop at rest was obtained, however, at stress poor agreement was found. Moreover, a pressure profile extracted from catheterization was imposed as a BC at the aorta at the level of the diaphragm. This undermines the clinical relevance of the CFD model as it explicitly requires invasive measurements and has thus little or no added value.

In [202] aortic flow was simulated in native and surgically treated coarctation to correlate detrimental hemodynamic indices with aortic arch morphology in late follow-up (Gothic, Crenel and Romanesque). Although magnitudes of peak velocity and wall shear stress showed no significant variation between the different arch types, their location altered no-

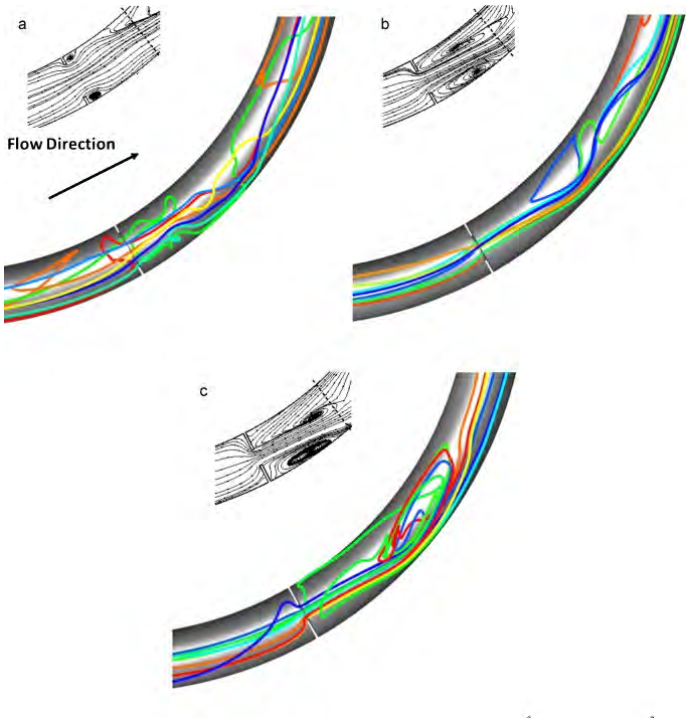

Figure 5.10: Instantaneous streamlines and particle tracking for (a) a coarctation with a 50% area reduction and a stenosis with an effective orifice area (EOA) of 1 cm^2, (b) a coarctation with a 75% area reduction and a stenosis with an EOA of 1 cm^2 and (c) a coarctation with a 90% area reduction and a stenosis with an EOA of 1 cm^2. Note the loss of symmetry of the trans-coarctation jet [201].

tably. Specifically, the Gothic arch had a unique location of peak WSS (see Figure 5.12), which might explain the high incidence of vascular dysfunction in this group. Whether these conclusions are general remains to be seen, as only one patient of each remodeling category was analyzed.

Most of the cited studies have not quantified the turbulent or disrupted flow conditions present in (repaired) CoA (with exception of [138]). An effort in this direction was made in [203], where the objective was to provide a validation of numerically predicted turbulent kinetic energy (TKE) in CoA against in vivo measurements. Promising results were obtained: a relatively small error ($\approx$10%) between both predictions of TKE persisted. Nevertheless, comprehensive understanding of the role of TKE in the progression of the disease and an indication of reference values of TKE in healthy subjects are missing.

It has been shown in literature [204–206] that the formation of atherosclerotic plaque in the descending aorta is related to altered indices of WSS compared to healthy subjects. The

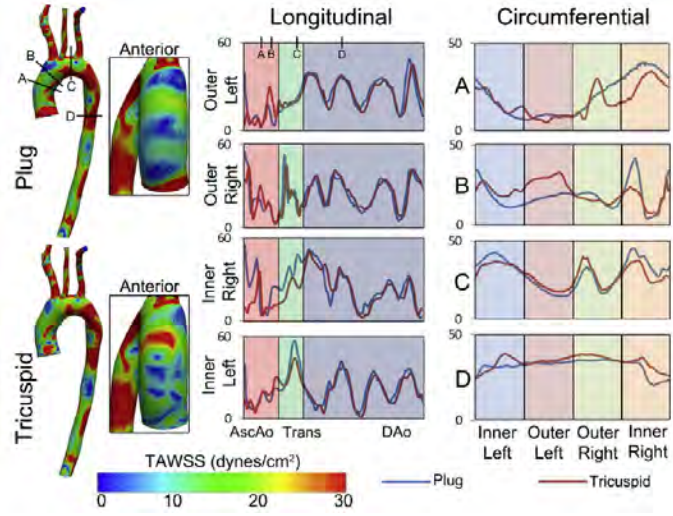

(a)

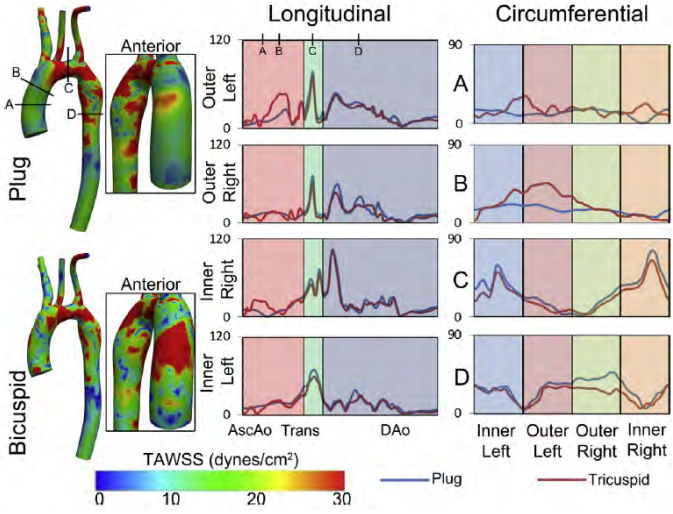

(b)

Figure 5.11: (a) Comparison of TAWSS between a plug and tricuspid aortic valve inlet velocity profile for the normal patient. (b) Comparison of TAWSS between a plug and bicuspid aortic valve inlet velocity profile for the patient with surgically corrected CoA. Spatial distributions of TAWSS are shown on the vessel (left) and the insets show the distribution along the anterior wall. Longitudinal and circumferential TAWSS was queried at specific locations to quantify regions of disparity between inlet velocity profiles [138].

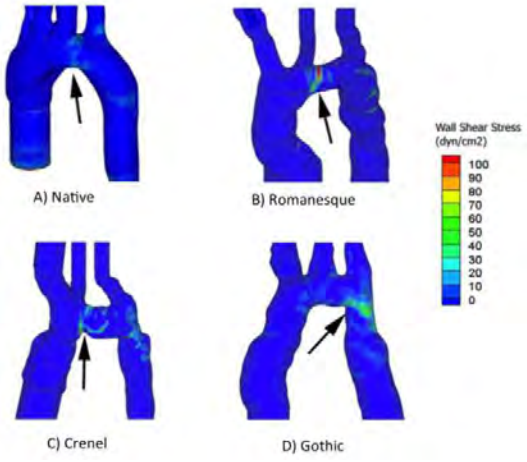

Figure 5.12: Wall shear stress (WSS) magnitude of each arch type. Arrows indicate the area of peak WSS as indicated in red [202].

objective of [207] was therefore, to quantify normal flow patterns and WSS distributions in 6 control subjects and oppose these results to those from age and gender-matched CoA patients treated by end-to-end anastomosis (shown in Figure 5.13). Findings of this study suggest that plaque may form in unique locations induced by surgical repair (see Figure 5.14). This analysis, furthermore, provided an intuitive way to visualize these locations, facilitating the examination of their contribution to morbidity in follow-up studies.

5.6.3 3D fluid-structure interaction (FSI) models

All of the above studies were performed under the rigid wall assumption. Considering one of the main functions of the aorta is to buffer the blood during systole in order to sustain blood flow during the diastolic phase, this simplification may corrupt the insights provided by these models. Hence, the compliance of the aorta should be taken into account in computational models of CoA [208]. The influence of rigid versus compliant wall modeling was analyzed in [209] for a simplified model of aortic coarctation (i.e. a curved tube with a local narrowing). This study demonstrated that aortic compliance has a significant impact on the magnitude of the antegrade diastolic (run-off) flow seen through the coarctation zone. Increased compliance further damps out systolic peak flow and magnifies the level of diastolic flow (depicted in Figure 5.15). This phenomenon is explained by the dilation of the proximal aorta during systole, resulting in cushioning of the upstream energy. This stored energy is later released downstream during diastole, generating an increased degree of diastolic run-off.

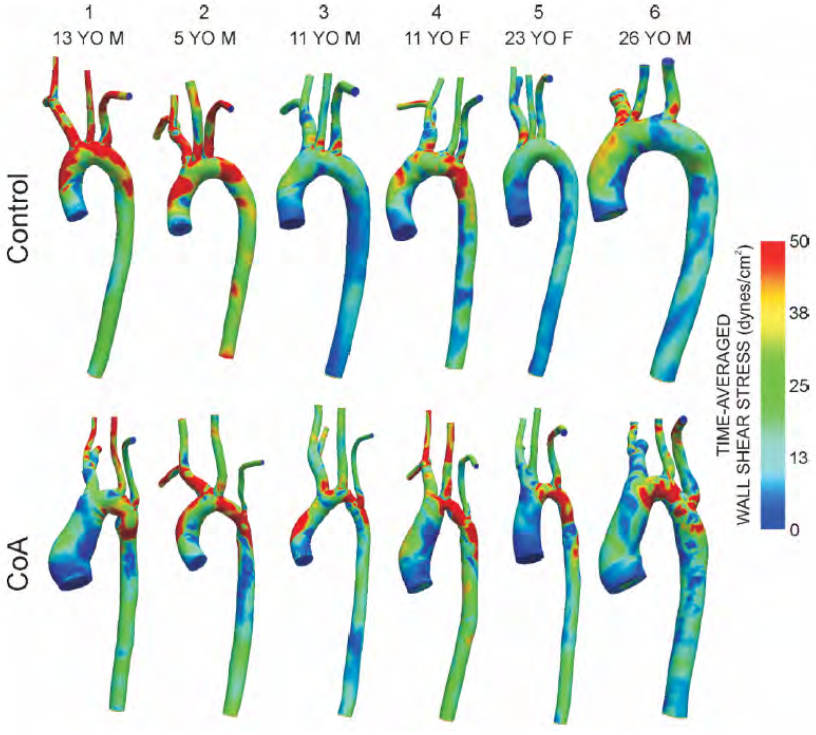

Figure 5.13: Distributions of time-averaged wall shear stress for the six control subjects (top row) and age- and gender-matched coarctation patients treated by resection with end-to-end anastomosis (bottom row) [207].

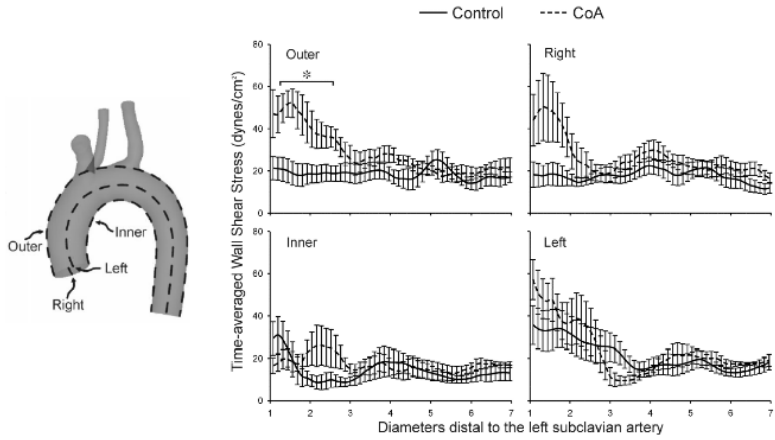

Figure 5.14: Ensemble-averaged longitudinal TAWSS plots comparing the six control subjects (solid lines) and age- and gender-matched coarctation patients treated by resection with end-to-end anastomosis (dashed lines) along the outer, anatomic right, anatomic left, and inner curvatures. *Statistically different from control subjects ($P < 0.05$). Data are expressed as mean $\pm$ SEM [207].

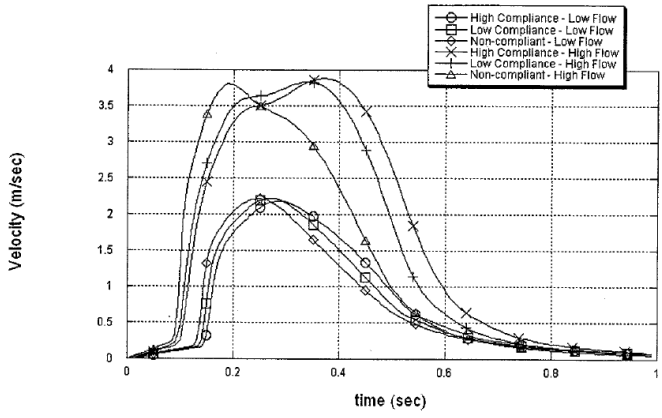

Figure 5.15: Flow velocities at coarctation site for low and high stroke volume runs for each of 3 compliance models considered [209].

In [45] an FSI model has been used to compute the reduction in cardiac load when comparing the pre- and post-intervention hemodynamic conditions. In this quite advanced yet elegant study, a lumped parameter model of the heart is coupled to a 3D patient specific model of an aorta with an aortic coarctation. The downstream circulation is modeled using three-element windkessel models and the surgical procedure is simulated by applying surgical guidelines to connect the aorta proximal and distal to the coarctation. As the surgical resection entails a decrease of the arterial resistance, a reduced afterload and contractility of the left ventricle were obtained. The reduced pressure loss in the post-intervention case is clearly visible in Figure 1.7.

The effect of a 'virtual' stent implantation was analyzed in [210]. The presence of the stent was modeled by including a stiff segment in a 3D model of a thoracic aorta. The geometry was extracted from MR images of a CoA patient of which the narrowed segment had been virtually corrected afterwards. Compared to a model with normal tissue properties throughout the whole aorta, no significant change in cardiac work and mean blood pressure was found. This pilot study falsifies the hypothesis that the presence of a noncompliant stent implicates adverse hemodynamic alterations [145, 211–218].

LaDisa et al. [219] performed the first full-scale application of 3D numerical models to a sampling of CoA patients: a moderate and severe native CoA and 2 post-operative cases. Models included arterial wall deformation and downstream vascular resistance and compliance. Combining clinical data and computational fluid dynamic tools, a procedure was developed to evaluate coarctation severity (blood pressure gradients, ΔBP), treatment outcomes and potential indices associated with long-term morbidity (such as TAWSS, OSI and cyclic strain) under resting and exercise conditions. Two intercostal arteries were included in the model of severe native CoA to represent the collateral blood flow from the level of the coarctation to the diaphragm. Most pronounced exercise-induced increase in ΔBP was reported for the moderate, native CoA (see Figure 5.16). For native CoA cyclic strains in the proximal aorta were prominent, but a notable reduction was found after treatment.

5.6.4 3D fluid-solid-growth models

One of the future challenges in image-based modeling of cardiovascular mechanics is the incorporation of vascular growth and remodeling [4]. Blood vessels have the particular ability to adapt both their shape and material properties to persistent hemodynamic alterations such as changes in blood pressure due to, for example, chronic hypertension. Arterial remodeling thereby develops in such a way that it attempts to maintain a preferred mechanical state (i.e. establish normal circumferential wall stress) [220]. In hypertension (commonly prevailing after CoA repair), smooth muscle cells proliferate and synthesize supplementary extracellular matrix proteins and glycoproteins to restore intramural stress to normal values [221–223]. Thickening and stiffening of the wall are, consequently, often observed in hy-

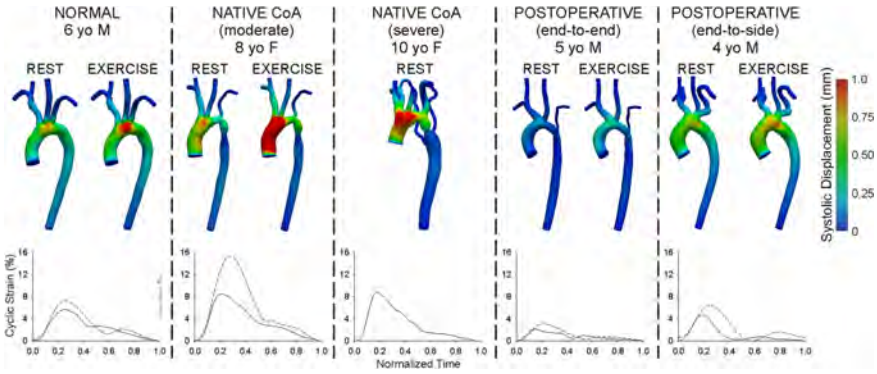

Figure 5.16: Color contours of systolic wall displacement mapped to the reference diastolic configuration and examples of associated cyclic strain plots in the ascending aorta during rest (solid lines) and simulated moderate exercise (dashed lines) [219].

pertensive CoA patients [198, 224, 225]. Vice versa, arterial wall remodeling will influence blood pressure and flow. This implicates the need to couple fluid-solid models with arterial growth and remodeling tools [226] to develop so-called fluid-solid growth (FSG) models [227].

Concerning the inclusion of wall remodeling after CoA repair, a first attempt in the direction of FSG models was made by Coogan et al. [228]. In this study local and systemic hemodynamic alterations, generated by distal aortic coarctation, were analyzed. The acute hemodynamic response was compared to the condition following early arterial wall remodeling (i.e. spatially varying wall thickening and stiffening). Although no strong coupling of the FSI model and wall remodeling was established in this study, this analysis provides unique clinical insights into the impact of vessel wall adaptation on the cardiovascular system. In particular, an increase in pressure, left ventricular work and wave speed were obtained after wall remodeling (illustrated in Figure 5.17). Calculated values of circumferential wall stress returned to normal values in the aorta (of which the stiffness and thickness were increased by 100 and 15% respectively), but were higher in the side branches of the aorta where less pronounced remodeling (an increase of 50 and 10%) was prescribed.

To improve our understanding of the coupling between hemodynamics, geometry and tissue properties, more experimental data is needed. Accordingly, Menon et al. [229] developed an in vivo rabbit model, allowing the quantification of coarctation-induced hemodynamic and vascular biomechanical indices and their corresponding effect on vascular properties and morphology. More specifically, a distinction was made between alterations found in untreated animals and the ones that had undergone surgical treatment by end-to-end anastomosis. For this purpose, a coupled experimental and computational approach was

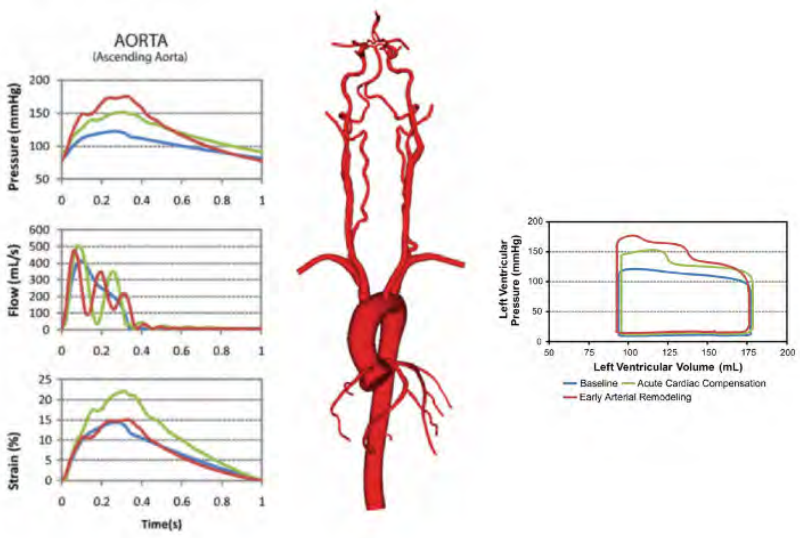

Figure 5.17: (left) Results comparing pressure, flow, and wall strain in baseline, acute cardiac compensation, and early arterial remodeling conditions. (right) Pressure-volume loops reflecting the workload of the left ventricle during baseline conditions, acute cardiac compensation, and early arterial wall remodeling. The cardiac workload was 8 476, 9 890, and 11 059 mmHg.mL for the baseline, acute cardiac compensation, and early arterial remodeling simulations, respectively [228].

used. Indices such as BP, flow, velocity, WSS and strain were obtained from image-based subject specific CFD models, whereas vascular morphology and function were revealed by histology and myograph results. Elevated systolic and mean BP in untreated CoA resulted in vascular thickening, disorganization and endothelial dysfunction, both proximal and distal to the coarctation segment. Despite normal values of BP in treated animals, proximal endothelial dysfunction and stiffening were observed.

5.6.5 Limitations and future prospects

The clinical results and implications of the cited literature should be interpreted with care and within the constraints of their limitations. Anyhow, compared to numerical studies performed a decade ago, huge improvements towards more realistic, physiological modeling have been made. These include the extraction of a patient specific anatomy, the application of appropriate BC (replicating downstream vascular resistance and compliance) and the modeling of arterial compliance (see Table 5.1, key features). Other aspects, such as, the incorporation of vascular remodeling and the inclusion of collateral blood flow are still in their early stage of development and require experimental or in vivo validation.

Apart from the modeling constraints, one should keep in mind that large scale clinical applications are lacking. All of the above numerical studies report results from a very

key features	**computational studies**
simulation of local flow patterns	[45, 138, 161, 201–203, 207, 209, 210, 219, 228, 229]
use of patient specific geometry	[45, 138, 152, 161, 202, 203, 207, 210, 219, 228, 229]
use of patient specific BC	[45, 138, 152, 161, 203, 207, 210, 219, 228, 229]
modeling of aortic compliance	[45, 152, 209, 210, 219, 228]
modeling of vascular remodeling	[228, 229]
modeling of collateral blood flow	[45, 210, 219]
validation	[152, 161, 203, 210, 229]
application	
number of cases studied	
1-3	[45, 138, 203, 209, 210, 228]
4-10	[152, 161, 201, 202, 207, 219, 229]
provide unique clinical data	[45, 138, 152, 201, 202, 207, 210, 219, 228, 229]

Table 5.1: Overview of the physiological aspects taken into account in recent computational studies of (repaired) CoA, indication of their validation (experimental or in vivo), their application and clinical relevance.

limited number of cases (see Table 5.1, applications) and should be confirmed in a more extensive study.

In spite of their restricted application, these preliminary studies support the hypothesis proposed by O'Rourke that hemodynamics and biomechanics play a crucial role in the prognosis of repaired coarctation. With recent advancements in computational modeling in mind, we believe that these simulations have the potential to address open clinical questions related to the long-term outcome of treated CoA.

5.7 FOCUS OF THE COMPUTATIONAL WORK PERFORMED IN THIS DISSERTATION

Motivated by the hypothesis of O'Rourke [11], suggesting that hemodynamics and vascular biomechanics are associated to the long-term morbidity of treated aortic coarctation, the main objective of this work is to evaluate the hemodynamic response in repaired CoA using computational models with varying complexity. While patient specific FSI models have the convenience of taking into account the full complexity of the problem under consideration, their high level of complexity may also hamper the analysis and insights provided. This work therefore begins by focusing on a very simplified model to analyze wave travel and reflection in repaired CoA (see chapter 6). In this model, the aorta is represented by a flexible tube and the effect of repaired CoA is modeled by including a stiff segment. Both, the propagation of a short pressure pulse and a physiological pulse are simulated and provide unique data that improves the understanding of the phenomena observed clinically in a complex patient specific setting.

Uncertainty exists on the factors contributing to the increased risk of cardiovascular morbidity among others the presence of a residual narrowing, leading to an additional resistance in the arterial system and a less distensible zone disturbing the buffer function of the aorta. As the many interfering factors and adaptive physiologic mechanisms present in vivo prohibit the study of the isolated impact of these individual factors, a numerical fluid-structure interaction model is developed, to predict the central aortic hemodynamics in coarctation treatment (see chapter 7). In this second study, a subject specific model of the aortic arch is applied and the functional impact of repaired CoA is modeled by including a segment with varying length and stiffness. Recurrent coarctation is studied by altering the diameter of the obstruction. These data provide highly detailed 3D information on instantaneous changes in pressure, flow and aortic dimensions. The results from chapter 7 are subsequently used to apply the reservoir-wave paradigm [230] to the aortic pressure and flow waves generated in the 3D fluid-structure interaction simulations and to critically evaluate its performance in a controlled setting - with direct access to gold standard information - where we directly impact on both the reservoir and the conduit function of the aorta (see chapter 8).

CHAPTER 6

Analysis of the hemodynamic impact of a local stiffening[1]

6.1 INTRODUCTION

The measured blood pressure is the resultant of forward pressure waves, traveling from the heart towards the peripheral arteries and backward pressure waves, generated by reflections along the arterial path and in the periphery. The later reflected compression waves (so-called as they produce a pressure increase while traveling) reach the heart, the less they generate an additional load on the heart. A compression wave reaching the heart in early systole (as is the case for older people with stiffened arteries or for patients with hypertension) leads to an increased systolic blood pressure and is a major risk factor for developing cardiovascular diseases [231–233]. The analysis of wave travel and reflection, sometimes referred to as 'pulse wave analysis', is increasingly used for the assessment of arterial and cardiovascular health and for the early diagnosis of cardiovascular risk.

One of the many possible applications of pulse wave analysis, is the study of wave reflections generated by a repaired aortic coarctation. Even after successful treatment a local stiffening remains, caused by the presence of the stent (see section 5.3.2) or the scar tissue (see section 5.3.1). This stiffening generates an impedance mismatch and is a source of wave reflections that reach the heart fast, given the short distance to the heart [234]. Anal-

[1] This chapter is based on the work *"Fluid-structure interaction simulation of pulse propagation in arteries: numerical pitfalls and hemodynamic impact of local stiffening."*, as published in *International Journal of Engineering Science* 77:1-13, 2014.

ysis of these wave reflections could thus be used to estimate the effect of the treatment of aortic coarctation on the load on the heart.

The study of wave reflections can either be based on experiments (using in vivo or in vitro pressure and velocity measurements), or on data obtained from computational models of various levels of complexity. With advances in computing power and numerical algorithms, computational simulations are extensively used for applications where experimental data are limited or unavailable. One-dimensional (1D) models are used to study wave propagation phenomena in the entire arterial tree or major parts of it (see, e.g. [59, 61, 235, 236]) whereas local flow field details can only be obtained from three-dimensional (3D) computational fluid dynamics or more complex fluid-structure interaction models (see, e.g. [32, 237, 238]).

As the high level of complexity, inherent in patient specific aortic models, may hamper the insights provided by these models, a simplified model of repaired aortic coarctation is used. The aim of this study is to simulate the pulse propagation in a locally stiffened tube (i.e. a simple model representative for an aorta with repaired aortic coarctation) and to analyze the hemodynamic impact of the stiff segment.

6.2 MATERIALS AND METHODS

6.2.1 FSI model

Figure 6.1: Simplified three-dimensional model of an aorta with repaired aortic coarctation.

The aorta is represented by a three-dimensional flexible tube and the effect of the repaired aortic coarctation is modeled by including a 5 cm long stiff segment, 15 cm distal to the inlet (see Figure 6.1).

Two cases are studied. In the first case, the positive half of a short sinusoidal pressure pulse (period T of 60 ms, amplitude of 1470 Pa which is representative for the foot of a physiological pulse) is imposed at the inlet and a time step size of 0.25 ms is used to resolve the flow field in time. A linear elastic material model is used to describe the wall behavior (Young's modulus 250 kPa, Poisson's ratio 0.49, density 1200 kg/m^3). The stiff segment is chosen six times stiffer than the flexible wall (Young's modulus 1500 kPa). In the second case, a physiological pressure pulse (period T of 1 s, amplitude of approximately 60 mmHg) is used as an inlet boundary condition. As the numerical dissipation is less significant due to

the large pulse period, a time step size of 5 ms is chosen for this case. As the deformations become more pronounced in this case, a hyperelastic material model is used (a reduced form of the generalized Mooney-Rivlin) with experimentally obtained coefficients for the human aorta (C_{10} = 18.9, C_{01} = 2.75, C_{20} = 590.4, C_{11} = 85.72 and C_{30} = 0 kPa) [114]. The behavior of the local stiffening is modeled using a linear elastic model (Young's modulus 1500 kPa).

In both cases a reflection free boundary is used (see section 2.2.1.1) at the outlet of the fluid domain to isolate the effects of reflections due to the presence of the stiff segment. The fluid domain is meshed using a structured grid with approximately 28000 cells. 1500 quadratic continuum elements are used to discretize the arterial wall.

6.2.2 Wave separation

To analyze the wave reflections generated by the local stiffening, the pressure waves are decomposed into their forward and backward propagating components. A condensed version of the mathematics behind wave separation is presented. More details can be found in [239].

If $\Delta p_{\pm}$ and $\Delta v_{\pm}$ represent the changes in time in pressure and velocity in the forward '+' and backward '-' waves at a given location, additivity requires

$$\Delta p = \Delta p_{+} + \Delta p_{-} \tag{6.1a}$$

$$\Delta v = \Delta v_{+} + \Delta v_{-}. \tag{6.1b}$$

From the characteristic decomposition it follows that a simple relation exists between the changes in pressure and velocity in any wavefront, given by the water hammer equations.

$$\Delta p_{\pm} = \pm \rho_f c \Delta v_{\pm} \tag{6.2}$$

In this equation ρ_f represents the blood density and c the wave speed. Remark that similar as in chapter 2 the velocity is denoted by the symbol v. Eqs. (6.1a), (6.1b) and (6.2) can be solved for the forward and backward pressure changes. This results in

$$\Delta p_{\pm} = \frac{1}{2}(\Delta p \pm \rho_f c \Delta v). \tag{6.3}$$

The forward and backward pressure waves are finally calculated by summing these wave fronts

$$p_{\pm}(t) = \sum_{i=0}^{t} \Delta p_{\pm}(i). \tag{6.4}$$

As the flow is initially at rest, no pressure waves are present at t = 0. A similar decomposition can be done for the flow velocity waves.

6.3 RESULTS

6.3.1 Wave separation analysis: short pressure pulse

In the straight tube, the presence of the stiff segment induces two backward waves. At the transition from the elastic tube to the stiff segment, the wave speed suddenly increases, causing the forward wave to be amplified and a backward compression wave (BCW) to be generated. The moment the pressure pulse leaves the stiff segment, the wave speed decreases again, causing the forward wave to be reduced and a backward expansion wave (BEW) to be created. This is demonstrated in Figure 6.2 (top), which shows the pressure and its forward and backward component proximal to (left), halfway (middle) and distal to (right) the stiff segment.

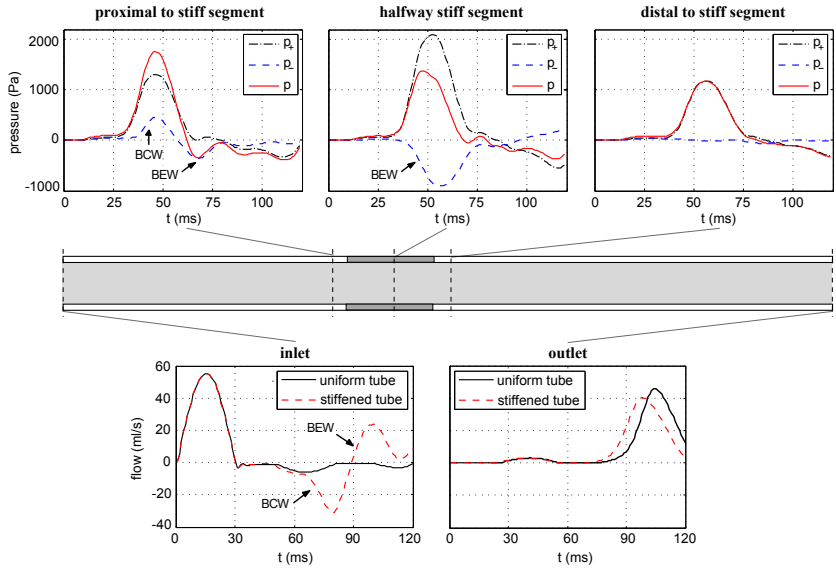

Figure 6.2: (top) Evolution of the pressure p and its forward p_+ and backward p_- component proximal to, halfway and distal to the stiffening for the case of a short pressure pulse. (bottom) Effect of a local stiffening on the inflow (left) and the outflow (right).

Proximal to the stiff segment these two backward waves overlap with a time delay τ given by

$$\tau = \frac{2L_{stiffening}}{c_{stiffening}} = 8.4 \text{ ms} \tag{6.5}$$

where $L_{stiffening}$ represents the length of the stiff segment and $c_{stiffening}$ the local wave speed.

The overall comparison with the flow in a uniform tube, representing a healthy aorta, is shown in Figure 6.2 (bottom). The presence of the stiffening significantly alters the flow

at the inlet of the model. The backward compression and expansion wave generated by the stiff segment can clearly be observed. At the outlet a small time delay between both pressure waves is visible, due to the increased wave speed in the stiff segment. The stiff segment reduces the amplitude of the flow wave by 11% compared to a straight tube.

6.3.2 Wave separation analysis: physiological pressure pulse

Figure 6.3 (top) shows the pressure and its forward and backward component proximal to (left), halfway (middle) and distal to (right) the stiff segment for the propagation of a physiological pressure pulse. Proximal to the stiffening the backward compression and expansion wave overlap and cancel each other out. As a result, only a small peak in the backward component can be distinguished (BCW), caused by the time delay between both waves. The backward expansion wave (BEW), generated at the distal end of the stiff segment, is clearly visible in Figure 6.3 (middle).

As can be seen in Figure 6.3 (bottom), the local stiffening has almost no effect on the hemodynamic response in case a physiological pressure pulse is imposed at the inlet. Only for the flow at the inlet of the model small changes are found.

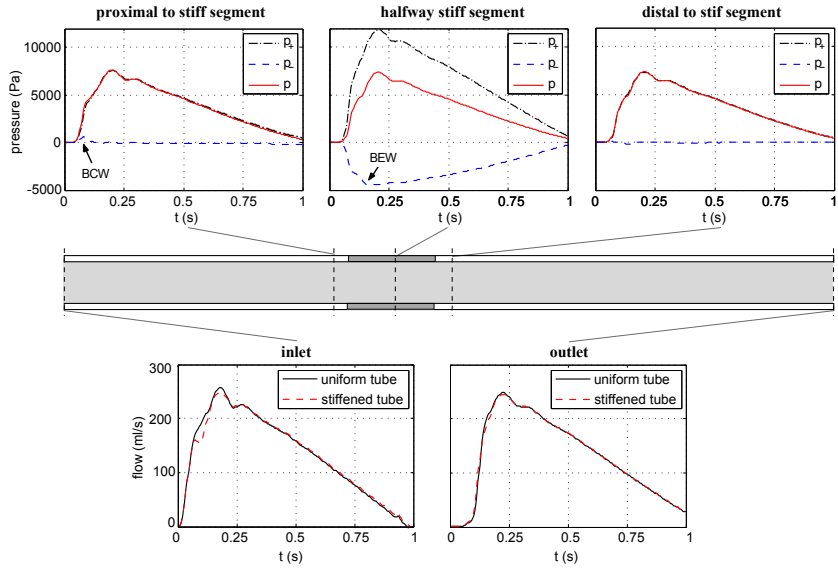

Figure 6.3: (top) Evolution of the pressure p and its forward p_+ and backward p_- component proximal to, halfway and distal to the stiff segment for the case of a physiological pressure pulse. (bottom) Effect of a local stiffening on the inflow (left) and the outflow (right).

6.4 DISCUSSION AND CONCLUSION

The grid and time step converged wave propagation in a simplified tube model of an aorta with repaired coarctation is studied. While other FSI studies on aortic coarctation focus on the reduction of the cardiac load when comparing the pre-intervention and post-intervention hemodynamic conditions [45] or the hemodynamic impact of surgical reconstructed aortic arches [240], this analysis focuses on the reflections generated by the local stiffening that remains after the treatment of aortic coarctation.

While patient specific FSI models have the convenience of taking into account the full complexity of the problem under consideration, their high level of complexity may also hamper the analysis and insights provided. In this work, a very simplified model of repaired aortic coarctation was used. The advantage of this model is that the only reflections present in the model originate from the local stiffening and can thus easily be interpreted. However, to obtain a complete analysis, a patient specific geometry should be applied, including the residual narrowing, which often remains after the treatment of aortic coarctation. This shortcoming will be addressed in chapter 7. Besides discrete reflections, generated at the branching of the aorta and by the residual narrowing and stiffening, also scattered wave reflections will be present, caused by the tapering of the aorta.

In a first case the propagation of a short pressure pulse is simulated. The main motivation for the study of this setup, is that the different reflections become clearly distinguishable. Indeed, the time delay τ between both waves is of the same magnitude as the duration of the pulse itself (8.4 versus 30 ms). The simulation of a short pulse consequently improves the understanding of the phenomena involved.

The simulation of a physiological pressure pulse, on the other hand, can be used to predict the actual hemodynamic impact of a local stiffening. Although the simulation of the short pulse suggests quite an important alteration of the hemodynamic quantities, no significant changes are found for the case of a physiological pressure pulse. This counter-intuitive result can, nonetheless, be explained by recalling the reflections induced by the stiff segment. At the transition from the flexible artery to the stiffening, a backward compression wave is generated, immediately followed by a backward expansion wave, created at the outlet of the stiffening. Proximal to the stiff segment, both waves overlap and cancel each other out, as such leaving the hemodynamic quantities almost undisturbed.

These results are in agreement with the results of the one-dimensional studies published in [241, 242]. In these studies a 1D model was developed to predict the hemodynamic impact of a stent, modeled as a local stiffening. Both studies concluded that the major effect of the presence of the stent is a small pressure build-up proximal to the stent. Increased stiffness and length of the prosthesis amplified this effect. In [241], the magnitude of the

reflected wave was less than 1 % of the normal pulse pressure, for all cases tested. In [242] larger pressure raises (up to 12%) were reported. However, this study did not use physiologically correct values for the dimensions and physical properties.

In practice, more than two backward waves are created. Particularly, the BEW generated at the distal end of the stiffening, will reflect in a forward compression wave (FCW) at the proximal end of the stiffening. This wave will re-reflect at the distal end of the stiff segment, creating a second BEW, which in turn, generates a second FCW and so on. As such, part of the wave energy will reach the outlet with a delay (as a sequence of compression waves). This explains the amplitude reduction at the outlet, observed in Figure 6.2. These phenomena are clearly illustrated in [43], in which the propagation of a 2.5 ms wide pulse is studied. Considering that each reflection is just a fraction of the original wave and the time delay between the different reflections is very small compared to the pulse period, these secondary reflections are not individually observable in the studied examples.

CHAPTER 7

Insights into the effect of local stiffness and residual narrowing on central hemodynamics seen in repaired aortic coarctation: a computational study

7.1 INTRODUCTION

Even after successful treatment of aortic coarctation, a high risk of cardiovascular morbidity and mortality remains. Uncertainty exists on the factors contributing to this increased risk among others the presence of a residual narrowing (recurrent coarctation) and a less distensible zone, caused by the presence of a stent or scar tissue.

As approximately 60% of the buffer capacity of the aorta is located in the proximal aorta [243], this local stiffening affects the 'cushioning' function of the aorta. To which extent the presence of a stent or a local stiffening reduces aortic compliance and whether this gives rise to adverse hemodynamic consequences remains a question [145, 211, 212, 214–218]. Especially in the setting of coarctation associated with vasculopathy and reduced compliance in the proximal aorta, some reports suggest that a noncompliant stent significantly diminishes complications compared to surgery [198, 224].

Clinically, recurrent coarctation is usually defined as a pressure difference of at least 20 mmHg between the upper and lower limbs. Recurrent coarctation is predominantly associated with somatic growth and is therefore more prevalent after correction in infancy and rather exceptional in adult repair. Recoarctation following stent implantation during

childhood has been reported in several studies [244–247] and is one of the major concerns and drawbacks for their widespread use in native coarctation treatment [248]. Nonetheless, this complication is not unique to stent implantation, as growth-induced recoarctation has also been observed following treatment by surgery or balloon angioplasty [170, 249–251]. Once recoarctation has developed, the local narrowing leads to an additional resistance in the arterial system (characterized by the ratio of the mean pressure to the mean flow rate) and disturbs the blood flow, resulting in an alteration and redistribution of the pressure fields and the shear stress exerted on the aortic wall [252, 253]. In addition, a local narrowing and stiffening generate wave reflections that reach the heart fast, given the short distance to the heart.

The many interfering factors and adaptive physiologic mechanisms present in vivo prohibit the study of the isolated impact of these individual factors. As experimental or computational studies more easily allow to mimic the alterations caused by a single parameter, these approaches are crucial in the understanding of central aortic hemodynamics following coarctation treatment.
Although literature on the hemodynamic effect of stent implantation is still sparse, preliminary computational studies [210, 241, 242] suggest that the influence of a noncompliant stent is very limited and falsify the hypothesis that the presence of a noncompliant segment implicates adverse hemodynamics.
With respect to the hemodynamic impact of a stenosis, some analytical work and experimental data have been reported in the past [254–256]. However, many of the previous studies focused on the added resistance to flow as a function of the obstruction severity (area reduction) rather than giving a detailed description of the flow patterns (such as the initiation and extension of flow separation distal to the stenosis and the initiation of turbulence). Generally, very simplified models were considered, restricting their physiological relevance. In [201] a 3D numerical model of the aorta including different severities of aortic coarctation was recently developed to examine the relationship between stenosis severity and hemodynamic conditions. Despite this model provides unique insights, some limitations still exists, such as a simplification of the aortic arch geometry, absence of the side branches and collateral blood flow and a rigid wall assumption.
Other more complex models of CoA (involving a patient specific geometry) were investigated (see chapter 5), but they do not include the study of hemodynamic alterations as a function of stenosis severity or coarctation stiffness solely [45, 138, 161, 202, 203, 207, 219, 228, 229].

With previous studies and the advancements in computational modeling in mind, we believe that numerical models allow for a direct quantification of the impact of the local stiffening and/or narrowing present after coarctation treatment. Since current models are an oversimplification of the physiological system or miss an extensive application and/or

parameter study, the aim of this research is to develop a relevant parameter model to predict the impact of (coexisting) stiffening and narrowing in CoA (repair). Varying lengths, stiffnesses and diameter reductions of the coarctation zone are studied and their results compared against the hemodynamic response in a healthy subject.

7.2 MATERIALS AND METHODS

We refer to chapter 4 for a detailed description of the patient specific FSI model of a normal aorta. The structural model, the flow model and the interaction between both, allow to predict the central hemodynamics in a healthy aorta. These results will be used as a reference for the other simulations performed in this chapter. More detailed information on the adopted coupling technique, the mesh construction and a discussion of the selected numerical and model parameters can also be found in chapter 4.

To model the functional impact of repaired CoA, a segment with varying length (L), stiffness (E_{CoA}) and diameter (D_{CoA}) is included (indicated by the colored zone in Figure 7.1). Three types of intervention are considered:

- resection by end-to-end anastomosis, resulting in circular scar tissue at the location where both ends of the aorta are sutured together. In [257] local elasticity properties of the aortic wall (such as the elasticity modulus E and stiffness-index β) indicate local increase in stiffness in the region of the surgical scar. Based on the stiffness indices and dimensions reported in this article, the elasticity modulus of the coarctation region in our model (E_{CoA}) is chosen to be equal to, 5 or 20 times stiffer than the unaffected aortic tissue (E_{Ao}). E_{Ao} is thereby defined as the mean slope of the stress-strain curve in the 0 to 10% strain range. A length (L) of, alternately, 1 and 2.5 cm is thereby selected.
- relief of the obstruction by stent deployment. In [258], a review on different stent types used in coarctation treatment is given and considerations to achieve successful stent implantation are discussed. The segment lengths applied in our research (2 and 5 cm) are chosen to cover the range of lengths of the stents currently used in coarctation repair. The presence of the noncompliant stent increases aortic stiffness. Accordingly, a 100 times stiffer material is used to mimic the wall behavior in the stented section.
- treatment with an interposition graft. In this case, the resected segment is replaced by a synthetic material, behaving much stiffer than the unaffected aortic tissue. As with stent implantation, this technique is most often used in patients who have exceeded their growth potential. Although from an interventional point of view, stent deployment and graft interpositioning are very different, both outcomes are similar from a

mechanical point of view. A such, the same material parameters and lengths are used to represent this type of repair.

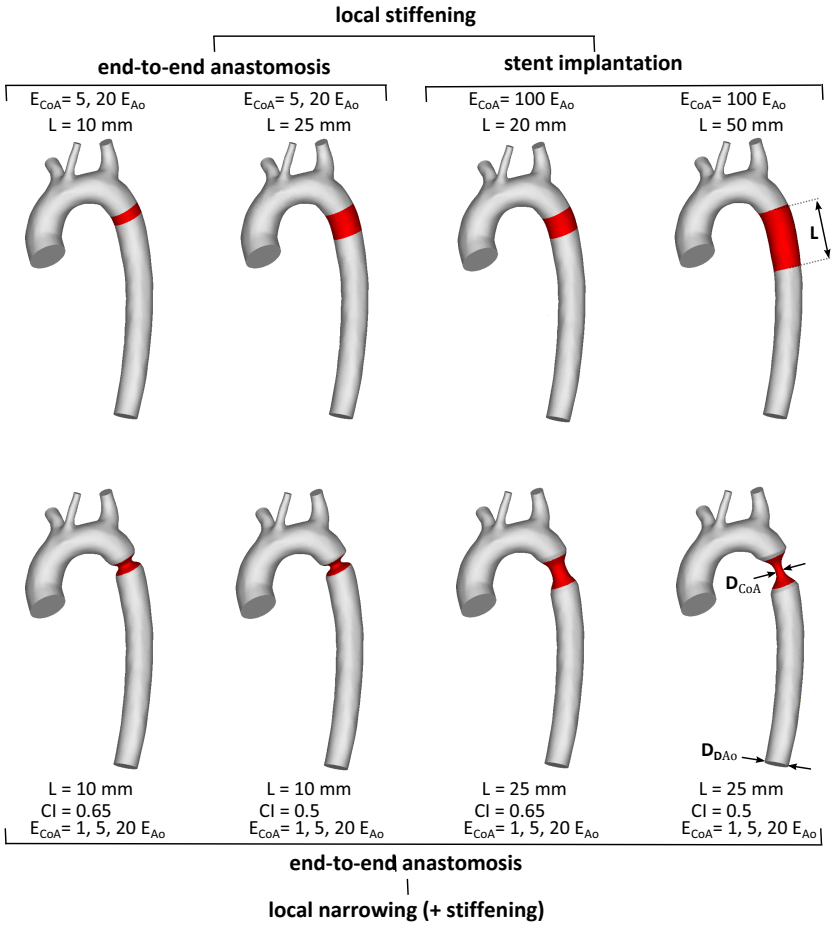

Figure 7.1: Parameter models of repaired CoA.

The severity of the residual stenosis is quantified by the coarctation index (CI), defined as the ratio of the diameter of the coarctation zone to the diameter of the descending aorta (D_{CoA}/D_{DAo}). The higher the CI, the lower the severity of the recurrent narrowing. Two gradations of severity are considered: an index of 0.5 indicating a severe stenosis which requires treatment and an index of 0.65, mimicking a mild narrowing, which does not necessitate intervention [155] (see Figure 7.1 bottom). An overview of the different parameter combinations used in this study can be found in Table 7.1 and Figure 7.1. Remark that the

		local stiffening		reCoA (+ stiffening)			
	CI	1		0.65		0.5	
	L (mm)	10	25	10	25	10	25
scar tissue	E_{CoA} = E_{Ao}	reference	reference	x	x	x	x
	E_{CoA} = 5 E_{Ao}	x	x	x	x	x	x
	E_{CoA} = 20 E_{Ao}	x	x	x	x	x	x
	L (mm)	20	50				
stent	E_{CoA} = 100 E_{Ao}	x	x				

Table 7.1: Overview of the model parameters (CI, L, E_{CoA}) used in this research to study the effect of CoA repair. 'reference' thereby refers to the healthy aorta and 'x' indicates which cases of repaired coarctation are studied.

models with recurrent stenosis (CI = 0.65 or 0.5) could also represent native (untreated) coarctation.

The aortic geometry is modified using the software 3-matic (Materialise). The consecutive construction steps in the modification process are shown in Figure 7.2. First, a cylinder with height L is projected on the aortic wall (see Figure 7.2 (a)). The axis of this cylinder is aligned with two centerline points of the aorta, located at a distance L from each other. Next, part of the aorta (exceeding the projected cylinder) is extracted (Figure 7.2 (b)) and the resulting contours are reconnected to the contours of the projected cylinder (Figure 7.2 (c)). The missing part of the aorta is replaced by a shorter, narrowed cylinder (Figure 7.2 (d)). Contours of the aortic wall and the cylinder are connected (Figure 7.2 (e)) and Laplace smoothing (1^{st} order, no compensation) is applied to obtain a smooth transition from the proximal and distal aorta to the coarctation segment (Figure 7.2 (f)). These consecutive operations result in a narrowing with the desired ratio of the coarctation diameter (D_{CoA}) to descending aorta diameter (D_{DAo}).

Figure 7.3 depicts the thereby obtained evolution of the radius of the maximal inscribed sphere along the aortic centerline (i.e. the largest sphere that is contained entirely in the aortic lumen at a certain centerline point) for different coarctation indices and lengths. The colored zone in this figure represents the coarctation region.

In all cases, the same boundary conditions were adopted, modeling acute cardiac compensation [228]. This allows to isolate the hemodynamic alterations caused by the presence of a local stiffening and/or narrowing. This approach is further supported by [259, 260] reporting a nearly unchanged cardiac output and heart rate after surgically induced stenosis.

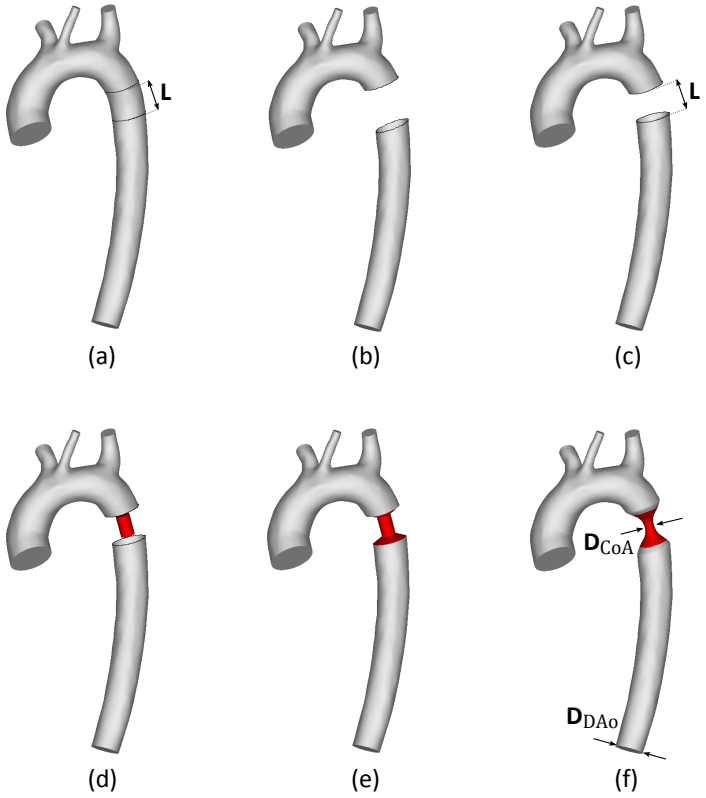

Figure 7.2: Illustration of the consecutive steps performed in 3-matic towards the generation of a model of recurrent CoA.

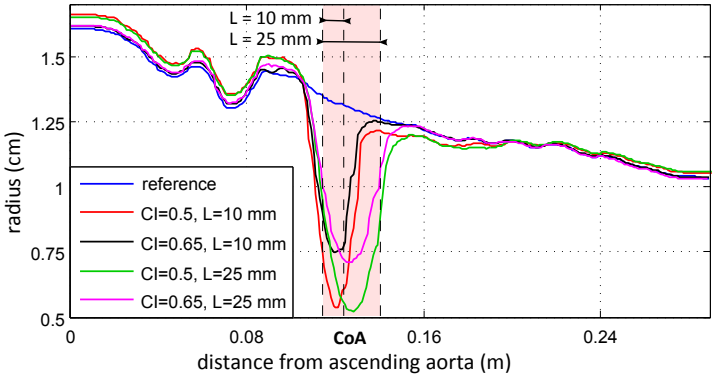

Figure 7.3: Evolution of the radius of the maximal inscribed sphere as a function of the distance from the model inlet (i.e. the ascending aorta).

7.3 RESULTS AND DISCUSSION

7.3.1 Impact of repaired CoA on hemodynamics

7.3.1.1 Impact of repaired CoA on proximal pressure

Figure 7.4 depicts the impact of a local stiffening and/or narrowing on the pressure at the ascending aorta, averaged over the cross section. In the top left panel, the effect of an isolated stiffening is shown for the two worst cases: circular scar tissue with a length of 25 mm (20 times stiffer than the unaffected aortic tissue; black curve) and a 50 mm long stent (red curve). As predicted by the model applied in chapter 6, in which a physiological pressure pulse was imposed as a boundary condition to a straight, flexible tube including a local stiffening, no significant alteration of the proximal pressure is retrieved. Only a small pressure build-up around peak systole is found, rising up to 8 mmHg with increasing stiffening and length. This fairly limited impact was addressed in chapter 6 and is comprehended by the analysis of the wave reflections induced by the stiffening. The backward compression wave generated at the transition from the flexible artery to the rigid segment is roughly canceled out by the expansion waves created at the distal end of the coarctation zone. As such, only local changes in pressure are found, related to the time delay between the backward waves. This finding is in agreement with the 1D studies performed in [241, 242] and the 3D FSI study published in [228], reporting negligible clinical consequences of a local stiffening on cardiac workload and aortic pressure. In [261] an experimental porcine model was developed to investigate the effect of a noncompliant stent. This study supports the conclusions from previous numerical studies, stating that no hemodynamic differences are found in the group with stent versus the reference group without stent.

The effect of a residual narrowing is illustrated in the right top panel of Figure 7.4. Here,

a more pronounced impact, covering the whole systolic phase is observed. A coarctation index of 0.65 increases peak systolic pressure by 10 mmHg (red and green curve), independent of the length of the coarctation zone, whereas an index of 0.5 elevates the load on the heart up to 31 and 41 mmHg for a segment with a length of 10 (black curve) or 25 mm (magenta curve) respectively. This progressive increase in proximal pressure with coarctation length might be explained by (1) the viscous losses which are proportional to stenosis length and inversely related to the coarctation diameter ($\sim D_{CoA}^{-4}$) and (2) the pressure losses due to the unsteady acceleration, which become more pronounced in the stenosis due to the increased velocities and the corresponding accelerations. The longer the stenosis, the more pronounced these latter pressure losses become. Remark that the pressure losses due to the unsteady acceleration should manifest in the slope of the pressure curves, as they are present during systole but become negligible around peak systole. As the slope of the pressure curves are more or less equal in all cases, we can conclude that the additional pressure drop due to the unsteady acceleration is very small.
The combined effect of a narrowing (CI = 0.5) and a stiffening is shown in the charts at the bottom of Figure 7.4. For a short segment (L = 10 mm) an additional stiffening will have a significant impact on the pressure evolution (up to 27 mmHg) whereas the impact for a longer stiffening is relatively limited (up to 9 mmHg). This different response between a short and a long segment might be explained by the difference in wall deformations. In the absence of a local stiffening, the short narrowed segment will experience pronounced deformations up to 29% as it is pulled apart by the proximal and distal part of the aorta. Conversely, for a long segment, these deformations are restricted to 12%. The smaller cross section in the latter case will result in a higher blood velocity and, as a result, in an elevated pressure drop across the coarctation. For a local stiffening (E_{CoA} = 20 E_{Ao}), the distentions of the local narrowing become significantly smaller. A deformation of 3% is retrieved for the short segment and 2.5% for the long segment. The difference in pressure evolution in this case can be explained by the difference in shape of the constriction rather than the difference in cross section (which is nearly equal in both cases). The smaller the divergion of the streamlines distal to the stenosis, the better the pressure recovery will be [148]. As such, a smaller pressure difference between the ascending and descending aorta is found in the case of a long stiffening which is characterized by a more gradual change in diameter.

7.3.1.2 Impact of repaired CoA on pressure drop

The comparison of the pressure distribution along the aorta between the reference case and the most severe case of repaired CoA (L = 10 mm, E_{CoA} = 20 E_{Ao} and CI = 0.5) is made in Figure 7.5 at the time of maximal instantaneous pressure drop (Δp_{max}) between the ascending and descending aorta (indicated in blue and red respectively). This pressure difference is also indicated in the charts on top of this figure and differs from the peak-to-peak pressure difference (Δp_{ptp}) often reported in literature, which is a nonphysiological

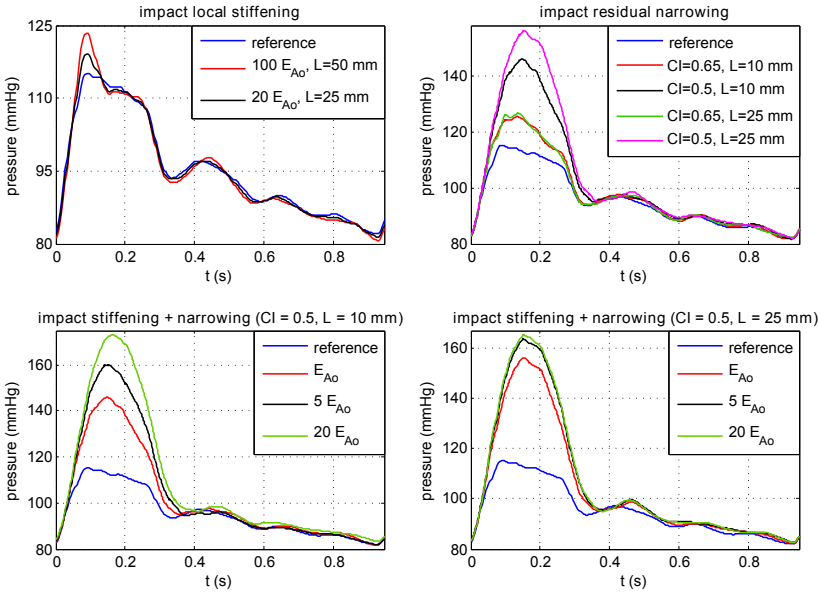

Figure 7.4: Impact of a local stiffening and/or narrowing on the pressure evolution at the ascending aorta as a function of time.

measurement as the maxima at the ascending and descending aorta occur at different points in time. Remark that the timing of Δp_{max} in the reference case and the case of repaired CoA is different.

For the normal aorta, a gradual decrease in pressure along the aortic length can be observed. The dominant factor determining the value of Δp_{max} in the reference case is the inertia of the blood related to the temporal blood acceleration during the systolic phase. In case of recurrent coarctation, the (unsteady) pressure drop adds to a convective acceleration term, caused by an increase in velocity at the transition from the aorta to the stenosis and is proportional to the velocity gradient. This convective acceleration obscures the unsteady acceleration and the associated pressure decrease along the aorta and causes the pressure to fall sharply as the constriction is approached. At the distal end of the coarctation, flow deceleration is accompanied by pressure recovery which, on the other hand, takes place over the entire descending aorta. Nevertheless, the conversion of kinetic energy into pressure is accompanied by energy losses related to turbulence development in the descending aorta. These losses together with the viscous losses explain the enlarged pressure drop (up to 36 mmHg) in case of repaired CoA.

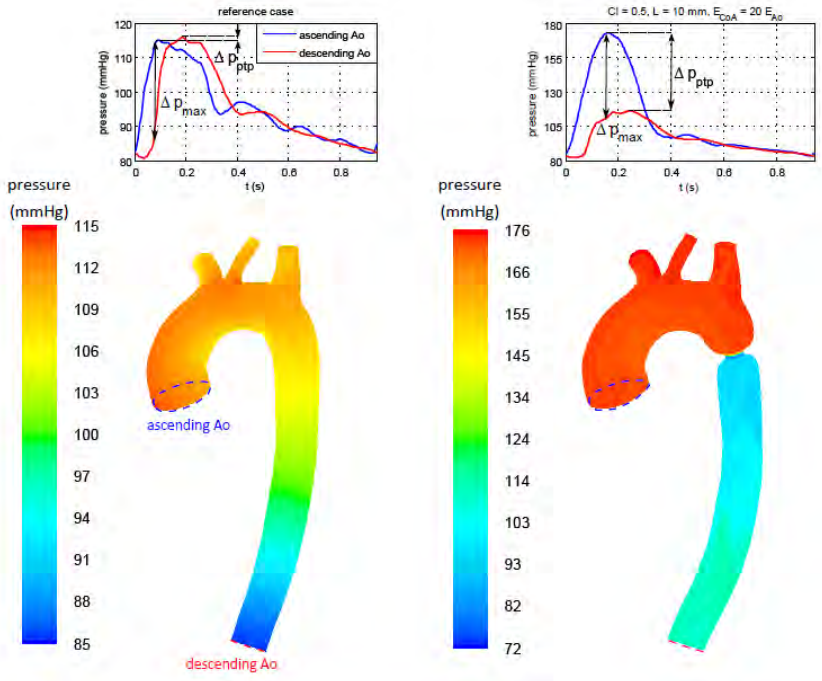

Figure 7.5: Comparison of the maximal pressure gradient in the reference case and in repaired CoA (L = 10 mm, E_{CoA} = 20 E_{Ao} and CI = 0.5).

Figure 7.6 depicts the influence of a stiffening and/or narrowing on Δp_{max}. As the windkessel parameters and the mean flow rate through the descending aorta are the same for the different models, the pressure at this boundary of the fluid domain is very similar for all cases. This explains why Δp_{max} follows the same trends as the ascending aortic pressure (Figure 7.4) around peak systole.

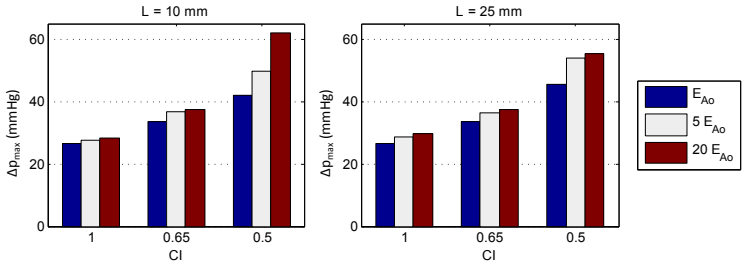

Figure 7.6: Impact of a local stiffening and/or narrowing on the maximal instantaneous pressure difference between the ascending and descending aorta.

The time-averaged pressure along the aorta is depicted in Figure 7.7, in which the location of the coarctation segment is indicated by the colored zone. In a normal aorta, the mean pressure decrease is limited to 0.8 mmHg. This value is mainly determined by two components: the convective acceleration, manifesting as a pressure reduction along the descending aorta as the cross section gradually decreases and velocities increase, and the viscous losses, both of which are insignificant considering the small pressure drop. As the time-averaged pressure evolution is considered, the pressure drop due to the unsteady acceleration will be negligible. As can be seen in the top left panel of Figure 7.7, the inclusion of a local stiffening hardly affects this pressure reduction.
Similar as for the pressure distribution at the time of maximal pressure gradient, a sharp fall of the mean pressure near the constriction is retrieved if a narrowing is present (right top panel). For a coarctation index of 0.65, the mean pressure reduces by 3.8 mmHg across the stenosis. This value further increases up to 9.1 and 11.3 mmHg for a more severe stenosis degree with a length of 10 mm and 25 mm respectively. This pressure drop is accompanied by pressure recovery, persisting through a larger part of the distal aorta. Severe coarctation (CI = 0.5) is characterized by a smaller pressure recovery of 25% and 21% for a length of 10 and 25 mm, whereas mild coarctation results in a recovery of 31%.

Remark that apart from the stenosis severity and geometry, the mean pressure drop and the pressure recovery furthermore depend on flow rate [262–269]. For exercise conditions, for example, an even more distinctive pressure drop will be found and question remains which pressure difference is most clinically relevant: the one that is present during daily

life or the worst case pressure drop, only temporary arising during exercise [270]. This feature suggests that an assessment of stenosis severity cannot be based on the pressure difference alone, but an additional measurement of blood flow is required.

As a second remark, we like to point out that, in this research, a circular symmetrical stiffening and narrowing are applied, mimicking stent implantation or resection by end-to-end anastomosis. Treatment outcomes of other procedures, such as patch aortoplasty or Waldhausen repair (see Figure 5.6 and 5.7) will, however, result in an asymmetrical stenosis and stiffening. In [262], it is demonstrated that this feature manifests in an even larger pressure difference across the stenosis and a worsened pressure recovery in the posterior descending aorta.

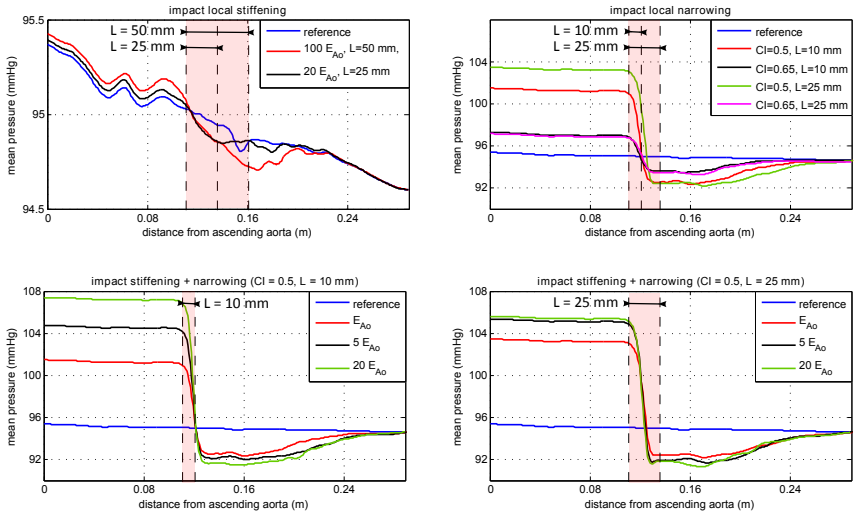

Figure 7.7: Impact of a local stiffening and/or narrowing on the time-averaged pressure evolution as a function of the distance from the model inlet (i.e. the ascending aorta).

7.3.1.3 Impact of repaired CoA on the flow patterns

Figures 7.9, 7.10, 7.11, 7.12, 7.13 and 7.14 show velocity magnitude contour images of the aortic arch at three different time points: peak systole (t = 0.094 s), the time point for which the pressure gradient between the ascending and descending aorta becomes maximal for the case of repaired CoA under consideration (t = 0.174 s) and a time point near the end of systole (t = 0.334 s). Comparison is made between the reference case (Figures 7.9, 7.11, and 7.13), and the worst case (in terms of pressure gradient across the CoA zone) of repaired CoA (CI = 0.5, L = 10 mm, E_{CoA} = 20 E_{Ao}) (Figures 7.10, 7.12 and 7.14). On the right, the corresponding velocity vectors at four locations along the descending aorta

are shown. These figures allow to study the impact of recurrent CoA and residual stiffening on the flow distribution. Note the different scales applied in these figures.
As reported in [201, 271], blood acceleration across the coarctation region generates complex flow distal to the stenosis. The shear layer around the flow jet, leaving the coarctation zone, is marked by a rapid growth of instabilities. Downstream vortices and swirling are produced especially in the deceleration phase, due to the development of turbulence in the expansion zone. The maximal velocity increases from a value of 1.2 m/s in the normal aorta to a value of 4.7 m/s in the repaired CoA and a shift towards the right outer wall is found. Distally, this magnitude decreases and distribution alteration results in a skewed axial velocity profile, characterized by a loss of symmetry and eventually a flow jet impacting on the posterior right outer wall.
This can be seen clearly in Figure 7.8, depicting the axial velocity profile downstream of the coarctation for different stenosis severities. In case of a normal aorta (column on the left) an almost uniform flow distribution throughout the cross sections in the descending aorta is obtained. At the end of the transverse aortic arch (plane a) lower axial velocities are found near the inner wall. These velocities become slightly negative in case a stiffening is included (E_{CoA} = 20 E_{Ao}, L = 10 mm) and result in a small flow separation zone. For a residual narrowing, the negative axial velocities in the two columns on the right of Figure 7.8 indicate the existence of a pronounced separation zone near the inner wall. This zone occupies a large share of the cross section which increases with increasing stenosis severity. Compared with the effect of a narrowing, the impact of a local stiffening is thus fairly limited.

Secondary flows, originating from the curvature of the aorta and the associated centrifugal forces become more significant with the presence of the constriction. These forces push the flow towards the outer wall. An irregular pattern is found if coarctation is present.

7.3.2 Quantification of arterial stiffening and aortic compliance

The aorta in the models of repaired CoA is expected to be less compliant compared to the reference case. Not only will the presence of a local stiffening and narrowing directly impact on the buffering capacity of the aorta in the CoA zone, their presence will also generate a high pressure drop across the coarctation zone, causing the proximal part to be subjected to much higher pressure levels. Since the arterial wall behaves in a hyperelastic way, these elevated pressures induce arterial stiffening and thus implicitly decrease the compliance of the proximal aorta. This nonlinear behavior is illustrated in Figure 7.15, showing the compliance-pressure relation of the 3D aorta model retrieved from static finite element simulations. Pressurizing the aortic wall from a level p to a level $p + \Delta p$ increases the model volume with ΔV. This allows to calculate the compliance as the ratio of the volume change ΔV to the pressure increase Δp. Both phenomena of compliance reduction

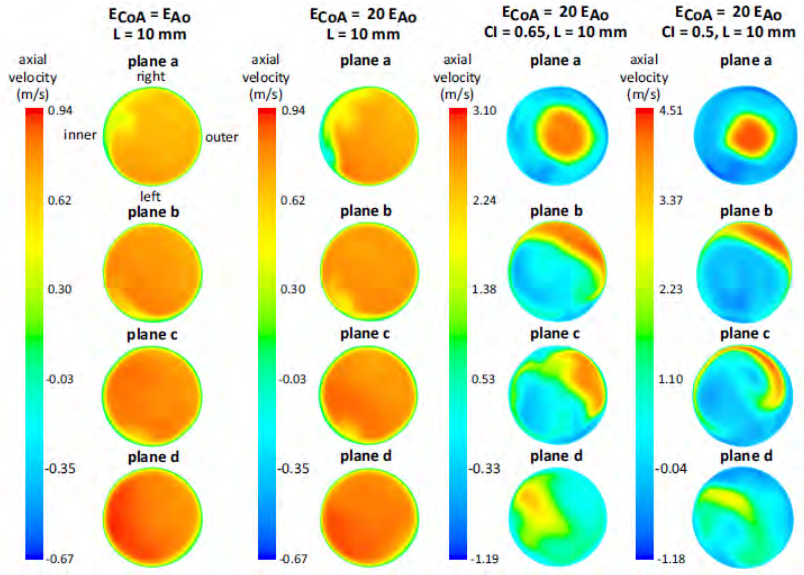

Figure 7.8: Contourplot of the axial velocity component in multiple planes along the descending aorta for different stenosis degrees (see Figure 7.13 for an indication of the plane locations). Note that the colormaps are different for each column.

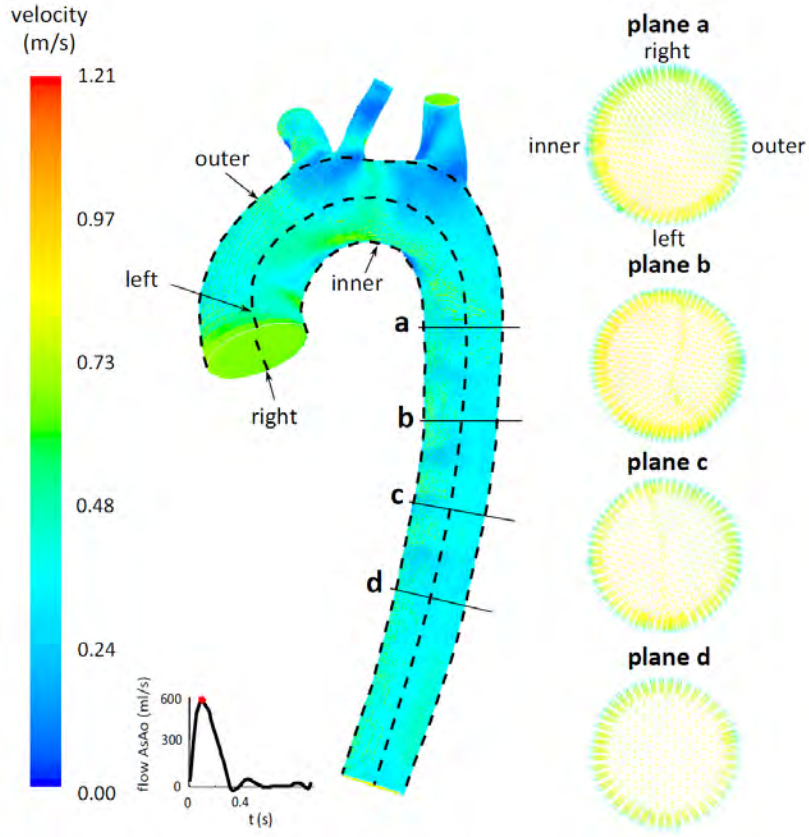

Figure 7.9: Contourplot of the velocity magnitude and corresponding velocity vectors along the descending aorta at peak systole (t = 0.094 s) (reference case).

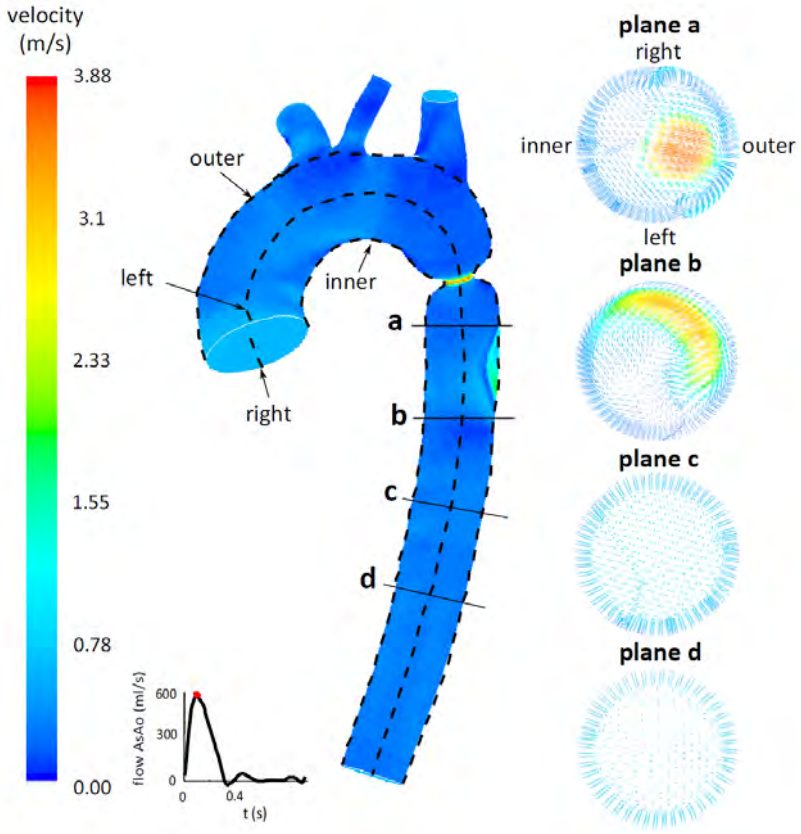

Figure 7.10: Contourplot of the velocity magnitude and corresponding velocity vectors along the descending aorta at peak systole (t = 0.094 s) (CI = 0.5, L = 10 mm, E_{CoA} = 20 E_{Ao}).

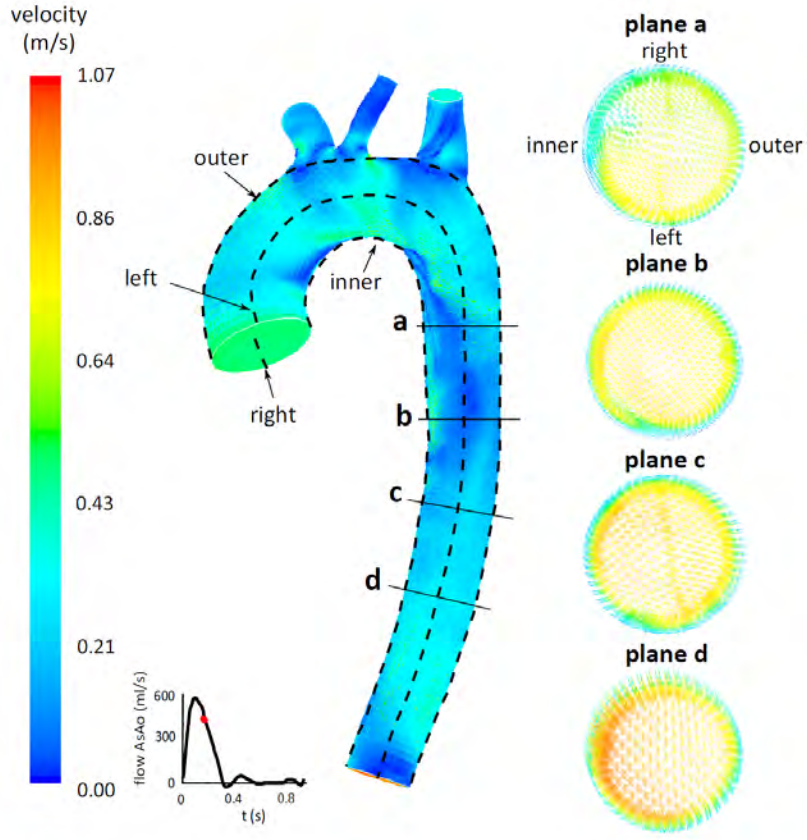

Figure 7.11: Contourplot of the velocity magnitude and corresponding velocity vectors along the descending aorta at t = 0.174 s (reference case).

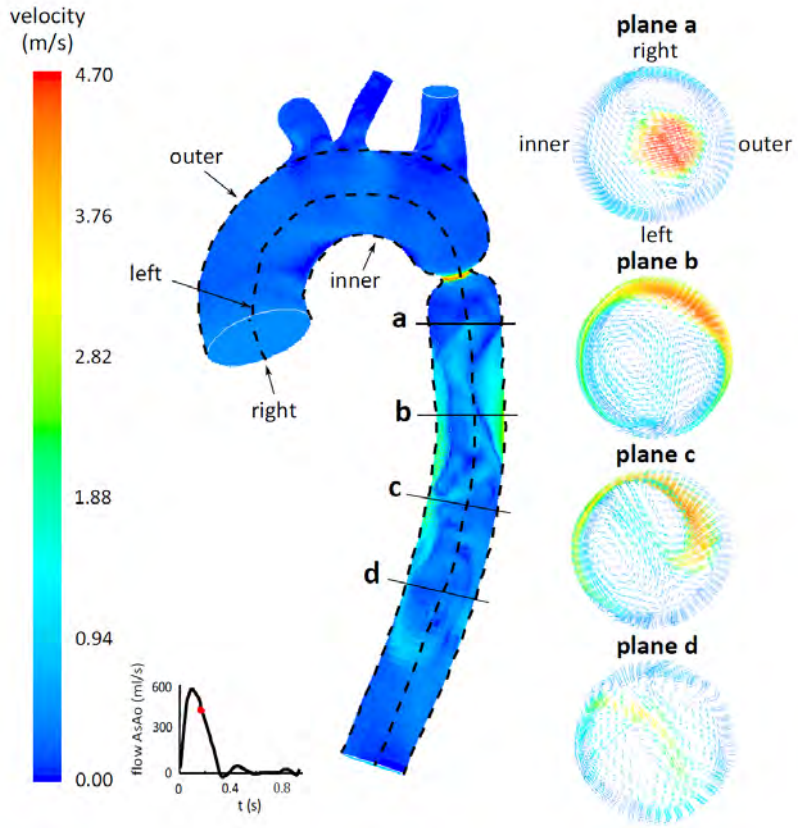

Figure 7.12: Contourplot of the velocity magnitude and corresponding velocity vectors along the descending aorta at t = 0.174 s, the time point for which the pressure gradient between the ascending and descending aorta becomes maximal (CI = 0.5, L = 10 mm, E_{CoA} = 20 E_{Ao}).

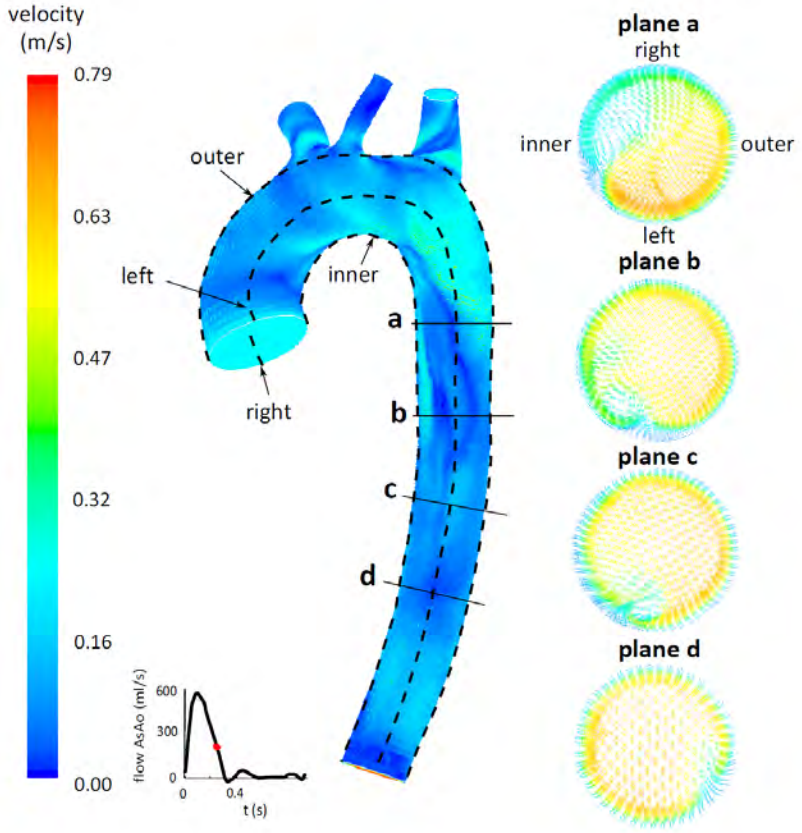

Figure 7.13: Contourplot of the velocity magnitude and corresponding velocity vectors along the descending aorta at t = 0.334 s (reference case).

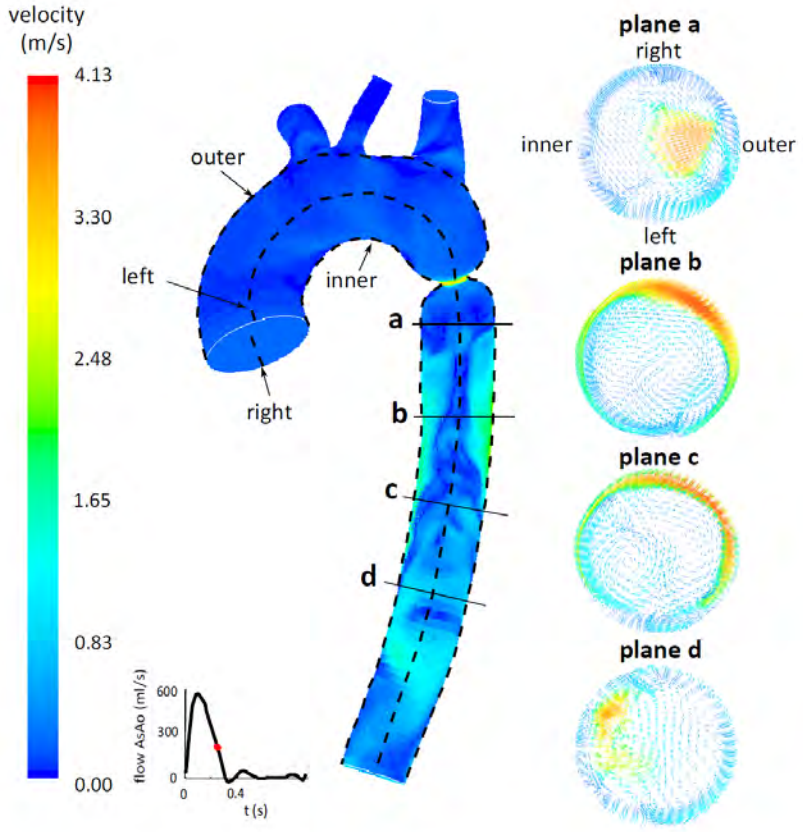

Figure 7.14: Contourplot of the velocity magnitude and corresponding velocity vectors along the descending aorta at t = 0.334 s (CI = 0.5, L = 10 mm, E_{CoA} = 20 E_{Ao}).

are demonstrated in Figure 7.15: (1) for a certain pressure level, the presence of a narrowing or a stent result in a somewhat decreased compliance, (2) for the individual models a significant reduction in compliance is found with increasing pressure. Remark that the absolute value of the compliance depends on the volume of the model applied in this study. Indeed, a lager volume would result in an elevated ΔV and, consequently, in an increased compliance. Emphasis is, however, put on the tendencies revealed by these simulations rather than the absolute compliance values.

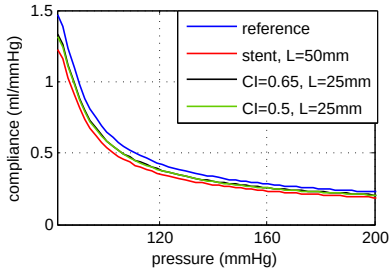

Figure 7.15: Aortic compliance as a function of pressure obtained from static finite element simulations (E_{CoA} = 20 E_{Ao} for the models with recurrent CoA and E_{CoA} = 100 E_{Ao} for the model including the stent).

To quantify the increase in stiffening proximal to the CoA zone, the stiffness index β [148, 257] is calculated by

$$\beta = \frac{\ln(p_{max}/p_{min})}{(D_{max} - D_{min})/D_{min}} \tag{7.1}$$

where p_{max} and p_{min} correspond to the systolic and diastolic blood pressure retrieved from the FSI simulations and D_{max} and D_{min} to the maximal systolic and minimal diastolic internal diameters respectively. Figure 7.16 depicts the stiffness index at the ascending aorta. Although the same material properties were used in this section of the aorta (both for the reference case and the repaired CoA models) an increase in β stiffness can be observed with increasing degree of stenosis severity (i.e. decreasing CI). This increase is fully ascribed to the increased proximal pressure and the corresponding hyperelastic wall behavior. The stiffening and the length of the coarctation segment have only a small impact on the β values of the ascending aorta.

7.3.3 Comparison of Doppler predicted pressure drops with peak-to-peak values

As pointed out in section 5.2, Doppler echocardiography is considered the gold standard for the noninvasive assessment of coarctation severity. In Figure 7.17 the Doppler predicted pressure drop ($\Delta p_{doppler}$) is shown for different cases of repaired CoA and is compared

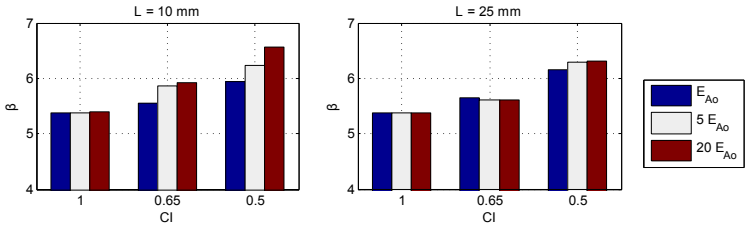

Figure 7.16: Impact of a local stiffening and/or narrowing on the stiffness index β at the ascending aorta.

with the peak-to-peak pressure drop (Δp_{ptp}) between a plane proximal to the CoA zone (plane a in Figure A.1 of the appendices) and the descending aorta. We refer to Figure 7.5 for a definition of Δp_{ptp}.

The main principle behind the prediction of pressure drops using Doppler velocities, is the conservation of energy, stating that potential energy is converted to kinetic energy as the flow accelerates through the stenosis. Using Eq. 7.2, velocities measured proximal to (v_P) and at the constriction site (v_{CoA}) itself can provide an estimate of the pressure difference across the coarctation zone.

$$\Delta p \approx 4(v_{CoA}^2 - v_P^2) \tag{7.2}$$

In this equation the pressure drop is expressed in mmHg an the velocities in m/s. This equation neglects the distal pressure recovery, in which kinetic energy is restored into potential energy and assumes 100% dissipation of the kinetic energy in the distal part (as would be obtained for a flow jet released in free space). The sudden transition of flow from a tube with a small section to a larger one is characterized by energy losses associated with the development of turbulence in the expansion zone [264, 272]. The magnitude of this dissipated energy depends on several factors, including stenosis geometry, severity and flow rate [263–269]. The more energy is dissipated by turbulent losses, the less pressure recovers and the better $\Delta p_{doppler}$ corresponds to Δp_{ptp}. In contrast to a sharp stenosis, a smooth divergion of the streamlines distal to the stenosis will result in a good pressure recovery and an bad agreement between $\Delta p_{doppler}$ and Δp_{ptp}. Overall, a progressive overestimation of Δp_{ptp} is found with increasing diameter (from CI = 0.5 to 0.65) and with stenosis length reduction (from L = 25 to 10 mm) (see Figure 7.17 bottom).

Previous studies [146, 148, 152–157] have investigated the errors made using the Doppler velocity information in the estimation of the pressure drop. Consistent with the results shown in Figure 7.17, these publications report an important overestimation of the actual pressure difference in the post-operative case, which might result in a false positive diagnosis of recurrent coarctation.

Remark that, as the pressure recovery takes place along a considerable part of the distal aorta, the position of the catheter or transducer determining the pressure drop will affect the measured pressure difference. Whether the pressure difference including the pressure recovery is of greater clinical significance than the maximal pressure drop at the constriction itself remains, nevertheless, unclear and should be subject of further research.

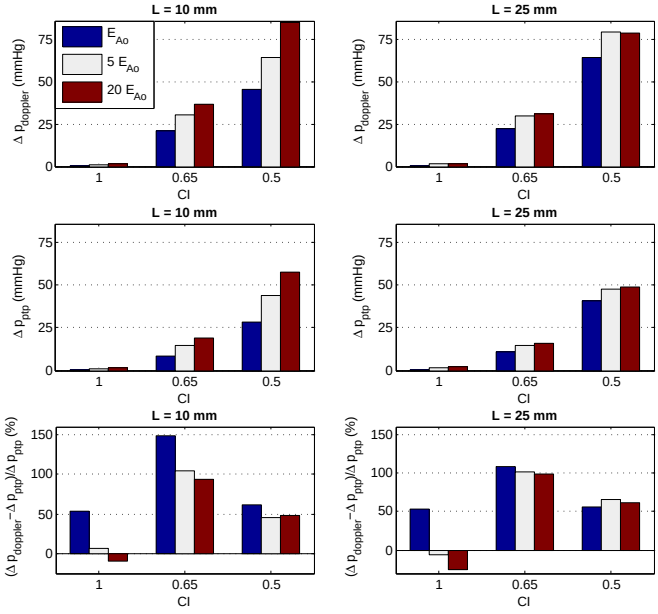

Figure 7.17: Comparison of the Doppler predicted pressure drop ($\Delta p_{doppler}$) and the peak-to-peak pressure drop (Δp_{ptp}) between a plane proximal to the CoA zone (plane a in Figure A.1) and the descending aorta as a function of the coarctation index, the stiffness and the length of the coarctation segment.

7.3.4 Wave separation and wave intensity analysis: study of wave reflections

As explained in section 6.2.2, the pressure wave p and velocity wave v at the ascending aorta are decomposed into their forward (+) and backward (-) propagating components (see Figure 7.18). These waves propagate with a speed $v + c$ and $v - c$ respectively, in which v represents the blood velocity and c the wave speed related to the elastic properties of the artery.

For a normal aorta, a dominant forward wave is present. As opposed to this forward wave, the backward wave is relatively small and arrives in late systolic phase where it persists during most of the diastolic phase. This backward wave is the resultant of discrete reflections, generated at the branching of the aorta and the distal boundaries of the fluid domain and

scattered wave reflections, caused by the tapering of the aorta.
The impact of a local stiffening (E_{CoA} = 100 E_{Ao}, L = 50 mm) and narrowing (CI = 0.5, L = 25 mm) on the generated wave reflections is shown in Figure 7.18 (middle and right column). In agreement with the results obtained in chapter 6, a local stiffening has almost no effect on the hemodynamic response. Only a small peak in the backward component (BCW) can be distinguished. At the ascending aorta (i.e. the proximal boundary of the fluid domain), this BCW re-reflects as a forward compression wave, which elucidates the small increase in p_+ and v_+ compared with their reference values.

The presence of a narrowing, on the other hand, manifests in a much more pronounced BCW compared with the one generated by a local stiffening and the one present in a normal aorta. Remark that the depicted forward and backward waves represent the resultant waves, which in fact consist of multiple discrete and scattered (re-)reflections. In the appendices an analysis of the successive generated wave reflections is provided. This decomposition enhances the understanding of the presence of an important BCW, persisting through the whole systolic phase. As for the model including the stiffening, this BCW re-reflects at the ascending aorta, resulting in an enlarged forward pressure wave. This forward wave p_+ adds up with the marked backward wave p_- to obtain the resultant wave p. Given the short distance to the heart, the BCW reaches the heart in early systole, leading to a pressure increase up to 41 mmHg compared with the reference case. The local narrowing thus manifests as an additional workload on the heart which might increase the risk of cardiovascular disease.

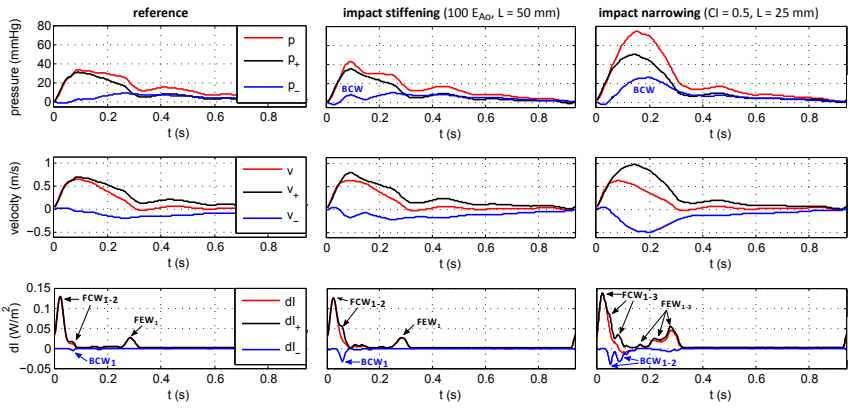

Figure 7.18: Impact of a local stiffening and narrowing on the backward (-) and forward (+) waves (top and middle) and the corresponding wave intensity dI.

Figure 7.19 illustrates the effect of a coexisting narrowing and stiffening on the resultant forward (indicated with a full line) and backward waves (dotted line). The amplitude of both

the forward and backward waves increase with increasing stenosis severity. As enlightened in the previous results, only for a short segment (L = 10 mm), an additional stiffening will have a considerable impact on the generated reflections.

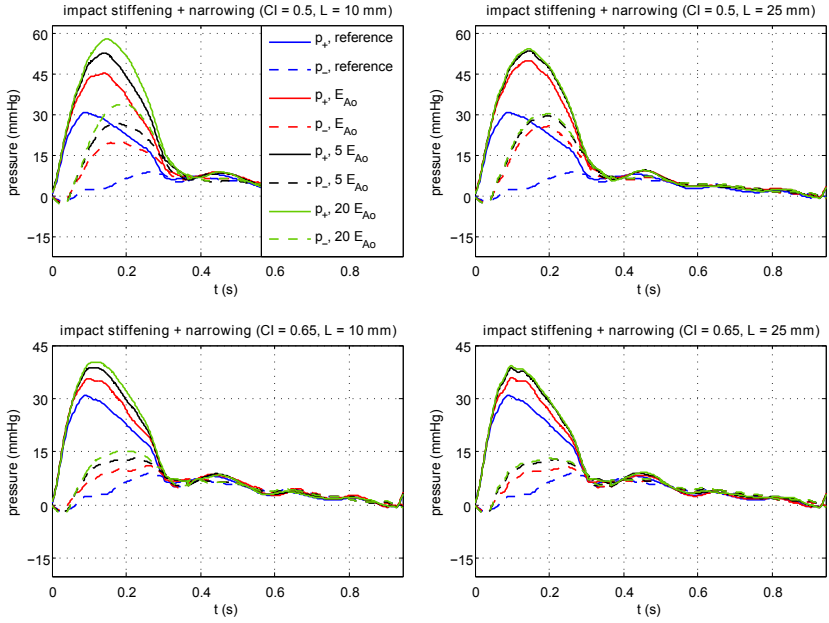

Figure 7.19: Impact of a local stiffening and/or narrowing on the forward p_+ and backward p_- waves.

More simplified, the hemodynamic impact of the distal aorta and the repaired coarctation zone can be represented by a single reflection site with a reflection magnitude RM. The reflection magnitude is given as the ratio of the amplitudes (i.e. the magnitude of the difference between the variable's extreme values) of the backward and forward propagating waves. The reflection magnitude calculated as such is shown in Figure 7.20, which elucidates the impact of the CoA through one single parameter. A narrowing increases the reflection magnitude up to 7% and 72% for a coarctation index of 0.65 and 0.5 respectively. For the most severe stenosis, an additional stiffening enlarges this number to 92%.

An alternative way to study wave propagation and reflection is provided by wave intensity analysis. This technique regards the waveforms p and v as the summation of successive wavefronts with a magnitude dp and dv. The net wave intensity (dI) given by $dp.dv$ represents the flux of energy, transported by the wavefronts. This property is positive in case of a dominant forward wave and negative for a dominant backward wave (see Table 7.2).

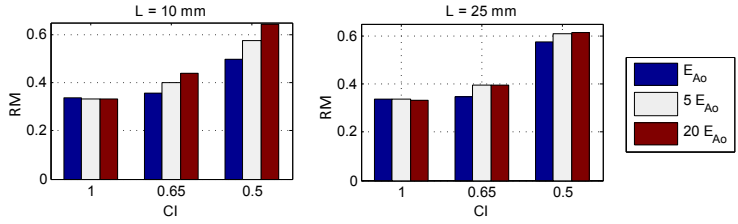

Figure 7.20: Impact of a local stiffening and/or narrowing on the reflection magnitude, defined as the ratio of the amplitudes of the forward and backward pressure wave.

As such, this method allows for an easy quantification of the direction, magnitude and timing of the waves present in the arterial system at a particular location and time during the cardiac cycle [239].

Figure 7.18 (bottom) depicts the wave intensity for the reference case (left), an aorta including a local stiffening (E_{CoA} = 100 E_{Ao}, L = 50 mm) (middle) and a model of recurrent coarctation (CI = 0.5, L = 25 mm) (right). Apart from the net wave intensity (dI, indicated in red), the wave intensity of the forward (dI_+, shown in black) and backward waves (dI_-, depicted in blue) is shown. Remark that the magnitude of dI depends on the sample frequency of the pressure and velocity wave. A sample interval of 4 ms is used to retrieve the results, illustrated in Figure 7.18.

In this figure, the first peak of dI (FCW_1) is related to the initial compression wave generated by the contraction of the left ventricle at the beginning of the systolic phase. For a normal aorta, this initial wave is reflected throughout the arterial tree and rearrives at the ascending aorta in mid-systole as a backward compression wave (BCW_1). Note that this peak is not visible in dI, as a dominant forward wave exists, masking the reflection. At the inlet of our model, this wavefront is re-reflected, resulting in the second peak in dI_+ (FCW_2). This is followed by a third positive peak (FEW_1), indicating a decompression at end-systole, caused by the relaxation of the left ventricle (both p and v are falling at that time in the cardiac cycle).

In case of a local stiffening, an increase of BCW_1 is found, caused by the reflection of the compression wave at the rigid segment. Although a more pronounced backward wave is obtained in this case, the dominant forward wave obscures the arrival of this wavefront and leads to a positive net wave intensity.

Compared with the reference case, an elevated forward compression wave (FCW_1) is required if a local narrowing is included to overcome the pressure drop across the coarctation zone. This FCW_1 reflects at the stenosis site as a backward compression wave (BCW_1), reaching the ascending aorta with a time delay of 0.034 s (i.e. the time needed for the wave to travel back and forth between the model inlet and the stenosis). The BCW_1 re-reflects at

	dp	dv	dI
forward	> 0 compression	> 0 acceleration	> 0 positive
	< 0 decompression	< 0 deceleration	
backward	> 0 compression	< 0 deceleration	< 0 negative
	< 0 decompression	> 0 acceleration	

Table 7.2: Overview of the relationship between the change in pressure and velocity for forward and backward waves [239].

the inlet, creating the forward wave FCW_2, which re-reflects at the constriction site as the backward compression wave BCW_2. This phenomenon repeats until the associated wave-front magnitudes become insignificant. In contrast with the previously discussed cases, the backward wave is eventually revealed by a negative net wave intensity ($dI < 0$). However, the timing and magnitude of this negative net wave intensity do not correspond with the arrival time and amplitude of the backward waves (BCW_1 and BCW_2) and could thus provide misleading information regarding the nature of the reflected wave and the distance to the reflection site. An evaluation of CoA severity based on the net wave intensity alone, would therefore result in a considerable underestimation of the backward compression wave and the associated obstruction significance.

After the contraction, the heart relaxes again, resulting in the forward expansion waves FEW_{1-3}. These peaks are also present in the reference case, but, especially FEW_{1-2} are far less pronounced. The forward expansion waves reflect at the stenosis region as backward expansion waves (BEW).

7.3.5 Comparison with other studies - impact of model assumptions

7.3.5.1 Impact of rigid wall modeling

An important feature of the aorta is its capacity to buffer blood during systole and sustain blood flow to the rest of the body during diastole. As approximately 60% of the buffer capacity of the aorta is located in the proximal aorta [243], the presence of (repaired) CoA might affect this property. Inclusion of this characteristic hallmark in the numerical model is thus necessary in order to quantify the disease severity correctly. Most CoA studies [138, 161, 201–203, 207, 229] are, however, performed under a rigid wall assumption.

That this oversimplification may corrupt insights and provide an incorrect diagnosis of CoA severity is illustrated by Figure 7.21. This figure compares the pressure drop and the velocity along the centerline of the aorta with recurrent coarctation obtained with a rigid wall simulation to the ones obtained using a flexible wall simulation. For the FSI simulations results are shown at two different times during the cardiac cycle. The red curve is obtained at peak systolic inflow (t = 0.094 s), whereas the black curve is retrieved at the time point

where the flow at the constriction site and thus, the pressure gradient becomes maximal (t = 0.174 s).

The CFD simulation strongly overestimates CoA severity as both the pressure drop across the coarctation (101 versus 57 mmHg) and the pressure difference between the ascending and descending aorta (62 versus 44 mmHg) are amplified. This substantial mismatch is related to the lack of compliance in the CFD simulation, which is responsible for the buffering and damping of the pressure pulse in the proximal aorta. Accordingly, velocities in the coarctation zone and the associated pressure drop exceed the ones reported in the FSI simulation. Increased aortic compliance will enhance this effect as it results in an enlarged dilation of the proximal aorta in systole and a further accumulation of stored upstream energy, which is released downstream in diastole. Also the amount of recovered pressure is overestimated by the CFD simulation (39 versus 23%), especially in the divergent section of the stenosis, a location where no recovery occurs in the FSI case. The diminished turbulent losses partially compensate the overestimation of the pressure drop across the CoA. This might explain the moderate agreement between measured pressure differences and the ones retrieved with rigid wall models [161]. Overall, the results shown in Figure 7.21 call for a fluid-structure interaction approach in the determination of pressure drops across the CoA using computational models.

7.3.5.2 Impact of reduced order modeling

A second simplification that should be treated with caution is the use of reduced order models in the assessment of pressure gradients [152], wave travel and reflection in aortic coarctation. To demonstrate the pitfalls associated with this approach, we refer to Appendix A at the end of this dissertation where the wave reflections generated by a local stiffening and narrowing are computed both with a full 3D FSI model and using theoretical reflection and transmission coefficients, deduced for the 1D flow in a flexible artery [273]. From this study, we conclude that the 1D theory accurately predicts the wave reflections generated by a local stiffening, but fails to capture the reflections correctly in case of a severe stenosis. This poor performance is explained by the flow patterns observed after recurrent narrowing which become very nonuniform (see Figure 7.8).

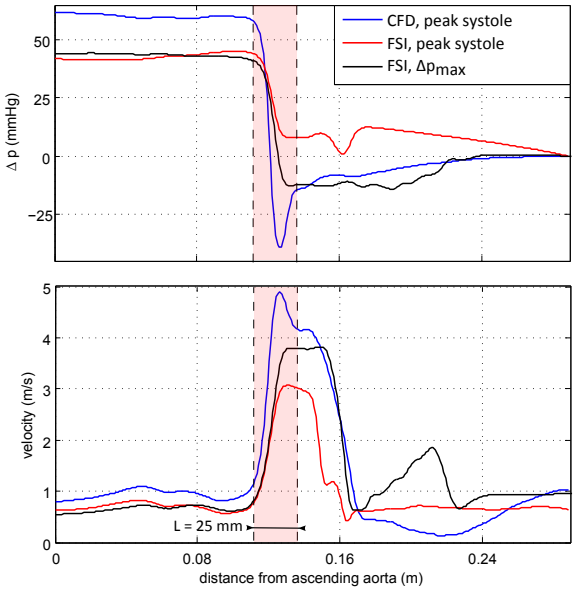

Figure 7.21: Comparison of the pressure drop (viewed from the descending aorta) and velocity along the aortic arch centerline obtained with a rigid wall simulation (CFD) and a flexible wall model (FSI) of recurrent coarctation (L = 25 mm, $E_{CoA} = E_{Ao}$ and CI = 0.5). The blue and red curve are obtained at peak systole (i.e. maximal inlet flow), the black curve is generated at a time point at which the pressure drop across the aortic arch reaches its maximum.

7.4 LIMITATIONS

As pointed out in section 7.2, the same boundary conditions were imposed in all cases, regardless of coarctation severity. This approach allows to isolate the hemodynamic alterations caused by the presence of repaired CoA and approximates the autoregulatory mechanisms of the cardiovascular system. The assumption of a constant cardiac output in (repaired) CoA implies an increased workload on the heart and is justified by the findings reported in [259, 260], stating that the cardiac output and the heart rate barely change after surgically induced stenosis. We, however, believe that, due to the elevated resistance at the coarctation site an early redistribution of flow will take place, manifesting as an increased flow through the subclavian and carotid arteries and a reduction of the descending aortic flow [228]. This was not accounted for in this study. Application of reduced order models at the distal boundaries of the fluid domain might resolve this problem. Since the pressure drop across the CoA is proportional to the flow rate through the constriction, the flow distribution adopted in our models represents the worst case distribution, associated with the highest pressure gradients.
Similar, the disregardance of the collateral network, bypassing part of the flow through the coarctation, will result in an overestimation of the actual pressure drop.

Another limitation of this research involves the lack of (viscoelastic) tissue surrounding the aorta [274]. As such, no physiological mechanism is present to damp the high frequency oscillations of the vessel wall. This explains, for example, the pressure and velocity wiggles along the descending aorta, observed in Figure 7.21 (black curve). Nevertheless, the highest frequency components will be damped due to numerical dissipation, related to the temporal discretization of the problem under consideration.

Alterations of the pressure evolution along the aorta and the coarctation affect the homeostatic mechanical state of the aorta. In response to these alterations, vascular growth and remodeling take place [220, 275, 276]. These adaptions include both changes in shape and material properties. In particular for the case of aortic coarctation, wall thickening is often observed along with a decrease in compliance of the proximal aorta due to prolonged hypertension [198, 221–225, 228, 229, 277]. Arterial remodeling in turn will modify the hemodynamic response. Although the stiffening of the arterial wall due to increased pressure is accounted for in the hyperelastic behavior of the wall, no actual solid-growth coupling is performed in this research. This might affect the long-term outcome associated with the presence of a stiffening and narrowing.

7.5 CONCLUSION

It is demonstrated that fluid-structure interaction modeling plays a significant role in the correct assessment of CoA severity. Buffering of the blood flow in the proximal aorta

damps out the pressure pulse and reduces the velocity in the constriction and the correlated pressure difference.
In the distal part of the aorta, the presence of a narrowing results in a highly nonuniform flow and the development of vortices. These observations question the use of 1D models in the prediction of stenosis-induced pressure drops and wave reflections.

In agreement with the results reported in chapter 6, it is found that the impact of an isolated stiffening on the hemodynamic response is fairly limited. Local changes in peak systolic pressure up to 8 mmHg are retrieved, whereas the flow distribution in the aorta and the mean pressure drop along the aorta remained more or less constant (0.8 mmHg). These simulation results are explained by the analysis of the wave reflections induced by the stiffening. The BCW, generated at the transition from the aorta to the stiffening, is almost completely compensated by the sequence of BEWs, created at the distal end of the stiffening. The resulting alterations of the hemodynamic quantities at peak systole are associated with the time delay between the respective backward waves.
Regarding the threshold for intervention, a peak-to-peak pressure difference of 20 mmHg between the upper and lower limbs is often used as an intervention criteria. This threshold compromises between the risks and benefits associated with treatment. Patients with mild coarctation are subjected to long-term hypertension or may require lifelong antihypertensive treatment. In addition, the blood pressures emerging during exercise will be much more pronounced than the ones appearing at rest [278, 279]. The success of noninvasive stent implantation in patients with more severe CoA, conjoined with the limited impact on the hemodynamic response may call for a revision of the threshold for intervention [280].

With respect to the presence of a residual narrowing, blood pressure alterations in the proximal aorta are much more pronounced, covering the whole systolic phase and are dominated by the convective acceleration across the CoA. This pressure drop is followed by pressure recovery persisting in a larger part of the descending aorta. Severe coarctation is characterized by a smaller pressure recovery (i.e. a larger energy dissipation due to the development of turbulence). For a short constriction (L = 10 mm) an additional stiffening will have a significant impact on the pressure evolution (up to 27 mmHg) whereas the impact for a longer stiffening (L = 25 mm) is relatively limited (up to 9 mmHg).

An evaluation of CoA severity based on the net wave intensity alone results in a considerable underestimation of the backward compression wave generated by the presence of a narrowing and provides misleading information regarding the distance to the reflection site.

CHAPTER 8

The aortic reservoir-wave as a paradigm for arterial hemodynamics: insights from 3D fluid-structure interaction simulations in a model of aortic coarctation

8.1 INTRODUCTION

The physiological interpretation of arterial pressure waveforms is still not fully understood. The waveform arises from the dynamic interaction between the heart and a complex 3D arterial network, and integrates effects of the dynamics of blood flow, wave travel and reflections. The complexity of the arterial tree, with its progressive branching and continuous change in geometric and mechanical properties gives rise to discrete and diffuse reflections and re-reflections, which superimpose and shape the waveform as measured when sampling the pressure using, for instance, a pressure catheter in the aorta [281, 282].

In order to allow for the interpretation of arterial hemodynamics, models or 'paradigms' can be used, providing a more tangible way to assess and quantify the relation between arterial physiology and the measured waveforms. Since a few years, a new paradigm has been put forward, where the pressure and flow waves are considered as the superposition of a 'reservoir pressure', directly related to changes in reservoir volume, and an 'excess pressure' which is ascribed to wave dynamics [230, 283]. We previously argued that the basic reservoir-wave model is, in essence, the time-domain equivalent of the 3-element windkessel model, a lumped parameter model of the arterial tree [284]. Together with others,

we also made a call for caution of over-interpretation of, especially, the excess pressure [285, 286]. In particular, the subtraction of a reservoir pressure from the aortic pressure waveform to yield the excess pressure significantly alters the interpretation of wave dynamics. Whether or not this approach leads to flawed insights (due to presumed suppression of compression waves and magnification of expansion waves) is still a matter of scientific debate [287, 288].

The data-set generated in chapter 7 is further applied in this study. Where the many interfering factors and adaptive physiologic mechanisms present in vivo prohibit the study of the isolated effect of these individual factors, our computational models provide clinically relevant insights which are impossible to obtain in an in vivo setting. The simulations not only account for the complex 3D anatomy of the aortic arch and descending aorta; they also respect the distensibility of the aorta and incorporate all aspects of fluid and wave dynamics. These data thus provide highly detailed 3D information on instantaneous changes in pressure, flow (velocity) and aortic dimensions, and may thus provide the perfect testing ground to assess the nature of the arterial reservoir pressure. The principal aim of this study is therefore to apply the reservoir-wave paradigm to the aortic pressure and flow waves generated in the 3D fluid-structure interaction simulations and to critically evaluate their performance in a controlled setting - with direct access to gold standard information - where we explicitly impact on both the reservoir and the conduit function of the aorta.

8.2 MATERIALS AND METHODS

8.2.1 3D model of the aorta - fluid-structure interaction simulations

For a detailed description of the reference model and the models of repaired coarctation, we refer to chapter 4 and 7. Four simulations from the data-set presented in chapter 7 were selected and are indicated in Figure 8.1:

(i) In the first case the geometric model as extracted from the MRI data was considered and uniform material properties were applied throughout the aortic wall (Figure 8.1, panel A). This simulation predicts normal aortic hemodynamics and is used as a reference for the other simulations.

(ii) Secondly, the impact of a stent on the hemodynamic response is modeled by including a 5 cm long segment, behaving 100 times stiffer than the unaffected aortic tissue (Figure 8.1, panel B). As approximately 60% of the buffer capacity of the aorta is located in the proximal aorta [243], this local stiffening reduces the 'cushioning function' of the aorta and might account for the increased morbidity observed after 'successful' CoA treatment.

(iii) Next, the effect of recurrent coarctation is modeled. Once recoarctation has developed, the increased arterial impedance will disturb the blood flow and alter hemodynamics,

which has been suggested to play an important role in the progression of cardiovascular malfunctioning [11]. In the third case a coarctation index ($CI = D_{CoA}/D_{Ao}$) of 0.65 is studied (Figure 8.1, panel C). To mimic the presence of the scar tissue after surgery, the wall in the stenosed region (length of 25 mm) was assumed to be 20 times stiffer than the rest of the aortic tissue [148].

(iv) Finally, severe recoarctation ($CI = 0.5$) was studied (Figure 8.1, panel D). The same length and material properties were adopted as in the previous case.

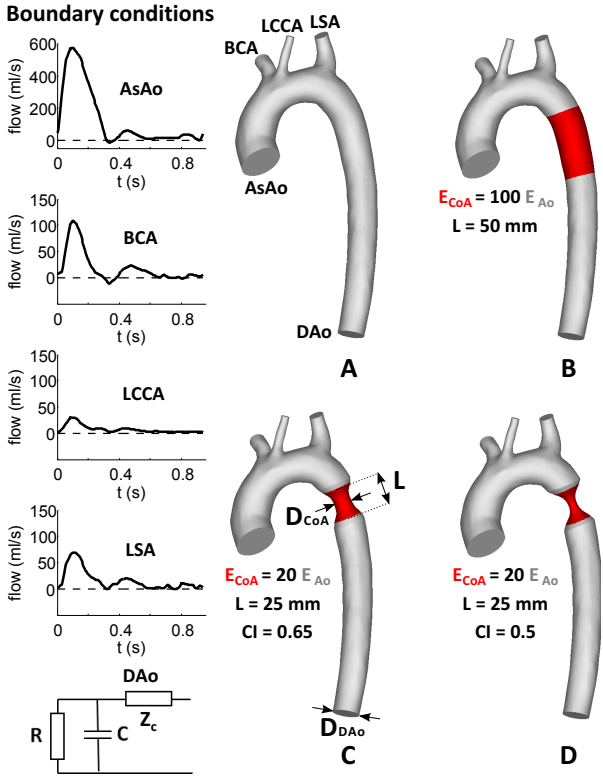

Figure 8.1: Methodological figure (setup(s)) and boundary conditions. Panel A: model of a normal aorta, panel B: model of aortic coarctation treated with an endovascular stent, panel C and D: model of a surgically treated aortic coarctation with recurrent coarctation, characterized by the coarctation index ($CI = 0.65$ and 0.5 resp.).

The FSI simulations provide waveforms of pressure (P_{ao}) and flow (Q_{ao}) in the ascending aorta (and in the complete fluid domain) for the 4 cases considered. P_{ao} is calculated as the average pressure over the cross-section; Q_{ao} is the flow across this cross-section. In addition, the intra-aortic volume $V_{ao}(t)$ is directly calculated from the changes in the model

volume as a function of time (which equals the difference between in- and outflow of the model).

8.2.2 Deriving aortic pressure from intra-aortic volume: P_{ao-vol} as aortic reservoir pressure reference

While the great value of the fluid-structure interaction simulations is that they capture all aspects of intra-aortic hemodynamics, wave travel and reflection, they do not allow to retrieve the intrinsic relation between pressure and aortic deformation as one would, for instance, retrieve from an ex vivo inflation experiment on an excised aorta, independent of pressure effects which are due to the motion of blood (see also further). We therefore performed separate finite element model simulations (Abaqus Standard, SIMULIA) on the four geometries, where the aortic models were statically loaded over the pressure range 75 to 225 mmHg to fully cover the range of pressure encountered during the FSI simulations. These simulations provide the relation between intra-aortic pressure and volume, which allows to mathematically assess the intrinsic P-V relation of the aortic model (via a second-order regression equation). This relation will then be used to translate the changes in intra-aortic volume (what we consider as the aortic reservoir) from the full fluid-structure interaction simulations into the associated pressure, P_{ao-vol}.

8.2.3 The reservoir-wave concept: reservoir and excess pressure

The reservoir pressure $P_{res}(t)$ was calculated following [230, 289] and was applied previously in [284] assuming a zero venous pressure value, which leads to the following equations:

$$P_{res}(t) = P_{res}(T_N)e^{-b(t-T_N)}, \qquad T_N \leq t \leq T \tag{8.1a}$$

$$P_{res}(t) = e^{-(a+b)t}\left[\int_0^t aP_{ao}(t')e^{(a+b)t'}dt' + P_{res}(0)\right], \qquad 0 \leq t \leq T_N \tag{8.1b}$$

with T the duration of the cardiac cycle, T_N the end of systole (dicrotic notch) and a and b rate constants of the system. The dicrotic notch was visually identified on the pressure waveform. $P_{res}(T_N)$, a and b were determined by fitting Eq 8.1a and requiring continuity at $P_{res}(T_N)$ using an unconstrained non-linear optimization routine (fminsearch) in Matlab (The Mathworks, Natick, MA), minimizing the sum of squares of the error between fitted and measured pressure data. $P_{res}(0)$, the reservoir pressure at t = 0, is assumed equal to the aortic pressure at the onset of systole. Finally, P_{res} was determined for the entire period using Eq 8.1a and 8.1b. The excess pressure, $P_{exc}(t)$ was subsequently derived as

$$P_{exc}(t) = P_{ao}(t) - P_{res}(t) \tag{8.2}$$

8.2.4 Windkessel model and frequency domain analysis

In this chapter, we also assess how well the classical windkessel formulation holds in the setting of aortic coarctation. We therefore fitted the 3-element windkessel model [55] to the ascending aorta pressure (P_{ao}) and flow (Q_{ao}) waveforms using the fminsearch (Nelder-Mead simplex) algorithm in Matlab with default convergence settings and without any constraints on the model parameter values. Flow was used as an input to the model, and the difference between the 3-element windkessel model response and P_{ao} was minimized. The root mean square (RMS) value of the difference between the 3-element windkessel pressure and P_{ao} is used as an indicator of the goodness of fit. Note that this 3-element windkessel model aims to mimic the behavior of the complete aorta model, thus the FSI computational domain with all its outlets and boundary conditions (which also includes another 3-element windkessel model at the outlet of the descending aorta).

We also derived input impedance, Z_{in}, from the pressure, P_{ao}, and flow, Q_{ao}, at the inlet as the ratio of the corresponding pressure and flow harmonics, obtained from Fourier-transform of pressure and flow using Matlab. Z_{in} is a complex number and is presented in the frequency domain in the modulus and phase notation, where the modulus represents the ratio of the amplitudes of corresponding pressure and flow harmonics, and the phase is the phase lag between both (with negative phase angles indicating that flow is leading pressure).

8.3 RESULTS

8.3.1 Hemodynamic data: ascending aorta pressure and flow velocities

The pressure and flow waveforms calculated at the level of the ascending aorta for the four different cases are given in Figure 8.2. Especially the presence of the aortic narrowing has a major effect on central aortic hemodynamics, with a significant increase in aortic systolic pressure from about 114 mmHg at baseline to 131 mmHg for a moderate recoarctation (CI = 0.65) to 165 mmHg for the most severe recoarctation (CI = 0.5). The presence of the stent increases ascending aorta systolic pressure to 122 mmHg. The reader is referred to chapter 7 for a further in-depth analysis on the hemodynamic impact of (repaired) aortic coarctation.

8.3.2 Reference data retrieved from the static finite element simulations

The static pressure-volume (P-V) relation of the 3D aorta model retrieved from static finite element simulations is displayed in Figure 8.3 and clearly shows the hyperelastic nature of the assumed material law, with progressive stiffening with increasing pressure. For each of the four models, the P-V data can be fitted using a second-order polynomial, with r^2 values > 0.999 (see Figure 8.3 for the regression equations).

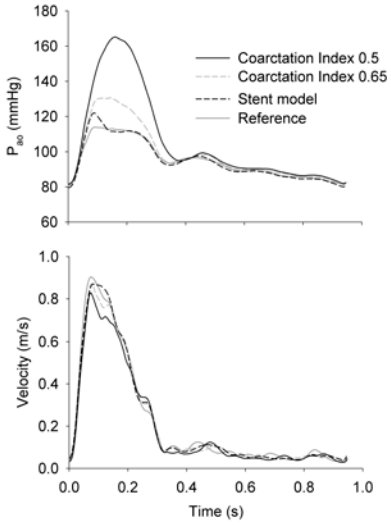

Figure 8.2: Ascending aorta pressure (top) and flow velocity (bottom) for the normal aorta and the 3 mechanical interventions.

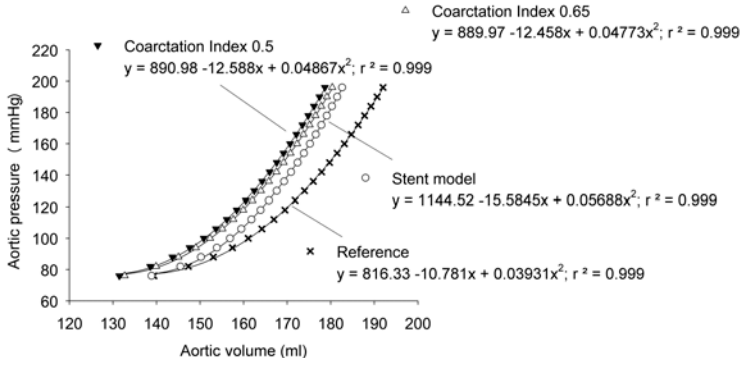

Figure 8.3: Pressure-volume relations for the 4 different models as obtained from static finite element simulations.

8.3.3 Application of the reservoir-wave paradigm to the data

The result of the reservoir-wave separation is shown in Figure 8.4, with panel A displaying the total, reservoir and excess pressure component for the most severe coarctation case. Aortic stiffening and/or narrowing has very little effect on reservoir pressure P_{res}, with only small differences in reservoir pressure between the different cases (Figure 8.4, panel B). In contrast, however, excess pressure increases drastically with the peak amplitude increasing from about 27 mmHg for the reference configuration to about 74 mmHg for the most severe coarctation (Figure 8.4, panel C).

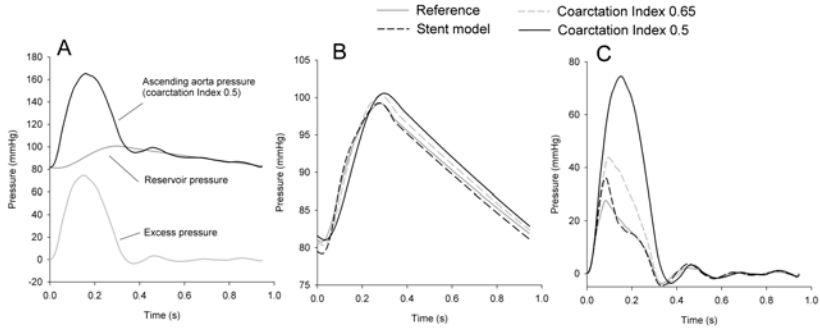

Figure 8.4: Panel A: application of the reservoir-wave paradigm to the pressure and flow data obtained using fluid-structure interaction simulations in the model with the most severe aortic narrowing. Panel B and C: overview of reservoir and excess pressure for the 4 cases considered.

8.3.4 Changes in aortic volume and associated P_{ao-vol} as reference for the reservoir pressure

The change in intra-aortic volume (V_{ao}) for the four considered cases and the corresponding pressures (P_{ao-vol}), calculated using the regression equations displayed in Figure 8.3, are shown in Figure 8.5 panels A and B. As expected, the reference model displays the largest intra-arterial volume throughout the complete cardiac cycle. The most severe coarctation case has the smallest volume at end-diastole, but not in systole due to the high pressure build-up proximal to the coarctation. Both coarctation cases are associated with the highest increase in P_{ao-vol}. Panel C displays the difference between ascending aorta pressure P_{ao} and P_{ao-vol}. For the reference and stent case, there is a short positive peak of about 10 mmHg, which rapidly decreases to a negative value of about -2 to -3 mmHg after about 0.1 s. The presence of the recurrent coarctation changes this pattern; the peak value increases to about 30 mmHg for the most severe case, with positive values throughout the entire systolic phase. Values are low in diastole for all cases.

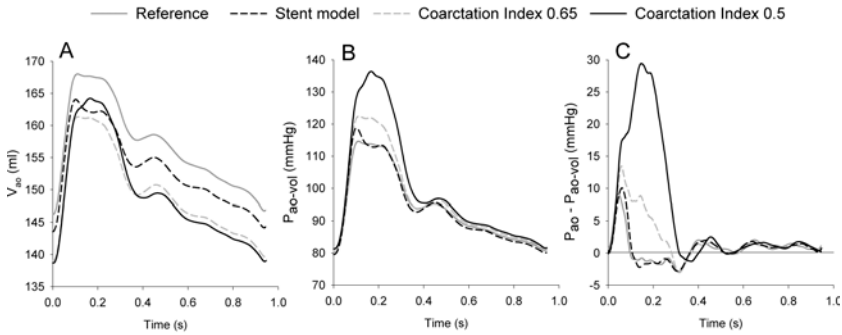

Figure 8.5: Panel A: variation of intra-aortic volume (V_{ao}) as a function of time, assessed from the difference between in- and outflow of the aorta models. Panel B: pressure associated with these volume changes (P_{ao-vol}) calculated using the pressure-volume relations shown in Figure 8.3. Panel C: difference between the pressure at the ascending aorta (P_{ao}) and the pressure associated with the aortic volume changes (P_{ao-vol}).

8.3.5 Pressure-volume relations of the aorta

The relation between intra-aortic volume and different definitions of pressure is displayed in Figure 8.6. The dark solid line represents the relation between ascending aorta pressure (P_{ao}) and volume (V_{ao}) as retrieved from the simulations, and displays a hysteresis loop that is running counter-clockwise for all simulated cases. The dashed line displays the relation between reservoir pressure P_{res} and intra-aortic volume (V_{ao}). Again, a loop is found which, however, runs clockwise. Both loops coincide in diastole, and follow the same trajectory as the static P-V relation (which is, by definition, also equal to the relation between aortic volume and P_{ao-vol}; grey solid line).

8.3.6 Windkessel model and frequency domain analysis

The 3-element windkessel model parameters obtained after fitting are given in Table 8.1. Systemic vascular resistance, R, remains fairly constant, while Z_c is elevated for all cases, with a tripled value for the most severe coarctation. Estimated total arterial compliance is (highly) reduced for both coarctation models, but is higher for the stented aorta model. The best fitting with lowest RMS is found for the normal aorta; the poorest fitting is obtained for the most severe recoarctation.

The input impedance of the four models is given in Figure 8.7. The value at 0 Hz, representing $R + Z_c$, is increased for all interventions, with the largest increase for the most severe coarctation. The presence of a rigid segment in the descending aorta introduces a peak in the impedance modulus in the 4-8 Hz band. The coarctation increases the impedance modulus over the complete frequency band, with the most pronounced effect for the most severe recoarctation.

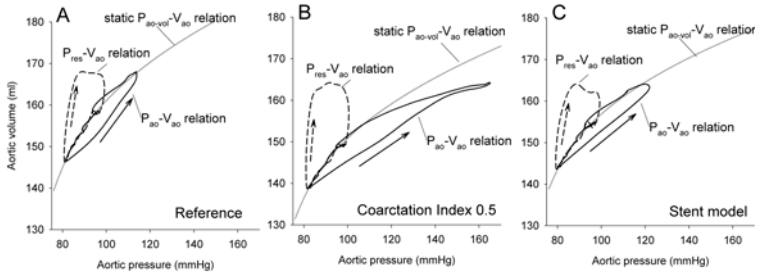

Figure 8.6: Pressure-volume relations for the normal aorta (panel A), the most severe aortic narrowing (panel B) and the stent model (panel C). The solid grey line displays the P-V relation obtained from static finite element simulations (i.e., the same data as displayed in Figure 8.3). The dark solid line is the relation between aortic pressure (P_{ao}) (Figure 8.2 A) and volume (V_{ao}) (Figure 8.5 A) as retrieved from the fluid-structure interaction simulations. A loop is found, which is followed in a counter clockwise manner. The dark dashed line is the relation between reservoir pressure (P_{res}) and volume (V_{ao}). Here also a hysteresis loop is found, which is looped in a clockwise manner. Note that the reservoir-wave concept relies on the intrinsic assumption of the reservoir pressure being directly proportional to the change in aortic reservoir volume, which is invalidated by this finding. Note that all relations follow the static P-V relation in diastole.

	R (mmHg.s/ml)	C (ml/mmHg)	Z_c (mmHg.s/ml)	RMS (mmHg)
Normal aorta	0.693	4.28	0.045	0.97
CI = 0.65	0.696	3.36	0.071	2.49
CI = 0.5	0.715	1.75	0.110	7.78
Stent model	0.686	4.43	0.052	2.28

Table 8.1: 3-element windkessel model parameters (R, C and Z_c) and goodness of fit (RMS) for the four considered cases.

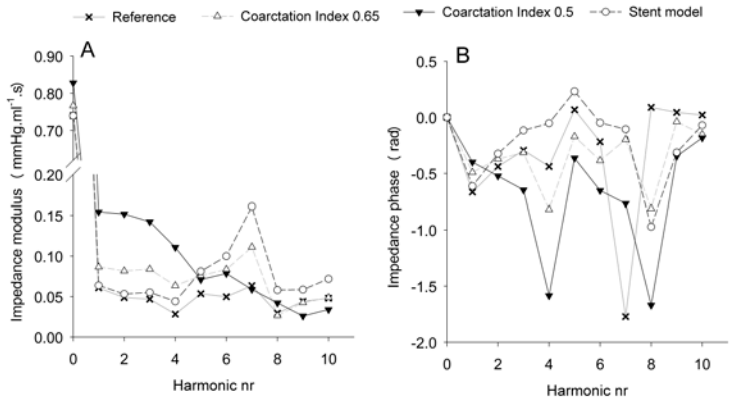

Figure 8.7: Input impedance modulus (left) and phase (right) for the normal aorta and following the three mechanical interventions. The rigid segment mainly affects the 4^{th} to 8^{th} harmonic, while the coarctation models have an impact on all harmonics.

8.4 DISCUSSION

The reservoir-wave analysis is, quoting Tyberg et al., '*based on the assertion that measured pressure and flow can be resolved into their volume-related (i.e., reservoir) and wave-related (i.e., excess) components. The change in reservoir pressure is assumed to be proportional to the difference between measured inflow and calculated outflow*' [287]. As it is virtually impossible to test this hypothesis in an in vivo setting, we applied the reservoir-wave paradigm to data obtained from numerical 3D fluid-structure interaction simulations of the aorta, allowing for the direct assessment of the intra-aortic pressure and volume, and hence of an accurate quantification of the aortic buffer.

In summary, we found no unequivocal relation between the intra-aortic volume, calculated as the difference between inflow and outflow, and the reservoir pressure for none of the simulated cases. When plotted in a pressure-volume diagram, hysteresis loops are found that are looped in a clockwise way, i.e., for a given volume, pressure is lower on the upslope than on the downslope (Figure 8.6). It is only in diastole that the relation between reservoir pressure and intra-aortic volume equals the P-V relation as derived from our reference simulations, and this for all cases considered. This observation thus indicates that in systole, the reservoir pressure as derived from the reservoir-wave analysis, is lower than the pressure that would be associated with the change in volume (P_{ao-vol}).

P_{ao-vol} is thus substantially higher than P_{res} in systole (as can be derived from Figures 8.4, 8.5 and 8.6), while both are more or less equal in diastole. P_{ao-vol} reflects the pressure that would exist if the changes in intra-aortic volume would occur in absence of blood flow, e.g. as one would obtain during a static inflation test of the excised aorta. This also implies that the difference between the actual pressure P_{ao} and P_{ao-vol} is to be explained by the dynamics of blood motion in the aorta (i.e. by the Navier-Stokes equations).
Figure 8.5, panel C displays the difference between the pressure as retrieved from the FSI simulation (P_{ao}) and P_{ao-vol}. For the normal aorta (as well as for the stent model), the dominant factor determining the pressure (gradients) in the fluid domain is the inertia of the blood related to the pulsatility of blood flow with the temporal acceleration and deceleration of the blood. This explains the short positive peak in P_{ao} - P_{ao-vol}: acceleration of the blood is related to a negative pressure gradient along the aorta and the pressure at the ascending aorta (P_{ao}) will therefore be higher than the mean pressure on the aortic wall. The negative pressure difference, on the other hand, is mainly associated with the deceleration of the flow, resulting in a positive pressure gradient and thus lower value of P_{ao} compared to the mean pressure on the aortic wall.

In the case of aortic narrowing (recurrent coarctation), however, there is not only acceleration and deceleration due to the pulsatility of the blood flow, but also due to the fact that flow velocity varies substantially along the length of the aorta, and is accelerated in

the descending aorta due to the narrowing and decelerated past the stenosis. This is the convective acceleration component, which is proportional to the velocity gradient along the aorta. This is illustrated in Figure 8.8, right panel, that shows the difference in mean velocity in a cross-section in the ascending aorta and in the narrowed section. The convective acceleration persists throughout complete systole, in contrast to the case of the normal aorta. As the constriction is approached, the flow accelerates and the pressure falls sharply. Distally, the aorta gradually restores to its normal dimensions. The flow deceleration is thereby accompanied by pressure recovery (i.e. kinetic energy is again restored into pressure). This transition is, however, associated with energy losses related to the development of turbulence in the expansion zone.

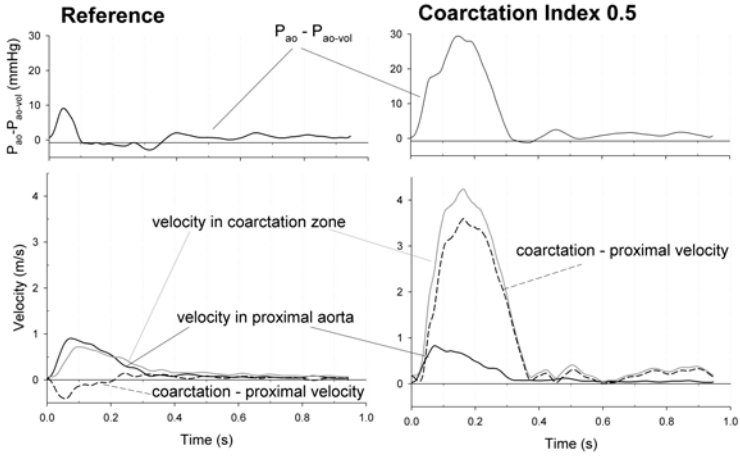

Figure 8.8: The top panels display the difference between P_{ao} and P_{ao-vol} (the same data as Figure 8.5, panel C) for the normal aorta and the most severe aortic coarctation. This difference is explained by the dynamics of blood flow. For the normal aorta, the dominant factor is the inertia of the blood and the acceleration and deceleration due to the pulsatility of the blood. Flow velocity is of the same order of magnitude along the aorta (bottom left). In case of aortic coarctation, the difference between velocity in the ascending aorta and in the narrowed zone is large, implying an important convective acceleration, which pertains throughout systole (bottom right). This explains the large difference between P_{ao} and P_{ao-vol}.

With the observation that reservoir pressure is not related to the volume in the aortic reservoir in systole, an intrinsic assumption in the wave-reservoir concept is invalidated and, consequently, also the assumption that the excess pressure is the component of pressure that can be attributed to wave travel and reflection. In our view, it is simply impossible to mathematically dissociate the pressure in a presumed reservoir pressure and wave component. Both are intricately linked, and the changes in aortic pressure (a local evolution of pressure with time) are not only explained by the aortic buffer (associated with the global pressure evolution), but also by wave travel and reflection taking place, which are most prominent in systole.

We previously argued that the reservoir-wave concept is the time-domain equivalent of the 3-element windkessel model. Both paradigms are a simplification of a more complex reality, and should be considered as such. We believe that our data, obtained in the complex hemodynamic setting of aortic coarctation exacerbating wave reflections, clearly pinpoint the limitations of both concepts in this setting.

(i) As for the 3-element windkessel model, the calculated input impedance (Figure 8.7) directly illustrates the problem. The model (as any lumped parameter model) does not explicitly account for wave travel and reflection, and assumes infinite wave speed (and wavelengths), conditions that are progressively better met with advancing age and increase in stiffness leading to less oscillatory input impedance patterns. Clearly, the presence of a proximal aortic stiffening or narrowing 'disturbs' the input impedance, with a marked increase in the impedance modulus in the low frequency range for the coarctation models and/or strong oscillations for the higher frequencies. This causes a high impact on the model parameters deduced from model fitting (Table 8.1), with a marked increase in characteristic impedance and a very strong reduction in estimated total arterial compliance, much higher than one would anticipate from the static pressure-volume relations (cfr. the change in slope of the different curves depicted in Figure 8.3). This clearly demonstrates that (i) the interpretation of characteristic impedance as a parameter reflecting the properties of the proximal aorta is not always justified, especially not in the cases considered here where the proximity of the aortic narrowing/stiffening appears in the input impedance spectrum in the mid-to-high frequency band; (ii) in the presence of strong reflections, fitting of the windkessel model is poor as reflected by the increased RMS value associated with the models mimicking repaired CoA. The use of (3-element) windkessel models and the derived model parameters should then be interpreted with caution, in line with previous observations [290].

(ii) Mirroring the high values of characteristic impedance, the reservoir-wave analysis leads to very high excess pressures, but to surprisingly little changes of the reservoir component, P_{res}. As for the 3-element lumped model, we believe that this again reflects the limitations of the reservoir-wave paradigm which are exacerbated in settings with complex hemodynamics.

This study clearly illustrates the limitations of simplified models and paradigms in complex settings as studied here and explicitly invalidates the assumption of a reservoir pressure directly proportional to changes in the aortic reservoir. This, however, does not necessarily imply that the application of these concepts is faulty by definition or that the paradigm cannot be useful from a clinical perspective. In fact, both the 3-element windkessel model as well as the reservoir-wave paradigm do pick up the hemodynamic impact of a mechanical

intervention on the descending aorta. The 3-element windkessel model has been the reference lumped parameter model since it was first described by Westerhof et al. in 1971 [55]. Despite its known limitations and refinements, the model has been a valuable tool in cardiovascular physiology research for a long time. The reservoir-wave paradigm has a shorter history, first being described in [230]. It has the advantage of being applicable in the time domain and underpins a very intuitive interpretation of arterial hemodynamics, and recent data in clinical trials have demonstrated that parameters calculated from the reservoir and excess pressure waveforms predicted cardiovascular events in univariate Cox proportional hazards modeling [291].

The problem, however, arises when applying simplified concepts in settings far beyond the underlying assumptions and its instructions of use. Further problems may arise due to over-analysis of the model as we believe is the case when using the excess pressure for subsequent hemodynamic analysis and wave decomposition. This study explicitly demonstrated that, for any of the considered cases, the reservoir pressure is not mathematically proportional to intra-aortic volume in systole, which is a key assumption in the reservoir-wave analysis. It is likely a factor contributing to the observation that the use of excess pressure for wave analysis leads to suppression of reflected compression waves and amplification or induction of backward expansion waves and thus to flawed interpretation [285].

While the merit of this computational study is the use of advanced fluid-structure interaction simulations and the availability of high resolution pressure, flow and geometrical data, it is a modeling study with associated intrinsic limitations and considerations. Within the context of this study, the most important consideration is probably the choice of the aortic domain that is considered as 'the reservoir'. The 3D model entails the ascending aorta, arch and the descending aorta. With the bulk of the aortic buffering capacity residing in the ascending aorta and arch [243], we feel that it is justified to consider the complete 3D domain as being representative for the aortic buffer. Other important assumptions relate to the boundary conditions, i.e. the imposed inflow, outflow and the distal windkessel model. These are based on and derived from MRI measurements on a healthy middle-aged volunteer that also provided the data for the normal aorta. Boundary conditions were assumed equal for all models. This approach has the advantage that the isolated effect of the mechanical intervention can be studied, but does not fully account for possible in vivo adaptations in response to (repaired) aortic coarctation, such as the development of an extensive collateral circulation or arterial wall remodeling.

CONCLUSIONS

Final remarks and conclusions

Conclusions

In recent years, image-based modeling experienced significant technical improvements that currently allow to study hemodynamic and biomechanical parameters in a wide spectrum of congenital cardiovascular pathologies. Other applications that are made possible with current computation techniques involve the planning of patient specific interventions and the design improvement and evaluation of endovascular devices. Few years ago, these applications were a research topic of only a few specialized groups, but the availability of commercial and open source simulation software and segmentation tools have exceptionally improved their widespread utilization. Apart from an extension of the applications, advances in computational methods permit the study of increasingly challenging problems. Among others, these concern flow instabilities and the development of turbulence in recurrent coarctation, the topic of this dissertation.

While patient specific fluid-structure interaction (FSI) models have the convenience of taking into account the full complexity of the problem under consideration, their high level of complexity may also hamper the analysis and insights provided. For this reason, a very simplified model of repaired aortic coarctation (CoA) was fist developed. The advantage of this model is that the only reflections present in the model originate from the coarctation and can thus easily be interpreted.

Although the simulation of the short pulse suggests quite an important alteration of the hemodynamic quantities, no significant changes were found for the case of a physiological pressure pulse. This counter-intuitive result can, nonetheless, be explained by recalling the reflections induced by the stiff segment. At the transition from the flexible artery to the stiffening, a backward compression wave is generated, immediately followed by a backward expansion wave (BEW), created at the outlet of the stiffening. Proximal to the stiff segment, both waves overlap and cancel each other out, as such leaving the hemodynamic quantities almost undisturbed. In practice, more than two backward waves are created. Particularly, the BEW generated at the distal end of the stiffening, will reflect in a forward compression wave (FCW) at the proximal end of the stiffening. This wave will re-reflect at the distal end

of the stiff segment, creating a second BEW, which in turn, generates a second FCW and so on. As such, part of the wave energy will reach the outlet with a delay (as a sequence of compression waves).

To obtain a complete analysis in a physiologically more relevant setting, a patient specific geometry was applied. Taking into account the fluid-structure interaction, the numerical model of the aorta yields pressure and flow wave data in line with known arterial physiology and can thus be used to provide complementary data that are difficult to obtain in vivo (such as pressure drops, wave reflections) or to simulate pathological conditions. The work described in this dissertation finally led to the development of an image-based computational model of repaired aortic coarctation. The application of this model gave rise to a number of useful insights that are summarized below.

It is demonstrated that fluid-structure interaction, the key feature in our model, plays a significant role in the correct assessment of CoA severity. Buffering of the blood flow in the proximal aorta damps out the pressure pulse and reduces the velocity in the constriction and the correlated pressure difference. In the distal part of the aorta, the presence of a narrowing results in a highly nonuniform flow and the development of vortices. These observations prohibit the use of 1D models in the prediction of stenosis-induced pressure drops and wave reflections and call for the patient specific 3D approach applied in this research.

In agreement with the results reported with the simplified model, it was found that the impact of an isolated stiffening on the hemodynamic response is fairly limited. With respect to the presence of a residual narrowing, blood pressure alterations in the proximal aorta are much more pronounced, covering the whole systolic phase and are dominated by the convective acceleration across the CoA. This pressure drop is followed by pressure recovery persisting in a larger part of the descending aorta. Severe coarctation is characterized by a smaller pressure recovery (i.e. a larger energy dissipation due to the development of turbulence). For a short constriction an additional stiffening will have a significant impact on the pressure evolution whereas the impact for a longer stiffening is relatively limited.

An evaluation of CoA severity based on the net wave intensity alone, results in a considerable underestimation of the backward compression wave generated by the presence of a narrowing and provides misleading information regarding the distance to the reflection site.

We also applied the reservoir-wave paradigm to data obtained from the 3D FSI simulations of the aorta, allowing for an accurate quantification of the aortic buffer. This study clearly illustrated the limitations of simplified models and paradigms in complex settings as studied here and explicitly invalidated the assumption of a reservoir pressure directly proportional to changes in the aortic reservoir.

Technical issues studied in this dissertation regarding the fluid-structure interaction ap-

proach included numerical dissipation and stability problems. The main findings with respect to these issues are listed below.
When solving a differential equation by a numerical approximation method, numerical dissipation and dispersion may occur. The study of these errors and their effect on the solution is sometimes overlooked in FSI simulations, where the numerical parameters are often optimized with respect to time efficiency and stability rather than accuracy. The numerical dissipation depends on three parameters: $\Delta t/T$ and $\Delta x/\lambda$, determining the temporal and spatial resolution of the wave harmonics and $t/\Delta t$, defining the number of consecutive time steps during which the dissipation occurs. It was shown that for a second-order upwind discretization scheme in combination with a second-order implicit time integration scheme, the numerical dissipation after a propagation time t increases more than linearly with increasing $\Delta t/T$ and with increasing $\Delta x/\lambda$. Since in cardiovascular simulations, the grid size is typically a few orders smaller than the wavelength of the present wave harmonics, the spatial resolution will have no significant effect on the numerical dissipation.

Coupled problems often use different time integration schemes to discretize the different sub-problems. This approach allows the different equations to be solved with schemes that are particularly suited to solve each individual sub-problem. Furthermore, coupled problems sometimes require different time step sizes in the different sub-problems. Especially for a partitioned solution strategy this approach can be advantageous. However, according to our experience with cardiovascular FSI simulations, coupling different time integration schemes and time step sizes can induce stability problems. Apart from the selected time integration schemes, the interpolation method applied during the sub-cycles strongly affects the stability and the accuracy of the solution. For parameter values that approximate the flow in an artery and a ratio of the fluid to solid time step size smaller than or equal to one, the combination of a backward Euler scheme with the Hilber-Hughes-Taylor scheme is stable. Compared to an FSI simulation for which the specified time step is adapted to the smallest required time scale, sub-cycling in the fluid significantly speeds up the calculation without loss in accuracy. If, on the other hand, the smallest required time step size is determined by the solid problem, the matching of the time step sizes of the fluid and the solid problem is very important to obtain a stable solution.

In conclusion, the main achievements of this research are:

(i) *The development of a simplified fluid-structure interaction model of repaired aortic coarctation as a first step towards a more complex physiological representation, providing deeper understanding with respect to wave propagation and reflection.*

(ii) *The development and validation of a patient specific fluid-structure interaction model of the aortic arch including (repaired) aortic coarctation.*

(iii) *The application of this model to gain insights into the effect of local stiffening and residual narrowing on central hemodynamics seen in repaired aortic coarctation.*

So did these achievements manage to explain the long-term morbidity observed after coarctation treatment? No, but we were able to highlight some important hemodynamic alterations due to the presence of a local stiffening and a residual narrowing in the post-interventional case. The correlation of these adverse hemodynamic consequences with the long-term morbidity remains, however, a topic of future research. This should further elucidate the role of disturbed flow patterns in the progression of the disease. As such, this research is certainly not an endpoint. Suggestions for future work are included in the next section (without the aim of being complete). We believe that in the near future, computational simulations will further improve understandings of the severity of hemodynamic and biomechanic alterations. Through the mutual interaction between engineers and clinicians, the regions of increased susceptibility can be identified and mitigated, consequently alleviating the potential genesis of long-term morbidity.

FUTURE PERSPECTIVES

Despite the insights computational models provide on the complexity of the blood flow in a patient specific setting, their application in clinical practice remains fairly limited. This is caused by two main restrictions. The first one involves the definition of simple clinically relevant diagnostic criteria. As CFD/FSI simulations render large data-sets it is sometimes difficult to extract a limited number of parameters to represent the physiological state under consideration.

Compared to diagnostic imaging acquisition the generation of computational simulation results remains challenging. This provides a second restriction in the clinical translation of the computational modeling approach. Their restricted clinical use makes it, moreover, more difficult to motivate their utility in extensive studies, which are required to prove their applicability. The utilization of CFD/FSI models in the management and prevention of cardiovascular diseases should therefore be encouraged. Although the development of the current models towards more physiological ones is an important feature, we also call for a major scientific use of the existing models (as they are presently available, acknowledging their limitations) to demonstrate the practical relevance of local hemodynamic simulations. An important application thereby includes the modification of current strategies in aortic coarctation treatment, which are based on mortality rates and the prevelance of hypertension, recoarctation and aneurysm formation following treatment. Using a computational approach, treatment options could instead be analyzed based on their ability to restore optimal hemodynamics.

The improving level of sophistication of the current computational models, taking into account the interaction between the blood flow, the deformation of the arterial wall and in some limited cases the impact of the surrounding tissue, requires more input data than the arterial geometry alone. A characterization of the mechanical behavior of the arterial wall and the surrounding structures (such as bones or muscles) is in these cases required. The assessment of these material properties in a patient specific setting calls for the development of new methods to extract tissue properties from medical image data based on an inverse solution strategy such as MRI-based elastography [292] or data assimilation techniques [293].

With respect to patient specific modeling, a long list of suggestions can be made to further include the full complexity of the pathogenesis of aortic coarctation and the physiology of the arterial system [200].

- As pointed out in chapter 1, a geometrical multiscale approach is required to quantify the interaction between local and global parameters in the cardiovascular system. For the case of repaired aortic coarctation, this encompasses the coupling of the 3D model of the aortic arch with 0D or 1D models of the distal circulation [13]. Another advantage of this approach is the modeling of the inherent flow redistribution that is associated with the resistance increase accompanying recurrent coarctation. In addition, the physiological boundary conditions allow the prediction of intervention outcome and exercise conditions where flow information (at the boundaries of the model) is not always clinically measurable.
- Inclusion of the intercostal and collateral blood vessels bypassing part of the flow through the coarctation [219]. This approach will result in a more accurate estimation of the actual pressure drop.
- Modeling of the (viscoelastic) tissue surrounding the aorta [274], which damps out the high frequency oscillations of the vessel wall.
- Inclusion of the solid-growth coupling. Alterations of the pressure evolution along the aorta and the coarctation affect the homeostatic mechanical state of the aorta. In response to these alterations, vascular growth and remodeling take place [220, 275, 276]. These adaptations include both changes in shape and material properties. In particular for the case of aortic coarctation, wall thickening is often observed along with a decrease in compliance of the proximal aorta due to prolonged hypertension [198, 221–225, 228, 229, 277]. Arterial remodeling in turn will modify the hemodynamic response.
- The vascular system is a complex setup in which biological, chemical and physiological factors interact. This stresses the need to extend numerical models with mass transport phenomena [294], system biology methods [295] and vascular remodeling.

- Apart from aortic compliance, which causes the aortic wall to deform during the systolic phase, also the beating of the heart will result in aortic wall motion (i.e. a translational motion of the aortic root). This was not accounted for in this research as only a radial displacement is allowed at the ascending aorta. Inclusion of this key feature will affect both the flow patterns in a normal and a diseased aorta [208].
- The quantification of the in vivo stresses present during imaging is another factor that should be included in order to obtain a correct estimation of wall displacement and the stress distribution throughout the blood vessel. Efforts towards the inclusion of prestress have been made by our research group [296], but should be combined with the fluid-structure interaction approach presented in this dissertation and also include residual stresses. This approach necessitates the need for a proper evaluation of the material properties, which vary along the length of the aorta [297] and in circumferential direction [298].

Appendices

APPENDIX A

Impact of reduced order modeling

In the following, the performance of the 1D theory in the setting of a locally stiffened or narrowed aorta is evaluated. Instead of using a 1D model, a theoretically deduced reflection and transmission coefficient will be applied to retrieve the forward propagating waves and the induced reflections. To calculate these coefficients, velocity information obtained from the 3D FSI simulations is used. We are aware that the use of 3D information in a 1D study might affect the results, but we believe that the insights provided remain valid. In addition, this section should provide a better understanding of (the importance of) wave trapping.

The reflection coefficient R is introduced, representing the ratio of the reflected wave to the incident wave. For the one-dimensional case, this coefficient depends on the area A and the wave speed c upstream (indicated with a subscript 0) and downstream (depicted with a subscript 1) of the discontinuity (i.e. the local narrowing or stiffening). Based on the conservation of mass and energy at the discontinuity, the Bramwell-Hill equation and the water hammer equations, Eq. A.1 can be derived

$$R = \left(\frac{1+m_0}{1-m_0}\right) \frac{\left(\frac{A_0}{c_0} - \frac{A_1}{c_1}\right)}{\left(\frac{A_0}{c_0} + \frac{A_1}{c_1}\right)} \tag{A.1}$$

in which m represents the Mach number (i.e. the ratio of the blood velocity v to the wave speed c). At the constriction site, part of the incident wave is transmitted given by the transmission coefficient T.

$$T = \left(\frac{1+m_0}{1+m_1}\right) + \left(\frac{1-m_0}{1+m_1}\right) R \tag{A.2}$$

	local stiffening		**reCoA**	
	R	T	R	T
$a \rightarrow b$	0.773	1.767	0.723	1.476
$b \rightarrow a$	-0.734	0.271	-0.963	0.366
$b \rightarrow c$	-0.722	0.279	-0.959	0.357

Table A.1: Overview of the reflection and transmission coefficients at different locations along the repaired CoA zone.

Static finite element simulations are performed and the Bramwell-Hill equation (Eq. 2.2) is used to calculate the wave speed c in a section proximal to (plane a in Figure A.1), halfway (plane b in Figure A.1) and distal to (plane c in Figure A.1) the repaired coarctation zone. Adopting the geometrical (A) information and the maximal velocity (v) (averaged over the cross section) from the 3D FSI simulations of the aortic flow, the reflection and transmission coefficient associated with the presence of a narrowing and stiffening can be defined. We thereby regarded the stenosis as a local discontinuous change in cross section. The coefficients, indicating the transition from the aorta to the constriction at the proximal end of the CoA, are given by $R_{a\rightarrow b}$ and $T_{a\rightarrow b}$, whereas the transition in the opposite direction is marked by $R_{b\rightarrow a}$ and $T_{b\rightarrow a}$. Similar, the transition from the constriction to the aorta at the distal end is represented by $R_{b\rightarrow c}$ and $T_{b\rightarrow c}$. The value of these coefficients is shown in Table A.1 for a model including a local stiffening (L = 50 mm, $E_{CoA} = 100E_{Ao}$) and a model including a residual narrowing (CI = 0.5, L = 25 mm, $E_{CoA} = E_{Ao}$).

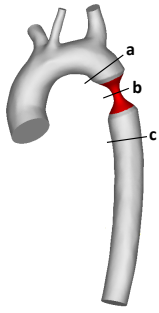

Figure A.1: Indication of the proximal plane (a), the plane halfway the CoA zone (b) and the distal plane (c) in the model of recurrent coarctation (CI = 0.5 and L = 25 mm).

First, a discussion of the reflections induced by a local stiffening is provided. At the transition from the flexible artery to the rigid segment, a backward compression wave is generated, given by the incident wave (p_+), multiplied by the reflection coefficient $R_{a\to b}$. Part of the original wave (i.e. $p_+ T_{a\to b}$) propagates through the constriction and is reflected at the distal end of the coarctation as a backward expansion wave given by $p_+ T_{a\to b} R_{b\to c}$ (of which a fraction $T_{b\to a}$ propagates to the ascending aorta). After a time delay of 0.0015 s (the time needed for the wave to propagate back and forth through the constriction), both waves overlap, resulting in the backward wave $p_{-,1Dmodel}$ shown in Figure A.2 on the left. Notice that this wave differs substantially from the backward wave retrieved from the 3D FSI model (p_-). In practice, however, not only two backward waves exists, but a sequence of expansion waves are generated due to wave trapping, each representing a fraction ($R_{b\to a} R_{b\to c} T_{b\to a}$) of the previous BEW and delayed by 0.0015 s. In Figure A.2 on the right, the backward wave $\text{BEW}_{\text{1-8, 1D model}}$ accounts for the first eight BEWs generated by the stiffening. The resultant of $\text{BCW}_{\text{1D model}}$ and $\text{BEW}_{\text{1-8, 1D model}}$ (i.e. $p_{-,\text{1D model}}$) corresponds well with the first peak of p_- (i.e. the backward wave retrieved from the FSI simulation). The remaining difference in p_- and $p_{-,\text{1D model}}$ is explained by the reflections induced in the descending aorta and at the distal boundaries of the fluid domain. Considering the longer distance between the heart and these reflection sites, these reflections typically arrive at a later stage in the cardiac cycle. The 1D theory thus predicts the wave reflections well in the case of a local stiffening.

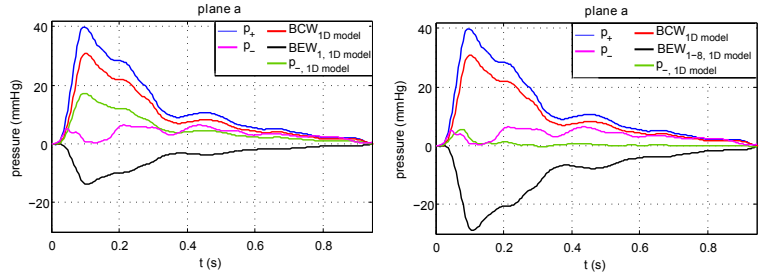

Figure A.2: Comparison of the backward waves proximal to the CoA segment (p_- and $p_{-,\text{1D model}}$), resulting from the FSI simulation (L = 50 mm, $E_{CoA} = 100 E_{Ao}$) and obtained using the reflection and transmission coefficients deduced from the 1D flow in a flexible artery. $p_{-,\text{1D model}}$ is thereby calculated as the sum of a backward compression wave ($\text{BCW}_{\text{1D model}}$) and the first (left) or the first eight (right) backward expansion wave(s) ($\text{BEW}_{\text{1, 1D model}}$ and $\text{BEW}_{\text{1-8, 1D model}}$ respectively), generated at the distal end of the coarctation zone.

Secondly, the reflections induced by a local stenosis are investigated. Similar as for the local stiffening, a backward compression and expansion wave are generated given by $p_+ R_{a\to b}$ and $p_+ T_{a\to b} R_{b\to c} T_{b\to a}$ respectively. Both waves ($\text{BCW}_{\text{1D model}}$ and $\text{BEW}_{\text{1, 1D model}}$)

are shown in Figure A.3, together with their resultant ($p_{-,\text{1D model}}$). In contrast to Figure A.3 (left) $p_{-,\text{1D model}}$ underestimates the backward wave predicted by the 3D FSI model. It is clear that a consideration of the BEWs, generated due to wave trapping, will result in a further decrease of $p_{-,\text{1D model}}$. This suggests that the 1D theory fails to predict the reflections generated in such a complex case and demonstrates the need for 3D models.
Recalling Figure 7.8 which shows the axial velocity component at different sections throughout the descending aorta, it can be observed that the flow indeed becomes very nonuniform for the case including a local narrowing (which is not observed if only a local stiffening is considered). Distal of the coarctation, only a restricted part of the cross section is characterized by a positive axial velocity. This limited positive cross sectional flow decreases the apparent cross section (A_c) which affects the reflection coefficient $R_{b\to c}$ at the distal end of the CoA.

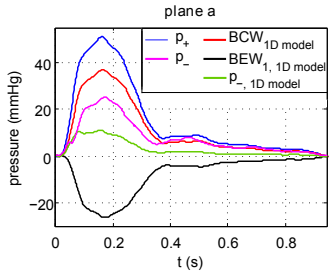

Figure A.3: Comparison of the backward waves proximal to the CoA segment (p_- and $p_{-,\text{1D model}}$), resulting from the FSI simulation ($CI = 0.5$, $L = 25$ mm, $E_{CoA} = E_{Ao}$) and obtained using the reflection and transmission coefficients deduced from the 1D flow in a flexible artery. $p_{-,\text{1D model}}$ is thereby calculated as the sum of a backward compression wave ($\text{BCW}_{\text{1D model}}$) and the first backward expansion wave ($\text{BEW}_{\text{1, 1D model}}$), generated at the distal end of the coarctation zone.

Figure A.4 compares the backward waves halfway the CoA segment (plane b in Figure A.1) predicted using the 3D FSI model (p_-) to the ones obtained applying the 1D reflection and transmission coefficients ($p_{-,\text{1D model}}$). It can be verified that the reflection at the distal end of the coarctation is overestimated.

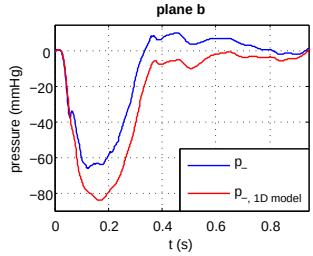

Figure A.4: Comparison of the backward waves halfway the CoA segment, resulting from the FSI simulation (p_-) (CI = 0.5, L = 25 mm, $E_{CoA} = E_{Ao}$) and obtained using the reflection coefficient R_{bc} deduced from the 1D flow in a flexible artery respectively ($p_{-,\text{1D model}}$).

List of Figures

List of Tables

Bibliography

[1] J. J. Bobby, J. M. Emami, R. D. Farmer, C. Newmann, Operative survival and 40 year follow up of surgical repair of aortic coarctation, British heart journal 65 (5) (1991) 271–276.

[2] W. E. Hellenbrand, H. D. Allen, R. J. Golinko, D. J. Hagler, W. Lutin, J. Kan, Balloon angioplasty for aortic recoarctation: Results of valvuloplasty and angioplasty of congenital anomalies registry, The American Journal of Cardiology 65 (11) (1990) 793 – 797.

[3] C. Ovaert, L. Benson, D. Nykanen, R. Freedom, Transcatheter treatment of coarctation of the aorta: A review, Pediatric Cardiology 19 (1) (1998) 27–44.

[4] C. Taylor, C. Figueroa, Patient-specific modeling of cardiovascular mechanics, Annual Review of Biomedical Engineering 11 (1) (2009) 109–134.

[5] C. G. Caro, K. Parker, The effect of hemodynamic factors on the arterial wall, in: A. G. Olsson (Ed.), Atherosclerosis-Biology and Clinical Science, Churchill Livingstone, Edinburgh, 1987, pp. 183–195.

[6] K. Perktold, G. Rappitsch, Mathematical modeling of arterial blood flow and correlation to atherosclerosis, Technology and Health Care 3 (3) (1995) 139–151.

[7] C. Taylor, D. Steinman, Image-based modeling of blood flow and vessel wall dynamics: Applications, methods and future directions, Annals of Biomedical Engineering 38 (3) (2010) 1188–1203.

[8] C. J. Slager, J. J. Wentzel, F. J. H. Gijsen, A. Thury, A. C. van der Wal, J. A. Schaar, P. W. Serruys, The role of shear stress in the destabilization of vulnerable plaques and related therapeutic implications, Nature Clinical Practice Cardiovascular Medicine 2 (9) (2005) 456–464.

[9] D. Tang, C. Yang, S. Mondal, F. Liu, G. Canton, T. S. Hatsukami, C. Yuan, A negative correlation between human carotid atherosclerotic plaque progression and plaque

wall stress: In vivo MRI-based 2D/3D FSI models, Journal of Biomechanics 41 (4) (2008) 727 – 736.

[10] F. P. Glor, B. Ariff, A. D. Hughes, L. A. Crowe, P. R. Verdonck, D. C. Barratt, S. A. M. Thom, D. N. Firmin, X. Y. Xu, Image-based carotid flow reconstruction: a comparison between MRI and ultrasound, Physiological Measurement 25 (6) (2004) 1495.

[11] M. F. O'Rourke, T. B. Cartmill, Influence of aortic coarctation on pulsatile hemodynamics in the proximal aorta, Circulation 44 (2) (1971) 281–292.

[12] C. A. Figueroa, I. E. Vignon-Clementel, K. E. Jansen, T. J. Hughes, C. A. Taylor, A coupled momentum method for modeling blood flow in three-dimensional deformable arteries, Computer Methods in Applied Mechanics and Engineering 195 (4143) (2006) 5685 – 5706.

[13] I. E. Vignon-Clementel, C. A. Figueroa, K. E. Jansen, C. A. Taylor, Outflow boundary conditions for three-dimensional finite element modeling of blood flow and pressure in arteries, Computer Methods in Applied Mechanics and Engineering 195 (29-32) (2006) 3776–3796.

[14] N. Wilson, K. Wang, R. Dutton, C. Taylor, A software framework for creating patient specific geometric models from medical imaging data for simulation based medical planning of vascular surgery, in: W. Niessen, M. Viergever (Eds.), Medical Image Computing and Computer-Assisted Intervention MICCAI 2001, Vol. 2208 of Lecture Notes in Computer Science, Springer Berlin Heidelberg, 2001, pp. 449–456.

[15] K. Pekkan, D. Frakes, D. de Zelicourt, C. W. Lucas, W. J. Parks, A. P. Yoganathan, Coupling pediatric ventricle assist devices to the Fontan circulation: Simulations with a lumped-parameter model, ASAIO Journal 51 (5) (2005) 618–628.

[16] L. Socci, F. Gervaso, F. Migliavacca, G. Pennati, G. Dubini, L. Ait-Ali, P. Festa, F. Amoretti, L. Scebba, V. S. Luisi, Computational fluid dynamics in a model of the total cavopulmonary connection reconstructed using magnetic resonance images, Cardiology in the Young 15 (2005) 61–67.

[17] D. A. de Zelicourt, K. Pekkan, J. Parks, K. Kanter, M. Fogel, A. P. Yoganathan, Flow study of an extracardiac connection with persistent left superior vena cava, The Journal of Thoracic and Cardiovascular Surgery 131 (4) (2006) 785 – 791.

[18] K. Pekkan, B. Whited, K. Kanter, S. Sharma, D. Zelicourt, K. Sundareswaran, D. Frakes, J. Rossignac, A. Yoganathan, Patient-specific surgical planning and

hemodynamic computational fluid dynamics optimization through free-form haptic anatomy editing tool (surgem), Medical & Biological Engineering & Computing 46 (11) (2008) 1139–1152.

[19] K. K. Whitehead, K. Pekkan, H. D. Kitajima, S. M. Paridon, A. P. Yoganathan, M. A. Fogel, Nonlinear power loss during exercise in single-ventricle patients after the Fontan: Insights from computational fluid dynamics, Circulation 116 (2007) 165–171.

[20] C. Pizarro, M. R. de Leval, Surgical variations and flow dynamics in cavopulmonary connections: A historical review, Seminars in thoracic and cardiovascular surgery. Pediatric cardiac surgery annual 1 (1) (1998) 53–60.

[21] A. L. Marsden, A. J. Bernstein, V. M. Reddy, S. C. Shadden, R. L. Spilker, F. P. Chan, C. A. Taylor, J. A. Feinstein, Evaluation of a novel Y-shaped extracardiac Fontan baffle using computational fluid dynamics, The Journal of Thoracic and Cardiovascular Surgery 137 (2) (2009) 394 – 403.

[22] P. Segers, N. Stergiopulos, P. Verdonck, R. Verhoeven, Assessment of distributed arterial network models, Medical & Biological Engineering & Computing 35 (6) (1997) 729–736.

[23] S. Mendis, P. Puska, B. Norrving, Global atlas on cardiovascular disease prevention and control, Tech. rep., World Health Organization (2011).

[24] P. Heidenreich, J. Trogdon, O. Khavjou, J. Butler, K. Dracup, M. Ezekowitz, E. Finkelstein, Y. Hong, S. Johnston, A. Khera, D. Lloyd-Jones, G. Nelson SA, Nichol, D. Orenstein, P. Wilson, Y. Woo, Forecasting the future of cardiovascular disease in the United States: a policy statement from the American Heart Association, Circulation Research 123 (8) (2011) 933–44.

[25] R. E. Klabunde, Cardiovascular Physiology Concepts, Lippincott Williams & Wilkins, 2011.

[26] F. J. H. Gijsen, E. Allanic, F. N. van de Vosse, J. D. Janssen, The influence of the non-Newtonian properties of blood on the flow in large arteries: unsteady flow in a 90 degrees curved tube, Journal of Biomechanics 32 (7) (1999) 705–713.

[27] P. J. Carreau, Rheological equations from molecular network theories, Transactions of the Society of Rheology 16 (1).

[28] D. Quemada, Rheology of concentrated disperse systems III. General features of the proposed non-Newtonian model. Comparison with experimental data, Rheologica Acta 17 (6) (1978) 643–653.

[29] O. Frank, The basic shape of the arterial pulse - 1st treatise - mathematical-analysis, Journal of Molecular and Cellular Cardiology 22 (3) (1990) 255–277.

[30] N. Westerhof, F. Bosman, C. J. Devries, A. Noordergraaf, Analog studies of human systemic arterial tree, Journal of Biomechanics 2 (2) (1969) 121–134.

[31] Y. Bazilevs, M. C. Hsu, Y. Zhang, W. Wang, X. Liang, T. Kvamsdal, R. Brekken, J. G. Isaksen, A fully-coupled fluid-structure interaction simulation of cerebral aneurysms, Computational Mechanics 46 (1) (2010) 3–16.

[32] P. Crosetto, P. Reymond, S. Deparis, D. Kontaxakis, N. Stergiopulos, A. Quarteroni, Fluid-structure interaction simulation of aortic blood flow, Computers & Fluids 43 (2011) 46–57.

[33] C. C. Long, M. C. Hsu, Y. Bazilevs, J. A. Feinstein, A. L. Marsden, Fluid-structure interaction simulations of the Fontan procedure using variable wall properties, International Journal for Numerical Methods in Biomedical Engineering 28 (5) (2012) 513–527.

[34] L. Formaggia, F. Nobile, A. Quarteroni, A. Veneziani, Multiscale modelling of the circulatory system: a preliminary analysis, Computing and Visualization in Science 2 (2-3) (1999) 75–83.

[35] J. P. Mynard, P. Nithiarasu, A 1D arterial blood flow model incorporating ventricular pressure, aortic valve and regional coronary flow using the locally conservative Galerkin (LCG) method, Communications in Numerical Methods in Engineering 24 (5) (2008) 367–417.

[36] P. J. Blanco, S. A. Urquiza, R. A. Feijoo, Assessing the influence of heart rate in local hemodynamics through coupled 3D-1D-0D models, International Journal for Numerical Methods in Biomedical Engineering 26 (7) (2010) 890–903.

[37] P. J. Blanco, R. A. Feijoo, S. A. Urquiza, A unified variational approach for coupling 3D-1D models and its blood flow applications, Computer Methods in Applied Mechanics and Engineering 196 (41-44) (2007) 4391–4410.

[38] P. J. Blanco, M. R. Pivello, S. A. Urquiza, R. A. Feijoo, On the potentialities of 3D-1D coupled models in hemodynamics simulations, Journal of Biomechanics 42 (7) (2009) 919–930.

[39] J. P. Archie, R. W. Feldtman, Critical stenosis of the internal carotid-artery, Surgery 89 (1) (1981) 67–72.

[40] P. J. Blanco, M. Discacciati, A. Quarteroni, Modeling dimensionally-heterogeneous problems: analysis, approximation and applications, Numerische Mathematik 119 (2) (2011) 299–335.

[41] A. de Moura, The geometrical multiscale modelling of the cardiovascular system: coupling 3D FSI and 1D models, Phd, Politecnico di Milano (2007).

[42] L. Formaggia, A. de Moura, F. Nobile, On the stability of the coupling of 3D and 1D fluid-structure interaction models for blood flow simulations, ESAIM-Mathematical Modelling and Numerical Analysis-Modelisation Mathematique Et Analyse Numerique 41 (4) (2007) 743–769.

[43] L. Formaggia, A. Veneziani, Reduced and multiscale models for the human cardiovascular system, Lecture notes VKI Lecture Series 2003-07, Brussels, 2003, Ch. 1.3.3.

[44] F. Nobile, Coupling strategies for the numerical simulation of blood flow in deformable arteries by 3D and 1D models, Mathematical and Computer Modelling 49 (11-12) (2009) 2152–2160.

[45] H. J. Kim, I. E. Vignon-Clementel, C. A. Figueroa, J. F. LaDisa, K. E. Jansen, J. A. Feinstein, C. A. Taylor, On coupling a lumped parameter heart model and a three-dimensional finite element aorta model, Annals of Biomedical Engineering. 37 (11) (2009) 2153–2169.

[46] K. Lagana, G. Dubini, F. Migliavacca, R. Pietrabissa, G. Pennati, A. Veneziani, A. Quarteroni, Multiscale modelling as a tool to prescribe realistic boundary conditions for the study of surgical procedures, Biorheology 39 (3-4) (2002) 359–364.

[47] F. Migliavacca, R. Balossino, G. Pennati, G. Dubini, T. Y. Hsia, M. R. de Leval, E. L. Bove, Multiscale modelling in biofluidynamics: Application to reconstructive paediatric cardiac surgery, Journal of Biomechanics 39 (6) (2006) 1010–1020.

[48] A. Quarteroni, A. Veneziani, Analysis of a geometrical multiscale model based on the coupling of ODEs and PDEs for blood flow simulations, Multiscale Modeling & Simulation 1 (2) (2003) 173–195.

[49] E. B. Shim, R. D. Kamm, T. Heldt, R. G. Mark, Numerical analysis of blood flow through a stenosed artery using a coupled multiscale simulation method, in: Computers in Cardiology 2000, Vol. 27 of Computers in Cardiology, IEEE, New York, 2000, pp. 219–222.

[50] D. A. Johnson, U. P. Naik, A. N. Beris, Efficient implementation of the proper outlet flow conditions in blood flow simulations through asymmetric arterial bifurcations, International Journal for Numerical Methods in Fluids 66 (11) (2010) 1383–1408.

[51] I. E. Vignon-Clementel, C. A. Figueroa, K. E. Jansen, C. A. Taylor, Outflow boundary conditions for 3D simulations of non-periodic blood flow and pressure fields in deformable arteries, Computer Methods in Biomechanics and Biomedical Engineering 13 (5) (2010) 625–640.

[52] P. J. Blanco, M. R. Pivello, S. A. Urquiza, N. Albuquerque de Souza e Silva, R. A. Feijoo, Coupled models technology in multi-scale computational haemodynamics, International Journal of Biomedical Engineering and Technology 5 (2-3) (2011) 132–156.

[53] J. S. Leiva, P. J. Blanco, G. C. Buscaglia, Iterative strong coupling of dimensionally heterogeneous models, International Journal for Numerical Methods in Engineering 81 (12) (2009) 1558–1580.

[54] P. Segers, E. R. Rietzschel, M. L. De Buyzere, S. J. Vermeersch, D. De Bacquer, L. M. Van Bortel, G. De Backer, T. C. Gillebert, P. R. Verdonck, Noninvasive (input) impedance, pulse wave velocity, and wave reflection in healthy middle-aged men and women, Hypertension 49 (6) (2007) 1248–1255.

[55] N. Westerhof, G. Elzinga, P. Sipkema, Artificial arterial system for pumping hearts, Journal of Applied Physiology 31 (5) (1971) 776–781.

[56] Y. B. Shi, P. Lawford, R. Hose, Review of Zero-D and 1-D Models of Blood Flow in the Cardiovascular System, Biomedical Engineering Online 10 (2011) 38.

[57] H. Suga, K. Sagawa, A. A. Shoukas, Load independence of the instantaneaous pressure-volume ratio of the canine left ventricle and effects of epinephrine and heart rate on the ratio, Circulation Research 32 (3) (1973) 314–322.

[58] T. Arts, P. H. M. Bovendeerd, F. W. Prinzen, R. S. Reneman, Relation between left-ventricular cavity pressure and volume and systolic fiber stress and strain in the wall, Biophysical Journal 59 (1) (1991) 93–102.

[59] F. van de Vosse, N. Stergiopulos, Pulse wave propagation in the arterial tree, Annual Review of Fluid Mechanics 43 (2010) 467–499.

[60] K. Perktold, G. Rappitsch, Mathematical modeling of local arterial flow and vessel mechanics, in: Computational Methods for Fluid-Structure Interaction, Vol. 306 of Pitman Research Notes in Mathematics Series, Longman Scientific & Technical, Harlow, 1994, pp. 230–245.

[61] A. Avolio, Multi-branched model of the human arterial system, Medical & Biological Engineering & Computing 18 (1980) 709–718.

[62] J. Alastruey, A. W. Khir, K. S. Matthys, P. Segers, S. J. Sherwin, P. R. Verdonck, K. H. Parker, J. Peiro, Pulse wave propagation in a model human arterial network: Assessment of 1-D visco-elastic simulations against in vitro measurements, Journal of biomechanics 44 (12) (2011) 2250–2258.

[63] W. Huberts, K. Van Canneyt, P. Segers, S. Eloot, J. Tordoir, P. Verdonck, F. van de Vosse, E. Bosboom, Experimental validation of a pulse wave propagation model for predicting hemodynamics after vascular access surgery, Journal of biomechanics 45 (9) (2012) 1684–91.

[64] G. A. Holzapfel, R. W. Ogden, Constitutive modelling of arteries, Proceedings of the Royal Society a-Mathematical Physical and Engineering Sciences 466 (2118) (2010) 1551–1596.

[65] M. Heil, A. L. Hazel, Fluid-structure interaction in internal physiological flows, Annual Review of Fluid Mechanics 43 (2011) 141–162.

[66] G. N. Hou, J. Wang, A. Layton, Numerical methods for fluid-structure interaction - a review, Communications in Computational Physics 12 (2) (2012) 337–377.

[67] T. Passerini, M. de Luca, L. Formaggia, A. Quarteroni, A. Veneziani, A 3D/1D geometrical multiscale model of cerebral vasculature, Journal of Engineering Mathematics 64 (4) (2009) 319–330.

[68] L. Formaggia, J. F. Gerbeau, F. Nobile, A. Quarteroni, On the coupling of 3D and 1D Navier-Stokes equations for flow problems in compliant vessels, Computer Methods in Applied Mechanics and Engineering 191 (6-7) (2001) 561–582.

[69] A. de Moura, C. Vergara, Flow rate boundary conditions and multiscale modelling of the cardiovascular system in compliant domains, in: Modelling in Medicine and Biology VI, Vol. 8 of Wit Transactions on Biomedicine and Health, Wit Press/Computational Mechanics Publications, Southampton, 2005, pp. 351–359.

[70] A. K. Wake, J. N. Oshinski, A. R. Tannenbaum, D. P. Giddens, Choice of in vivo versus idealized velocity boundary conditions influences physiologically relevant flow patterns in a subject-specific simulation of flow in the human carotid bifurcation, Journal of Biomechanical Engineering-Transactions of the Asme 131 (2) (2009) 8.

[71] K. R. Moyle, L. Antiga, D. A. Steinman, Inlet conditions for image-based CFD models of the carotid bifurcation: Is it reasonable to assume fully developed flow?, Journal of Biomechanical Engineering-Transactions of the Asme 128 (3) (2006) 371–379.

[72] J. G. Heywood, R. Rannacher, S. Turek, Artificial boundaries and flux and pressure conditions for the incompressible Navier-Stokes equations, International Journal for Numerical Methods in Fluids 22 (5) (1996) 325–352.

[73] L. Formaggia, J. F. Gerbeau, F. Nobile, A. Quarteroni, Numerical treatment of defective boundary conditions for the Navier-Stokes equations, SIAM Journal on Numerical Analysis 40 (1) (2002) 376–401.

[74] A. Veneziani, C. Vergara, Flow rate defective boundary conditions in haemodynamics simulations, International Journal for Numerical Methods in Fluids 47 (8-9) (2005) 803–816.

[75] A. Veneziani, C. Vergara, An approximate method for solving incompressible Navier-Stokes problems with flow rate conditions, Computer Methods in Applied Mechanics and Engineering 196 (9-12) (2007) 1685–1700.

[76] L. Formaggia, A. Veneziani, C. Vergara, A new approach to numerical solution of defective boundary value problems in incompressible fluid dynamics, SIAM Journal on Numerical Analysis 46 (6) (2008) 2769–2794.

[77] L. Formaggia, A. Veneziani, C. Vergara, Flow rate boundary problems for an incompressible fluid in deformable domains: Formulations and solution methods, Computer Methods in Applied Mechanics and Engineering 199 (9-12) (2010) 677–688.

[78] J. S. Leiva, P. J. Blanco, G. C. Buscaglia, Partitioned analysis for dimensionally-heterogeneous hydraulic networks, Multiscale Modeling & Simulation 9 (2) (2011) 872–903.

[79] M. P. Spencer, A. B. Denison, The square-wave electromagnetic flowmeter - theory of operation and design of magnetic probes for clinical and experimental applications, Ire Transactions on Medical Electronics 6 (4) (1959) 220–228.

[80] H. J. Kim, I. E. Vignon-Clementel, J. S. Coogan, C. A. Figueroa, K. E. Jansen, C. A. Taylor, Patient-specific modeling of blood flow and pressure in human coronary arteries, Annals of Biomedical Engineering 38 (10) (2010) 3195–3209.

[81] A. Baretta, C. Corsini, A. L. Marsden, I. E. Vignon-Clementel, T. Y. Hsia, G. Dubini, F. Migliavacca, G. Pennati, Respiratory effects on hemodynamics in patient-specific CFD models of the Fontan circulation under exercise conditions, European Journal of Mechanics B-Fluids 35 (2012) 61–69.

[82] P. J. Blanco, P. R. Trenhago, L. G. Fernandes, R. A. Feijoo, On the integration of the baroreflex control mechanism in a heterogeneous model of the cardiovascular system, International Journal for Numerical Methods in Biomedical Engineering 28 (4) (2012) 412–433.

[83] P. J. Blanco, R. A. Feijoo, Sensitivity analysis in kinematically incompatible models, Computer Methods in Applied Mechanics and Engineering 198 (41-44) (2009) 3287–3298.

[84] B. Rousselet, E. J. Haug, Design sensitivity analysis in structural mechanics. Effects of shape variation, Journal of Structural Mechanics 10 (3) (1982) 273–310.

[85] K. W. Chow, C. C. Mak, A simple model for the two dimensional blood flow in the collapse of veins, Journal of Mathematical Biology 52 (6) (2006) 733–744.

[86] F. Y. Liang, S. Takagi, R. Himeno, H. Liu, Biomechanical characterization of ventricular-arterial coupling during aging: A multi-scale model study, Journal of Biomechanics 42 (6) (2009) 692–704.

[87] J. Janela, A. Moura, A. Sequeira, Absorbing boundary conditions for a 3D non-Newtonian fluid-structure interaction model for blood flow in arteries, International Journal of Engineering Science 48 (2010) 1332–1349.

[88] E. Jarvinen, M. Lyly, J. Ruokolainen, P. Raback, Three-dimensional fluid-structure interaction modeling of blood flow in elastic arteries, in: ECCOMAS CFD, Swansea, United Kingdom, 2001.

[89] E. Isaacson, H. Keller, Analysis of Numerical Methods, Dover, 1994.

[90] A. Quarteroni, Numerical Models for Differential Problems, Springer, 2009.

[91] J. Ferziger, M. Peric, Computational Methods for Fluid Dynamics, Springer, 2002.

[92] S. V. Patankar, Numerical Heat Transfer and Fluid Flow, Hemisphere, 1980.

[93] H. M. Hilber, T. J. R. Hughes, R. L. Taylor, Improved numerical dissipation for time integration algorithms in structural dynamics, Earthquake Engineering & Structural Dynamics 5 (1977) 283–292.

[94] J. Degroote, K.-J. Bathe, J. Vierendeels, Performance of a new partitioned procedure versus a monolithic procedure in fluid-structure interaction, Computers and Structures 87 (11-12) (2009) 793–801.

[95] R. LeVeque, Numerical Methods for Conservation Laws, Birkhäuser, 1992.

[96] M. Breuer, G. D. Nayer, M. Münsch, T. Gallinger, R. Wüchner, Fluids-structure interaction using a partitioned semi-implicit predictor-corrector coupling scheme for the application of large-eddy simulation, Journal of Fluids and Structures 29 (2012) 107 – 130.

[97] C. Kassiotis, J.-B. Colliat, A. Ibrahimbegovic, H. Matthies, Multiscale in time and stability analysis of operator split solution procedures applied to thermomechanical problems, Engineering Computations 26(1-2) (2009) 205–223.

[98] A. Valli, F. Carey, A. Coutinho, On decoupled time step/subcycling and iteration strategies for multiphysics problems, Communications in Numerical Methods in Engineering 24 (2008) 1941 – 1952.

[99] M. Putti, C. Paniconi, Time step and stability control for a coupled model of surface and subsurface flow, in: Proceedings of the XVth International Conference on Computational Methods in Water Resources, Vol. 55, Elsevier, Chapel Hill, NC, USA, 2004, pp. 1391–1402.

[100] J. M. Connors, J. S. Howell, A fluid-fluid interaction method using decoupled subproblems and differing time steps, Numerical Methods for Partial Differential Equations 28(4) (2012) 1283–1308.

[101] N. Mahjoubi, A. Gravouil, A. Combescure, N. Greffet, A monolithic energy conserving method to couple heterogeneous time integrators with incompatible time steps in structural dynamics, Computer Methods in Applied Mechanics and Engineering 200 (9-12) (2010) 1069 – 1086.

[102] M. M. Joosten, W. G. Dettmer, D. Perić, On the temporal stability and accuracy of coupled problems with reference to fluid-structure interaction, Numerical Methods in Fluids 64 (2010) 1363–1378.

[103] J. Vierendeels, K. Dumont, E. Dick, P. Verdonck, Analysis and stabilization of fluid-structure interaction algorithm for rigid-body motion, AIAA journal 43 (2005) 2549–2557.

[104] S. Piperno, C. Farhat, B. Larrouturouc, Partitioned procedures for the transient solution of coupled aroelastic problems Part I: Model problem, theory and two-dimensional application, Computer Methods in Applied Mechanics and Engineering 124 (1995) 79 – 112.

[105] A. Quarteroni, M. Tuveri, A. Venezian, Computational vascular fluid dynamics: problems, models and methods, Computing and Visualization in Science 2 (2000) 163–197.

[106] K. Perktold, G. Rappitsch, Mathematical modeling of local arterial flow and vessel mechanics, in: Computation Methods for fluid Structure Interaction. Pitman Research Notes in Mathematics, 1994, pp. 230–245.

[107] J. Degroote, S. Annerel, J. Vierendeels, Stability analysis of Gauss-Seidel iterations in a partitioned simulation of fluid-structure interaction, Computers and Structures 88 (2010) 263–271.

[108] L. Taelman, J. Degroote, A. Swillens, J. Vierendeels, P. Segers, Pulse wave analysis of grid and time step converged fluid-structure interaction calculations, in: Proceedings of the Vth International Conference on Advanced Computational Methods in Engineering, Luik, Belgium, 2011.

[109] P. Fischer, F. Loth, S. E. Lee, S.-W. Lee, D. Smith, H. Bassiouny, Simulation of high-Reynolds number vascular flows, Computer Methods in Applied Mechanics and Engineering 196 (2007) 3049 – 3060.

[110] J. Degroote, P. Bruggeman, R. Haelterman, J. Vierendeels, Stability of a coupling technique for partitioned solvers in FSI applications, Computers and Structures 86(23-24) (2008) 2224 – 2234.

[111] U. Küttler, W. Wall, Fixed-point fluid-structure interaction solvers with dynamic relaxation, Computational Mechanics 43 (1) (2008) 61–72.

[112] C. Michler, E. H. van Brummelen, R. de Borst, An interface Newton-Krylov solver for fluid-structure interaction, International Journal for Numerical Methods in Fluids 47 (10-11) (2005) 1189–1195.

[113] Website pyFormex, `http://pyformex.berlios.de`.

[114] P. Prendergast, C. Lally, S. Daly, A. Reid, T. Lee, D. Quinn, F. Dolan, Analysis of prolapse in cardiovascular stents: A constitutive equation for vascular tissue and finite-element modelling, Journal of Biomechanical Engineering - Transactions ASME 125 (2003) 692–699.

[115] G. De Santis, P. Mortier, M. De Beule, P. Segers, P. Verdonck, B. Verhegghe, Patient-specific computational fluid dynamics: structured mesh generation from coronary angiography, Medical & Biological Engineering & Computing 48 (4) (2010) 371–380.

[116] P. W. Longest, S. Vinchurkar, Effects of mesh style and grid convergence on particle deposition in bifurcating airway models with comparisons to experimental data, Medical Engineering & Physics 29 (3) (2007) 350 – 366.

[117] L. Antiga, B. Ene-Iordache, L. Caverni, G. P. Cornalba, A. Remuzzi, Geometric reconstruction for computational mesh generation of arterial bifurcations from CT angiography, Computerized Medical Imaging and Graphics 26 (4) (2002) 227 – 235.

[118] Y. Liu, K. Pekkan, S. Jones, A. Yoganathan, The effects of different mesh generation methods on computational fluid dynamic analysis and power loss assessment in total cavopulmonary connection, Journal of biomechanical engineering 126 (5) (2004) 594–603.

[119] R. Biswas, R. C. Strawn, Tetrahedral and hexahedral mesh adaptation for CFD problems, Applied Numerical Mathematics 26 (12) (1998) 135 – 151.

[120] J. Bols, G. D. Santis, J. Degroote, B. Verhegghe, P. Segers, J. Vierendeels, Automated hexahedral mesh generation in a complex vascular tree: the extended Treemesh method, in: Proceedings of the ASME 2013 SBC, 2013, p. V01AT13A019.

[121] J. Bols, L. Taelman, Simultation of the fluid-structure interaction in a membrane pump, mater thesis, University of Ghent (2010).

[122] J. Degroote, Development of algorithms for the partitioned simulation of strongly coupled fluid-structure interaction problems, Doctoraatsthesis, Universiteit Gent Faculteit ingenieurswetenschappen (2009-2010).

[123] D. Bergsma, Birth defects: atlas and compendium, Williams and Wilkins Co, Baltimore, 1974.

[124] P. Rao, Coarctation of the aorta, Seminars in nephrology 15 (1995) 87–105.

[125] C. Ferencz, J. D. Rubin, R. J. McCarter, J. I. Brenner, C. A. Neill, L. W. Perry, S. I. Hepner, J. W. Downing, Congenital heart disease: Prevalence at livebirth: The Baltimore-Washington infant study, American Journal of Epidemiology 121 (1) (1985) 31–36.

[126] K. L. McBride, L. Marengo, M. Canfield, P. Langlois, D. Fixler, J. W. Belmont, Epidemiology of noncomplex left ventricular outflow tract obstruction malformations (aortic valve stenosis, coarctation of the aorta, hypoplastic left heart syndrome) in texas, 1999-2001, Birth Defects Research Part A: Clinical and Molecular Teratology 73 (8) (2005) 555–561.

[127] C. R. W. Edwards, S. Davidson, Davidson's Principles and Practice of Medicine, Churchill Livingstone, Edinburgh, 1995.

[128] Coarctation of the aorta, `http://en.wikipedia.org/wiki/Coarctation_of_the_aorta`.

[129] Fetal circulatory system, `http://cnx.org/content/col11496/1.6/`.

[130] E. Rodriguez-Cruz, L. M. Ettinger, Hypertension, eMedicine Pediatrics: Cardiac Disease and Critical Care Medicine (2010) .

[131] A. Bocelli, S. Favilli, I. Pollini, R. Bini, P. Ballo, E. Chiappa, A. Zuppiroli, Prevalence and long-term predictors of left ventricular hypertrophy, late hypertension, and hypertensive response to exercise after successful aortic coarctation repair, Pediatric Cardiology 34 (3) (2013) 620–629.

[132] J. W. Vriend, B. J. Mulder, Late complications in patients after repair of aortic coarctation: implications for management, International Journal of Cardiology 101 (3) (2005) 399 – 406.

[133] R. Brouwer, M. Erasmus, T. Ebels, A. Eijgelaar, Influence of age on survival, late hypertension, and recoarctation in elective aortic coarctation repair - Including long-term results after elective aortic coarctation repair with a follow-up from 25 to 44 years, Journal of Thoracic and Cardiovascular Surgery 108 (3) (1994) 525–531.

[134] O. H. Toro-Salazar, J. Steinberger, W. Thomas, A. P. Rocchini, B. Carpenter, J. H. Moller, Long-term follow-up of patients after coarctation of the aorta repair, The American Journal of Cardiology 89 (5) (2002) 541 – 547.

[135] S. Chen, A. Donald, C. Storry, J. Halcox, P. Bonhoeffer, J. Deanfield, Impact of aortic stenting on peripheral vascular function and daytime systolic blood pressure in adult coarctation, Heart 94 (2008) 919–924.

[136] S. Daniels, Repair of coarctation of the aorta and hypertension: does age matter?, Lancet 358 (2001) 89.

[137] M. E. Brickner, L. D. Hillis, R. A. Lange, Congenital heart disease in adults, New England Journal of Medicine 342 (4) (2000) 256–263.

[138] D. C. Wendell, M. M. Samyn, J. R. Cava, L. M. Ellwein, M. M. Krolikowski, K. L. Gandy, A. N. Pelech, S. C. Shadden, J. F. L. Jr., Including aortic valve morphology in computational fluid dynamics simulations: Initial findings and application to aortic coarctation, Medical Engineering & Physics 35 (6) (2013) 723 – 735.

[139] C. Ward, Clinical significance of the bicuspid aortic valve, Heart 83 (1) (2000) 81–85.

[140] R. M. Freedom, Congenital heart disease: textbook of angiocardiography, Futura, Armonk, NY, 1997.

[141] Aortic valves, `http://my.clevelandclinic.org/heart/disorders/congenital/congenvalve.aspx`.

[142] C. E. G. Head, V. C. Jowett, G. K. Sharland, J. M. Simpson, Timing of presentation and postnatal outcome of infants suspected of having coarctation of the aorta during fetal life, Heart 91 (8) (2005) 1070–1074.

[143] C. Wren, Z. Reinhardt, K. Khawaja, Twenty-year trends in diagnosis of life-threatening neonatal cardiovascular malformations, Archives of Disease in Childhood - Fetal and Neonatal Edition 93 (1) (2008) 33–35.

[144] K. L. Brown, D. A. Ridout, A. Hoskote, L. Verhulst, M. Ricci, C. Bull, Delayed diagnosis of congenital heart disease worsens preoperative condition and outcome of surgery in neonates, Heart 92 (9) (2006) 1298–1302.

[145] E. Rosenthal, Stent implantation for aortic coarctation: the treatment of choice in adults?, Journal of the American College of Cardiology 38 (2001) 1527–1527.

[146] D. E. Teien, H. Wendel, J. Björnebrink, L. Ekelund, Evaluation of anatomical obstruction by Doppler echocardiography and magnetic resonance imaging in patients with coarctation of the aorta, British Heart Journal 69 (4) (1993) 352–355.

[147] S. B. Greenberg, R. K. Balsara, E. N. Faerber, Coarctation of the aorta: diagnostic imaging after corrective surgery, Journal of thoracic imaging 10 (1) (1995) 36–42.

[148] S. D. Mey, P. Segers, I. Coomans, H. Verhaaren, P. Verdonck, Limitations of Doppler echocardiography for the post-operative evaluation of aortic coarctation, Journal of Biomechanics 34 (7) (2001) 951 – 960.

[149] J. J. Hom, K. Ordovas, G. P. Reddy, Velocity-encoded cine MR imaging in aortic coarctation: functional assessment of hemodynamic events, RadioGraphics 28 (2) (2008) 407–416.

[150] P. A. Araoz, G. P. Reddy, H. Tarnoff, C. L. Roge, C. B. Higgins, MR findings of collateral circulation are more accurate measures of hemodynamic significance than arm-leg blood pressure gradient after repair of coarctation of the aorta, Journal of Magnetic Resonance Imaging 17 (2) (2003) 177–183.

[151] J. Günthard, P. T. Buser, R. Miettunen, A. Hagmann, F. Wyler, Effects of morphologic restenosis, defined by MRI after coarctation repair, on blood pressure and arm-leg and Doppler gradients, Angiology 47 (11) (1996) 1073–1080.

[152] L. Itu, P. Sharma, K. Ralovich, V. Mihalef, R. Ionasec, A. Everett, R. Ringel, A. Kamen, D. Comaniciu, Non-invasive hemodynamic assessment of aortic coarctation: Validation with in vivo measurements, Annals of Biomedical Engineering 41 (4) (2013) 669–681.

[153] A. Aldousany, T. DiSessa, B. Alpert, S. Birnbaum, E. Willey, Significance of the Doppler-derived gradient across a residual aortic coarctation, Pediatric Cardiology 11 (1) (1990) 8–14.

[154] K. C. Chan, D. F. Dickinson, G. A. Wharton, J. L. Gibbs, Continuous wave Doppler echocardiography after surgical repair of coarctation of the aorta, British heart journal 68 (2) (1992) 192–4.

[155] J. S. Carvalho, A. N. Redington, E. A. Shinebourne, M. L. Rigby, D. Gibson, Continuous wave Doppler echocardiography and coarctation of the aorta: gradients and flow patterns in the assessment of severity, British heart journal 64 (1990) 133–137.

[156] P. A. Kappetein, G. L. Guit, A. J. Bogers, H. W. Weeda, K. H. Zwinderman, J. P. Schönberger, H. A. Huysmans, Noninvasive long-term follow-up after coarctation repair, The Annals of Thoracic Surgery 55 (5) (1993) 1153 – 1159.

[157] E.G. Mühler, J.M. Neuerburg, A. Rüben, R. Grabitz, R. Gunther, B. Messmer and G. von-Bernuth, Evaluation of aortic coarctation after surgical repair: role of magnetic resonance imaging and Doppler ultrasound, British heart journal 70 (3) (1993) 285–290.

[158] C. A. Warnes, R. G. Williams, T. M. Bashore, J. S. Child, H. M. Connolly, J. A. Dearani, P. del Nido, J. W. Fasules, T. P. Graham, Z. M. Hijazi, S. A. Hunt, M. E. King, M. J. Landzberg, P. D. Miner, M. J. Radford, E. P. Walsh, G. D. Webb, Guidelines for the management of adults with congenital heart disease: A report of the American College of Cardiology/American Heart Association Task Force on practice guidelines, Circulation 118 (23) (2008) 714–833.

[159] S. Muzzarelli, A. K. Meadows, K. G. Ordovas, M. D. Hope, C. B. Higgins, J. C. Nielsen, T. Geva, J. J. Meadows, Prediction of hemodynamic severity of coarctation by magnetic resonance imaging, The American Journal of Cardiology 108 (9) (2011) 1335 – 1340.

[160] J. C. Nielsen, A. J. Powell, K. Gauvreau, E. N. Marcus, A. Prakash, T. Geva, Magnetic resonance imaging predictors of coarctation severity, Circulation 111 (5) (2005) 622–628.

[161] I. Valverde, C. Staicu, H. Grotenhuis, A. Marzo, K. Rhode, Y. Shi, A. Brown, A. Tzifa, T. Hussain, G. Greil, P. Lawford, R. Razavi, R. Hose, P. Beerbaum, Predicting hemodynamics in native and residual coarctation: preliminary results of a Rigid-Wall Computational-Fluid-Dynamics model (RW-CFD) validated against clinically invasive pressure measures at rest and during pharmacological stress, Journal of Cardiovascular Magnetic Resonance 13 (1) (2011) 1–4.

[162] J. Marek, J. Skovranek, B. Hucin, V. Chaloupecky, P. Tax, O. Reich, M. Samanek, Seven-year experience of noninvasive preoperative diagnostics in children with congenital heart defects: comprehensive analysis of 2,788 consecutive patients, Circulation 86 (6) (1995) 488–495.

[163] H. Ntsinjana, M. Hughes, A. Taylor, The role of cardiovascular magnetic resonance in pediatric congenital heart disease, Journal of Cardiovascular Magnetic Resonance 13 (1) (2011) 1–20.

[164] J. L. Gibbs, Treatment options for coarctation of the aorta, Heart 84 (1) (2000) 11–13.

[165] C. Crafoord, G. Nylin, Congenital coarctation of the aorta and its surgical treatment, Journal of Thoracic Surgery 14 (1945) 347–361.

[166] A. M. Gaca, J. J. Jaggers, L. T. Dudley, G. S. Bisset, Repair of congenital heart disease: A primer – part 2, Radiology 248 (1) (2008) 44–60.

[167] K. Vossschulte, Plastic surgery of the isthmus in aortic isthmus stenosis, Thoraxchirurgie 4 (5) (1957) 443–450.

[168] H. Aebert, J. Laas, P. Bednarski, U. Koch, M. Prokop, B. HG., High incidence of aneurysm formation following patch plasty repair of coarctation, European Journal of Cardio-Thoracic Surgery 7 (4) (1993) 200–204.

[169] J. A. Waldhausen, D. L. Nahrwold, Repair of coarctation of the aorta with a subclavian flap, Journal of Thoracic and Cardiovascular Surgery 51 (4) (1966) 532–533.

[170] P. Pollack, M. D. Freed, A. R. Castaneda, W. I. Norwood, Reoperation for isthmic coarctation of the aorta: follow-up of 26 patients, The American journal of cardiology 51 (10) (1983) 1690–1694.

[171] J. E. Lock, T. Niemi, B. A. Burke, S. Einzig, W. R. Castaneda-Zuniga, Transcutaneous angioplasty of experimental aortic coarctation, Circulation 66 (6) (1982) 1280–6.

[172] Balloon angioplasty, `http://en.wikipedia.org/wiki/Angioplasty`.

[173] R. R. Liberthson, D. Pennington, M. L. Jacobs, W. M. Daggett, Coarctation of the aorta: Review of 234 patients and clarification of management problems, The American Journal of Cardiology 43 (4) (1979) 835 – 840.

[174] J. E. Connolly, Prevention of spinal cord complications in aortic surgery, The American Journal of Surgery 176 (2) (1998) 92 – 101.

[175] B. D. Thanopoulos, L. Hadjinikolaou, G. N. Konstadopoulou, G. S. Tsaousis, F. Triposkiadis, P. Spirou, Stent treatment for coarctation of the aorta: intermediate term follow up and technical considerations, Heart 84 (1) (2000) 65–70.

[176] B. D. Thanopoulos, L. Hadjinikolaou, G. N. Konstadopoulou, G. S. Tsaousis, F. Triposkiadis, P. Spirou, Stent treatment for coarctation of the aorta: intermediate term follow up and technical considerations, Heart 84 (1) (2000) 65–70.

[177] N. Jenkins, C. Ward, Coarctation of the aorta: natural history and outcome after surgical treatment, QJM 92 (7) (1999) 365–371.

[178] M. Cohen, V. Fuster, P. M. Steele, D. Driscoll, D. C. McGoon, Coarctation of the aorta. Long-term follow-up and prediction of outcome after surgical correction, Circulation 80 (4) (1989) 840–5.

[179] A. Rothman, Coarctation of the aorta: an update, Current problems in pediatrics 28 (2) (1998) 33–60.

[180] M. M. d. C. S. Maia, V. D. Aiello, M. Barbero-Marcial, M. Ebaid, Coarctation of the aorta corrected during childhood. Clinical aspects during follow-up, Arquivos Brasileiros de Cardiologia 74 (2000) 174 – 180.

[181] P. M. Clarkson, M. R. Nicholson, B. G. Barratt-Boyes, J. M. Neutze, R. M. Whitlock, Results after repair of coarctation of the aorta beyond infancy: A 10 to 28 year follow-up with particular reference to late systemic hypertension, The American Journal of Cardiology 51 (9) (1983) 1481 – 1488.

[182] A. B. Stewart, R. Ahmed, C. M. Travill, C. G. Newman, Coarctation of the aorta life and health 20-44 years after surgical repair, Heart 69 (1993) 65–70.

[183] J. E. Rubay, T. Sluysmans, V. Alexandrescu, K. Khelif, D. Moulin, A. Vliers, P. Jaumin, C. H. Chalant, Surgical repair of coarctation of the aorta in infants under one year of age. Long-term results in 146 patients comparing subclavian flap angioplasty and modified end-to-end anastomosis, The Journal of cardiovascular surgery 33 (1992) 216–222.

[184] M. Koller, M. Rothlin, A. Senning, Coarctation of the aorta: review of 362 operated patients. Long-term follow-up and assessment of prognostic variables, European heart journal 8 (1987) 670–679.

[185] P. A. Abbruzzese, E. Aidala, Aortic coarctation: an overview, Journal of Cardiovascular Medicine 8 (2007) 1558–2027.

[186] L. Bergdahl, A. Ljungqvist, Long-term results after repair of coarctation of the aorta by patch grafting, The Journal of thoracic and cardiovascular surgery 80 (1980) 171–188.

[187] G. V. Knyshov, L. L. Sitar, M. D. Glagola, M. Y. Atamanyuk, Aortic aneurysms at the site of the repair of coarctation of the aorta: A review of 48 patients, The Annals of Thoracic Surgery 61 (3) (1996) 935 – 939.

[188] B. J. Maron, J. O. Humphries, R. D. Rowe, E. D. Mellitis, Prognosis of surgically corrected coarctation of the aorta: A 20-year postoperative appraisal, Circulation 47 (1) (1973) 119–126.

[189] I. C. Omeje, M. Valentikova, M. Kostolny, M. Sagat, M. Nosal, J. Siman, V. Hraska, Improved patient survival following surgery for coarctation of the aorta, Bratislavske lekarske listy 104 (2) (2003) 73–77.

[190] E. N. Oechslin, Does a stent cure hypertension?, Heart 94 (2008) 828–829.

[191] L. Swan, H. Ashrafian, M. Gatzoulis, Repair of coarctation: a higher goal?, Lancet 359 (2002) 977–978.

[192] D. S. Celermajer, K. Greaves, Survivors of coarctation repair: fixed but not cured, Heart 88 (2) (2002) 113–114.

[193] A. Hager, S. Kanz, H. Kaemmerer, J. Hess, Exercise capacity and exercise hypertension after surgical repair of isolated aortic coarctation, The American Journal of Cardiology 101 (12) (2008) 1777 – 1780.

[194] M. de Divitiis, P. Rubba, R. Calabrò, Arterial hypertension and cardiovascular prognosis after successful repair of aortic coarctation: A clinical model for the study of vascular function, Nutrition, Metabolism and Cardiovascular Diseases 15 (5) (2005) 382 – 394.

[195] S. E. Fletcher, M. R. Nihill, R. G. Grifka, M. P. O'Laughlin, C. E. Mullins, Balloon angioplasty of native coarctation of the aorta: Midterm follow-up and prognostic factors, Journal of the American College of Cardiology 25 (3) (1995) 730 – 734.

[196] F. Bouchart, A. Dubar, A. Tabley, P. Y. Litzler, C. Haas-Hubscher, M. Redonnet, J. P. Bessou, R. Soyer, Coarctation of the aorta in adults: surgical results and long-term follow-up, The Annals of Thoracic Surgery 70 (5) (2000) 1483 – 1488.

[197] T. A. Johnston, R. G. Grifka, T. K. Jones, Endovascular stents for treatment of coarctation of the aorta: Acute results and follow-up experience, Catheterization and Cardiovascular Interventions 62 (4) (2004) 499–505.

[198] C. M. Ong, C. E. Canter, F. R. Gutierrez, D. R. Sekarski, D. R. Goldring, Increased stiffness and persistent narrowing of the aorta after successful repair of coarctation of the aorta: relationship to left ventricular mass and blood pressure at rest and with exercise, American heart journal 123 (6) (1992) 1594–1600.

[199] A. N. Pelech, W. Kartodihardjo, J. A. Balfe, J. W. Balfe, P. M. Olley, F. H. Leenen, Exercise in children before and after coarctectomy: Hemodynamic, echocardiographic, and biochemical assessment, American Heart Journal 112 (6) (1986) 1263 – 1270.

[200] J. F. LaDisa, Jr., C. A. Taylor, J. A. Feinstein, Aortic coarctation: Recent developments in experimental and computational methods to assess treatments for this simple condition, Progress in Pediatric Cardiology 30 (12) (2010) 45 – 49.

[201] Z. Keshavarz-Motamed, L. Kadem, 3D pulsatile flow in a curved tube with coexisting model of aortic stenosis and coarctation of the aorta, Medical Engineering & Physics 33 (3) (2011) 315 – 324.

[202] L. Olivieri, D. Zélicourt, C. Haggerty, K. Ratnayaka, R. Cross, A. Yoganathan, Hemodynamic modeling of surgically repaired coarctation of the aorta, Cardiovascular Engineering and Technology 2 (4) (2011) 288–295.

[203] A. Arzani, P. Dyverfeldt, T. Ebbers, S. Shadden, In vivo validation of numerical prediction for turbulence intensity in an aortic coarctation, Annals of Biomedical Engineering 40 (4) (2012) 860–870.

[204] M. D. Hope, A. K. Meadows, T. A. Hope, K. G. Ordovas, D. Saloner, G. P. Reddy, M. T. Alley, C. B. Higgins, Clinical evaluation of aortic coarctation with 4D flow MR imaging, Journal of Magnetic Resonance Imaging 31 (3) (2010) 711–718.

[205] A. Frydrychowicz, A. F. Stalder, M. F. Russe, J. Bock, S. Bauer, A. Harloff, A. Berger, M. Langer, J. Hennig, M. Markl, Three-dimensional analysis of segmental wall shear stress in the aorta by flow-sensitive four-dimensional-MRI, Journal of Magnetic Resonance Imaging 30 (1) (2009) 77–84.

[206] J. J. Wentzel, R. Corti, Z. A. Fayad, P. Wisdom, F. Macaluso, M. O. Winkelman, V. Fuster, J. J. Badimon, Does shear stress modulate both plaque progression and regression in the thoracic aorta? Human study using serial magnetic resonance imaging, Journal of the American College of Cardiology 45 (6) (2005) 846 – 854.

[207] J. F. Jr. LaDisa, R. J. Dholakia, C. A. Figueroa, I. E. Vignon-Clementel, F. P. Chan, M. M. Samyn, J. R. Cava, C. A. Taylor, J. A. Feinstein, Computational simulations demonstrate altered wall shear stress in aortic coarctation patients treated by resection with end-to-end anastomosis, Congenital Heart Disease 6 (5) (2011) 432–443.

[208] S. Jin, J. Oshinski, D. P. Giddens, Effects of wall motion and compliance on flow patterns in the ascending aorta, Journal of Biomechanical Engineering 125 (3) (2003) 347–354.

[209] C. G. DeGroff, W. Orlando, R. Shandas, Insights into the effect of aortic compliance on Doppler diastolic flow patterns seen in coarctation of the aorta: A numeric study, Journal of the American Society of Echocardiography 16 (2) (2003) 162 – 169.

[210] J. S. Coogan, F. P. Chan, C. A. Taylor, J. A. Feinstein, Computational fluid dynamic simulations of aortic coarctation comparing the effects of surgical- and stent-based treatments on aortic compliance and ventricular workload, Catheterization and Cardiovascular Interventions 77 (5) (2011) 680–691.

[211] J. F. LaDisa, C. A. Taylor, J. A. Feinstein, Endovascular treatment strategies for coarctation of the aorta, in: H. Rousseau, J.-P. Verhoye, J.-F. Heautot (Eds.), Thoracic Aortic Diseases, Springer Berlin Heidelberg, 2006, pp. 363–374.

[212] T. S. Hornung, L. N. Benson, P. R. McLaughlin, Interventions for aortic coarctation, Cardiology in Review 10 (3) (2002) 139–148.

[213] M. J. Mullen, Coarctation of the aorta in adults: do we need surgeons?, Heart 89 (1) (2003) 3–5.

[214] V. Mahadevan, M. J. Mullen, Endovascular management of aortic coarctation, International Journal of Cardiology 97 (2004) 75 – 78.

[215] E. De Caro, I. Spadoni, R. Crepaz, M. Saitta, G. Trocchio, C. MG, G. Pongiglione, Stenting of aortic coarctation and exercise-induced hypertension in the young, Catheterization and Cardiovascular Interventions 75 (2) (2010) 256–261.

[216] S. P. Sanders, Endovascular stent treatment of aortic coarctation, American Heart Journal 139 (6) (2000) 936 – 938.

[217] A. G. Magee, G. Brzezinska-Rajszys, S. A. Qureshi, E. Rosenthal, M. Zubrzycka, J. Ksiazyk, M. Tynan, Stent implantation for aortic coarctation and recoarctation, Heart 82 (5) (1999) 600–606.

[218] D. Boshoff, W. Budts, L. Mertens, B. Eyskens, T. Delhaas, B. Meyns, W. Daenen, M. Gewillig, Stenting of hypoplastic aortic segments with mild pressure gradients and arterial hypertension, Heart 92 (11) (2006) 1661–1666.

[219] J. F. J. LaDisa, C. Alberto Figueroa, I. E. Vignon-Clementel, H. J. Kim, N. Xiao, L. M. Ellwein, F. P. Chan, J. A. Feinstein, C. A. Taylor, Computational simulations for aortic coarctation: representative results from a sampling of patients, Journal of biomechanical engineering 133 (9).

[220] J. D. Humphrey, Mechanisms of arterial remodeling in hypertension: Coupled roles of wall shear and intramural stress, Hypertension 52 (2) (2008) 195–200.

[221] H. Wolinsky, Response of the rat aortic media to hypertension: Morphological and chemical studies, Circulation Research 26 (4) (1970) 507–522.

[222] T. Matsumoto, K. Hayashi, Mechanical and dimensional adaptation of rat aorta to hypertension, Journal of biomechanical engineering 116 (3) (1994) 278–283.

[223] S. Laurent, P. Boutouyrie, P. Lacolley, Structural and genetic bases of arterial stiffness, Hypertension 45 (6) (2005) 1050–1055.

[224] G. B. Kim, S. J. Kang, E. J. Bae, Y. S. Yun, C. I. Noh, J. R. Lee, Y. J. Kim, J. Y. Lee, Elastic properties of the ascending aorta in young children after successful coarctoplasty in infancy, International Journal of Cardiology 97 (3) (2004) 471 – 477.

[225] J. Xu, T. Shiota, R. Omoto, X. Zhou, S. Kyo, M. Ishii, M. J. Rice, D. J. Sahn, Intravascular ultrasound assessment of regional aortic wall stiffness, distensibility, and compliance in patients with coarctation of the aorta, American Heart Journal 134 (1) (1997) 93 – 98.

[226] A. Valentín, L. Cardamone, S. Baek, J. Humphrey, Complementary vasoactivity and matrix remodelling in arterial adaptations to altered flow and pressure, Journal of The Royal Society Interface 6 (32) (2009) 293–306.

[227] C. A. Figueroa, S. Baek, C. A. Taylor, J. D. Humphrey, A computational framework for fluid-solid-growth modeling in cardiovascular simulations, Computer Methods in Applied Mechanics and Engineering 198 (2009) 3583–3602.

[228] J. S. Coogan, J. D. Humphrey, C. A. Figueroa, Computational simulations of hemodynamic changes within thoracic, coronary, and cerebral arteries following early wall remodeling in response to distal aortic coarctation, Biomechanics and modeling in mechanobiology 12 (1) (2013) 79–93.

[229] A. Menon, D. C. Wendell, H. Wang, T. J. Eddinger, J. M. Toth, R. J. Dholakia, P. M. Larsen, E. S. Jensen, J. F. L. Jr., A coupled experimental and computational approach to quantify deleterious hemodynamics, vascular alterations, and mechanisms of long-term morbidity in response to aortic coarctation, Journal of Pharmacological and Toxicological Methods 65 (1) (2012) 18 – 28.

[230] J.-J. Wang, A. B. O'Brien, N. G. Shrive, K. H. Parker, J. V. Tyberg, Time-domain representation of ventricular-arterial coupling as a windkessel and wave system, Heart and Circulatory Physiology 284 (4) (2003) 1358–1368.

[231] J. Murgo, N. Westerhof, J. Giolma, S. Altobelli, Aortic input impedance in normal man: relationship to pressure wave forms, Circulation 62 (1980) 105–116.

[232] M. O'Rourke, Mechanical principles. Arterial stiffness and wave reflection, Pathologie Biologie (Paris) 47 (1999) 623–633.

[233] M. O'Rourke, W. Nichols, Changes in wave reflection with advancing age in normal subjects, Hypertension 44 (2004) E10–E11.

[234] T. Murakami, A. Takeda, Enhanced aortic pressure wave reflection in patients after repair of aortic coarctation, Annual Thoracic Surgery 80 (3) (2005) 995–1000.

[235] S. Sherwin, V. Franke, J. Peiro, K. Parker, One-dimensional modelling of a vascular network in space-time variables, J. Eng. Math.Journal of Engineering Mathematics 47 (2003) 217–250.

[236] K. Azer, C. Peskin, A one-dimensional model of blood flow in arteries with friction and convection based on the womersley velocity profile, Cardiovascular Engineering 7 (2007) 51–73.

[237] C. Taylor, C. Figueroa, Patient-specific modeling of cardiovascular mechanics, Annual Review of Biomedical Engineering 11 (2009) 109–34.

[238] F. van de Vosse, J. de Hart, C. van Oijen, D. Bessems, T. Gunther, Finite-element-based computational methods for cardiovascular fluid-structure interaction, Journal of Engineering Mathematics 47 (2003) 335–68.

[239] K. Parker, An introduction to wave intensity analysis, Medical & Biological Engineering & Computing 47 (2009) 175–188.

[240] S. Pittaccio, F. Migliavacca, R. Balossino, G. Dubini, E.-T. Frund, V. Hjortdal, M. Smerup, E. Morre-Pedersen, M. R. De Leval, MRI-based multiscale models for the hemodynamic and structural evaluation of surgically reconstructed aortic arches, Journal of applied biomaterials and biomechanics 5 (1) (2007) 11–22.

[241] J. Charonko, S. Ragab, P. Vlachos, A scaling parameter for predicting pressure wave reflection in stented arteries, Journal of Medical Devices - T. ASME 3 (2009) 10.

[242] L. Formaggia, F. Nobile, A. Quarteroni, A one dimensional model for blood flow: Application to vascular prosthesis, in: Mathematical Modeling and Numerical Simulation in Continuum Mechanics, Springer-Verlag Berlin, Berlin, 2002, pp. 137–153.

[243] N. Stergiopulos, P. Segers, N. Westerhof, Use of pulse pressure method for estimating total arterial compliance in vivo, American Journal of Physiology 276 (2) (1999) 424–428.

[244] Z. R. Bulbul, E. Bruckheimer, J. C. Love, Fahey, W. E. J T Hellenbrand, Implantation of balloon-expandable stents for coarctation of the aorta: implantation data and short-term results, Catheterization and cardiovascular diagnosis 39 (1) (1996) 36–42.

[245] C. Duke, E. Rosenthal, S. A. Qureshi, The efficacy and safety of stent redilatation in congenital heart disease, Heart 89 (2003) 905–912.

[246] M. A. Hamdan, S. Maheshwari, J. T. Fahey, W. E. Hellenbrand, Endovascular stents for coarctation of the aorta: initial results and intermediate-term follow-up, Journal of the American College of Cardiology 38 (5) (2001) 1518 – 1523.

[247] J. S. de Lezo, M. Pan, M. Romero, A. Medina, J. Segura, M. Lafuente, D. Pavlovic, E. Hernández, F. Melián, J. Espada, Immediate and follow-up findings after stent treatment for severe coarctation of aorta, The American Journal of Cardiology 83 (3) (1999) 400 – 406.

[248] A. N. Redington, A. M. Hayes, S. Y. Ho, Transcatheter stent implantation to treat aortic coarctation in infancy, British Heart Journal 69 (1) (1993) 80–82.

[249] C. Ovaert, B. W. McCrindle, D. Nykanen, C. MacDonald, R. M. Freedom, L. N. Benson, Balloon angioplasty of native coarctation: clinical outcomes and predictors of success, Journal of the American College of Cardiology 35 (4) (2000) 988 – 996.

[250] A. T. Yetman, D. Nykanen, B. W. McCrindle, J. Sunnegardh, I. Adatia, R. M. Freedom, L. Benson, Balloon angioplasty of recurrent coarctation: A 12-year review, Journal of the American College of Cardiology 30 (3) (1997) 811 – 816.

[251] R. J. Walhout, J. C. Lekkerkerker, G. H. Oron, G. B. Bennink, E. J. Meijboom, Comparison of surgical repair with balloon angioplasty for native coarctation in patients from 3 months to 16 years of age, European Journal of Cardio-Thoracic Surgery 25 (5) (2004) 722–727.

[252] D. L. Fry, Certain histological and chemical responses of the vascular interface to acutely induced mechanical stress in the aorta of the dog, Circulation Research 24 (1) (1969) 93–108.

[253] S. Rodbard, Dynamics of blood flow in stenotic vascular lesions, American heart journal 72 (5) (1966) 689–704.

[254] J. Brice, D. Dowsett, R. Lowe, Hemodynamic effects of carotid artery stenosis, British Medical Journal 2 (1964) 1363–1366.

[255] D. Byar, R. V. Fiddian, J. T. Quereau, M. Hobbs, E. A. Edwards, The fallacy of applying the poiseuille equation to segmental arterial stenosis, American Heart Journal 70 (1965) 216–224.

[256] B. Eklöf, S. I. Schwartz, Critical stenosis of the carotid artery in the dog, Scandinavian Journal of Clinical & Laboratory Investigation 25 (4) (1970) 349–353.

[257] H. Verhaaren, S. D. Mey, I. Coomans, P. Segers, D. D. Wolf, D. Matthys, P. Verdonck, Fixed region of nondistensibility after coarctation repair: In vitro validation of its influence on Doppler peak velocities , Journal of the American Society of Echocardiography 14 (6) (2001) 580 – 587.

[258] M. R. Ebeid, Balloon expandable stents for coarctation of the aorta: current status and technical considerations, Images in Paediatric Cardiology 5 (2) (2003) 25–41.

[259] D. P. Giddens, R. F. Mabon, R. A. Cassanova, Measurements of disordered flows distal to subtotal vascular stenoses in the thoracic aortas of dogs, Circulation Research 39 (1) (1976) 112–9.

[260] B. I. Tropea, S. P. Schwarzacher, A. Chang, C. Asvar, P. Huie, R. K. Sibley, C. K. Zarins, Reduction of aortic wall motion inhibits hypertension-mediated experimental atherosclerosis, Arteriosclerosis, Thrombosis, and Vascular Biology 20 (9) (2000) 2127–2133.

[261] J. Pihkala, G. K. Thyagarajan, G. P. Taylor, D. Nykanen, L. N. Benson, The effect of implantation of aortic stents on compliance and blood flow. An experimental study in pigs, Cardiology in the Young 11.

[262] D. F. Young, F. Y. Tsai, Flow characteristics in models of arterial stenoses I. Steady flow, Journal of Biomechanics 6 (4) (1973) 395 – 410.

[263] K. Isaaz, R. Rieu, R. Pelissier, Effects of the shape of pre- and post-stenotic regions on the accuracy of Doppler in measuring pressure gradients across long segment stenosis (Abstr), Journal of the American College of Cardiology 11 (1988) 21.

[264] K. Isaaz, R. Rieu, R. Pelissier, Doppler derived pressure gradients: effects of energy losses associated with stenosis geometry (Abstr), European Heart Journal 12 (1991) 131.

[265] R. A. Levine, A. Jimoh, E. G. Cape, S. McMillan, A. P. Yoganathan, A. E. Weyman, Pressure recovery distal to a stenosis: Potential cause of gradient overestimation İ by Doppler echocardiography, Journal of the American College of Cardiology 13 (3) (1989) 706–715.

[266] W. Voelker, H. Reul, T. Stelzer, A. Schmidt, K. R. Karsch, Pressure recovery in aortic stenosis: An in vitro study in a pulsatile flow model, Journal of the American College of Cardiology 20 (7) (1992) 1585 – 1593.

[267] H. Baumgartner, H. Schima, G. Tulzer, P. Kühn, Effect of stenosis geometry on the Doppler-catheter gradient relation in vitro: A manifestation of pressure recovery, Journal of the American College of Cardiology 21 (4) (1993) 1018 – 1025.

[268] J. Niederberger, H. Schima, G. Maurer, H. Baumgartner, Importance of pressure recovery for the assessment of aortic stenosis by Doppler ultrasound: Role of aortic size, aortic valve area, and direction of the stenotic jet in vitro, Circulation 94 (8) (1996) 1934–1940.

[269] E. G. Cape, M. Jones, I. Yamada, M. D. VanAuker, L. M. Valdes-Cruz, Turbulent/viscous interactions control Doppler/catheter pressure discrepancies in aortic stenosis: The role of the Reynolds number, Circulation 94 (11) (1996) 2975–2981.

[270] C. Clark, The fluid mechanics of aortic stenosis-II. Unsteady flow experiments, Journal of Biomechanics 9 (9) (1976) 567 – 573.

[271] B. Liu, The influences of stenosis on the downstream flow pattern in curved arteries, Medical Engineering & Physics 29 (8) (2007) 868 – 876.

[272] R. Comolet, Statique et dynamique des fluides non visqueux, Mécanique expérimentale des fluides, Masson, 1982.

[273] Reflection and transmission of waves, `http://www.bg.ic.ac.uk/research/k.parker/wave_intensity_web/wia-6-1.pdf`.

[274] P. Moireau, N. Xiao, M. Astorino, C. Figueroa, D. Chapelle, C. Taylor, J.-F. Gerbeau, Biomechanics and Modeling in Mechanobiology 11 (1-2) (2012) 1–18.

[275] G. H. Gibbons, V. J. Dzau, The emerging concept of vascular remodeling, New England Journal of Medicine 330 (20) (1994) 1431–1438.

[276] B. L. Langille, Arterial remodeling: relation to hemodynamics, Canadian Journal of Physiology and Pharmacology 74 (7) (1996) 834–841.

[277] A. Vitarelli, Y. Conde, E. Cimino, S. D'Orazio, S. Stellato, D. Battaglia, V. Padella, F. Caranci, G. Continanza, O. Dettori, L. Capotosto, Assessment of ascending aorta distensibility after successful coarctation repair by strain doppler echocardiography, Journal of the American Society of Echocardiography 21 (6) (2008) 729 – 736.

[278] J. Leandro, J. F. Smallhorn, L. Benson, N. Musewe, J. W. Balfe, J. D. Dyck, L. West, R. Freedom, Ambulatory blood pressure monitoring and left ventricular mass and function after successful surgical repair of coarctation of the aorta, Journal of the American College of Cardiology 20 (1) (1992) 197 – 204.

[279] S. E. Cyran, M. Grzeszczak, K. Kaufman, H. S. Weber, J. L. Myers, M. M. Gleason, B. G. Baylen, Aortic recoarctation at rest versus at exercise in children as evaluated by stress Doppler echocardiography after a good operative result, The American Journal of Cardiology 71 (11) (1993) 963 – 970.

[280] A. C. Marshall, S. B. Perry, J. F. Keane, J. E. Lock, Early results and medium-term follow-up of stent implantation for mild residual or recurrent aortic coarctation, American Heart Journal 139 (6) (2000) 1054 – 1060.

[281] W. R. Milnor, Hemodynamics, Williams & Wilkins, Baltimore, Maryland, 1989.

[282] N. Westerhof, P. Sipkema, G. C. Van Den Bos, G. Elzinga, Forward and backward waves in the arterial system, Cardiovascular Research 6 (6) (1972) 648–656.

[283] A. Hughes, J. Wang, Jiun, C. Bouwmeester, J. Davies, N. Shrive, J. Tyberg, K. Parker, The reservoir-wave paradigm, Journal of Hypertension 30 (9) (2012) 1880–1881.

[284] S. Vermeersch, E. Rietzschel, M. Buyzere, L. Bortel, T. Gillebert, P. Verdonck, P. Segers, The reservoir pressure concept: the 3-element windkessel model revisited? Application to the Asklepios population study, Journal of Engineering Mathematics 64 (4) (2009) 417–428.

[285] J. P. Mynard, D. J. Penny, M. R. Davidson, J. J. Smolich, The reservoir-wave paradigm introduces error into arterial wave analysis: a computer modelling and in-vivo study, Journal of Hypertension 30 (12) (2012) 2446.

[286] P. Segers, A. Swillens, S. Vermeersch, Reservations on the reservoir, Journal of Hypertension 30 (4) (2012) 676–678.

[287] J. V. Tyberg, J. C. Bouwmeester, K. H. Parker, N. G. Shrive, J.-J. Wang, The case for the reservoir-wave approach, International Journal of Cardiology 172 (2) (2014) 299 – 306.

[288] N. Westerhof, B. E. Westerhof, Crosstalk proposal: Forward and backward pressure waves in the arterial system do represent reality, The Journal of Physiology 591 (5) (2013) 1167–1169.

[289] J. Aguado-Sierra, J. Alastruey, J.-J. Wang, N. Hadjiloizou, J. Davies, K. H. Parker, Separation of the reservoir and wave pressure and velocity from measurements at an arbitrary location in arteries, Proceedings of the Institution of Mechanical Engineers, Part H: Journal of Engineering in Medicine 222 (4) (2008) 403–416.

[290] P. Segers, S. Brimioulle, N. Stergiopulos, N. Westerhof, R. Naeije, M. Maggiorini, P. Verdonck, Pulmonary arterial compliance in dogs and pigs: the three-element

windkessel model revisited, American Journal of Physiology - Heart and Circulatory Physiology 277 (2) (1999) 725–731.

[291] B. Hametner, S. Wassertheurer, A. D. Hughes, K. H. Parker, T. Weber, B. Eber, Reservoir and excess pressures predict cardiovascular events in high-risk patients, International Journal of Cardiology 171 (1) (2014) 31 – 36.

[292] D. Woodrum, A. Romano, A. Lerman, U. Pandya, D. Brosh, P. Rossman, L. Lerman, R. Ehman, Vascular wall elasticity measurement by magnetic resonance imaging, Magnetic Resonance in Medicine 56 (3) (2006) 593–600.

[293] M. Sermesant, P. Moireau, O. Camara, J. Sainte-Marie, R. Andriantsimiavona, R. Cimrman, D. Hill, D. Chapelle, R. Razavi, Cardiac function estimation from MRI using a heart model and data assimilation: Advances and difficulties, Medical Image Analysis 10 (4) (2006) 642 – 656.

[294] C. Ethier, Computational modeling of mass transfer and links to atherosclerosis, Annals of Biomedical Engineering 30 (4) (2002) 461–471.

[295] T. Ideker, T. Galitski, L. Hood, A new approach to decoding life: Systems biology, Annual Review of Genomics and Human Genetics 2 (1) (2001) 343–372.

[296] J. Bols, J. Degroote, B. Trachet, B. Verhegghe, P. Segers, J. Vierendeels, Inverse modelling of image-based patient-specific blood vessels: zero-pressure geometry and in vivo stress incorporation, ESAIM: Mathematical Modelling and Numerical Analysis 47 (2013) 1059–1075.

[297] W. Nichols, M. O'Rourke, McDonald's Blood Flow in Arteries: Theoretical, Experimental and Clinical Principles, Hodder Arnold, New York, 2005.

[298] M. Draney, C. Xu, C.and Zarins, C. Taylor, Circumferentially nonuniform wall thickness and lamellar structure correlates with cyclic strain in the porcine descending thoracic aorta, in: ASME Summer Bioengineering Conference, Key Biscayne, Florida, 2003.